Design and development of novel absorber coating for solar collector applications

Claire Heather TREASE

This thesis dissertation is being submitted in partial fulfilment of the requirements of Kingston University for the award of Doctor of Philosophy

January 2017

Supervisors

Prof. P. Foot

Prof. A Augousti

Dedication and acknowledgements

This thesis is dedicated to my mum and dad. It is the second PhD thesis dedicated to my parents (the other being my younger brother's) but the help they gave me through this process has been indispensable and I wanted to acknowledge just how valuable that support has been. I want to express my deepest gratitude to my supervisors, Professor Foot and Professor Augousti, for allowing me freedom to explore and develop as a researcher. A big thank you goes to the technicians that made it possible for me to conduct my experiments, especially Richard Giddens, Simon Crust and Wendy Brosnan. I also want to thank Professor Pierscionek for her enthusiasm and encouragement with respect to stretching the boundaries of my research. Lastly, I want to thank my partner Dr. Mike Longman – it's been a long journey but we made it!

Although one is surrounded by colleagues, a PhD is ultimately a solitary experience and is as much an exploration of personal qualities as it is of scientific investigation. At an early age pupils are streamed into either arts or sciences and my background is in arts. I came to science late in life, but have found scientific exploration to be as inventive as painting a picture and it requires just as much in the way of imaginative processes. It could be argued that science is more creative as the very real boundaries constraining the work really stretch ones imagination. I am glad that I had a background in art, as it taught me the ability to keep trying new things – the essence of scientific research. Both disciplines are also an exercise in interpretation and I feel it is not a coincidence that many great scientists are also artists.

The written thesis is the very tip of the iceberg when it comes to representing the process of completing a PhD; just like the final painting does not wholly convey the journey that was made to complete the finished picture. For me the main feature that is missing from a written thesis is a true conveyance of the constantly improving, iterative processes involved in conducting scientific research. Having the confidence (almost the ability in fact) to make a mistake and then try again is needed in both disciplines as they both require constant refinement. Finally, learning a physical science has given me a deeper understanding of the world which in turn has conferred upon me a greater wonderment of the nature which inspires my artwork.

Abstract

Global average power consumption is 17 terawatts (10^{12} W) and the rate of solar energy received at the Earth's surface is more than 120 petawatts (10^{15} W). Therefore, the earth receives as much solar energy in one day as is used by the entire world in 20 years. Solar thermal collectors use absorber coatings and layers to convert incident radiation, via photothermal conversion, into useful energy i.e. heat. Re-radiation of this heat is minimised using a solar selective surface. Patterning non-thermal curing epoxy resins, in the micron scale, using electrohydrodynamic instability (EHD) patterning, could mitigate some of the challenges presented by other materials and methods used to produce these surfaces such as cost. Therefore, this was the objective of this study.

As a contribution to the field of electrohydrodynamic instability patterning, the method of using this process to shape a thin, non-thermal curing epoxy resin film, was developed and the materials and equipment used are presented. Epoxy pillared surfaces, with pillar spacings from 3-200 µm, were manufactured on silicon substrates using 30, 61 or 162 V and electrode gaps ranging from 3 – 40 µm. A way of replicating the fabricated surfaces using moulding was also developed and is also described here. The patterned surfaces were replicated onto various substrates and were tested for their interaction with infrared (IR) radiation. In order to explore the range of versatility of this technique for fabricating functional surfaces the structures surfaces were also tested as substrates for tissue culture.

To gain a better understanding and hence control over the use of electrohydrodynamic instability patterning with an epoxy resin, theories and numerical models of the process of electrohydrodynamic instability patterning were examined. Comparisons between predictions of results given by theory and our practical results are discussed since it was found that there was more disagreement between our results and theory when lower electric fields were being used. The studies of the interaction of the surfaces with IR radiation, and for use as tissue culture substrates, is also assessed and commented on. Lastly improvements that could be made and future work that could be undertaken is suggested.

Contents

List of Figures Chapter 1

List of Figures Chapter 2

List of Figures Chapter 3

List of Figures Chapter 4

List of Abbreviations

AC	Alternating current
AR	Antireflection
CNT	Carbon nanotube
CSP	Concentrated solar power
CVD	Chemical vapour deposition
DC	Direct current
De	Deborah number
DEGBA	Diglycidyl Ether of Bisphenol-A
EHD	Electrohydrodynamic
GM	General model
IMS	Industrial Methylated Spirit
IR	Infrared
ITO	Indium tin oxide
LD	Leaky dielectric
LPCVD	Low pressure chemical vapor deposition
MIT	Massachusetts Institute of Technology
MWCNT	Multiwalled carbon nanotube
Mw	Molecular weight
NIR	Near infrared
PANi	Polyaniline
PD	Perfect dielectric
PDMS	Polydimethylsiloxane
PECVD	Plasma-enhanced chemical vapor deposition
PMMA	Poly(methyl methacrylate)
PS	Polystyrene
PTFE	Polytetrafluoroethylene
PV	Photovoltaic
PVA	Polyvinyl alcohol
Re	Reynolds number
RF	Radio frequency
SEGS	Solar Energy Generating Systems
SEM	Scanning electron microscope
SERs	Surface-enhanced Raman spectroscopy
TEOS	Tetraethyl orthosilicate
THF	Tetrahydrofan
TISS	Thickness insensitive spectrally selective
UV	Ultraviolet
Vis	Visible

1. Introduction

Solar energy still has the potential to grow dramatically (Energy Initiative Massachusetts Institute of Technology, 2015). To demonstrate this global average power consumption is 17 terawatts and the rate of solar energy received at the Earth's surface is more than 120 petawatts (Chu & Meisen, 2011) (Energy Initiative Massachusetts Institute of Technology, 2015). This means that the earth receives as much solar energy in one day as is used by the entire world in 20 years (Chu & Meisen, 2011). Energy payback time is the time it takes for the cell to collect as much energy as was used in its production and is dependent on the type of system and its location. If there was no net gain solar energy would be useless. In a report prepared by the Fraunhofer Institute for Solar Energy Systems the payback times for solar cells was approximately 2.5 years in Northern Europe and approximately 1.5 years in the South. Assuming a lifespan for the solar cell of 20 years, although most are more than this, the energy payback is around 10 to 20 times more (Fraunhofer Institute for Solar energy Systems, ISE, 2016).

The installed capacity of solar energy has more than trebled in four years however its contribution to global power generation is still low at 1.1% (BP p.l.c, 2016). A study carried out by MIT in 2015 found that to realise the potential of solar energy, large cost reductions are still required and that the streamlining of manufacturing processes would be one route to achieving this (Energy Initiative Massachusetts Institute of Technology, 2015). For solar energy devices to be able to compete commercially with existing technologies they must be reliable, simple to manufacture and inexpensive (Trease, et al., 2013).

Solar energy collection devices can be roughly divided into two groups. Photovoltaic (PV) devices; which use photoinduced electron-hole production to convert incident radiation into electrical energy and solar thermal devices collect incident solar radiation and convert it to heat via photothermal conversion in a layer of absorber material; the heat is then transferred to a working fluid which is used for space heating or concentrated in high-temperature applications to drive a turbine to produce electrical energy. Solar absorber layers have been developed that use many methods to convert the sun's energy. Absorber layers for solar thermal devices have been produced that consist of micro- and nano-structured surfaces in which to trap radiation. Some collector layers for solar thermal devices have been developed that consist of a single layer of material as well as those that consist of many thin layers.

Both types of solar devices use antireflective (AR) layers to couple energy into the working layers and obtain the maximum efficiency. Antireflection layers can also consist of micro-/nano-structured and patterned surfaces (Trease, et al., 2013). Typically, the equipment costs and materials used in the production of the absorber and antireflection surfaces of these devices is high and has inhibited the large-scale uptake of these technologies.

The technique of electrohydrodynamic (EHD) patterning presents a simple method of creating micro- and nano-structured surfaces and despite having been known about for around 15 years, it has yet to be fully developed (Schäffer, et al., 2001). The use of electrohydrodynamic surface instabilities, offers the potential to pattern a surface at the micro-scale and smaller, using comparatively cheap equipment and materials, and it also requires no dedicated facilities such as a clean-room. The result could be lower costs involved in fabricating solar energy equipment.

The aim of this project is to investigate the feasibility of the use of EHD to develop a fabrication method for a structured layer that could have potential as an absorber coating for solar energy collection devices, or possibly be used as an antireflection layer.

Chapter 2 outlines the basic theoretical concepts that underpin the use of solar selective surfaces, their development as materials for use in solar devices and some of the methods involved in fabricating and characterising them. A review of the patents that have been published for solar selective surfaces is also presented.

Chapter 1 introduces the current state of the art with regards to EHD patterning. It reviews the progression that has been made in understanding the physical process. It also reviews theories which have given greater understanding of this process and can be used to design surfaces of the desired geometry. Chapter 1 Section 1.2 introduces the materials and applications to which EHD patterning has already been successfully applied.

Theories surrounding the mathematical interpretation of EHD patterning are summarised in Chapter 1 Section 1.3 and the assumptions that were made in the formulation of the theories are stated.

The experimental methods that were employed during the process of this study are covered in Chapter 2. This chapter presents the methods employed in fabricating the EHD patterned surfaces including manufacturing thin films from a cold cure epoxy, measuring the film thickness and measuring some other materials characteristics.

The surfaces that were fabricated from EHD experiments are given in Chapter 3. The response of some selected surfaces to IR transmission is also shown and the application of the surfaces as cell growth surfaces is introduced.

An analysis of the results of the EHD experiments is discussed in Chapter 4. A comparison of the results of the EHD experiments, with the results predicted by some of the theoretical models proposed is examined. The mathematical basis and assumptions made in theories are inspected and their applicability to the experiments performed here is assessed. Conclusions from this investigation, a critical analysis of this study and future work proposed are also covered in Chapter 4.

1.1 Solar Selective materials for photothermal energy conversion

Solar thermal systems are one of the two main methods for utilising the enormous potential of available solar energy (the other being photovoltaics). There are many designs of these systems on the market, but, for domestic low temperature use (approximately 150°C and below), they generally come in a flat plate or evacuated tube type device. Solar thermal collectors use absorber coatings and layers to convert incident radiation, via photothermal conversion, into useful energy i.e. heat (Bostrom, 2008). These coatings are typically very thin (on the scale of micrometres and less) and there are many ways in which solar energy is trapped in these working layers. Methods include surface roughness or surface patterning methods, which trap radiation between structures protruding from the surface and multi-layered coatings, which use the principles of interference to trap radiation between the layers.

Solar thermal collectors convert incident radiation into heat via photothermal conversion (Bostrom, 2008). The heat is transferred to a working fluid and used mainly for heating and electricity production (Figure 1.1). Device efficiency is determined by the fraction of energy lost compared with the amount of energy converted. Losses can be via conduction and convection which are minimised by using glazing and insulation (Bostrom, 2008). Energy can also be lost by re-radiation which is minimised using a solar selective surface (Bostrom, 2008).

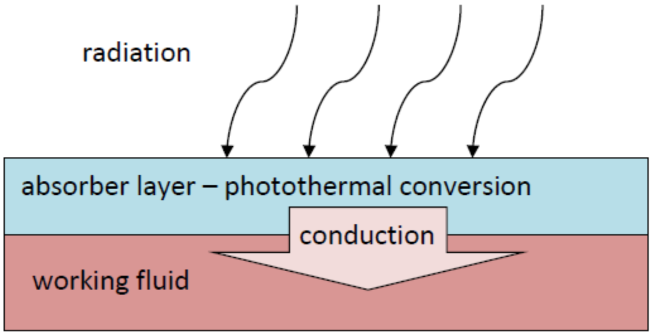

Figure 1. 1 Photothermal energy conversion.

Solar selective coatings began to be patented around the 1950's. A review of the patented coatings has been completed with a view to assessing the current state of the art. This review is summarised here from Trease, Hadavinia and Barrington 2013 (Trease, et al., 2013). The full paper can be found in Appendix A.

1.1.1 Solar selective surfaces: the state of the art

Radiation is an energy emission in the form of electromagnetic waves which travel at the speed of light. When radiation, such as solar radiation, is incident on a material, that material will absorb, reflect or transmit a fraction of the incident radiation. These properties are functions of the surface and its temperature and of the angle and wavelength of the incident radiation. They are related by the following:

$$\rho + \tau + \alpha = 1 \tag{1.1}$$

where ρ is reflectance, τ is transmittance and α is solar absorptance which are fractions.

Solar absorptance (α) is characterised by the ratio of the radiation absorbed by a material, to that of the solar radiation incident to the material and an ideal solar absorber would absorb all the incident solar radiation (Duffie & Beckman, 2006). At thermal equilibrium, for a given wavelength, the absorptance of a material is equal to its emittance ($\alpha = \varepsilon$) (Duffie & Beckman, 2006). The term absorptance is conventionally use when referring to solar selective surfaces since it is assumed that radiation is not transmitted through the layer, unlike the term absorbtion which refers to the amount of radiation that is absorbed when a beam is transmitted through a sample.

A theoretical perfect absorber, which absorbs all incident radiation, is known as a 'blackbody'. The reflectance of a blackbody would be $\rho = 0$. Since all the incident radiation is being absorbed, there is also no transmission hence $\tau = 0$. Therefore at thermal equilibrium, since absorption and emittance are equal ($\alpha = \varepsilon$), the radiant flux emitted by a blackbody at a given temperature is also at the maximum permissible according to (1.1) (Duffie & Beckman, 2006) (Trease, et al., 2013). At a given temperature and wavelength, the emittance (ε) of a real material is defined as the ratio of its radiance to that of a blackbody. This value is always less than one, since the radiance of a real material is never as great as that of a theoretical perfect absorber/emitter.

The emittance spectrum of a blackbody surface is entirely dependent on its temperature. The emittance spectra of 3 theoretical blackbodies, at the typical functioning temperatures of low temperature solar thermal devices, are shown on the left in Figure 1.2. Cooler bodies emit radiation with less energy, and hence at longer wavelengths. The solar spectrum is shown on the right in Figure 1.2. The range of the solar emittance spectrum is at lower wavelengths than that of the solar devices. The figure shows that an efficient surface would need to have high absorbance at wavelengths below 2.5-3 µm which correspond with the solar spectrum, and low emittance at wavelengths of around 2.5-3 µm and above to reduce thermal losses.

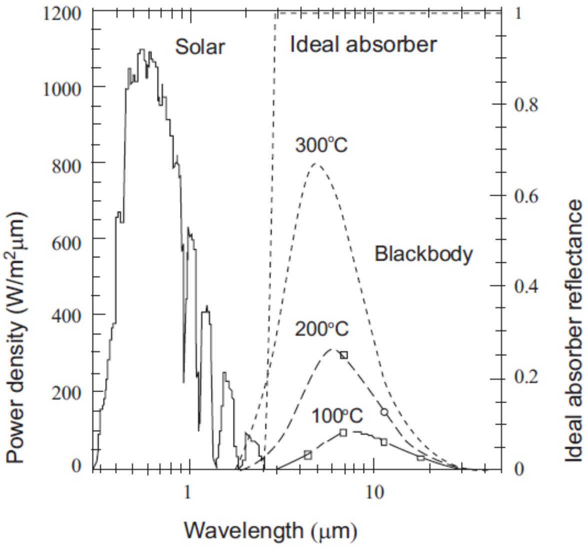

Figure 1. 2 Solar spectrum at air mass 1.5, with 3 blackbody emission spectra and the reflectance of an ideal solar selective coating (Katumba, et al. 2008).

As the temperature of the surface defines its emission spectrum, it also defines the wavelength of its peak emissive power. For materials at the temperature of solar thermal collecting devices (generally between 100 and 300 degrees for low to mid temperature devices) the peak emissive power is above a wavelength of around 2.5-3µm in the infrared (IR) spectrum. Conversely (due to the surface temperature of the sun at around 5000 degrees) the peak solar radiant power is below this, across the wavelengths of 0.3–3µm (Trease, et al., 2013) (Duffie & Beckman, 2006) (Kennedy, 2002). Both emissive peaks are shown in Figure 1.2.

Since emittance and absorptance at thermal equilibrium are equal ($\alpha = \varepsilon$) and, for a solar selective material, it can be assumed that none of the incident radiation is transmitted through the material, so $\tau = 0$. Therefore per equation (1.1), absorptance and hence emittance can be defined in terms of reflectance.

$$\rho = 1 - \alpha \text{ or } \varepsilon \tag{1.2}$$

Accordingly, it is possible to design materials that are both highly absorbing in the solar spectrum and have low emittance in the spectrum of their operating temperature, by changing its reflectance at the different wavelengths. A surface which changes its reflectance depending on the wavelength of the incident radiation is termed a selective surface. These reflectance requirements are also shown by the dotted line in Figure 1.2.

Non-selective coatings have a constant value of reflectance across the entire spectrum and so, as the temperature of the device increases, more energy is lost due to thermal emittance (Lampert, 1987). A solar selective surface that changes its reflectance at around 2.5-3µm absorbs virtually all the incident solar radiation but the energy is not then re-emitted as heat as the device warms up.

Solar selective coatings were first conceived during the 1950's when the need was identified for the absorber materials to become selective. This meant that higher temperatures could be achieved without the associated increase in emitted radiation. Solar selective coatings became evaluated by their solar absorptance and emittance (Tabor, 1959). The functionality of solar absorber coatings is defined out of 1 for both their ability to absorb radiation and their ability to emit radiation. In a review, published in 1983, Bogaerts and Lampert stated α and ε aims of 0.95 and 0.1 respectively (Bogaerts & Lampert, 1983). As the selective properties of solar absorber materials have improved the goals are now high. In 2002 Kennedy stated an aim for the coatings of devices operating at 500°C to have a solar absorptance of $\alpha= 0.98$ and thermal emittance of $\varepsilon= 0.05$ (Kennedy, 2002).

1.1.2 Methods of selectivity

Many design options and physical mechanisms can be used to selectively absorb solar radiation and many varieties have been patented. Single layer absorber coatings (such as paints or metal oxides) typically use an absorbing layer in conjunction with the reflecting metallic surface of the pipe containing the working fluid (Figure 1.3). The metal itself is highly reflecting and so has low emittance, however the coating has high absorbance. Once the heat has been transferred to both the pipe and the working fluid by conduction, the low emittance of the metal minimises the heat energy is lost. Single-layer coatings have been refined to multi-layer coatings which increases the absorption and selectivity of the device.

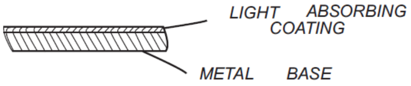

Figure 1. 3 Early patented cermet absorber coating (Tabor 1959).

The transition metals show selective absorbance although none are intrinsically selective to the solar spectrum (Tabor, 1959) (Bogaerts & Lampert, 1983) (Agnihotri & Gupta, 1981). Alternative layers of thin transparent metallic layers and dielectric layers function by trapping radiation between them and are called interference stacks. The multiple reflections between the layers increase the path length of the beam of solar radiation and hence increases absorption (Bogaerts & Lampert, 1983). Semiconductor layers, in tandem with a reflective metallic layer, absorb solar radiation due to their bandgap energies and have also been used as selective absorber materials (Tabor, 1959).

One of the most frequently used types of coating is a metal/ceramic composite or cermet. These materials consist of metal particulates in a dielectric matrix. The scattering effect of the metallic particles in the dielectric material, increases the path length of the beam of radiation within the layer and this enhances absorption. Examples include black chrome, developed by Tabor, and other metal oxide coatings (Tabor, 1959).

Structured surfaces (wavefront discriminators) have been developed which are selective to solar radiation; sometimes with pores or needle like structures which are at a scale comparable to the wavelength of the radiation spectrum being targeted (Figure 1.4). Shorter-wavelength radiation is absorbed by multiple reflections between the protrusions, whilst the surface acts as a smooth surface to longer wavelengths (Bogaerts & Lampert, 1983).

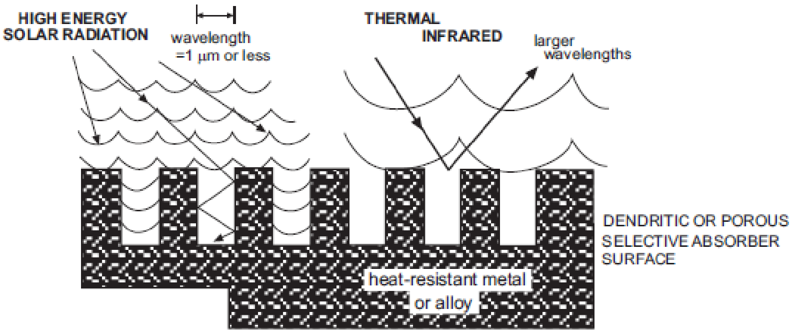

Figure 1. 4 Wavefront discriminating surface (Bogaerts and Lampert 1983).

Paint coatings are also a significant class and have utilised absorption methods ranging from semiconductor particulates to metal oxide pigments. Many selective surfaces use several of these methods combined to show selective behaviour such as a semiconductor with a structured surface.

Currently, a wide variety of solar devices exist for collecting and converting solar radiation to useful energy ranging, from solar ponds to power towers. Solar selective absorber materials are used in many types of device but predominantly in solar heaters, such as flat plate and parabolic trough collectors and in photovoltaic devices. Solar heaters can essentially be divided into two types: concentrating and non-concentrating (Selvakumar & Barshilia, 2012).

The non-concentrating types are typically used for domestic hot water and space heating purposes. They generally consist of either a flat plate coated in a solar absorbing material covering a series of pipes through which a fluid flows to be heated; or of a series of evacuated glass tubes containing an inner tube through which a working fluid flows. The inner tube is coated with a solar absorbent coating, which heats upon exposure to solar radiation, thus heating the working fluid (Selvakumar & Barshilia, 2012) (Kalogirou, 2009). In evacuated tube collectors, the coating operates in a vacuum. Therefore, the coating must be stable at high temperature not only in this environment but also in air, in case the vacuum is breached (Kennedy, 2002). Non-concentrating systems are generally considered to be low (T < 100°C) to mid (100°C < T < 400°C) temperature range devices (Kennedy, 2002) (Kalogirou, 2009).

Concentrating solar power (CSP) systems consist of a configuration of reflectors in the form of a trough or a series of mirrors that focus the sun's rays to heat a working fluid. These are the parabolic trough or power tower type collectors and are generally used for electricity generation. Concentrating devices typically operate across the mid to high (T > 400°C) temperature ranges (Kennedy, 2002) (Kalogirou, 2009). Both concentrating and non-concentrating types require solar absorbent coatings to obtain maximum efficiency.

1.1.3 Common deposition methods

The deposition of thin films and coatings encompasses many different techniques and methods. The early solar selective coatings mostly used electrodeposition and chemical immersion, but chemical vapour deposition (CVD) and vacuum deposition were also utilised (Bogaerts & Lampert, 1983).

During electrodeposition, the substrate is immersed in an electrolytic bath and the coating is deposited from this electrolyte (Tabor, 1959). Thermal oxidation was also used to deposit oxides on surfaces such as stainless steel, whereby the substrate was fired in an oven in air and the deposited surface was dependent on firing times and temperature (Sharma, 1981).

Chemical vapour deposition (CVD) deposits atoms or molecules on to a substrate from a chemical vapour precursor containing the coating material. The precursor material undergoes either thermal decomposition or a reduction, usually by hydrogen at high temperature, to deposit the coating. Additional gasses can be introduced into the system to produce compounds such as oxides (Mattox, 2010). CVD has many variants; plasmas can be used to decompose the vapour in plasma enhanced CVD (PECVD) and low pressure environments can also be used (LPCVD) (Mattox, 2010).

PVD is also an atomistic process that deposits an overlay material, onto a surface, atom by atom. The material to be deposited, or target material, is placed in a chamber with the substrate. The target material is then vaporised from a liquid or solid. It travels across the chamber to the substrate, in the form of molecules or atoms, where it condenses (Mattox, 2010).

Physical vapour deposition (PVD) processes, including vacuum (evaporation) deposition and sputtering, enable good control over many process parameters such as pressure during deposition. This allows a large variety of materials, including graded cermets, to be produced (Mattox, 2010). During evaporation deposition, the material to be deposited (target material) is thermally vaporised. This is achieved by heating the material with tungsten coils or elements or by a high-energy electron beam. During sputter deposition, the target material is vaporised by a physical rather than a thermal process by being bombarded with atoms. Momentum transfer ejects atoms from the surface of the target material (Mattox, 2010).

1.1.4 Cermets

Metal blacks and other single layer cermets

Initially single layer cermets, in the form of metal blacks (metal oxides), were the most widely developed material for solar selective surfaces and deposition methods were primarily electroplating or wet chemical etching.

Around the beginning of the 1990's, the Council of Scientific and Industrial Research (CSIR) in India filed the first in a series of patents for solar selective coatings which contributed significantly to the manufacture of solar absorber plates. US5019223 (Grips, et al., 1991), disclosed an improved black chromium plating bath and was patented in several countries including Australia, Europe, Canada and the US. It has since been licensed to at least 15 companies and became known as the Nalsun coating (Rajagopal, 1999).

This widely employed commercial coating became one of the most utilised in India (Rajagopal, 1999). Prior art coatings required temperatures of less than 20°C with current densities of between 430-2153mA/cm^2. These techniques entailed significant cooling due to the high current densities. The process disclosed in the Nalsun patent required no refrigeration i.e. was performed at room temperature and at normal current densities 86-323mA/cm^2 (previous coatings deposited at room temperature tended to be powdery) (Grips, et al., 1991). Moreover, since the bath did not contain any organic additives, it was free of the carbon that introduced carbonaceous impurities which diminished the coating's solar collection ability. The optical properties of this coating were $\alpha = 0.97$ and $\varepsilon = 0.1$. The bath comprised an aqueous solution of free chromic acid containing ions of nitrate, borate and fluorosilicate and it was the use of these three catalysts that produced a black chrome coating at room temperature and low current densities (Grips, et al., 1991).

Manufacturing techniques were moving away from wet chemical methods and electroplating since, by utilising chemicals such as cyanide and ammonium hydroxide, these processes involve the production of waste materials that have environmental implications (Straub, 1977) (Schardein & Lloyd, 1978). Thus, deposition processes such as evaporation were becoming far more widely employed and these expanded the range of materials used in absorber coatings (Lazarov & Mayer, 1997) (Hall & Gunning, 1993).

Other significant contributions to the field of solar thermal absorbers were made during the 1990's. M. Lazarov researched and developed the reactive evaporation deposition process of a new cermet coating of the chemical form MNxOy. Here x and y ranged from around 0.1 to 0.7 and M was a group IV metal, preferably titanium, producing the coating known as TiNOx. This coating improved upon the properties of previous coatings of this composition type and especially increased their stability (Lazarov & Mayer, 1997) (Lazarov & Mayer, 1998). In particular, Lazarov identified the importance of the nanoscale voids as a decisive feature of the functionality of the coating.

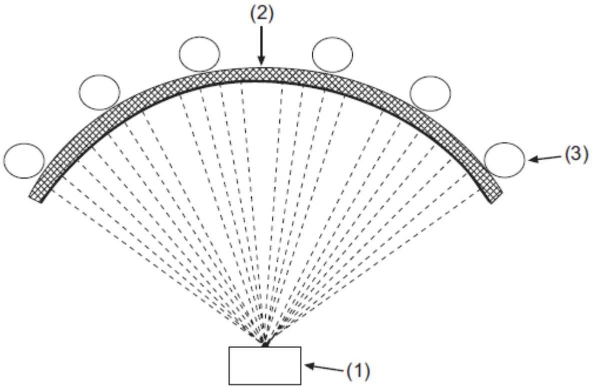

Figure 1. 5 Metal substrate (2) passed over an electron beam evaporator (1) being held in place by rollers (3) (Lazarov and Mayer 1998).

Multilayer Coatings

The deposition of black chrome is carried out as a single layer however at a microscopic scale, it contains gradations, where the metallic chrome content increases with depth (Selvakumar & Barshilia, 2012). Many coatings however are purposefully deposited as multiple layers. The individual layers in these coatings serve many purposes. Some additional layers are part of the optically active system, such as the inclusion of highly IR reflective layers to impart low emissivity to the coating. Others are added, to aid adhesion for example, and do not contribute to the optically active layers of the coating.

Interference stacks are multilayer coatings which absorb radiation due to multiple reflections between alternate metal/dielectric layers, as described previously. Some have been patented, but the majority of multilayer coatings utilise a cermet absorber layer, in combination with other materials such as reflective layers, to form an absorber tandem (Schmidt, 1966).

Graded cermets, where the metal volume fraction changes throughout the layer as a function of depth, or composed of multiple cermet layers with varying volume fractions, are the result of purposefully manipulating process parameters during deposition. The refractive index of the material changes in accordance with the variation in volume fraction so aiding absorption (Kennedy, 2002). Over several decades, most particularly during the 1990's, the University of Sydney made significant contributions to the field of solar thermal energy, including multilayer solar selective coatings and manufacturing processes. Many of these coatings involved the use of graded cermet layers and layers with differing volume fractions (Harding, et al., 1978) (Yin, et al., 2009) (Zhang & Mills, 1997) (Mills, 1986) (Zhang, et al., 1996).

The biggest obstacle to the progress of large scale solar thermal electricity installations has been, and to a great extent still is, the development of low cost deposition processes and absorber coatings that operate at elevated temperatures. In the mid-nineties, Zhang patented a new commercial scale manufacturing process for coating collector tubes. The patent was for a cylindrical DC magnetron sputtering techniques which was subsequently used by the Beijing company Turbosun to manufacture solar collector tubes (Zhang & Mills, 1997) (Zhang, et al., 1998) (Zhang, 2000).

During the 1980's, Luz International installed a large solar power station using parabolic trough concentrating solar collectors in the Mojave Desert, California. This Solar Electricity Generating System (SEGS) plant had a rating of up to 80MW (Boyle, 2004). Zhang's patented process was aimed at replacing the molybdenum aluminium oxide ($Mo\text{-}Al_2O_3$) coatings, such as those used at the SEGS plant in Luz, since the process involved lower costs than those incurred with the $Mo\text{-}Al_2O_3$ coatings (Zhang, et al., 1998).

Having performed a numerical optimisation study on the configuration of cermets with respect to gradation and layering, Zhang also published an individual patent for a cermet composed of layers with differing metal volume fractions. The thickness of the layers was designed so that they were substantially IR transparent (Zhang, et al., 1996). Zhang had begun with a ten-layer model which converged to close to a double layer cermet as shown in Figure 1.6, demonstrating that the ideal configuration was two layers (Zhang, 2000). The model demonstrated that the benefits of adding further layers were diminishingly marginal (Zhang, et al., 1996).

The outer layer had a high metal volume fraction and the inner layer a low metal volume fraction conferring different refractive indices to the materials. Solar radiation was therefore absorbed by internal absorption and phase cancellation interference (Zhang, et al., 1996) (Zhang, et al., 1998).

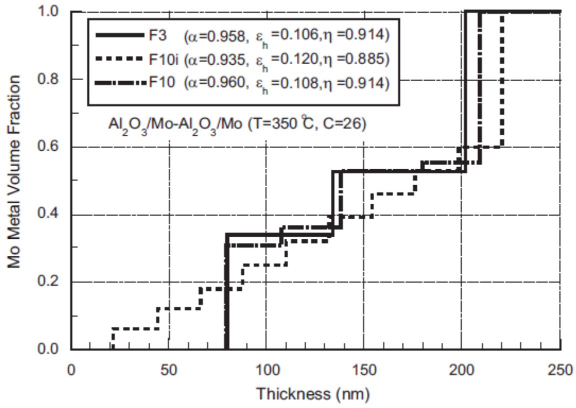

Figure 1. 6 Optimisation of cermets layers for 3 different layer configurations showing the Mo volume fraction and thickness of each layer and the absorptance (α), hemispherical emittance (ε) and photo-thermal conversion efficiency (η) values for the 3 coatings (Zhang 2000).

Since 2000, few patents for cermet absorber coatings deposited as single layers have been sought and recent patented cermet coatings tend to consist of multiple layers. Devices operating at higher temperatures leads to greater issues with degradation, the reduction of adherence of the layers and the diffusion of the metal substrate, all of which are accelerated by the increase in temperature. The diffusion of the metal into the optical layers results in the reduction of the properties of the coating. These issues have led to increasingly complex designs including multiple diffusion barriers within the optically active layers. Design software that allows theoretical optimisation of the layering, is increasingly utilised and has resulted in complex coatings with improved properties. Vapour and sputter depositions and sol-gel techniques have become the favoured deposition processes. The cermet layers are often deposited with varying volume fractions, such as those developed by Zhang, but some coatings still use a constant volume fraction in the cermet layers (Zhang, 2000).

Even now metal blacks are used. In the patents US6692836 (Reichert & Ganz, 2004) and US2020073988 (Reichert & Ganz, 2002) ,Reichert and Ganz patented a multilayer coating with a layer of chrome oxide as the absorber. The coating contained 4 layers as shown in Figure 1.7. The intermediate layer (2), on the surface of the substrate (1), inhibited the corrosion of the substrate as did layer (7) on the underside of the substrate. The other three top layers served as the optically active layers and included a low emittance metallic layer (6) of Au, Ag, Cu, Cr, Al and/or Mo, a high absorbance layer of chromium oxide CrOx where $0 < x < 3$ (5) and an antireflective (AR) layer of SiOy where $1 \leq y \leq 2$ (4). These could be deposited in a variety of ways including sputtering and chemical vapour deposition (CVD). Layer (8) is an optional decorative layer.

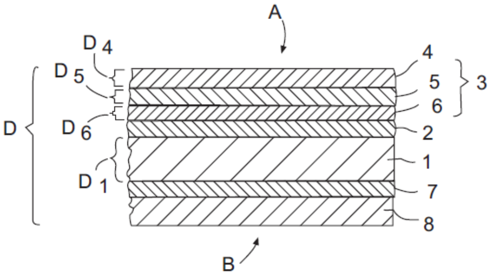

Figure 1. 7 Single volume fraction multilayer coating. Side B is the side remote from the optical system (Reichert and Ganz 2004).

Kennedy at the National Renewable Energy Laboratory (NREL) Colorado identified several potential materials that could be used to obtain high temperature selective coatings. These were combined in multiple layers using modelling software to optimise performance (Kennedy, 2008). A patent was subsequently published containing these coatings shown in Figure 1.8 (Kennedy, 2010). Multiple layers were modelled since they are simpler to model than entire cermet layers (Kennedy, 2008). The materials chosen were those with high melting temperatures including titanium, zirconium and hafnium metal carbides, oxides and nitrides, the highest of which was hafnium carbide (HfC) with a melting temperature of 3316°C (Kennedy, 2010).

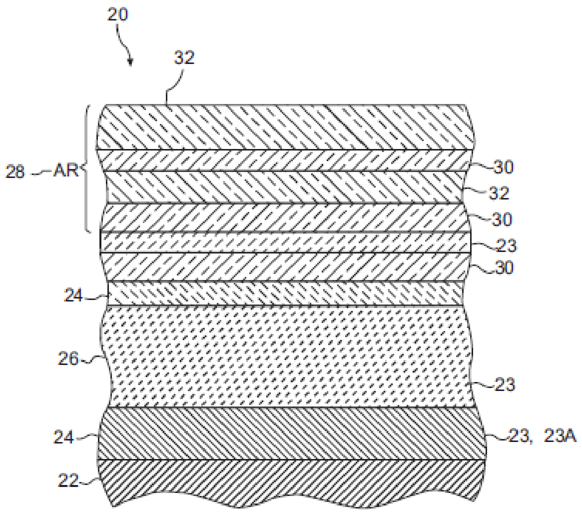

Figure 1. 8 NREL multilayer stack (C Kennedy 2010).

In the NREL multilayer stack (Figure 1.8) (22) is the substrate material, (24) is an optional IR reflective layer of a noble metal or TiSi, (26) is the absorber layer consisting of various compounds including TiAlN or compounds of Zr or Hf and the AR layer (28) consisted of alternately deposited materials of high and low refractive indices (30, 32) such as titania and silica (Kennedy, 2010).

From 2008, Schott Solar AG assigned several US patents and European patents with US equivalents, for multilayer coatings using cermets addressing a variety of issues. In the patent US7793653 (Kuckelkorn & Graf, 2010) presented a method of depositing an oxide layer on the surface of a substrate, which reduced diffusion and enhanced the adherence of the absorber material which was deposited over the oxide. The oxide was produced by polishing the substrate and then adjusting the surface to a roughness of r < 0.3μm. The diffusion barrier layer was then formed from thermal oxidation of the substrate. The depth of the oxide created depended on the initial surface roughness i.e. the greater the roughness the thicker the oxide layer. The oxide was followed by a metallic reflective layer, a cermet absorber layer and an antireflective layer with the absorber layer being deposited under vacuum conditions.

NREL recognised that alternate layers can resolve modelling issues regarding the use of cermets and similarly in the patent US2011249326 (Yuste, et al., 2011) presented a process whereby a mixture of dielectric and metallic layers were alternately deposited. This avoided the complicated process of constructing an entire cermet in one layer.

During vapour deposition, stoichiometry is conditioned by the composition and pressures of the gases in the vacuum chamber in relation to the evaporation rate and hence consumption of the reactive gasses. The evaporation rate is dependent on cathode power and, thus, the deposition process can be complicated and difficult.

Vapour Deposited Graded and Varying Volume Fraction Cermets

In 2009 CSIR patented a sputter deposited multilayer cermet coating, the aim of which was to produce a material suitable for use in high temperature applications whilst using environmentally friendly processes (Barshilia, et al., 2009). In the patent US7585568 (Barshilia, et al., 2009) presented a coating that contained two absorber materials comprising a layer of titanium-aluminium nitride (TiAlN) with high hardness and a second layer of titanium-aluminium oxynitride (TiAlON) that had high thermal stability and higher hardness. A third anti-reflection layer of silicon nitride (Si_3N_4) which had high hardness and oxidation resistance was also added. The first absorber layer had a high metal volume fraction and the second absorber layer a lower metal volume fraction. The novelty of this coating was that it had a very high thermal stability in air.

Hultmark published the patent US6171458 (Hultmark, 2001) assigned to Sunstrip, now S-Solar, who have successfully commercialised solar absorber coatings. Hultmark's invention was for a graded cermet and its coating process by sputter deposition. The important inventive step was that reactive oxygen gas was fed into the sputter deposition chamber, and that the deposited metal partly oxidised whilst it was being deposited. This created a coating which was a grain mixture of both metal and metal oxide. The amount of metal in the coating was decreased at the surface by an increase of oxygen during deposition. The metals Ni, Cr, Co, Mo, or a similar mixture could be used but the preferred embodiment was a nickel chromium alloy. The optical properties were $\alpha = 0.96$ and $\varepsilon = 0.1$. The method involved in the patent reduced manpower by 60% so reducing manufacturing costs and furthermore no environmentally harmful products were created by the sputtering process.

Antonaia published the patent W02009107157 which contained a multilayer coating again using a graded cermet this time of tungsten-aluminium oxide (W-Al_2O_3) (Antonaia & Esposito, 2009). The reflective layer used was tungsten and the antireflective layer was aluminium or silicon oxide. The object of the invention was to obtain a coating which was also operable at 580°C and was deposited by DC, radio frequency (RF) and reactive sputtering. The W-Al_2O_3 graded cermet performed well at high temperatures with high absorption in the solar spectrum. A layer of W-Al_2O_3 was first deposited on the steel substrate to prepare for the tungsten (W) IR reflective layer. The W-Al_2O_3 layer promoted the growth of the reflective phase of W which was next deposited. The layer which then followed was that of the graded W-Al_2O_3 cermet layer which was finally coated with an antireflective layer of alumina or silica (Antonaia & Esposito, 2009).

Sol-gel Deposited Cermets

The sol-gel process has been known for over a century. It was one of the first deposition techniques used for solar absorbers and, whilst not one of the preferred methods originally, has been utilised throughout the development of the coatings (Greenberg, 1977). Many of the substantial advances that were made in this field began in the 1980's and more recently sol-gel techniques have become one of the favoured deposition methods. During the process, chemical reactions are used to create an inorganic network in a solution forming a gel and any precursors which can form this kind of network can be used (Orel & Orel, 1990). The technique allows good control over particle size and high homogeneity throughout the deposited material, both necessary for the deposition of thin coloured layers of material (Dimitriev, et al., 2008).

The sol-gel process provides many advantages over other deposition methods in that it is both low temperature and low cost. It offers the ability to manipulate many aspects of the coating including microstructure and purity (Bayati, et al., 2010). Avoidance of the use of complex vapour deposition processes is often a stated reason for using the process (Es-Souni, 2009) (Clasen & Nejati, 2010).

Another common feature of sol-gel deposited coatings is the use of nanoscale particles (Bostrom, 2008). After joint research, Bostrom and Westin have both published nickel-alumina sol-gel deposited coatings with equivalents assigned to Sunstrip (Bostrom, 2008) (Boström, et al., 2008) (Westin, et al., 2006). Bostrom patented a coating containing absorber layers with varying volume fractions the layers of which are shown in Table 1 (Bostrom, 2008). The preferred embodiment is nickel nanoparticles in an alumina dielectric. The gel deposition consists of mixing alumina and nickel precursor solutions in the required ratios and spin-coating the resulting mixture onto a substrate. This layer is cured by heating in an oxygen free atmosphere or by UV light prior to the final heating to cure the silica antireflective layer (Bostrom, 2008). The material produced contains metallic nickel. Tetraethoxysilane (TEOS) is used as a precursor to deposit the silica layer and the solution is again spin coated. The object of the coating was to provide improved absorptance and cost efficiency and avoid vacuum deposition techniques by using ambient pressure.

Table 1. 1 Coating Layers in patent US20080210219 (Bostrom 2008).

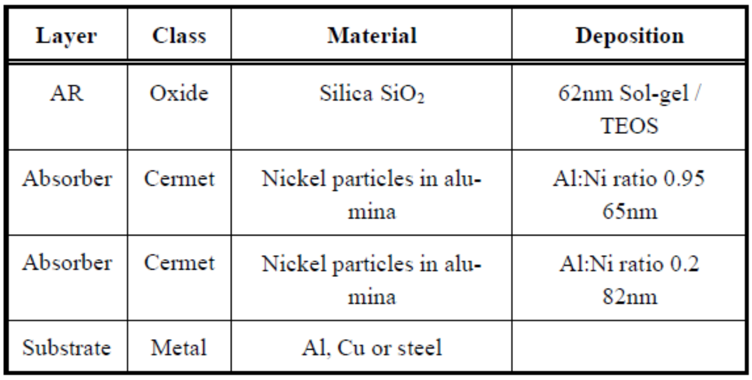

Layer	Class	Material	Deposition
AR	Oxide	Silica SiO_2	62nm Sol-gel / TEOS
Absorber	Cermet	Nickel particles in alumina	Al:Ni ratio 0.95 65nm
Absorber	Cermet	Nickel particles in alumina	Al:Ni ratio 0.2 82nm
Substrate	Metal	Al, Cu or steel	

A metal salt solution was prepared by combining solutions of two or more metal salts for a sol-gel coating in WO2006073357. The first solution contained at least one metal-alkoxide compound capable of forming a ceramic oxide, the metal preferably being selected from one of the Al, Fe, Ga, Mg or Ca lanthanides. The metal in the second solution should be more easily reducible and could be selected from Co, Ni, Cu, Pt, Ag, Au, Bi, Pb, Sn, Fe, Ru, W, Mo, or V. The resultant mixed solution could be applied to a substrate in many ways including painting, dipping or spin coating.

Patent US20090269487 (Es-Souni, 2009) also described a sol-gel deposited film avoiding the complexity of PVD coatings and the vacuums required. The invention was based on known techniques but with the novel step of adding silver ions, in the form of silver nitrate, to a titanium dioxide precursor solution. The dried material therefore contained between 50-70% silver. Another inventive step was the illumination of the coating, with visible light at a power density of 25-75Wcm^{-2}, during the drying and crystallizing stages. Both steps increased the absorption of the material.

There are however improvements to be made to sol-gel deposition processes. Patent US20100035081 (Clasen & Nejati, 2010) presents a technique whereby the cermet coating was formed by spraying or immersion in an alcohol or aqueous solution thus avoiding vacuum deposition methods and avoided the use of expensive metal alkoxides.

The solution contained the ceramic component of the cermet in the form of nanoscale particles and the metallic portion of the cermet in the form of its ions.

1.1.5 Paints

Historically solar water heaters have been coated with black paint and, during the early developments of solar selective coatings, paints were used as alternatives to the more complicated and expensive deposition methods of wet chemical and electroplating. Despite this, there are fewer patented paint coatings than cermets, although paints, such as Solarect-Z and Solkote Hi/SORB-II, have enjoyed commercial success (Kennedy, 2002). The selectivity of paint coatings has raised several issues. Some paints that have been used for solar applications, such as Thurmulox with both α and ε =0.8-0.85, show practically no selectivity and are used for their ease of application and cost benefits (Bogaerts & Lampert, 1983). Many of the black paints produced can only be termed as moderately selective since they show high absorptance across the solar spectrum but they often also have high emittance in the IR spectrum, for example Solarsorb C-1077 with α = 0.9 and ε = 0.6-0.8 (Bogaerts & Lampert, 1983).

Paint coatings have three essential elements: the pigment, the binder and the solvent (Orel & Orel, 1990). A thickness sensitive spectrally selective (TSSS) paint results when the low emissivity of the metal substrate confers a low emissivity to the coating. Hence, the paint needs to be applied in a thin layer and so is termed thickness sensitive (Orel & Orel, 1990) , (Hoeflaak & Jonkers, 1985). In addition to spectrally selective absorber particles or pigments, the paints can also have reflective metallic flakes added. The metal flakes take on the role of imparting low emittance to the coating as opposed to using the low emittance properties of the substrate material. Such paints are therefore termed thickness insensitive spectrally selective (TISS) paints (Orel & Orel, 1990).

Initially, paint coatings often used semiconductor materials as absorber particles. For example, US4011190 (Telkes, 1977), published in 1977, developed a pigment of reflective metallic particles such as zinc, coated with an absorbent semiconductor such as copper sulphide.

Whilst paint coatings present many benefits with regards to their ease of deposition they also have many issues associated with them. One issue with TSSS paints is that the binder material, which is usually a polymer, exhibits high emittance and can readily degrade at temperature (Lampert, 1987). To overcome the issues of the optical properties of the binder, US4153753 (Woodman & Fischer, 1979) developed a novel approach whereby an absorbing pigment, such as oxides of copper, cobalt, iron, or nickel, was simply pushed into the surface of the substrate, or a binder was applied to the substrate and the powdered absorber material was applied to the sticky surface of this binder material.

Transfer-Electric GmbH. Germany, who produce Solarlack, a solar absorber paint with $\alpha = 0.95$ and $\varepsilon = 0.86$, assigned a paint coating patent filed in the mid 1970’s in several countries including Germany and the UK. GB2004770 (Reuter & Menzel, 1979) disclosed a paint coating, using a carbon black pigment in the form of furnace soot. Carbon black is used as it behaves substantially as a black-body absorber. This coating addressed the issue of brittleness due to ageing that occurs in organic paints which are essentially plastics containing about 5% by weight of carbon black pigment. This brittleness renders the coating unable to withstand the extreme temperature fluctuations of the solar cycle. The coating in GB2004770 was achieved by using a mixture of an aqueous alkali silicate solution and an aqueous carbon black dispersion and in one embodiment was ageing and temperature resistant from - 60°C to over 400°C.

The challenge of developing a highly selective paint coating was commented on in 1986 by Lampert. He stated that a highly selective paint did not exist at that time and that there were few that exhibited solar selectivity and were commercially available. He also observed that if a stable paint coating, that offered the selectivity of black chrome, could be developed the solar coating industry would be revolutionized (Lampert, 1987). Although paint coatings have not seen the same volume of patented designs and process as other coatings, many advances have been made, some during the 1980’s. Various pigments were used including metal oxides and spinels (Hoeflaak & Jonkers, 1985) (Woodman, 1981) (Van Buskirk, 1982). Aluminium flakes were used in TISS paints due to lower costs (Hoeflaak & Jonkers, 1985).

Other binder materials have also been developed. Needham utilised carbon black in an arylene sulfide polymer, chosen for its high thermal stability and the availability of materials (Needham, 1981); Van Buskirk utilised fluorine containing binders such as copolymers of vinylidene fluoride (Van Buskirk, 1982). As with the other coating types, increasing their operating temperatures was a focus for development.

Many of the early absorber coatings developed were for domestic use at low temperature (below 100°C). However the eighties saw the first real advances in electricity generation from solar thermal collectors (Boyle, 2004). This requires higher operating temperatures and is achieved by constructions such as parabolic trough concentrator systems. Power towers, having a central receiver in conjunction with a field of heliostats (Figure 1.9), were also developed in addition to the parabolic trough plants such as those developed by Luz (Boyle, 2004). Incident solar radiation (14) is reflected (16) from reflective surfaces (11) to the collector (10) at the top of the tower (12).

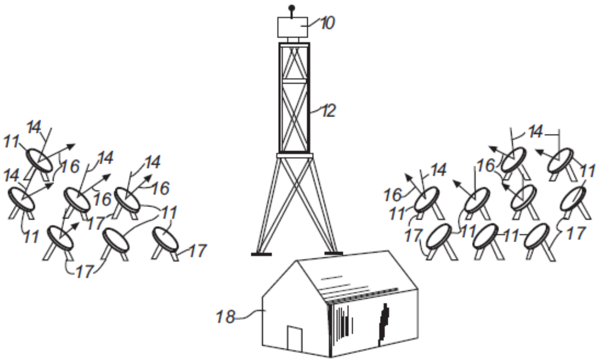

Figure 1. 9 Solar power tower with a field of heliostats.

Many selective coatings fail at high temperature. In order to overcome this, in a patent assigned to Exxon, who have also commercially produced solar paint, Muenker patented a high temperature coating designed for use in power tower type devices that operate at more than 287°C (Bogaerts & Lampert, 1983) (Muenker & Young, 1981). The coating contained a mixture of metal ferrite or oxide pigments such as cobalt oxide and nickel zinc ferrite. The coating could be applied by plasma flame spraying or in a conventional paint fashion with a silicate binder. Muenker also focussed on the value of absorbency to increase the operative properties of the material, achieving an α value of around 0.95. The extent of the emittance value was not considered an issue and resulted in $\varepsilon = 0.9$.

Over recent years several new paint coatings have been commercialised and much research into paint coatings has been carried out by Orel (Orel & Orel, 1990) (Orel, et al., 1996) (Kunic, et al., 2011). Orel has patented many solar thermal coatings particularly in Slovenia and in 2010 Alanod, who produce several solar coatings, including Mirosol, assigned WO2010133693 (Selvakumar & Barshilia, 2012) (Kozelj, et al., 2010). This patent disclosed black and coloured paint coatings applied by a coil-coating process amongst others. The properties of the pigments were altered by dispersion in an aminosilane solvent solution. The binders used include silicon-polyester and the core of the invention was that the mixing process led to a bonding of silanes onto the pigment surface thus altering its properties. The resultant pigment gave enhanced covering efficiency and formed a stable dispersion at much higher loads than others. It can be used in both TISS and TSSS paints.

Norsk Hydro ASA, who have recently launched the coating Hyselect, have assigned at least two solar thermal absorber patents, one for a commercialisation process for a sol-gel based multilayer coating where the absorber layer contained pigments as in a paint coating (Norsk Hydro ASA, 2010). Filed in 2007 and assigned to Hydro Aluminium Deutschland GmbH, US20100236543 (Oetting, et al., 2010) disclosed a coil coating manufacturing process which had the benefit of lower costs. An adhesion or primer coat was initially applied and the coating was multi-layered with the thicknesses of the functional coats between 0.0005 and 0.02mm. In the main embodiment of the invention roller coaters and a sol-gel process are used, but a spray or powder coating technique could also be used. The coil-coating process mitigates the costs of the vacuum locks required for PVD or CVD installations. Nanoparticles were used in the absorber layer which consists of metallic oxides or pigments such as titanium nitrite or titanium dioxide. The final material was an antireflective layer.

1.1.6 Semiconductors

Semiconductors were among the first class of materials to be researched and patented for solar selective absorbers. They have an inherent selectivity which is a result of interactions with photons that have energies greater than the bandgap of the semiconductor material (Bogaerts & Lampert, 1983). One early solar absorbent coating patent published in 1961 consisted of a layer of semiconductor black coating, such as vacuum deposited tellurium, between two layers of rock salt (Golay, 1961).

During the 1970’s, whilst the selective properties of coatings based on semiconductor materials were well understood, there were also fewer patents published for solar selective surfaces based on semiconductor materials than for cermets and other multilayer coatings. Semiconductors were utilised as pigments in paints as described previously but were also deposited as layers in various designs. When deposited over a reflective metal substrate they acted as an absorber in a semiconductor tandem. This type of coating was patented by McMahon after research into the use of lead sulphide (PbS) on an aluminium substrate. Most semiconductors are reflective, however PbS has an unusual surface topology which reduces its reflectance and so aids its absorptance. McMahon's coating achieved optical properties of $\varepsilon = 0.03$ and $\alpha = 0.9$ (McMahon & Green, 1997) (McMahon & Jasperson, 1974).

Semiconductors were also used as heat mirrors in conjunction with an absorber layer such as black enamel. In this case the semiconductor layer is transparent to radiation in the visible range but reflects IR radiation so imparts low emissivity to the coating (Bogaerts & Lampert, 1983) (Agnihotri & Gupta, 1981). In 1983, Bogaerts and Lampert stated that relatively little attention had been paid to this design although De Jong still patented two coatings using this concept (Bogaerts & Lampert, 1983) (De Jong, 1978) (De Jong, 1980).

At the beginning of the 1980’s, several semiconductor based selective coating patents were published, but semiconductor based absorbers have not had the same commercial success as cermet or paint coatings (De Jong, 1980) (Allerd, et al., 1986) (Spanoudis, 1982). In 1980 De Jong patented an improvement to the previously published indium oxide on enamel coating, to overcome faults of the enamel being attacked by the semiconductor layer and the environmental implications of spraying organic solutions onto hot surfaces. A fluorine doped tin oxide is used in a similar deposition method whereby it is sprayed onto an enamel surface which is in the process of cooling (De Jong, 1980).

The combination of the optical properties of both a layer of a conventional semiconductor combined with a manipulated surface topology was also utilised in some patented coatings (Gilbert, et al., 1981) (Craighead & Howard, 1981). Craighead patented an etched semiconductor surface. This surface was silicon, germanium or gallium arsenide etched by reactive sputtering to produce columnar voids in the semiconductor layer as shown in Figure 1.10 (Craighead & Howard, 1981). In recent years, few coatings using conventional semiconductors have been patented.

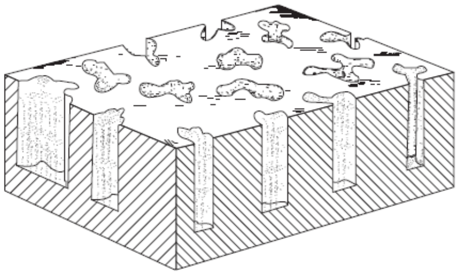

Figure 1. 10 Reactive sputter etched semiconductor surface.

1.1.7 Surface texturing

The modifications to the optical properties of a surface which can be made by altering its topology have been used in other ways since the initial development of selective surfaces. Again, such coatings have not had the same commercial success as paint and cermet coatings. The basic principles of the designs of these surfaces have changed little but refinements have been made to manufacturing processes.

Assigned to US Energy Research, US4048980 (Googin, et al., 1977) discloses a carbon coating containing micropores which effectively behave as “black holes” to visible radiation. US4148294 (Scherber & Dietrich, 1979) also produced a microporous oxide coating (12) in which the pores were subsequently filled with microscopic nickel rods (14) shown in Figure 1.11. The spacing of the rods is too close to allow the emission of low frequency IR radiation.

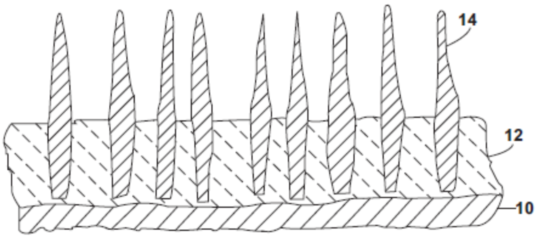

Figure 1. 11 Microporous oxide with pores filled with nickel rods (Scherber and Dietrich 1979).

GB2016527 (Schneiders, et al., 1979) developed a method of depositing a layer of metal that created a specific crystal structure. The crystals were of a size and configuration that resulted in the creation of pores of a scale comparable to visible light.

Surface topology was developed with the aim of producing coatings that were able to exhibit both high absorption and low emission in just one layer of material. For example, GB2102025 (Watase, et al., 1983) patented a surface formed by several cycles of AC electrolytic etching of an aluminium substrate, creating a surface of recesses. The average diameter of the recesses was equal to the wavelength of solar radiation, giving the coating properties of α around 0.84-0.85 and ε around 0.25-0.29. When the same surface was then blackened by anodising in a nickel salt bath, α was increased to 0.95 and ε was reduced to 0.2 (Watase, et al., 1983). US4574778 (Raynaud, et al., 1986) patented a process that resulted in a selective surface of nickel oxide (3) covered in a layer of angled nickel oxide asperite disks (5) as shown in Figure 1.12.

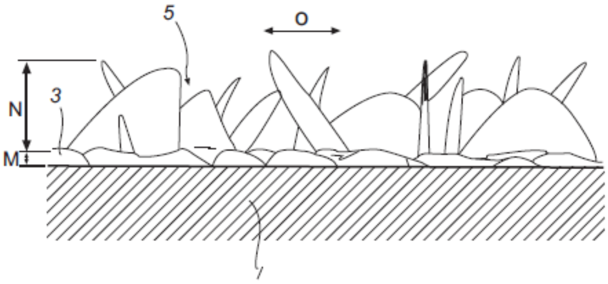

Figure 1. 12 Surface of asperite disks where the thickness M of the porous nickel oxide is around 0.2µm and of the disk or platelet layer N is around 2 µm. The distance (O) between the apex of the platelets is around 1 µm (Raynaud, Morin and Brossard 1986).

US4442829 (Yanagida, et al., 1984) patented a method whereby the purity of an aluminium substrate, of at least 99.92%, was used to develop a very thin film on its surface with good conformity. The conformity resulted from the purity of the base metal. The film was a microporous oxide and the pores were then filled with metal particles by an electrolysis process achieving properties of α = 0.87 and ε = 0.02.

Developments in microtechnology manufacturing methods have contributed a new range of thin film deposition and manipulation methods to be used. Surface texturing procedures of plasma etching and reactive ion etching were used by US4521442 (Guarnieri, 1985). In this invention, the surface of a substrate is coated with a polyimide resin which is then etched by a reactive or plasma process to produce a surface of needle-like projections. The surface disclosed in US4582111 (Kuehn, et al., 1986) is of similar needle like structures but in this case formed from a metal oxide. The structured oxide layer is then coated with a very thin layer of metal (between 40-200 nm thick) which conforms to the structure of the oxide surface without filling the valleys.

Some microstructured coatings result in a composite coating such as the filling of a pored structure with pigments. Debe patented a process to form a composite material. This consisted of encapsulated micro-pillars of an inorganic material, such as metal oxides or sulphides, in a polymeric matrix. The microstructures preferably have mono or polycrystalline regions and comprise at least one inorganic and one organic material (Debe, 1997).

Sandia National Laboratories assigned a microstructured absorber patent invented by Mahoney (Mahoney, et al., 2003). The patent disclosed a pinnacled structure using metals. Mahoney aimed to address economic issues and environmental impacts in the manufacture of solar selective coatings. Metal pinnacles were manufactured on the surface of a substrate which scatter and absorb short wave radiation. The average height of the pinnacles is between 100-1000 nm with an aspect ratio (height divided by width) of between 5 and 20. The protruding nanoscale structures provide good absorption to emittance ratios but are liable to mechanical, thermal and environmental degradation and hence need protection. As a result, the other element of this patent is a protective coating for the structures created by a sol-gel process.

Chen also patented a coating of cone shaped protuberances (Chen, et al., 2010). The patent covers many embodiments including protuberances which could be in a geometric configuration or have a random distribution. The protuberances are preferably constructed in a deposited metallic layer although multiple metallic layers could be used. In some embodiments, the protuberances can be covered with either a dielectric layer constructed from a single material or one that consists of multiple layers of alternating dielectric materials forming a photonic crystal (a periodically structured material whose configuration affects the propagation of electromagnetic radiation) (Flory, et al., 2011). The configuration of the protuberances selectively enhances radiation absorption (Chen, et al., 2010).

WO2011117256 (Ostermann, 2012) presented a method for the reliable reproduction of a selective layer where a metal substrate was coated with a porous oxide by DC anodisation. The pores then undergo AC pigmentation by a metal thus creating a composite material. The preferred metal substrate is aluminium to create aluminium oxide (Al_3O_2).

A structure of truncated nanoscale cones comprising ZnO was developed in DE102010034901 with the objective of reducing reflection. The cones were either deposited over an absorber material such as CdO or Si which covered a substrate, or were embedded in the layer of absorbing material, with the peaks of the cones protruding through the surface of the layer. The dimensions of the structures are smaller than the wavelengths of the incident radiation. Where the cones are embedded in the absorber layer they form a material with a varying refractive index across its thickness (Chen & Lux-Steiner, 2012).

1.1.8 Carbon nanotube coatings

Structured coatings using carbon incorporating carbon nanotubes (CNTs) have been published. Carbon nanotubes are unique with regards to their combination of mechanical, thermal and electronic properties and can demonstrate both metallic and semiconducting behaviour (Wijewardane, 2009). Single walled carbon nanotubes (SWCNTs) have a nanometre-sized diameter and are several microns long along the tube axis. The wavelengths of visible light lie between these two lengths which gives the carbon nanotubes unusual optical properties (Saito, et al., 2004).

The construction of vertically aligned layers of carbon nanotubes has proved to be problematic. In the patent US20110236619 (Sansom, et al., 2011) outlined a material and its fabrication route that was composed of vertically aligned CNTs. The material could be used as a solar absorber material in many solar thermal systems including mid and high temperature applications. The material is shown in Figure 1.13 A6, where layer (100) is the CNT layer and layer (116) is an anchor layer which could consist of various materials such as epoxies or metals. The CNTs protruded through the anchor layer and the heat collected from incident light was conducted along the lengths of the tube into the working fluid (Sansom, et al., 2011). The stated absorptance for CNTs in an anchored layer is 99.9% of incident light between the wavelengths of 270nm to 2.6µm, a significant improvement on previously quoted absorptance values for most materials (Sansom, et al., 2011).

The formation of the anchored CNTs is also shown. In Figure 1.13. A1, a vertically aligned CNT layer (100) was grown on a substrate (108). The two ends (102, 104) and the central section (106) of the CNTs were also defined. In Figure 1.13 A2 a fluid layer (110) was deposited, by spin coating for example, onto a separate substrate (112) and the CNT array was inverted and pushed into the fluid layer. In Figure 1.13 A3, the fluid is cured changing its state (116) and anchoring the CNT array. The growth substrate layer (108) and the anchor layer substrate (112) were both removed leaving the ends of the CNT array anchored in the cured layer (116). Finally, in Figure 1.13 A6, the cured layer is selectively removed so that both ends of the CNTs are exposed (Sansom, et al., 2011).

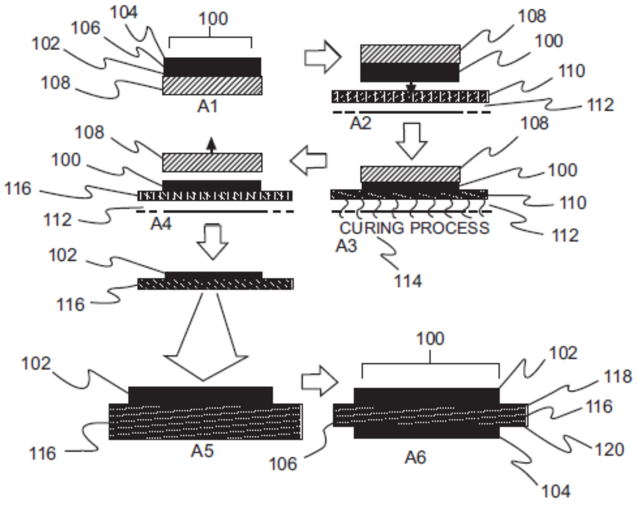

Figure 1. 13 Anchored carbon nanotubes (Sansom, Gharib and Rinderknecht 2011).

US20100258111 (Shah, et al., 2010), assigned by Lockheed Martin, presented a carbon nanotube coating with a variety of configurations. For example, a fibre tow was infused with nanotubes (120) and this tow could be wound around receiver tubes (110), fitting into grooves (215) cut into the surface for this purpose as shown in Figure 1.14. Infusing the tow with nanotubes allowed them to be applied to a substrate in an aligned configuration.

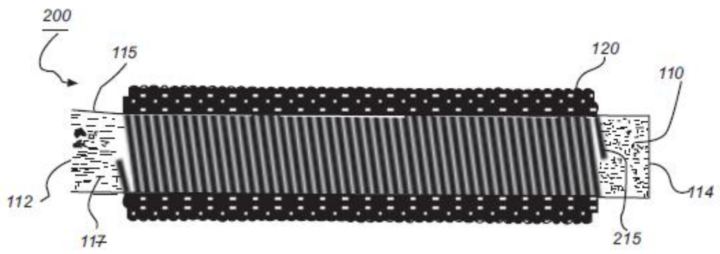

Figure 1. 14 Wound CNT infused tow (Shah, et al. 2010).

1.1.9 Future developments

The absorption properties of a material are dependent on its structure at a very small scale which is the realm of micro and nano technology. An inspection of the processes and materials used in solar thermal absorber coatings show many similarities to the microtechnology industry, such as the use of titanium nitride (TiN) and aluminium oxide (Al_2O_3) and nitride (AlN) and also CVD, PVD and thermal oxidation techniques (Franssila, 2010). Many of the requirements of the materials and processes are also similar such as good coating conformity and control over layer thickness. Hence, developments in the microtechnology industry have had impacts upon the absorber field since its initial inception.

The dimensions of nanoscaled particulates can be manipulated to achieve different optical properties to that of the bulk material, so when used in composite coatings these offer many possibilities (Oelhafen & Schüler, 2005). Furthermore, the optical constants of the nanostructured composites can be tuned by controlling the metal content of the coating and the size and shape of the metal clusters, thus extending the parameters that can be adjusted to obtain the desired qualities in a material (Rincón, et al., 2007). Coatings engineered at the nanoscale seem to offer a great deal of future potential.

Recent developments for combined PV and solar thermal devices could also prove to be an important area for future developments. The PV and thermal components collect radiation at different wavelengths. These devices can be designed to collect a wide spectrum of the incident radiation thus increasing the overall collection efficiency (Ostermann, 2011).

1.1.10 Adapting EHD patterning to produce solar selective coatings

Many different methods are used to deposit and shape the thin films and micro-/nano-structured surfaces used in solar selective coatings. Electrodeposition and chemical immersion have been used to deposit thin layers of oxides such as black chrome; as has thermal oxidation. Modern methods more often now use chemical vapour deposition (CVD), dip-coating and other vacuum methods such as physical vapour deposition. Vapour deposition has many variants such as the use of plasmas and low pressure environments. Vacuum methods offer many parameters that can be altered to control the film layer deposited and include deposition time, temperature, pressure and gaseous environment. They do however require expensive and specialist equipment.

The processes used in the preparation of surfaces that are composed of CNTs are long and complex.

Patterned layers are often created using etching and photolithographic techniques which are ubiquitously used in microfabrication. During this process, a micro-patterned design is transferred onto a UV-sensitive resist material coated onto the substrate to be patterned. Several different processes can be used to etch the pattern into the underlying material, depending on the nature of the material. Wet-etching methods immerse the substrate in a liquid bath which etches the material; dry methods use a beam of gas ions to ‘wear away’ unwanted material. Again, these methods use specialist and expensive equipment and often a clean room environment is necessary.

Domestic solar heating devices rarely exceed a couple of hundred degrees Celsius, and so in this study epoxy resin was used as the patternable material as it will withstand this temperature. They have good environmental stability, and they are cheap and easily obtainable. Patterning epoxy resins in the micron scale using EHD could mitigate some of the challenges presented by other materials and methods.

Hitherto, most of the work done with EHD patterning has been with thermoplastics. A few studies have experimented with UV cure polymers, filler materials and polydimethylsiloxane (PDMS), but to our knowledge a cold curing epoxy resin has not been used. The use of a cold curing resin introduces new complexities into the process. Many of the parameters that govern the process are no longer constants, such as the relative permittivity, conductivity and the viscosity of the epoxy, and these change as the material cures. Most of the theories that predict the growth behaviour of the pillars and patterns use constants for these values so they may not be relevant for the material used here. A few studies of EHD with conducting materials have been carried out, but the process is still not well understood. The main objective of this study was to produce a functional material however, control of the process was needed so some discussion of current theories was necessary. The EHD process has not yet been commercially developed, possibly because it is still difficult to control without the use of micro patterned masks, but several studies have used it as a way of producing functional materials such as porous layers and substrates for Raman spectroscopy.

1.2 Electrohydrodynamic Instability Patterning

1.2.1 EHD patterning

During electrohydrodynamic instability patterning an electric field is applied to a thin polymer film by way of a flat-plate capacitor as shown in Figure 1.15. Two electrodes are held at a fixed distance apart by insulating spacers. A thin liquid epoxy film is coated onto one of the electrodes. When a voltage is applied to the electrodes, an electric field exists between them, in both the epoxy film and the air gap. The difference in the electric fields destabilises the surface of the epoxy film, and surface waves form which grow in amplitude over time. Eventually they bridge the gap between the two electrodes.

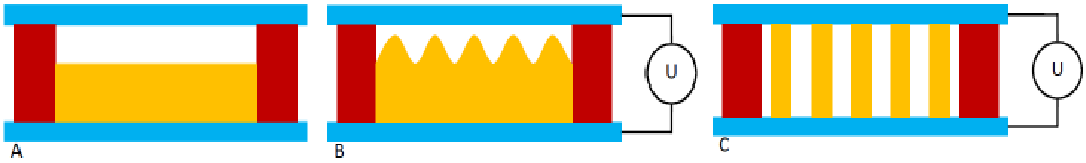

Figure 1. 15 Schematic of the EHD patterning process, blue - electrode, red - spacer, yellow - patternable fluid, A. no applied voltage B. initial instability C. fully evolved structures.

Electrohydrodynamic instability patterning uses the electric field that exists between the two electrodes of a flat plate capacitor to destabilise and pattern the surface of a fluid. On the macroscale, the technique of using an electric field to destabilise the interface between two fluid layers has been understood for several decades (Melcher, 1963). Over the last 15 years there have been developments in its use as a micro and nanoscale fabrication method.

In 1999 Chou *et al* demonstrated how a surface patterned plate, held a small distance (in the order of microns) from a polymer melt, caused the self-formation of pillars in the polymer (Chou & Zhang, 1999). This method did not use an external applied voltage and, although still not well understood, the effect has since been attributed to contact potentials (arising through charge transfer between the polymer and the metal at the interface) between the different layers (Chou & Zhang, 1999) (Akande & Adedoyin, 2001). Around the same time Schäffer *et al* produced a study whereby electric fields, caused by an applied voltage rather than contact potentials, were used to destabilise the surface of a fluid polymer melt to produce a pillar array (Schäffer, et al., 2001). Much of the work since has been with thermoplastics, primarily poly(methyl methacrylate) (PMMA) and polystyrene (PS), although other materials have been patterned, such as UV cure polymers and sol-gels (Dickey, et al., 2006) (Schäffer, et al., 2001) (Voicu, et al., 2007).

The simplicity and versatility of the EHD technique is its main attraction. It could be used as a fabrication method in many areas such as fluid channels for microfluidic applications and functional surfaces for optics. The simplest version of the method does not require expensive photolithography equipment and the cleanroom facilities that accompany it (Yu, et al., 2008). Hence it has the potential to reduce costs significantly and make micro and potentially nano fabrication techniques available to a wider range of researchers and industries.

Conventional photolithography is also limited by the wavelength of light and diffraction effects, and currently structures smaller than around 100nm are difficult to manufacture by this method. EHD could offer an alternative solution to this challenge, as it is theoretically possible to produce patterns at this scale. Recently there have been some developments in the use of this fabrication technique for a variety of functional materials such as micro-lens arrays and vapour sensing (Lee, et al., 2011) (Manigandana, et al., 2010).

On the microscale, electrostatic stress at the interface between the different layers overcomes the stabilising effects of surface tension to produce patterns. The stress at the interface is caused by the change in the electric field that occurs between the various layers of materials due to the difference in their permittivities. In response to the electrostatic stress at the surface the fluid begins to deform and flow. Ordinarily, columns are produced, although a range of other shapes can also be fabricated.

Micro and nano scale patterning effects have been predicted mathematically using a variety of modelling techniques, including linear and non-linear simulations. The movement of the material has been modelled as Stokes flow or creeping flow, where viscous forces dominate the inertial forces and the Reynolds number of the regime is small $Re \ll 1$. Calculations of the process have been based on a fluid dynamics analysis technique called linear stability analysis using a thin film lubrication theory, since the electrode gap is very much smaller than the electrode area (Gambhire & Thaokar, 2011)

(Schäffer, et al., 2001). Linear stability analysis enables stable states in fluid dynamics to be calculated for small amplitude perturbations. This represents the initial stages of the EHD patterning process where small amplitude waves form across the surface of the liquid polymer in response to the electrostatic stress at the interface. Fluids are generally considered to be Newtonian (Pease & Russel, 2004).

1.2.2 Modelling and experimentation

The original models described only the early stage undulations and modelled the waves whilst the growth was still in the linear regime and had not formed into defined discs which spanned both the top and bottom electrodes. Experimentally it was found that the wavelength of the long-term growth did not deviate significantly from the values calculated for the early onset perturbations, and so it was felt that this model adequately predicted the wavelength of the overall structures.

The model proposed by Schäffer *et al* assumed that the materials were perfect dielectrics and that only polarisation charges in a single layer of polymer thin film created the surface instability. Charging at the air/polymer interface, caused by the finite conductivity of the film, was considered to be negligible and was discounted. This premise was demonstrated experimentally using an AC voltage which, in Schäffer's work, produced similar results to a DC voltage. The model showed that a wide range of wavelengths at the interface are unstable but it is the wavelength which grows fastest in amplitude that dominates the overall pattern of the instability. Thus, the fastest growth wavelength is that of the final columns (Schäffer, et al., 2001).

Initially, the materials to be patterned were thermoplastics and, although a variety of materials have now been used, the majority have still been thermoplastics (Lau & Russel, 2011) (Lin, et al., 2002) (Manigandana, et al., 2010) (Wang, et al., 2014) (Morariu, et al., 2003) (Wu, et al., 2006) . Thermoplastics can be heated to form a softened malleable material which can be shaped and then cooled to fix the surface patterning in place.

Shäffer *et al* reduced the scale of the process, from the large-scale gravity limited case, where electrostatic forces large enough to overcome the effects of gravity were required, to the micron and sub-micron scale. At this scale the phenomenon was governed by electrostatic and capillary forces; the effects of gravity were negligibly small in comparison and so were not included in the models.

The work of Shäffer *et al* was with thin films of PMMA, PS and brominated polystyrene (PBrS) that were heated to 170°, above their glass transition temperature, to enable the material to flow. A relatively small voltage, of between 30-50 V, was applied and the average thickness of the polymer film was 100nm (Schäffer, et al., 2001). The electric field was altered across the width of the electrodes by varying the height of the spacers from 100nm to 1μm over a distance of several mm.

At the micron and submicron scale, electrostatic forces destabilise the polymer film surface against surface tension forces which attempt to stabilise it. At these scales, Schäffer found there was no lower threshold for the electric field to produce the EHD instability, although voltage limits required for patterning at the micron scale have since been investigated (Yang, et al., 2013). The linear stability model of Schäffer *et al* described the experimental results well (Schäffer, et al., 2001).

Polymer bilayers, where the air gap was replaced with a polymer, produced a smaller pillar spacing (Lin, et al., 2002). A layer of thermoplastic coated with PDMS and thermoplastic bilayers were both patterned with 50V applied for the duration of a day. The thickness of the bilayer was approximately 1.25 μm and the resulting centre to centre spacing of the columns was 12.9 μm, some 10 times larger than the electrode spacing (Lin, et al., 2002). The interfacial tension at the interface between the two thermoplastics was lower than for the thermoplastic/PDMS bilayer, so the former combination produced a smaller characteristic wavelength which agreed with values predicted by theory.

The practical results of Lin et al were in good agreement with theoretical models which also were predicting the early stages of the instability. It was found that the distance between the columns in the later stages of the process did not deviate significantly from those predicted earlier in the process. So, the theory that predicted the deformation in the early stages was considered to predict the overall result well and it seemed that the distance between the columns was preserved throughout the entire growth of the columns (Lin, et al., 2002).

Morariu *et al* also used thermoplastics in a PS-PMMA bilayer, but with the addition of an air gap above the second polymer layer. The heat and voltage were applied for 24 h as the molecular weight of the polymers was high. This meant that the polymer melts had high viscosities resulting in long process times for the formation of columns. Polymers of a lower molecular weight would decrease the viscosity and process times of the experiments (Morariu, et al., 2003).

The bilayer produced core and shell structures shown in Figure 1.16. The electrostatic pressure at the PS/air interface was larger than the pressure at the PS/PMMA interface. As a result, the PS layer formed into pillars first. Once exposed to the air, the PMMA experienced an increase in the electrostatic pressure at its surface and so it began to deform, creating a coating around the PS columns (Morariu, et al., 2003).The subsequent selective removal of the PS core left crater like structures.

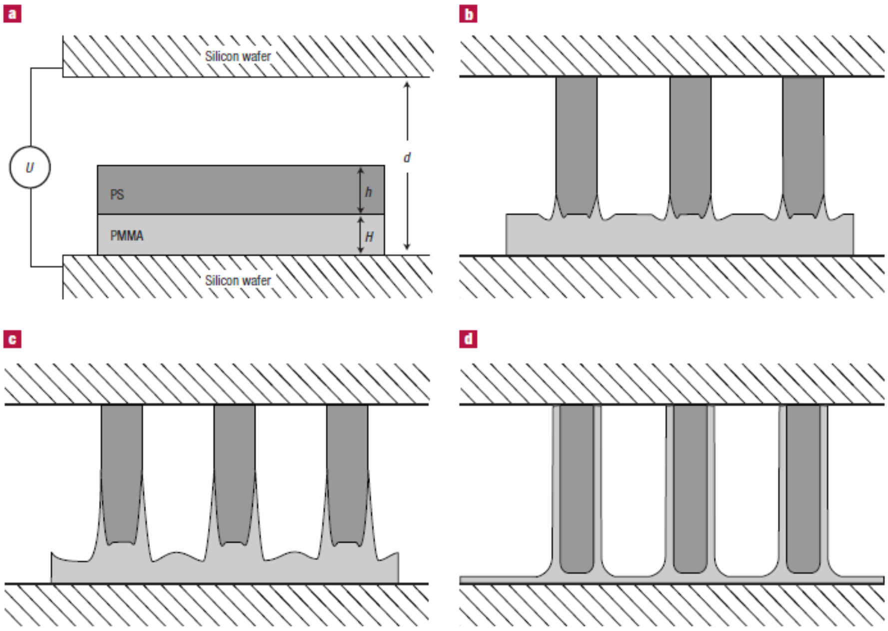

Figure 1. 16 Core/shell structures formed by a PS and PMMA bilayer a. initial bilayer b. initial instability c. secondary instability forming d. formed core/ shell structures (Morariu, Voicu, Schäffer, Lin, Russel, & Steiner, 2003).

The core/shell structures formed had good long-range order and this was probably because of the long-time periods taken for the pattern fabrication of around 24 h. Such time scales are too long to be practical and other studies have aimed at lowering them by using materials with a lower viscosity (Dickey, et al., 2006).

A great deal of effort has been put into developing models that accurately predict experimental results and the fact that materials do not behave as perfect dielectrics was incorporated into many of the numerical models proposed.

In 2004 Pease and Russel developed a general model in which the polymer behaved as a leaky dielectric. The model took account of mobile charges within the polymer, which accumulate at the interface between the polymer and the air. The perfect dielectric case was then a special case of the general model. In addition to the applied voltage, the model included the effects of contact potentials at the interfaces between the various layers (Pease & Russel, 2004).

In reality, contact potentials and conductivities of the polymers modelled were not known accurately, and thus, contact potentials were neglected in the calculations. Only the applied potential was used to compare experimentally-derived data with that of the predictions given by the proposed model. The discrepancies between the experimentally-measured wavelengths and those derived from theory varied between from around 1-5 µm for wavelengths between 2 and 20 µm. The lack of correlation between experimental data and the modelling results led to the suggestion that experiments monitoring the presence and conductivity of free charges could be useful (Pease & Russel, 2004). It was proposed that the electrical breakdown of the air and/or the polymer could be causing the disparity between the theory and the gathered data. Since the electrode gaps were less than a few microns, it was suggested that Fowler-Nordheim emission could be occurring. In this phenomenon, electrons are exchanged at an interface and the voltage is shielded, so the resulting pillar spacings were unexpectedly large compared to those predicted by theory.

Pease and Russel found that, when the applied voltage was high, discrepancies between predicted wavelengths and experimental results meant that the electrical breakdown of materials could limit the reduction in the scale of pillars achievable. The arrangement of the pillars formed at the highest voltages (in this study 90V), were chaotic and it was suggested that the use of larger voltages meant that a larger range of wavelengths compete for dominance. The disorder implied that the use of a higher voltage also led away from hexagonal ordering; the same condition that also predicts tightest column packings (Pease & Russel, 2004). The model also suggested that the use of leaky dielectrics could produce smaller wavelengths, although leaky dielectrics are more susceptible to breakdown for a given voltage (Pease & Russel, 2004). The paper stated that experimental data fitted better with the model given by Schäffer *et al* than the general model proposed, possibly because this model sought to cover a greater range of experimental parameters.

A significantly beneficial development of the EHD process would be to fabricate surfaces that are not possible by photolithography, which is limited by the wavelength of light. Efforts have been made to reduce the scale of the patterns being produced and there are a number of ways in which this can be achieved. One way predicted by theory, is to increase the electric field between the electrodes by using a higher voltage. Experimentally it has been found that the use of higher voltages means that the patterns become more chaotic and disordered very quickly. The process of deforming the surface of the liquid in this process is dynamic. Competition between the electrostatic stress and capillary pressure at the interface determines the arrangement of the patterns which form, and so requires models that predict the entire time evolution of the process.

Shankar *et al* modelled the interface between two leaky dielectrics in addition to the perfect dielectric–perfect dielectric systems (PD-PD) and leaky dielectric-perfect dielectric systems (LD-PD). They showed that when the two fluids are modelled as leaky dielectrics the scale of the instability drops dramatically (up to a factor of 1/50) compared to two perfect dielectrics (Shankar & Sharma, 2004). They also demonstrated that when the system is composed of two leaky dielectrics the relative viscosities of the two fluids had a marked effect on the resulting wavelength (Shankar & Sharma, 2004).

Verma *et al* used 3D non-linear simulations to show that the patterns produced over the entire growth of the process are dependent on the ratio of the thickness of the air gap to the thickness of the polymer film, or the ‘fill factor’ (Verma, et al., 2005). The formation of columns or discs lowers the electrostatic energy at the interface between the polymer and the air but increases the overall surface tension. As a result, when the electrostatic force is neutralised by the formation of columns, surface energy again takes over and to reduce surface tension the columns can merge and coalesce, thus coarsening the ordered hexagonal packing shown in Figure 1.17 (Verma, et al., 2005).

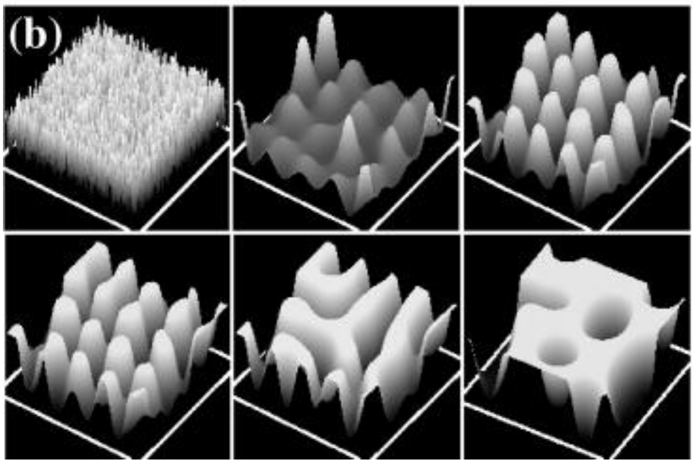

Figure 1. 17 Six stage evolution of pattern coarsening (Verma, Sharma, Kargupta, & Baumik, 2005).

In the latter stages of the process, for a larger fill factor, coalescence will occur but for a very low value <0.25, hexagonal arrays form. In fact, they found that modelling predicts that increasing the volume fraction leads to a steady increase in disorder until at >0.75 coalescence occurs rapidly. Simulations showed that it was the ratio alone, and no other parameters, that governed the magnitude of the coalescence of the pillars and that the scale of the thicknesses involved are unimportant. The phenomenon was likened to dewetting due to van der Waals forces (Verma, et al., 2005).

The long heating and cooling cycles, more than 24 h in some cases, associated with the high viscosities of thermoplastics were avoided by Dickey *et al* by using a number of photocurable polymers. UV radiation was used to polymerize and so solidify the patterns. Dickey *et al* designed and constructed a dedicated machine for the EHD patterning process called the ‘active gap tool’ (Figure 1.18) which allowed the top electrode to be positioned accurately using servo motors. A mercury lamp with an intensity of 3.5mW/cm^2 was used to cure the polymers so, in addition to their lower viscosity, they had the benefit that they could be cured quickly when required before the pattern changed and coarsened (Dickey, et al., 2006). The liquid polymer layer was 800nm thick and 3 µm electrode gaps were used with a voltage around 40V.

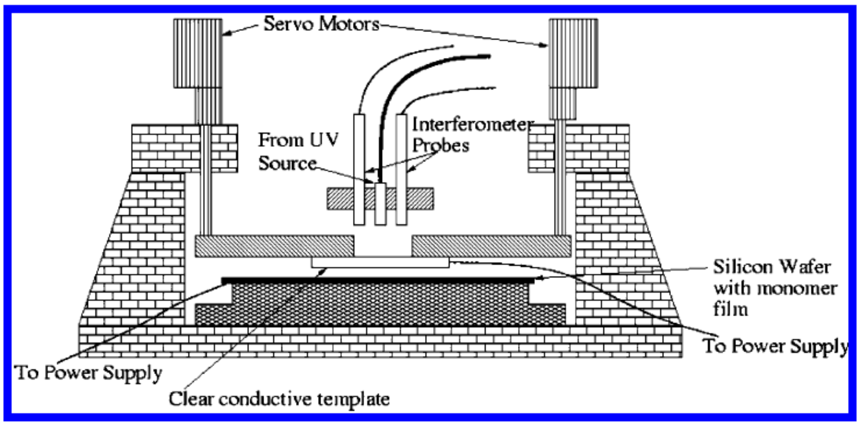

Figure 1. 18 Active gap tool schematic (Dickey, et al., 2006).

The relatively high dielectric constant of the UV cure materials was also preferable from the perspective of manufacturing smaller-scale patterns. This created a greater difference in the electric fields and thus smaller pillar spacings. This is the only other study where an epoxy material was patterned, but in this case it was cured via UV irradiation and the other UV cure polymers were used in preference due to their lower viscosities. The wavelengths of the columns in this study were around 30 µm, although in this study linear stability analysis predicted this value to be 40 µm (Dickey, et al., 2006). The columns were again around 10 times larger than the electrode gap, and given the aspect ratio of the patterns being created in this and other experimental works, they are better described as discs rather than columns.

Kim and Lu presented a 3D model that linked the early instability (small amplitude undulations) to the final patterns (fully evolved columns) for a single thin polymer film. The evolving structures were modelled using a process of diffusion; the interface between the air and the polymer was presented as a concentration field (Kim & Lu, 2006). This model however, assumed that there were no free charges in the media i.e. it was a perfect dielectric. They found that when the film was very thin the interaction between the film and the substrate could hinder the evolution of the pillars in comparison to a thicker film. They also showed that, when all other parameters are the same, a thicker film produced more densely packed pillars (Kim & Lu, 2006).

Voicu *et al* patterned a TiO_2 sol-gel by EHD. No heat source was required since the sol solidified by the evaporation of the solvent. Similarly to Schäffer *et al*, the distance between the two electrodes ranged from 500nm to 1µm over a distance of 2cm, so that the electric field changed across the sample. The EHD patterned sol was then pyrolysed at 400°C and the columns retained their shape, although there was a subsequent volume reduction of 85% (Voicu, et al., 2007). The use of a patterned electrode enabled lined patterns to be created. Raised shapes on the top electrode created areas where the electric field in the electrode gap was higher. The sol then formed patterns that followed the ridges on the top electrode, causing lines rather than discs to be created in the sol. A spacer distance of 425nm and a voltage of 70V were used. In comparison to the use of thermoplastics, the time taken for the patterns to appear was shorter, at less than 30min (Voicu, et al., 2007).

Experiments with more complex layers, such as polymer bilayers and trilayers, required different models from those that described a single interface between two materials that were generally a polymer melt and air. Bandyopadhyay and Sharma modelled the two interfaces which exist in a polymer bilayer (i.e. polymer/polymer and polymer/air interfaces). The instability or waves at each interface could be in phase with each other, in which case the overall material deformed by bending, or out of phase, in which case the polymer is deformed by squeezing (Figure 1.19). Bandyopadhyay and Sharma presented a linear stability analysis of the polymer bilayer model for both the interface between the top polymer and the air and the interface between both polymers, using a non-linear simulation to confirm the linear results (Bandyopadhyay & Sharma, 2007).

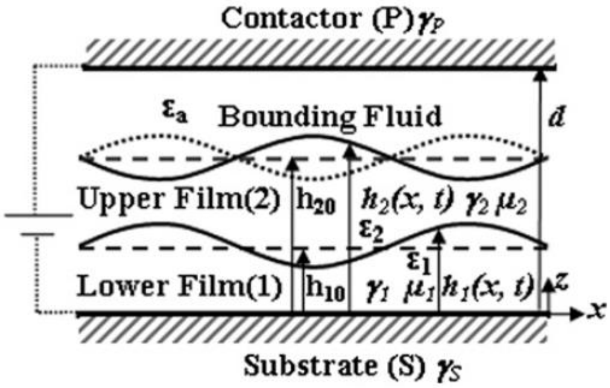

Figure 1. 19 In phase bending and out of phase squeezing in a polymer bilayer (Bandyopadhyay & Sharma, 2007).

The use of an AC field provides another parameter that can be altered to control the morphology of the surfaces produced. Roberts and Kumar produced a leaky dielectric model for an AC field. This model was described as making ‘analysis more complex but physically more appropriate to the actual experimental conditions' (Roberts & Kumar, 2009). Results of non-linear simulations and linear stability analysis using an AC field gave qualitative agreement with each other. The DC case was represented by a field with a frequency equal to zero (Roberts & Kumar, 2009).

Using the above model, as the frequency increased in an AC field, the movement of charge through the fluid was inhibited, because the oscillation time is much less than the time it takes for charge transport. The material effectively behaved as a perfect dielectric as charges could not move to the interface quickly enough, and so did not build up at the interface as they did with a DC field (Roberts & Kumar, 2009).

Models demonstrated that allowing minuscule amounts of charge accumulation at the interface (as would be the case where a leaky dielectric was exposed to a DC field) led to a dramatic increase in growth rate of the columns and an increase in the fastest growing wavenumber. AC fields in leaky dielectrics produced lower growth rates and wavenumbers since it is the charging at the interface that produces smaller wavelengths (Roberts & Kumar, 2009). Applying an AC field, after pillars had been produced using a DC field, had the effect of thinning the pillars. This was a result of the force at the tip of the pillar decreasing with the drop in effective voltage over the period of the AC field. Some of the material at the tip then dropped away from the top electrode, thus thinning the pillar (Roberts & Kumar, 2009).

Reddy *et al* presented a non-linear analysis of a polymer bilayer which modelled the entire formation of columns. The objective was to determine the conditions that would be required to produce a pattern of core/shell columns which, when one of the polymers was then selectively removed, would leave an array of hollow pillars. Patterns depended largely on the comparative permittivity of the two films (Reddy, et al., 2010). The material with the higher permittivity formed the core of the columns. 2D and 3D analyses of a polymer bilayer under a patterned electrode were presented. The use of patterned electrodes, and the careful choice of permittivities of the polymers, demonstrated that there was a potential for complex structures to be produced. Under some conditions the top layer polymer descended into the bottom layer of polymer rather than forming columns (phase inversion) (Reddy, et al., 2010).

A decrease in the thicknesses of both the air gap and the polymer is predicted to reduce the scale of pattern and the reduction in the scale of the patterned surfaces has been a significant objective in this area. Hence the conditions that are required to produce a hexagonal pattern were examined by Tian *et al*. The model used was based on the formation of hexagonal cells during convection processes developed in the 1960's and which were later employed for studying Turing patterns (Tian, et al., 2011). The influence of the thickness ratio of the air gap to the polymer film was examined, and it was also found that as the columns of polymer contacted the top electrode, intermolecular forces influenced further development and these needed to be included in the models (Tian, et al., 2011).

As efforts have been made to reduce the scale of the instabilities, higher voltages and smaller electrode gaps have increasingly been employed in experimentation. This has led to the possible invalidation of some of the proposed models. The presence of surface charge alters the surface tension of the polymer film, termed the electrocapillary phenomenon. Many proposed models use a thin film approximation and Pease and Russel demonstrated that this condition held when the square of the ratio of the electrode separation to the electrocapillary length was very much less than unity (Pease & Russel, 2004). When high voltages and small electrode gaps are being used, this condition is frequently unmet and so Gambire and Thaokar proposed a General Model (GM) without the lubrication approximation (Gambhire & Thaokar, 2011).

The wavelengths predicted by the GM deviated from previous models which used a thin film approximation. The study provided a method whereby the validity of the thin film model to be used with given experimental conditions, could be assessed (Gambhire & Thaokar, 2011). The GM allowed the condition where the wavelength of the instability is comparable to the electrode separation to be modelled (as this condition would invalidate the thin film approximation). Further studies investigated the interactions between the time period of the applied field, the charge relaxation time and the time it took for the instability to grow (Gambhire & Thaokar 2012).

Li *et al* also developed a nonlinear model to describe the entire formation process. In addition to fully modelling the entire evolution of the structured surfaces, this model included the short range molecular forces that would be involved as the polymer touched and began to wet the top electrode. The inclusion of this part of the pattern formation process was described as a ‘major modelling challenge’ (Li, et al., 2013). The inclusion of van der Waals molecular forces in the model was employed to simulate this aspect of the process. A critical voltage was identified, at which the electrostatic stress exceeded the Laplace pressure at the film surface and the interface became unstable and deformed into columns. However, in their analysis, Li *et al* modelled the air and the polymer as perfect dielectrics. Again, trapped charges or conducting channels in the polymer were proposed as the reason why some experimental data did not agree with theory (Li, et al., 2013).

As the EHD process offers a method for producing patterns of a scale smaller than can be achieved by conventional photolithography, Li *et al* examined the potential for producing sub-30nm patterns (Li, et al., 2013). The perfect dielectric equation was used according to Shäffer *et al*, and nanometre patterned electrodes were used in the model. The instability in the polymer replicated the patterns on the electrode. The model showed that the ability of the pattern to be replicated accurately was complex, and exact replication did not occur for many reasons. For example, if the initial polymer layer was not thick enough there was not enough polymer to fill in the gap between the electrodes. For given fabrication parameters, such as voltage and electrode gap, the minimum size of the pattern that could be replicated was ascertained. The model predicted that features as small as 25nm could be fabricated (Li, et al., 2013). Whilst this limit is smaller than the scale that can currently be produced accurately using photolithography, a mask patterned at this scale had to be fabricated, which to some extent negated the full benefit of using EHD patterning.

The different materials that can be patterned have a wide variety of viscosities. In most models the viscosity of the polymer only affects the rate at which the columns form and does not alter the overall wavelength or spacing. A model produced by Esplin *et al* encompassed both DC and AC fields and treated the polymers as viscoelastic materials rather than simply viscous ones. Using a DC field, the inclusion of the viscoelastic behaviour was found to alter the growth rate of the undulations but did not change the wavelength (Espin, et al., 2013). With an AC field however the wavelength was found to decrease slightly. The effect was greatest when the relaxation time of the polymer and the frequency of the field were comparable (Espin, et al., 2013).

1.2.3 Control of EHD instability patterns using patterned electrodes

Under a flat electrode, EHD patterning shows order on a local scale but only over a range of a few periods. Typically, a single pillar grows and then destabilises the polymer film around it, so that further pillars form. Nucleation domains for the pillars extend across the distance of several pillars. Irregular boundaries in the pattern occur where the domains meet and the hexagonal pattern becomes disordered. One way of removing this irregularity is to control the domains of pattern formation using structured or masked top electrodes, where the electrode is covered with a relief pattern. The raised relief pattern on the top electrode creates an area below the raised pattern where the electric field is higher. This accelerates the formation of structures; the undulations caused at the fluid/air interface then follow the shape of the mask. Masked electrodes can be created by etching and conventional photolithography techniques.

Masks have been used to constrain disc formation within a series of small areas to produces surfaces with long-range order (Figure 1.20 a.) and they have also been used to produce surfaces which replicate the mask pattern exactly (albeit mirrored) (Figure 1.20 b.) (Li, et al., 2014) (Wu, et al., 2006) (Voicu, et al., 2007) (Li, et al., 2014).

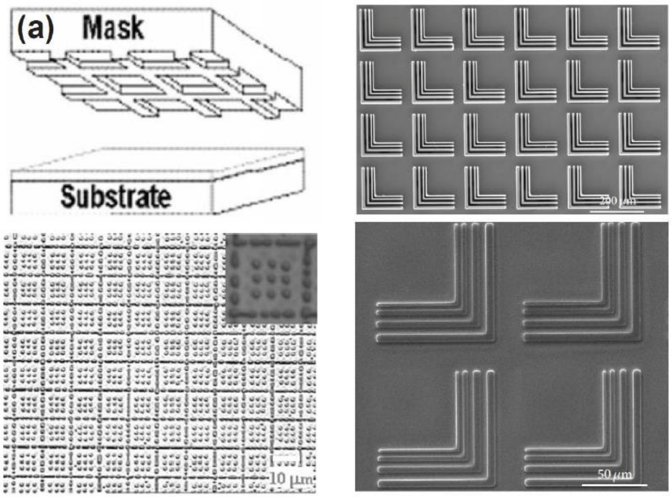

a b

Figure 1. 20 Masked EHD patterning producing a. surfaces of pillars with long-range order (Wu, Pease, & Russel, 2006) and b. electrode replication (Li X., Ding, Shao, Tian, & Liu, 2014).

Replicating a pattern on a mask by EHD patterning usually works by pillars forming in line under the raised areas of the masked electrode. The individual pillars then merge to create continuous lines and curves in a process of ‘controlled’ coarsening of the pattern, an occurrence which in other circumstances is unwanted.

Replicating the electrode patterns accurately presents several issues subsequently examined by Li *et al*. The periodicity of the pillars is dependent on several parameters including the applied voltage, and in some cases the period can be much smaller than the mask pattern (Li, et al., 2014). This can leave gaps in the lines produced, as the pillars may not merge together to 'fill in' the area below the masked pattern. In other cases, the spacer gap can be too large for the pillars to merge beneath it and fill the mask shape, simply because there is not enough polymer to fill the entire volume (Li, et al., 2014). To replicate accurate patterns Li *et al* used voltages between 20 and 100V and spacer gaps of 3-4 µm. When the pattern on the mask was being replicated, it was found that the voltage and spacer height affected the fidelity of pattern replication (Li, et al., 2014).

Obtaining a surface of pillars that have long-range order have been explored using a masked electrode that creates controlled nucleation points for the pillars. Once pillars have formed at these points, they constrain and influence the pattern of pillar formation between them. As a result, disc arrays have been produced with a long-range order much larger than the natural domain size that would occur with a flat electrode.

Wu *et al* used intersecting lines of ridges that acted as boundaries between the different developing domains of pillars (Figure 1.20 a). The geometry and spacing of each ridge was designed to allow a single line of pillars to form beneath it. This confined the area in which further pillars could form into small compartments, bounded by lines of pillars. The boundary pillars grew under ridges on the upper electrode, so they were of a different height to those in the centre of the bounded area. The difference in height was minimised by the optimisation of the mask design. The instability wavelengths between the bounding pillars and those in the centre areas were also slightly different, which can be seen in Figure 1.20 a, but again good electrode design reduced this difference (Wu, et al., 2006).

Regular arrays of filled raised shapes, such as squares, on the top electrode created a higher electric field beneath them where pillars formed. Pillars formed beneath the corners of the shapes first and then filled in the central areas so the spread of the pillars was constrained to the area beneath each raised shape (Figure 1.21). This created regular arrays of pillars that were all the same height. (Wu, et al., 2006). The design of the shapes was similar to the natural domain size of the pillar arrays that would be produced with a flat electrode and this enhanced the regularity of the patterns. The work showed that the tendency for the pillars to form into hexagonal arrays could also be overcome using masks and that other patterns could be fabricated (Wu, et al., 2006).

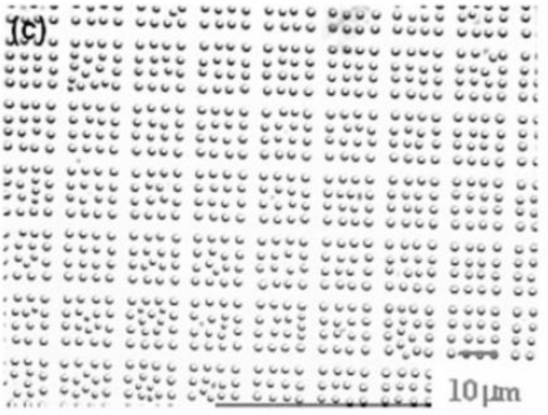

Figure 1. 21 Long-range order produced by arrays of raised squares on the top electrode (Wu, Pease, & Russel, 2006).

In order to produce long range periodicity without the use of lithographically produced surfaces, Wang *et al* used patterns of projected light to stimulate a layer of photoconductive hydrogenated amorphous silicon (a-Si:H) material coated onto one of the electrodes. The photoconductive patterns induced nucleation sites for discs whose spacing then controlled the overall order of the pillar arrays produced. The scale and configuration of the patterns were easily changed by altering the pattern of the projected light (Wang, et al., 2014). This technique overcame the need to use a mask produced by photolithography, although PECVD techniques were used to deposit the photoconductive layer (Wang, et al., 2014).

Masks have been also used to create a pattern of concentric rings in PMMA. An electrode was patterned with cylindrical protrusions and these acted as nucleation points for the centre column of the concentric rings. The height of the raised circles on the mask ranged from 10 to 40 nm with a diameter of 3µm.The rings took 1h to form at 90°C with an electrode spacing of around 160nm (Deshpande, et al., 2004).

The majority of the experimental work has been carried out using voltages of between 50V-200V with spacer and polymer layers ranging from the order of nanometres to around 5µm. However, Yu *et al* used patterned electrodes to create surfaces structured at the mesoscale. Accordingly, layer thicknesses and voltages were larger than most previously used. An electrode spacing of 60µm and a polymer layer of around 25µm were used with a voltage of 600V to produce microchannels of 100µm in width (Yu, et al., 2008). COMSOL, a physics modelling software package, was employed to model the electrical potential distribution under a patterned electrode. As expected, the electric potential decreased sharply in the area between the raised patterns on the top electrode. The inside of a tube was also patterned by winding a wire around an aluminium bar as the master electrode (Yu, et al., 2008).

Mesoscopic patterns using a mask were also created in a pre-cured PDMS film by Pattader *et al*. The partially cured PDMS was patterned with a masked electrode. Once structures had formed at an initial voltage it was increased. Secondary structures in the patterned film were then produced with a different spacing due to the higher field used to create them. The secondary structures were produced before the initial patterns changed and in this way complex arrangements were produced. This can be seen in Figure 1.22 where the larger diameter pillars are produced first with the application of 30V and the smaller pillars are then formed by increasing the potential to 70V. Pre-curing the PDMS increased its viscosity, enabling the patterns to be maintained (Pattader, et al., 2011).

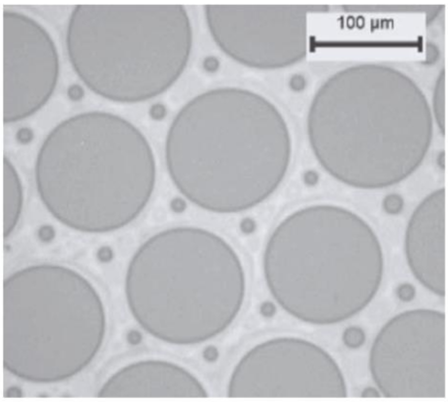

Figure 1. 22 Different scale of pillars produced when an applied voltage is increased from 30 to 70V (Pattader, Banerjee, & Bandyopadyay, 2011).

1.2.4 Reducing the scale of the instability

Conventional photolithography is a technique universally used in micro and nanofabrication; however, the wavelength of radiation and diffraction is a limiting factor in reducing the size of features that can be produced. As a result, effort has gone into reducing the wavelength of the patterns formed by EHD patterning to the nanometre scale. Several parameters can be changed to reduce the size of EHD patterns, such as increasing the voltage and decreasing the polymer thickness; patterned electrodes can also be used.

Some of the fundamental limitations on reducing the wavelength of the instabilities have been examined, such as the dielectric breakdown of the polymer (Lau & Russel, 2011). In most of the experimental work reported, the wavelengths rarely fall into the submicron scale and are generally between 1.6 and tens of microns. Lau and Russel found that values of wavelength rarely fell below 1 µm, even when the theory predicted it. The limitations in reducing the thickness of both the polymer layer and the electrode spacing were explored both theoretically and experimentally, as was increasing the voltage (Lau & Russel, 2011).

In addition to using an air gap between the polymer and the top electrode, a room-temperature ionic liquid was used to maximise the voltage drop in the polymer layer. The higher field in the polymer enhanced the difference in the electric field between the two layers, and so reduced the wavelength of instability (Lau & Russel, 2011). Pattern variability within the samples occurred with the higher voltages (>30V) predicted to be required to produce smaller wavelengths and this was attributed to dielectric breakdown in both the air and the polymer layer. Voltages below 20 V gave smaller wavelengths than those predicted by the perfect dielectric theory; but larger than those predicted by the leaky dielectric theory; this was attributed to breakdown of the air layer. Experiments at higher than 30V produced results that did not agree with the models. It seemed likely that air was breaking down in some experiments whilst in others both layers were breaking down leading to larger variations of wavelengths and disorder (Lau & Russel, 2011). The findings of this study agree with many of the predictions by Pease and Russel (Pease & Russel, 2004).

Theory suggests that increasing the dielectric constant of the polymer also leads to smaller wavelengths. Inorganic materials generally have higher dielectric constants than many of the thermoplastic polymers used, so these have been tested as fillers to create composite materials with higher dielectric constants (Bae, et al., 2008). Gold nanoparticles were dispersed in a PS matrix to observe the effect that this had during an EHD experiment (Bae, et al., 2008). The gold increased the dielectric constant of the liquid PS which consequently reduced the wavelength of the surface instabilities.

Bae tried several other fillers such as titanium dioxide and silica with similar results (Bae, 2012). The titania produced the greatest effect with the wavelength decreasing from approximately 7 µm to 4.5µm at the highest concentration. Although there was a decrease in the wavelength in line with an increase in filler concentration, it was found that this only occurred for titania concentrations up to 3% by volume. Most of the fillers did not migrate through the material in response to the electric field as they had good compatibility with the polymer matrix. The incorporation of fillers into a thermoplastic may also impart higher strength to the polymer (Bae, 2012).

1.2.5 Applications of EHD patterned surfaces

The process of patterning materials using EHD has yet to be developed for use in a wide range of applications, although some groups have been successful in producing functional surfaces using the EHD technique.

Polystyrene pillar arrays have been used to form porous membranes. An array of PS pillars was created using conventional EHD methods with an applied voltage of 200V (Yan, et al., 2004). To form the membrane, a dam was built around the pillars. The dam was filled with a nylon polymer and the PS pillars were then selectively removed using tetrahydrofuran (THF), resulting in a porous nylon membrane. The membranes were tested with water and were found to have good size selectivity and liquid permeability (Yan, et al., 2004).

PS surfaces were topographically structured using hot embossing and a PDMS mould fabricated from an EHD-patterned surface. These were used in tissue culture to investigate how a patterned surface affected the motility and shape of fibroblast cells (Frey, et al., 2006).

A polyaniline (PANi) conducting polymer was used to produce a vapour sensing device with improved sensitivity. PANi monolayers were created by the Langmuir Blodgett technique. In this process a monolayer of a material is created on the surface of a liquid and then transferred to a substrate by passing the substrate through the monolayer. 10 monolayers were used to produce a film 60nm thick of both the doped and undoped forms of PANi. A voltage of 200V was used to pattern the PANi film at a temperature of

220°C. Modelling the undoped form (PANi-EB) as a perfect dielectric found good agreement with the experimental results (Manigandana, et al., 2010).

The patterned PANI surfaces were then used to sense HCl vapour. The vapour converts un-doped PANi to its conducting form and the increase in conductivity was used to sense the presence of the HCl. The construction of a surface covered in pillars increased the area to volume ratio over which there was an interaction between the PANi and the HCl vapour, hence improving the sensitivity (Manigandana, et al., 2010).

Another group produced a functional material using multiwalled carbon nanotubes (MWCNT's). These were dispersed in PS. During the EHD process the nanotubes aligned within the forming pillars. The MWCNT composite material produced shorter instability wavelengths than pure PS (Eder, et al., 2011). A voltage of 120V was applied over a gap of around 1 µm. A thin layer of the top surface of the fabricated PS/MWCNTs pillars was removed by plasma etching which exposed the ends of the nanotubes to form a brush. It was found that the MWCNTs were aligned due to electrostatic torque exerted on them by the field and by shear forces caused by the polymer flow. It was also found that there was a greater density of the MWCNT's at the tops of the pillars. The effect that the alignment of the nanotubes had on the electrical conductivity of the PS layer was also considered (Eder, et al., 2011). The inclusion of the MWCNTs did reduce the electrically resistivity of the composite in comparison to pure PS. When aligned, the nanotubes formed connected pathways through the polymer allowing a conducting route for a current to flow. The typical loading of MWCNTs was 1.5%wt.

The use of a polymer with a very low viscosity (PDMS) combined with rapid crosslinking allowed structures with very high aspect ratios, up to 186 (compared to previously reported values of 0.29-0.83) to be fabricated. The structures had the potential to be used as optical wave guides (Grilli, et al., 2011).

A trilayer of thermoplastics (ethyl cellulose, polyvinyl alcohol and polyvinyl acetate), patterned by the EHD technique, was used to create a surface of metal-coated structures which enhanced Raman scattering (surface enhanced Raman scattering or SERS). This improved the use of the technique for molecular analysis. Arrays of pillars were fabricated, around 0.5µm in diameter and 2µm spacing, comprising concentric layers of the three different polymers. The resulting polymer pillar surface was coated with a layer of gold 20nm thick (Mahajan, et al., 2012). The stability of the discs as they formed was controlled by organising the layers of polymers according to their surface tension and viscosity which stabilized the breakup of the coaxial layers of fluid polymers. The surface of pillars with the highest aspect ratios produced the best results. The scalability of EHD was beneficial for the production of surfaces used for SERS as they could be tuned to different wavelengths and hence could be very sensitive to detecting different molecules (Mahajan, et al., 2012).

A micro lens array was fabricated in a liquid crystal material using a patterned master electrode. The master was used to create well-defined arrays of columns. Removal of the top electrode split the columns in half between the two electrodes and the remaining material on the bottom electrode adopted a hemispherical shape (Figure 1.23) (Lee, et al., 2011). Regular arrangements of these hemispheres made up the lens array.

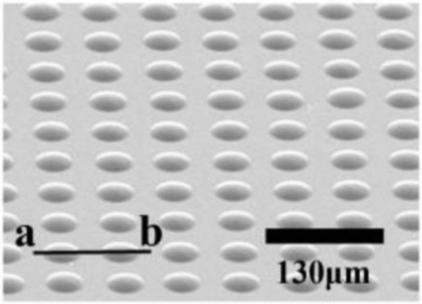

Figure 1. 23 Microlens array (Lee, Kim, Kim, Yu, Gwag, & Kim, 2011).

Despite its versatility, the EHD technique has yet to be refined sufficiently for large scale roll out across industry. However, it still has great potential for small scale production of micropatterned surfaces for testing in settings where photolithographic techniques are unavailable. A variety of polymers have been used with this technique; however, the range of materials that can be structured has still to be explored thoroughly, especially sol-gels. Whilst modelling has had some success in predicting the behaviour of thin films in this process, there are still some challenges to overcome especially with regard to developing a comprehensive theory which encompasses all conditions.

1.3 Modelling and theoretical background of electrohydrodynamic patterning

A number of methods of modelling the process of patterning by electrohydrodynamic instabilities have been proposed. The principal methods are overviewed here with the objective of using the results from the practical experiments carried out in this study and comparing them to the values predicted by some of the modelling methods proposed. The type of material used in the experiments performed in this study had different qualities to many of those studied previously and on which these theories were based, these mainly being thermoplastics. The dielectric properties and viscosity of thermoplastics are approximately constant during EHD patterning; however, for the epoxy resin used here these parameters vary. Also, many of the experiments performed previously have also used smaller electrode spacings and polymer layers and often higher electric fields to those used here. The area of interest in the models is the interface between the polymer and the gap material. In these experiments, air has been used as the gap material, although it is possible to use other materials such as organic liquids (Wu & Russel, 2009).

The simplest method of modelling the interface between the polymer and the gap material is based on a 1D analysis. The method examines the evolution of sinusoidal waves, by use of the Navier-Stokes equation of motion, and allows a velocity profile to be defined in the polymer due to the electrostatic pressure induced at the interface. This is then combined with linear stability analysis, a fluid dynamics analysis technique that allows stable states in fluids to be determined. A term for the interfacial pressure, and simplification of the equation of motion at the interface, yield a dispersion relation for a spectrum of capillary waves that are assumed to exist at the surface of the fluid polymeric material, which are coupled to the electrostatic pressure created by the application of a voltage. The dispersion relation allows a range of wavenumbers at the interface to be modelled and the time constant at each wavenumber shows whether the wave is damped or amplified. The employment of linear stability analysis means that only the early stages of the process are modelled and the full evolution of liquid polymer surface is not attained (Pease & Russel, 2004). However, experimental results from previous studies have demonstrated that for most scenarios the change between the early onset patterning and the fully evolved structures is similar enough for this method to be appropriate (Pease & Russel, 2004). A more complete explanation is given below.

Most of the models are based on the electrode gap being small in comparison to the instability so a generalised model allows a greater range of experimental parameters to be included and this is also outlined below.

1.3.1 Overview of a 1D solution

Thin liquid films behave differently to bulk liquids. This is due to the dominance of interfacial tension over other forces that exist in the bulk of the material, in contrast to thicker materials where the bulk forces dominate. In very thin films, minimisation of the surface energy of the fluid dominates all other factors (Goldberg-Oppenheimer, 2011). Surface tension is the excess free energy per unit area at an interface which is caused by the molecules at the surface experiencing different attractive forces to those in the bulk material (Harkema, 2005). Liquid interfaces form shapes which minimise the surface energy by adopting a profile where the surface area to volume ratio is minimised (Harkema, 2005).The capillary length of an interface between two fluids is a characteristic length defined by gravity, density and surface tension which can be used to characterise the relative importance of interfacial forces compared to bulk forces. Interfacial forces in the behaviour of a material dominate when the thickness of a film is below the capillary length for the material.

The surfaces of thin films are never completely flat since heat, causing thermal motion, moves molecules around. This motion creates capillary waves on the surface which can couple to other forces. Models for the process of EHD patterning assume that a spectrum of capillary waves already exists on the surface and that the waves have a lateral sinusoidal fluctuation with amplitudes which are much smaller than the overall thickness of the film. In modelling this, liquids are assumed to be incompressible and Newtonian (Goldberg-Oppenheimer, 2011). The capillary waves increase the surface area of the thin film, whilst surface tension acts to reduce the surface area (Harkema, 2005). When the capillary waves couple to other forces they are either damped or amplified. The Navier-Stokes equations for hydrodynamics can be used to predict the behaviour of the fluid surface.

The free film interface is described by a sinusoidal function with wavenumber (*q*), growth rate (τ^{-1}) and amplitude (*u*): (Schäffer, et al., 2001).

$$h(x,t) = h_0 + ue^{iqx+\frac{t}{\tau}}$$

(1.3)

Here h_0 is the initial film thickness (m), *u* is amplitude (m), *q* is wavenumber (cm^{-1}) and τ^{-1} is growth rate.

This function models the perturbations at the interface as stationary waves which grow in amplitude over time.

1.3.2 Detailed description of the 1D solution

The Navier-Stokes equation of motion describes the movement of an infinitesimally small volume element being moved by forces acting upon it. The motion of the fluid interface is described by the Navier-Stokes equation if the average velocity and the interfacial pressures are known (Voicu, 2009). The Navier-Stokes equation is given by:

$$\rho\left(\frac{\partial v}{\partial t} + (v \cdot \nabla)v\right) = -\nabla p + \eta\Delta v + \rho g$$

(1.4)

where ρ (kg m^{-3}) is density, *p* is pressure (Pa), η is viscosity (Pa s) and *g* is gravity and *v* is velocity (m s^{-1}).

Several assumptions, described in section 1.3.2 *Hydrodynamics*, simplify this equation to (Schäffer, 2001):

$$0 = -\nabla p + \eta\Delta v$$

(1.5)

The equations model the acceleration in the fluid in response to external forces. The Navier-Stokes equation describes the flow of the liquid, due to the modulation of the interface, giving a velocity profile through the depth of the film. The Navier-Stokes equation for incompressible fluids, which necessarily conserves momentum in the fluid, is used in conjunction with the continuity equation which conserves mass: flow mostly takes place in the lateral direction (Goldberg-Oppenheimer, 2011).

Two equations are then required to perform a linear stability analysis for the interface profile. The first is the equation for a velocity profile of Poiseuille type flow in a highly viscous film in response to a pressure gradient derived from a much-simplified Stokes equation: the second is the continuity equation (Schäffer, 2001).

Hydrodynamics

The equation of motion for the interface can be defined by using boundary conditions of no-slip at the polymer substrate surface and no lateral stress at the film surface (Schäffer, 2001).The modulation of the polymer/ air gap interface by an applied pressure causes a flow in the liquid. A velocity profile of a Poiseuille-type flow through the cross-section can be constructed (Goldberg-Oppenheimer, 2011).

The general Navier-Stokes equation for the x coordinate which describes volume flow is simplified by a number of assumptions (Schäffer, 2001). Comparatively high viscosities means velocities are slow and the flow is also steady, that the films are thinner than the capillary length and will not be affected by gravity (for most liquids this is between 1-3mm) and that for waves with a longer wavelength and smaller amplitude than the initial depth of the fluid the flow in the film is assumed to be a steady laminar flow caused by a pressure gradient in the x direction. The flow is in the direction of decreasing pressure (Goldberg-Oppenheimer, 2011) (Schäffer, 2001).

The Poiseuille flow *j* is given by:

$$j = \frac{h^3}{3\eta}\left(-\frac{\partial p}{\partial x}\right) \tag{1.6}$$

Where h (m) is the interface height in the y direction, η is the fluid viscosity (Pa s) and the differential term is the lateral pressure gradient with respect to the x co-ordinate (Schäffer, et al., 2001).

The no-slip condition at the liquid/substrate interface means that at the interface the fluid has zero velocity relative to the substrate. It is also assumed in the model, that stress within the fluid is equal to the surface pressure at the liquid/air interface. Once the velocity profile is described a continuity equation for the conservation of mass allows the profile of the interface to be calculated and allows an equation of motion for the film surface to be defined (Goldberg-Oppenheimer, 2011).

Knowledge of the interfacial pressure, which is the agent causing the movement, can then be used to calculate the dynamics of the film.

Interfacial pressure

The pressure at the interface *p(h)* (Pa) is the sum of the atmospheric pressure (p_o), the Laplace pressure (p_L) and the external pressure ($p_{ex}(h)$), which here is the electrostatic pressure (Voicu, 2009).

$$p(h) = p_0 + p_l(h) + p_{ex}(h) \tag{1.7}$$

The interfacial pressure at the liquid/air boundary must be known to calculate the dynamics at the interface. When a high enough electric field is used, only the electrostatic and Laplace pressure need to be considered (Schäffer, et al., 2001).

Laplace pressure and van der Waals forces

Van der Waals forces are intermolecular forces arising from permanent and semi-permanent electric dipole moments within molecules. These include the force between permanent dipoles (Keesom forces), the force between a permanent and an induced dipole (Debye force) and the force between induced dipoles (London forces).

Molecules at the surface of a film experience different forces to those in the bulk material. They are not surrounded on all sides by like molecules, and the difference in their interactions with these molecules leads to free surface energy. A liquid will always adopt a geometry that minimises its surface area and thus its free surface energy. The Laplace pressure is the difference in the pressure across a curved interface between two media and is essentially the difference in pressure that exists on the inside compared to the outside of a curved surface (Goldberg-Oppenheimer, 2011) (Schäffer, 2001). When the field is high enough the electrostatic pressure is also far larger than disjoining pressure in the film and so this is also neglected in the model.

The excess surface pressure here is the pressure created by the surface charge density induced by the electric field. So P_{ex} is P_{el} in these equations (Goldberg-Oppenheimer, 2011).

Excess surface pressure and EHD in perfect dielectrics

When a dielectric material is subjected to a large electric field, this causes a build-up of displacement charges and consequently an effective surface charge density due to the polarisation of the surface molecules. This is turn creates electrostatic pressure at the interface and if it is sufficiently large enough can be modelled as the dominant pressure at the interface combined with the Laplace pressure (Goldberg-Oppenheimer, 2011).

The electrostatic pressure overcomes the stabilising surface tension and alters the shape of the interface. Charges are effectively pulled towards the top electrode, which reduces the energetically-unfavourable increased electrostatic potential energy of the system. The electrostatic pressure is dependent on the strength of the electric field and the relative permittivity of the polymer layer (Goldberg-Oppenheimer, 2011).

The electrostatic pressure is calculated from the variation of free energy with respect to film thickness per unit area of the interface (Goldberg-Oppenheimer, 2011).

$$p_{el} = \frac{1}{A}\frac{\delta F}{\delta h} = -\frac{U^2}{2A}\frac{\partial C}{\partial h}$$

(1.8)

where *A* is area (m^2), *F* is the free energy stored in the capacitor (J), *h* is the film thickness (m), *U* (V) is the applied voltage and *C* is the capacitance (F) and the energy stored in a capacitor *C* with a constant applied voltage *U* (V) and F_0 (*J*) is the free energy in the absence of the applied voltage. is (Goldberg-Oppenheimer, 2011):

$$F = F_0 - \frac{1}{2}CU^2$$

(1.9)

The calculation of free energy is derived from the free energy stored due to capacitance. The air and polymer layers are modelled as two capacitors in series (assuming the relative permittivity of air is 1):

$$\frac{1}{C} = \frac{1}{C_{air}} + \frac{1}{C_{polymer}} = \frac{d-h}{\varepsilon_0 A} + \frac{h}{\varepsilon_0 \varepsilon_p A} = \frac{\varepsilon_p d - (\varepsilon_p - 1)h}{\varepsilon_0 \varepsilon_p A}$$

(1.10)

where *C* is the capacitance (F), *d* is the electrode spacing (m), ε_0 is the permittivity of a vacuum ($\approx 8.854 \times 10^{-12} Fm^{-1}$), ε_p is the relative permittivity of the polymer, *h* is the film thickness (m) and *A* is the area (m^2).

This leads to a definition of the pressure due to the electric field given by: (Goldberg-Oppenheimer, 2011)

$$p_{el} = -\frac{1}{2}\frac{\varepsilon_0\varepsilon_p(\varepsilon_p - 1)U^2}{[\varepsilon_p d - (\varepsilon_p - 1)h]^2}$$

(1.11)

Excess surface pressure in leaky dielectrics

For a material with a small but finite conductivity, the conduction of charges lowers the field in the bulk polymer. However, the free charges present in the material accumulate at the interface and add to the polarisation charges there. Thus, the electrostatic pressure at the interface is increased and higher than if the polymer were behaving as a perfect dielectric. The bulk of the potential difference crosses the air-gap and the electric field in the air layer is considered to be higher than in the polymer and it is this imbalance which creates patterns in a leaky dielectric (Goldberg-Oppenheimer, 2011). The electrostatic pressure in this case is given by (1.120 where ε_g is the relative permittivity of the gap fluid (Goldberg-Oppenheimer, 2011):

$$p_{el} = -\frac{1}{2}\frac{\varepsilon_g\varepsilon_0 U^2}{(d - h_0)^2}$$

(1.12)

Linear Stability Analysis

Linear stability analysis can then determine whether a perturbation will grow or remain stable and is now used to define a dispersion relation which describes the evolution of sinusoidal waves at the interface. Dispersion relations typically model how waves of different lengths move at different speeds, the dispersion relation in this model relates the wavelength or wavenumber to an amplitude growth rate and predicts which wavenumber will grow at the fastest rate.

Defining a dispersion relation

The equation of motion for the film surface derived from the Navier-Stokes equation is given by:

$$\frac{\partial h}{\partial t} = \frac{\partial}{\partial x}\left(\frac{h^3}{3\eta}\frac{\partial p}{\partial x}\right)$$

(1.13)

where *p* is pressure (Pa) and *t* is time (s).

The Laplace pressure is given by:

$$P_L = -\gamma \frac{\partial^2 h}{\partial x^2}$$

(1.14)

The derivative of the equation of motion is:

$$\frac{\partial h}{\partial t} = \frac{h^2}{\eta}\left(\frac{\partial h}{\partial x}\right)\left[\frac{\partial p}{\partial x}\right] + \frac{h^3}{3\eta}\left[\frac{\partial^2 p}{\partial x^2}\right]$$

(1.15)

This is then combined with the term for the interfacial pressure, the electrostatic pressure and the Laplace pressure. The ever-present capillary wave-like fluctuations at the interface are coupled to the electrostatic and Laplace pressures. Keeping the terms linear (linear stability analysis) produces an equation that predicts the evolution of the interface (Schäffer, 2001). The pressure is inserted into the derivative of the equation of motion and the nonlinear terms discarded to simplify the equation. This is coupled to the capillary wave spectrum allowing a dispersion relation to be defined, which may be simplified to:

$$\frac{1}{\tau} = -\frac{h^3}{3\eta}\left(\gamma q^4 + \frac{\partial p_{el}}{\partial h} q^2\right)$$

(1.16)

Here τ^{-1} is the growth rate (s), γ is surface tension (Nm^{-1}) and q is the wave vector with a magnitude of the wavenumber (cm^{-1}) (Harkema, 2005).

The dispersion relation is used to calculate the evolution of the capillary waves with relation to time and formulates a time constant for each wavenumber. The graph of the time constant against wavenumber shows the wavenumber with the fastest growth, which relates to the wavelength of the instability and the final pillar spacing (Figure 1.24). The time constant determines the rate at which waves of that number grow and, depending on the sign of the growth constant, whether waves of that number are amplified or damped: a negative time constant signifies that the wavenumber is damped (Figure 1.24) (Harkema, 2005).

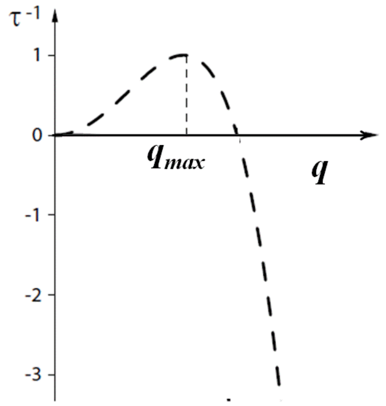

Figure 1. 24 Graphical interpretation of the dispersion relation. Where the graph is above the line of $\tau^{-1} = 0$, the wavenumbers are amplified. Below this line, they are dampened by surface tension (adapted from (Voicu, 2009).

For a perfect dielectric, the maximum growth wavelength which is the spacing of the fabricated pillars, is then given by:

$$\lambda = 2\pi \sqrt{\frac{\gamma U}{\varepsilon_0 \varepsilon_p (\varepsilon_p - 1)^2}} E_p^{-\frac{3}{2}} \tag{1.17}$$

Where γ is the surface tension (Nm^{-1}), U the applied voltage (V), ε_0 the permittivity of free space (8.8542×10^{-12} Fm^{-1}), ε_p the permittivity of the polymer and E_p the electric field in the polymer(Vm^{-1}) (Schäffer, et al., 2001).

The electric field in the polymer is given by:

$$E_p = \frac{U}{(\varepsilon_p d - (\varepsilon_p - 1)h)} \tag{1.18}$$

Where d is the electrode spacing (m) and h the initial thickness of the polymer (m) (Schäffer, et al., 2001).

1.3.3 Overview of a generalized linear stability analysis

Pease and Russel developed a model which investigated the forces which drive the process in more detail by including the Maxwell stress tensor at the polymer-air interface which acts on bound and free charges (Pease & Russel, 2002). The model also enabled explicit definitions of the wavelength for both a perfect dielectric (no current flow through the polymer) and a leaky dielectric (a current can flow through the polymer) under the lubrication approximation, a condition that assumed that linear scales in the direction parallel to the electric field were small in comparison to the size of the instability. In their model, they found that the inclusion of free charge at the polymer/air interface reduced the scale of the instability (Pease & Russel, 2003).

Their model also allowed the lubrication approximation to be relaxed by altering the way the parameters were scaled. Several of the terms in the equations were made dimensionless to both simplify the analysis and to highlight important relationships between parameters. Pease and Russel's model allowed for other materials to fill the gap between the polymer and the top electrode (Pease & Russel, 2003).

Assumptions

The model made several assumptions: the mask and substrate were conductors but the gap fluid was not, the ratio of the viscosity of the gap fluid to the polymer was small so the viscosity of the gap fluid was neglected and there was no insulating oxide on either electrode but the model did allow for this to be included. The model assumes a DC potential and that the slow variation of the electric field means that Maxwell equations are simplified by neglecting magnetic fields. This enabled a quasi-steady or quasi-electrostatic approximation to be made. The bulk materials are assumed to be electrically neutral, whereas charge is allowed to accumulate at the upper and lower interfaces of the polymer. The model encompasses the electrical behaviour of the polymer to range from a perfect dielectric where polarization effects in the material affect the instability, to a perfect conductor where free charge influences the electric fields (Pease & Russel, 2003).

Development of the model

A schematic of the model is shown in Figure 1.25:

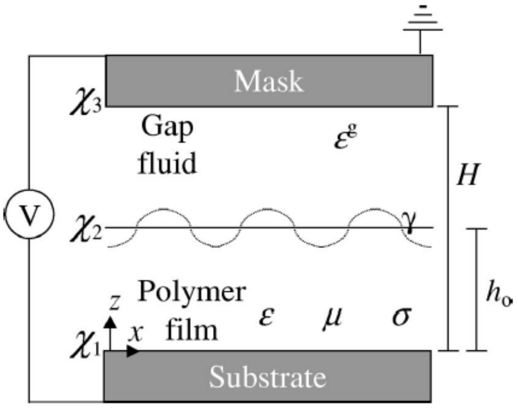

Figure 1. 25 Schematic of the system (Pease and Russel 2003).

In Figure 1.25, the schematic of the system: *H* represents the electrode gap (m), h_o the initial polymer thickness (m), ε^g is the relative permittivity of the gap fluid, γ is the surface tension of the polymer (Nm^{-1}), ε is the relative permittivity of the polymer, μ is the viscosity of the polymer (Pa s) and σ is the conductivity (S/m) of the polymer. *X* represents the potential at each interface (V) (Pease & Russel, 2003).

Initially the potential at each interface is defined using both the contact potentials and the applied voltage. The surface charge density at the interfaces is then equal to the jump in the normal component of the electric displacement vector across the interface. Balancing the surface charges then defines the quasi-electrostatic description. Pease and Russel based this on work performed by Saville (Saville, 1997).

The quasi-electrostatic description means that the definition of the time dependent charge balance at each interface can be derived. Free charge is assumed not to diffuse across the interfaces and the potentials and fields in the polymer and gap material can then be defined which are then used to determine the interfacial charge (Pease & Russel, 2003) . The field from the quasi-electrostatic definition couples to the fluid dynamics due to stress imbalances at the polymer/gap interface. Stress at the interface operates in 3D, so a tensor is used to condense all the 3D components of stress into a simple 3x3 matrix expression. A reduced Maxwell stress tensor is used to denote the physical momentum caused by the electromagnetic forces acting at the interface.

At the polymer/air interface the tensor is manipulated to give the balance for the normal and tangential stresses at the interface. These are defined using the viscosity of the fluid, the velocity of the polymer, pressure in the polymer compared to ambient pressure, interfacial tension and the curvature at the interface. The gap fluid viscosity is assumed to be negligible.

The model then shows that the polymer experiences electrical and hydrodynamic stresses which the air does not (Pease & Russel, 2002). Describing the mean curvature κ of the interface using the special case of 2 coordinates gives an expression that allows a simpler definition of the unit normal to the surface and tangential vectors to be defined. Interpreting the normal stress balance in these equations highlights the forces which drive this process (Pease & Russel, 2003). Bulk motion is described by the Stokes equation and continuity.

The flow is assumed to be slow and to have no slip at the polymer/substrate boundary. A description of the film height at the polymer/air boundary, as a function of time, is defined by using the assumption that the velocity in the fluid vanishes at the substrate boundary. A perfect dielectric is modelled by setting the free charge at the polymer/gap interface to zero and then ignoring the charge balance. With the equations describing the interface height at the boundary defined, the model is then scaled and dimensionless variables are introduced.

Scaling the Navier- Stokes equations simplifies the analysis and allows improved insight into the problem. In order to allow an applied voltage to become a dominant factor in the model, the scale for potential includes the applied voltage. Also, the relative permittivity of the gap fluid can be introduced rather than using the assumption that the gap fluid is air. The inclusion of the applied voltage and the relative permittivity of the gap fluid in the scaling generalises the model and relaxes the lubrication approximation. Lateral velocity and interfacial charges are scaled by balancing terms in the continuity equation. Balancing electrical and pressure forces in the normal stress balance gives the pressure scale. The normal stress balance allows an electrocapillary scale length to be defined. A dimensionless bulk conductivity S is defined which represents the ratio of a time scale for free charge conduction to the process time scale. The process time scale is short when electric fields are strong but long when surface tension and high viscosity retard the motion of the fluid. Gravity and inertia are excluded (Pease & Russel, 2003).

Four dimensionless groups are important: the polymer thickness to gap ratio, the gap to electrocapillary length ratio, the ratio of dielectric constants and the bulk conductivity parameter *S* which is given by Pease and Russel (Pease & Russel, 2003):

$$S = \frac{\sigma\mu\gamma H^3}{\varepsilon^{g^3}\varepsilon_o^3 \mathrm{X}^4}$$

(1.19)

Where σ is the conductivity (S/m), H is the electrode gap height (m), ε^g is the permittivity of the gap fluid, ε_o is the permittivity of free space and X is the potential arising from the applied potential and the contact potentials (V).

The bulk conductivity parameter *S* is used for defining experimental conditions where conduction is fast and allows a simplified method of predicting the wavelength of the surface which is described in the *Leaky Dielectric* section further below.

Linear stability analysis can now be performed using a base case steady state with a perturbation. As the fluid velocities are assumed to be zero the unknowns are the potentials in the fluid and the gap and the pressure in the polymer film. The analysis is then different for perfect dielectrics and leaky dielectrics.

Perfect dielectric

For a perfect dielectric polarisation charge only is allowed to exist. The base case potentials are defined however, due to the lack of free charge at the polymer/gap interface, the electric fields in the polymer and gap fluids are related to the ratio of the relative permittivities of these materials. This situation is more complicated than with a leaky dielectric where the current flow in the polymer means the field in the polymer is assumed to be negligible and is disregarded. With a perfect dielectric however the field in the polymer is non-zero. The perturbed equations are then defined and these definitions contain the ratio of *H/L* which the lubrication approximation neglects. This ratio combines the height of the electrode gap *H* and the parameter *L* which represents the electrocapillary length which is set by competition between surface tension and electrical forces (Pease & Russel, 2004). The parameter L is defined as ($\gamma H^3/\varepsilon^g\varepsilon_o X^2$).

Combining the perturbed equations allows the height *h* of the polymer at the interface to be defined which, when substituted into the kinematic boundary condition and manipulated, allows the growth exponent *m* of a spectrum of wavenumbers to be described for both the lubrication and non-lubrication (containing *H/L*) scenarios. The growth exponent *m* for the non-lubrication approximation perfect dielectric is given below:

$$m = \frac{S_o C_o - k\frac{H}{L}h_0}{2k^3\frac{H^3}{L^3}\left(k^2\frac{H^2}{L^2}h_o^2 + C_o^2\right)} \times \left(\frac{k^3\frac{H}{L}}{\left(T_o + \frac{\varepsilon}{\varepsilon^g}T_{1mo}\right)} \frac{\frac{\varepsilon}{\varepsilon^g}\left(\frac{\varepsilon}{\varepsilon^g} - 1\right)^2}{\left(h_o + \frac{\varepsilon}{\varepsilon^g}(1 - h_o)\right)^2} - k^4 \right)$$

(1.20)

$$where\ S_o = \sinh\left(h_o k\frac{H}{L}\right) \quad C_o = \cosh\left(h_o k\frac{H}{L}\right)$$

$$T_o = \tanh\left(h_o k\frac{H}{L}\right)\ T_{1mo} = \tanh\left(\frac{kH(1 - h_o)}{L}\right)$$

k=wavenumber (cm^{-1}), *ε*= relative permittivity of the polymer and h_o=initial polymer thickness (Pease & Russel, 2004)

A graph of the growth exponent *m* for a given set of experimental parameters is shown in Figure 1.26 using (1.20) (the Mathcad worksheet is shown in Appendix B). The wavenumbers that have a positive exponent are amplified; those that have a negative exponent are dampened. When the growth exponent *m* equals zero and crosses the x axis, the associated wavenumber is described as the critical wavenumber (k_{crit}) where the wavenumbers beyond this maximum are dampened by surface tension and so do not grow.

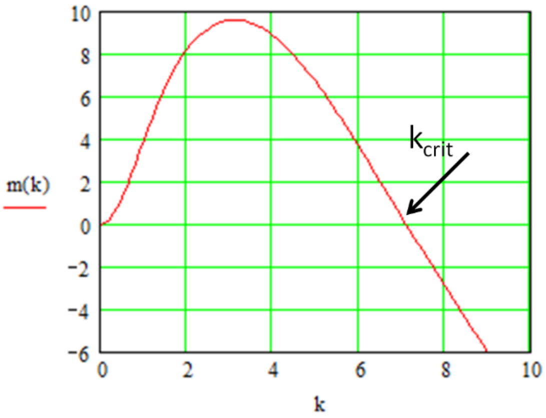

Figure 1. 26 Growth exponent m using (1.20) with an electrode gap of 2.5µm and epoxy thickness of 2µm and an applied potential of 60V for a perfect dielectric without the lubrication approximation.

Including and excluding the ratio of the height and the length *H/L* allows the definition of the critical wavenumber (the wavenumber above which all waves are dampened) for both the lubrication and non-lubrication approximations to be made.

Under the lubrication approximation (not containing *H/L*) the equation for the growth exponent can be simplified. The maximum growth exponent k_{max} can then be expressed which is associated with a specific wavenumber *k* which is typically the spacing of the final array of pillars and this is also expressed as an equation for the associated maximum growth wavelength for a perfect dielectric under the lubrication approximation:

$$\lambda_{max} = \frac{2\left(2^{1/2}\right)\pi\gamma^{1/2}\left(\varepsilon^{g}h_{o} + \varepsilon(H - h_{o})\right)^{3/2}}{|\chi|(\varepsilon\varepsilon^{g}\varepsilon_{o})^{1/2}|\varepsilon - \varepsilon^{g}|}$$

(1.21)

(Pease & Russel, 2004)

For the non-lubrication approximation, the expressions for the critical wavenumber and the critical wavelength can be defined by using an expansion of (1.20). Then, comparing the definitions of the critical wavelength k_{crit} both with and without the lubrication approximation, enables a condition to be derived which determines when the lubrication approximation applies. The transition value of *H/L* is defined as:

$$\left(\frac{H}{L}\right)_{transition} = \left|\frac{\varepsilon + \varepsilon^g}{\varepsilon - \varepsilon^g}\right| \left(\frac{\varepsilon^g h_o + \varepsilon(H - h_o)}{\varepsilon H}\right)^{1/2}$$

(1.22)

When

$$\frac{H}{L} \ll \left(\frac{H}{L}\right)_{transition}$$

(1.23)

then the lubrication approximation can be applied (Pease & Russel, 2004).

Leaky dielectric

A similar approach is taken to analyse a leaky dielectric. The potentials in the polymer and gap fluids are determined. The conductivity in the polymer means that the electric field in the polymer disappears and the potential is assumed to drop across the air gap. The field in the gap is based on the interfacial height which increases as the gap decreases and is the driving force for the pillar growth. The boundary condition and stress balance enables the pressure in the polymer film to be defined and the film is in tension due to the sub-ambient pressure in the film (Pease & Russel, 2003).

A similar procedure to the perfect dielectric is applied to the leaky model for defining equations in the perturbed state. By finding fluid velocities, potentials and pressure these can be combined into the kinematic boundary condition which allows a definition for the perturbation amplitude with respect to time to be defined.

The equation for the perturbation amplitude can be expressed as a matrix. The eigenvalues of the matrix relate to two growth exponents *m*. One is always negative and can be interpreted as stabilizing and so the instability is based on the other eigenvalue. Under the lubrication approximation the growth exponent equation is greatly simplified. Limiting cases such as when high conductivities i.e. when *S*>>1, exist also provide simplifications given by (Pease & Russel, 2004):

$$m = \frac{S_o C_o - k\frac{H}{L}h_0}{2k^3\frac{H^3}{L^3}\left(k^2\frac{H^2}{L^2}h_o^2 + C_o^2\right)} \times \left(\frac{k^3\frac{H}{L}}{(1-h_o)^2}\frac{1}{T_{1mo}} - k^4\right)$$

(1.24)

Again, when the lubrication approximation is assumed the growth exponent can be simplified and a characteristic wavelength for a leaky dielectric can be defined:

$$\lambda_{max} = \frac{2^{3/2}\pi\gamma^{1/2}(H-h_o)^{3/2}}{|\chi|(\varepsilon^{g}\varepsilon_o)^{1/2}}.$$

(1.25)

(Pease & Russel, 2004)

For the non-lubrication approximation for a leaky dielectric, an asymptotic expansion of the growth exponent results in a definition of the critical wavenumber which can then be defined in terms of the critical wavelength. For a given ratio of permittivities, the critical wavenumber is always greater for the leaky dielectric than for the perfect dielectric, implying that there will be less ordering in the leaky dielectric. A definition for the maximum wavelength however is not stated in the literature. Similarly to the perfect dielectric case, the validity of the lubrication approximation can be determined using the transition value of *H/L*:

$$\left(\frac{H}{L}\right)_{transition} = \left(\frac{H-h_o}{H}\right)^{1/2}$$

(1.26)

Again when $\frac{H}{L} \ll \left(\frac{H}{L}\right)_{transition}$ the lubrication assumption holds.

The equations in the theories detailed in this section have been used to compare with data derived from the EHD experiments. The applicability of these theories to the surfaces fabricated in epoxy completed in this study are discussed in the Discussion Chapter 4.

2. Experimental Chapter

2.1 EHD patterning

Materials which were purchased from Sigma Aldrich were – PMMA (Mw 180 000), PS (Mw 289 000), PVA, titanium (n) butoxide, benzoylacetone, 1-pentanol, trypsin and media. Human eye lens epithelial cells B-3 and human liver epithelial cells (hepatocellular carcinoma) HepG2 were purchased from ATCC. PDMS (Sylgard 184) was purchased from Dow Corning, ITO slides (70-100 ohms per square metre, 25x25mm) were purchased from Diamond Coatings. Silicon wafers were purchased from ML Solar and epoxy (Araldite, Locktite and Evo-stik) was purchased from Halfords.

There are a number of different approaches to practical EHD patterning which have been covered in Chapter 1. In this chapter materials and methods that were used in this project are presented. The key features of the experimental arrangement are the electrodes and contacts, the spacers, the voltage supply and the patternable polymer (Figure 1.15).

The aims were to produce pillared surfaces whose pattern could be controlled using the manufacturing parameters used to produce pillars with a spacing of 2.5μm. In order to gain an understanding of the method of EHD patterning, the technique of producing EHD patterned surfaces in a titanium dioxide sol-gel devised by Voicu was initially replicated (Voicu, et al., 2007). Methods of producing spin coated thin films from PMMA, PS and PDMS were modified from sources in the literature (Hall, et al., 1998). Once an understanding of the EHD patterned method had been developed using sol-gel, an epoxy resin was introduced. Infrared reflectance and transmissions spectra were used to estimate the thickness of the films again using methods found in the literature (Hind & Chomette, 2011). Control of the thickness was an important aspect of controlling the manufacturing parameters and thus the overall EHD patterns produced.

2.2 Spin coating

Spin coating is a technique ubiquitously used in the industries that require thin films for use in many devices, ranging from optics to microprocessors. Film from nanometres to several microns can be obtained in a large variety of materials, including sol-gels and thermoplastics. In this work spin coating was used to produce the thin films for the insulating spacers and patternable polymers in the EHD experiment.

Mass production spin-coating techniques are highly automated and for R&D purposes spin coating often offers the best solution for fabricating good quality thin films in small batches. In this project a desktop Dynapert spin-coater was used, and the coating solution was distributed onto a substrate in very small quantities from a hand-held pipette.

This general method of producing thin films is based on spreading a liquid across a surface by centrifugal force. A substrate such as a silicon wafer is attached, typically by suction, to a chuck which rotates. The coating liquid can be dispensed before the chuck moves (static dispensing) or whilst it is in motion (dynamic dispensing) (University of Louisville: Micro/Nanotechnology Centre, 2013) (Brewer Science, n.d.). Generally, the spin speeds used are upwards of 1000rpm, although it is possible to obtain a good coating with a lower speed.

Film formation during spin coating primarily depends on viscosity and spin speed, although many other parameters affect the spinning process such as spin time, solvent evaporation and humidity (Sahu, et al., 2009). So typically, in practice the thickness of a resulting film is altered by adjusting the spin speed. This is especially true where the solvent used is very volatile since the spin time of the process is controlled by the drying time of the film which can be a matter of seconds. As a result, this means that good control over the thickness can be achieved for a given concentration and the range of thicknesses is relatively small (for a given concentration) (Ossila, n.d.).

In static dispensing the fluid is deposited whilst the chuck is stationary and is spread once the chuck rotates. During dynamic dispensing the fluid is applied to the centre of the substrate whilst it is in motion. In dynamic dispensing the fluid spreads from the centre of the substrate and the leading edge of the fluid, called an edge bead, is slightly thicker because of the meniscus that forms due to surface tension. Once most of the excess liquid has been ejected from the substrate, the layer continues to thin by material being lost from the edge. Any volatile agents within the material are evaporated which also causes further thinning and, in many cases such as when a polymer is being deposited from solution, solidifies the layer.

In this study, uncured epoxy resin was deposited from solution so that, as the volatile solvents evaporated, what was left was still a liquid, albeit a very viscous one. PDMS was coated in this way also leaving a liquid coating and thermoplastics were coated from solution leaving thin solid films (Hall, et al., 1998).

Both dispensing methods were tried and it was found that during static dispensing evaporation of the solvent caused ridges to develop in the deposited coating before rotation started, which caused roughness in the finished film. Dynamic dispensing however eliminated this problem and produced even layers. During the dynamic dispensing used in this study, only a small amount of fluid (typically between 1- 100µl) was deposited in the centre of the rotating substrate. Speeds of 1000-4000 rpm were favoured, since the lower speeds also produced issues with edge beads causing ridges in the final film.

The epoxy was deposited from solution due to its high viscosity when solvent free, which meant that it was not possible to achieve micro-thin layers by spin coating without addition of a solvent. The requirement for the fluid to have a low viscosity is a disadvantage for this technique as it can limit the maximum thickness of material that can be deposited in a good quality, even coating.

Solvent choice is an important factor in spin coating since a fluid that does not wet the substrate will leave a poor-quality film as a result. In this study the solvents used were predominantly toluene and acetone both of which sufficiently wet the main substrates used, these being indium tin oxide (ITO) coated glass and silicon.

In practice, generally the amount of liquid dispensed onto the substrate does not influence the final thickness of the coating; however, in this study, small substrate areas were being coated (between 0.5 and 2cm^2) and the amounts of fluid used were also small (typically in the region of 10-100 µl) so it was found to affect the final thickness. For that reason, the amount of fluid used for the epoxy film which was to be patterned was measured and was between 10 and 100µl so that the thickness of spin coated film was consistent (Ossila, n.d.) (Taylor, 2001).

For dynamic deposition, a low spin speed is normally used first during fluid dispensation and then the speed is increased so the layer is thinned. The coatings in this study were small areas using small amounts of fluids and it was found that by using this method ridges were left in the film due to the drying of the edge bead as it spread during the

initial slow-speed stage. For this reason, the material was deposited at the final spin speed in order to achieve an even coating (Taylor, 2001).
Cleaning the substrates prior to coating is also very important since particulates and dust will result in pinholes and streaks in the coating. Substrates were cleaned with deionised water, acetone and industrial methylated spirits (IMS) and were wiped dry using low lint clean room wipes. Particles in the deposited fluid can also cause defects in the film, so the solutions were filtered before use.

Only a very small central area (between 0.5 and 1cm^2) of the electrode required the epoxy film coating. For initial experiments, the excess epoxy around the edge of the electrode was removed using electronics grade low-lint swabs. However, this was found to introduce dust into the coated epoxy and so an alternative method was developed. During spin coating the area that did not require the epoxy film for the EHD experiment was masked, using a thin PVC film which was removed once the epoxy had been coated. This left a small coated area in the middle of the electrode with a smaller edge bead that could be removed cleanly using a low-lint swab.

During spin coating many other factors, in addition to speed, contribute to the resulting thickness of the film including viscosity, duration and evaporation of volatiles. All of these factors can be manipulated to change the thickness of the final film. In this study the concentration (and thus viscosity), duration and spin speed were all used to vary the film thicknesses.

2.3 Electrodes

Several different materials were tested for use as electrodes. The electrodes needed to be flat (ideally optically flat) and electrically conductive. Gold/palladium (Au/Pd) sputter-coated glass slides were tested. The coatings were estimated to be of the order of 6nm in thickness and were created with a DC sputter coater at a setting of 2kV 20mA and the coating time was between 15 and 30s. These were not found to be of use as there was a significant amount of discharge across the electrode gap when the voltage was applied (Figure 2.1). Also, they were very easily scratched and marked.

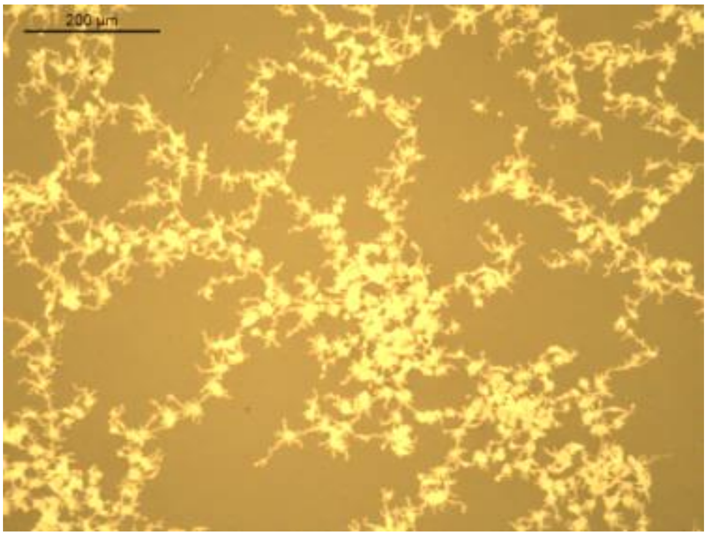

Figure 2. 1 Optical micrograph of damage to an Au/Pd sputter coated electrode (scale bar 200 µm).

The preferred electrode materials were doped silicon wafers and indium tin oxide (ITO)-coated glass slides since they were both flat and electrically conductive furthermore ITO is a transparent conductor so allowed the electrodes to be optically aligned. For the ITO slides an overall resistance of 70-100 ohms per square metre was found to be sufficient since current flow was not required. The surface roughness was an important consideration since an irregular electrode surface meant that the electric field between the plates was not even, leading to irregularities in the fabricated pattern. ITO slides of 2.5cm square were used. The ITO was removed from the outer edges of the slide using a 50% HCl etch so that only the central square and a path to allow electrical conduction remained (Figure 2.2). This ensured that the area in contact with the spacer material was not conductive.

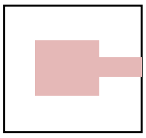

Figure 2. 2 ITO (pink) geometry after etching on glass slide.

The thickness of the ITO was in the region of 70-90nm. As ITO is a transparent conductor the ITO/glass slides were generally used as the top electrode to allow the alignment of the two electrodes. Electrical contacts were made by the attachment of thin foil to the conductive ITO using electrically conductive carbon glue.

Silicon wafers with a variety of orientations were generally used as the bottom electrode. Electrical contact was again made by attaching a thin metal foil connected to the voltage source. The use of thin foil allowed the positioning of the electrodes to be manipulated to obtain the optimum alignment during the experiment.

Both the ITO slides and silicon wafers were washed in deionised water, IMS and acetone before use and dried with a low lint clean room wipe.

2.3.1 Spacer materials

Many different materials and arrangements were experimented with to obtain the ideal spacer layer and configuration. Spacers needed to be in the order of microns thick with no ridges. In the literature, this challenge has been resolved in many different ways such as by the use of silicon oxide sputtered pads, etched pillars (Schaffer, 2001), etched glass (Bae, et al., 2008) and a customised tool referred to as an active gap tool where the position of the top electrode could be adjusted easily by using servo motors (Dickey, et al., 2006). The materials used here were spin coated polymers such as epoxy resin, polydimethylsiloxane (PDMS) and thermoplastics such as PS and PMMA. Other thin polymer films were also tested such as PTFE, PVA and EVA/PVDC/EVA films.

The spacers needed to be electrically insulating and of a uniform thickness. A large variety of spacer thicknesses were used in this study between 0.5 to 50µm. Most of the spacers were spin coated, as in the case of PVA, PS, PMMA and epoxy, from solution and some of the spacer geometries tested are shown in Figure 2.3.

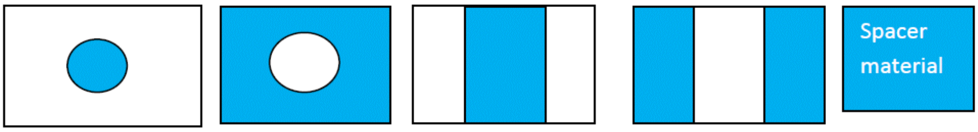

Figure 2. 3 Spacer patterns.

A spin-coatable PVA solution was prepared by dissolving 80% hydrolysed polyvinyl alcohol (PVA) (0.5g) in water (2ml) by agitating it for 15 min at 80°C. Once the solution was cool a further 5ml of ethanol (IMS) was added.

PS and PMMA were used in preference to PVA since they were easier to dissolve. PMMA (Mw 180 000) and PS (Mw 289 000) were dissolved in toluene using a variety of concentrations up to 10% by weight. Higher concentrations meant the solutions were more viscous and did not produce an even coating and it was found that 10% by weight was the maximum concentration that would produce even layers. Uneven coatings were also the result of using spin speed slower than 1500 rpm, which typically did not produce even coatings. These factors limited the thickness of the layers produced and it was found that layers of over 10 µm were difficult to obtain from a PS or PMMA solution.

The PDMS was generally used in a 10:1 ratio of PDMS base to curing agent and normally coated onto the silicon wafer which composed the bottom electrode. When a very thin PDMS coating was required, it was thinned with hexane to obtain PDMS films in the region of nanometres. The inclusion of large amounts of solvent did introduce issues with very thin coatings of PDMS since the tended to rupture and dewet and form droplets.

The most effective spacer configuration was found to be where the spacers were arranged in two thin strips (0.5 by 1.5cm) along opposite edges of the bottom electrode. This pattern was fabricated by removing the excess material in the centre of the electrode with a surgical blade.

2.4 Voltage source

For voltages up to 60V a variable DC voltage source was used. A current limiting resistor was included in the circuit for safety. When over 60V was required, a DC voltage source delivering 400V was used and a 15MΩ limiting resistor placed in the circuit which lowered the voltage drop across the capacitor to 162V. A handheld multimeter was used in series in the circuit to monitor stray current flow during EHD pattern fabrication. The voltage drop across the capacitor cell was measured with a benchtop ISO-Tech IDM-201N multimeter.

2.5 Patternable polymer

2.5.1 Sol-gel

The layer to be patterned needed to be soft so it could be hardened once the patterns had taken shape. Initially a titanium dioxide (TiO_2) sol-gel mixture was used according to the procedure set out by Voicu (Voicu, et al., 2007).

Titanium n-butoxide (Aldrich Chemicals) and benzoylacetone (Aldrich Chemicals) (10 mmol of each) were reacted in methanol (12.5 ml) for 2h at room temperature to produce a spin-coatable TiO_2 precursor. Then 1-pentanol (37.5 ml) was added to dilute the Ti-butoxide precursor and the mixture was stirred for another 15 min (Voicu, et al., 2007). A sample amount of the sol was air dried and pyrolysed and the resulting material tested using X-Ray Diffraction (Bruker D8 Advance) to confirm that it was TiO_2.

Various amounts of the TiO_2 precursor (from 1 – 10µl) were deposited onto a spin coater running at a speed of 3500rpm. Using only a small amount of liquid prevented the sol from spreading very far and covering the spacers during coating. The liquid was typically spun for around 10s, after which the electrode was removed from the spin coater and the top electrode applied. The application of the top electrode arrested the evaporation of the solvent from the TiO_2 sol, so the layer remained a liquid when the voltage was first applied.

A voltage was then applied to the electrode sandwich, which was left for 1h to ensure that the solvent was fully evaporated from the sol while the voltage was still on. Overall the tests using the sol-gel gave unsatisfactory results. The sol was found to dry very rapidly often before the pillars had evolved; however, some results were obtained shown in Figure 2.4.

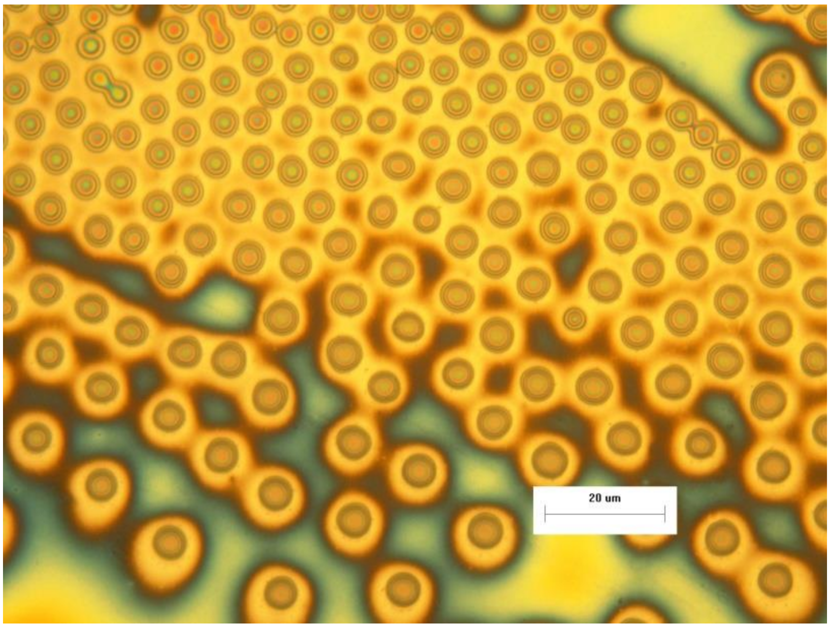

Figure 2. 4 Optical micrograph of a TiO_2 sol-gel EHD instability pattern (scale bar 20µm).

2.5.2 Epoxy Resin

The use of the known method described above served to provide a better understanding of the EHD patterning process and most of the remaining research was completed by using a room temperature curing epoxy resin as the patternable liquid.

The overall objective using epoxy resins was to produce a cheap, easily fabricated coating that could be used for solar collectors. Epoxies are widely available and not expensive; they have good resistance to environmental and thermal degradation and, once a crosslinking agent is added, transform from a deformable liquid to a glassy solid. A number of commercially available 2-part epoxy adhesives (Evo-Stik, Araldite and Locktite) were tried as they cured at room temperature and so avoided the complication of requiring a heat source to cure them.

An epoxy resin is a substance consisting of molecules containing two or more epoxy groups that can be crosslinked. A brief overview of the chemistry of epoxy resins is included here for completeness, although it is a large subject area and a comprehensive examination is not within the scope of this work.

The simplest epoxy resin is produced by reacting epichlorohydrin with bisphenol A to produce the molecule commonly known as diglycidyl ether of bisphenol A (DGEBA) (Figure 2.5) (Dow Plastics, 1999).

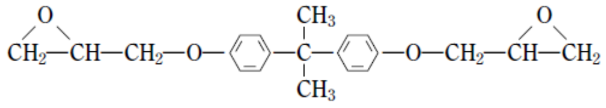

Figure 2. 5 The simplest epoxy molecular structure (Dow Plastics 1999).

The higher molecular weight structures with a central repeating unit are exemplified by:

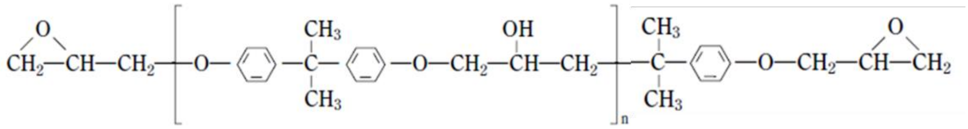

Figure 2. 6 Higher weight epoxy molecules (Dow Plastics 1999).

The epoxy group (Figure 2.7) is the 3-atom ring at either end of the molecule containing an oxygen atom. The shape of this unit means that it is under strain and hence highly reactive.

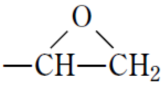

Figure 2. 7 Epoxy group (Dow Plastics 1999).

A crosslinking agent is required to solidify the epoxy and several materials are used, some of the most common are substances that contain amine groups (Dow Plastics, 1999) (Nils Malmgren AB, n.d.). The use of an amine rather than other crosslinking agents means that the epoxy can be hardened at room temperatures. The epoxy that was predominantly used in this study (Evo-Stick Control) was cured by using an amine and so this reaction is discussed here.

The hydrogen in a primary amino group reacts with the oxygen in the epoxy group to form a secondary amine and an OH group (Figure 2.8).

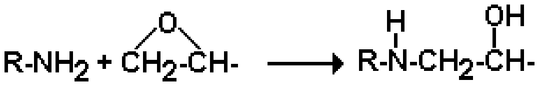

Figure 2. 8 Initial reaction step (Nils Malmgren AB n.d.) (Dow Plastics 1999).

The reaction continues as the hydrogen in the secondary amine reacts with another epoxy group (Figure 2.9).

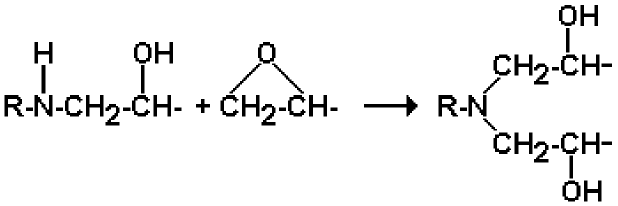

Figure 2. 9 Further reaction step (Nils Malmgren AB n.d.) (Dow Plastics 1999).

Although the curing reaction is exothermic, the amount of heat produced is dependent on the volume of epoxy. In these experiments, only micrograms of the material in a thin film were used, so the heating was negligible.

Initially the reaction rate of the epoxy is high due to the number of reactive molecules available and the low viscosity of the material. As more epoxy molecules react the reaction slows and the viscosity increases. A room-temperature epoxy will achieve 70-80 percent of its overall hardness in 24h. To all intents and purposes, it is solid and can be used in this state although there may be unreacted molecules still within the material (Nils Malmgren AB, n.d.).

For an epoxy resin Evo-Stick Control has a low average molecular weight (MW<700) but this value is typical for epoxies used as fillers and glues. Its low molecular weight means that it does not require the presence of a solvent to be a liquid at room temperature and so can be used for these kinds of applications. This means that as the material solidifies, there is little change in its volume.

The initial challenge was to obtain a form of the room temperature cure epoxies that could be deposited as a thin film, since in its raw form the resin itself is very viscous and could not be spin coated. It was very important to obtain a smooth solution, as particulates would stop even coatings being produced during spin coating, thus disrupting the EHD patterning process.

Several commercially produced epoxies were tested, including Evo-Stik, Araldite and Locktite. Initially, equal amounts of the two parts were combined and then this mixture was diluted with varying amounts of common solvents such as ethanol, propanol, petroleum ether and chloroform. The resulting solution was then applied to glass slides by dip coating and by spin coating with the latter being the preferred technique. Although the bulk of the combined epoxy material dissolved well in many of the solvents tested (acetone, toluene, methanol, ethyl acetate for example) the initial films still had a rough surface when spin coated. Examination with an optical microscope showed small grains in the coatings as shown in Figure 2.10.

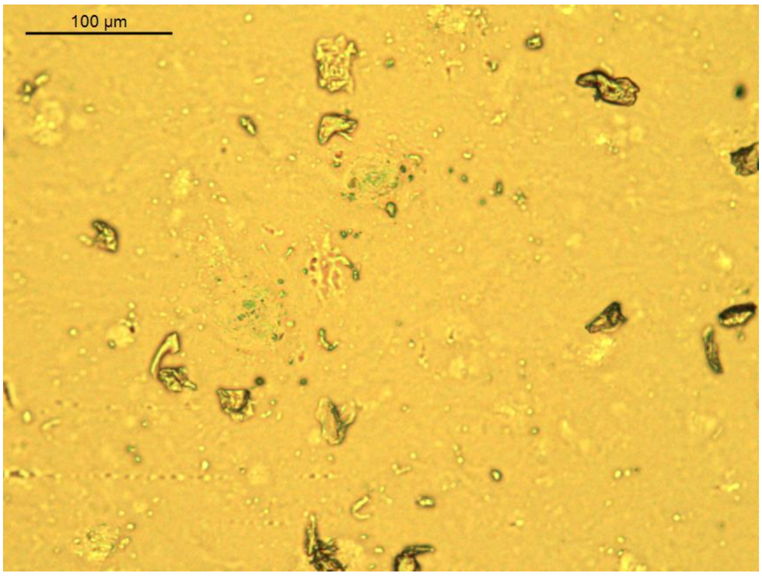

Figure 2. 10 Optical micrograph of epoxy coating showing the grainy surface.

Some of the epoxies showed a great deal of phase separation upon spin coating (Figure 2.11).

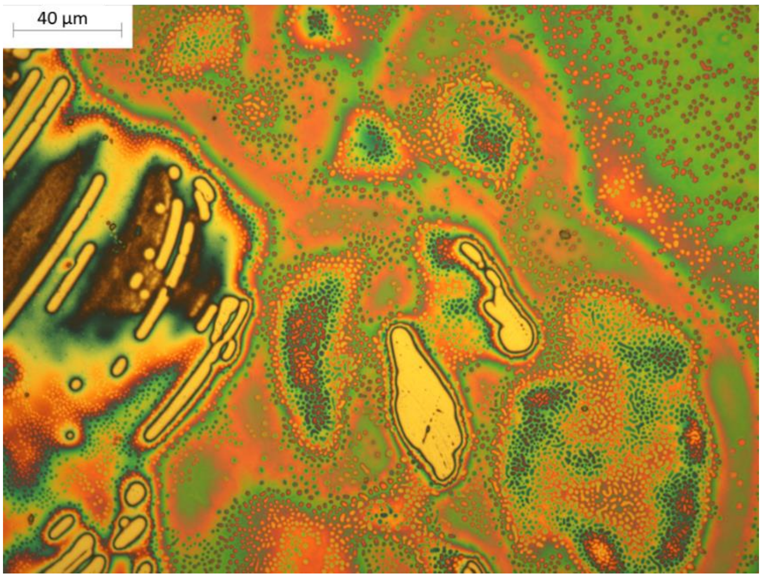

Figure 2. 11 Optical micrograph of phase separation in spin-coated Locktite epoxy resin.

Several samples showed several dewetting issues, especially once spin coated. This was probably due to the wetting capabilities of the solvents used, since the adhesive properties of epoxy itself are very good (Figure 2.12).

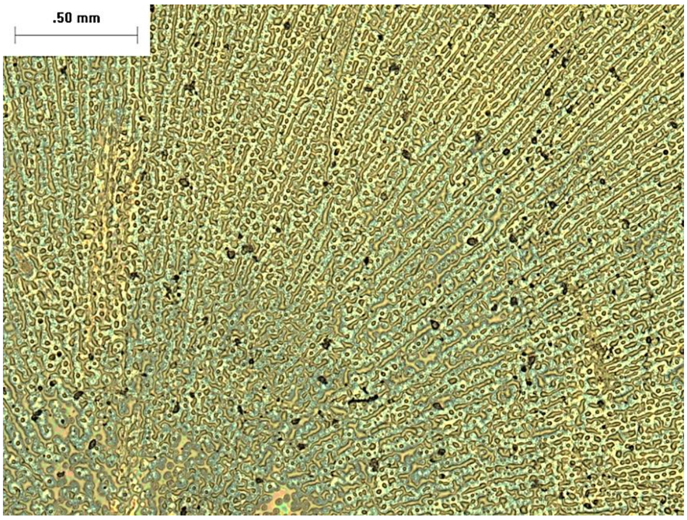

Figure 2. 12 Optical micrograph of Locktite detwetting during spin coating.

Further investigation into the use of epoxy resulted in better quality surfaces when the two parts were dissolved in separate solvents before they were combined. It was found that the individual components of the two-part epoxies dissolved better in different solvents. The two solvents themselves were also required to be miscible. This resulted in mixtures, which coated the silicon wafers without dewetting, separating or forming grains (Figure 2.13).

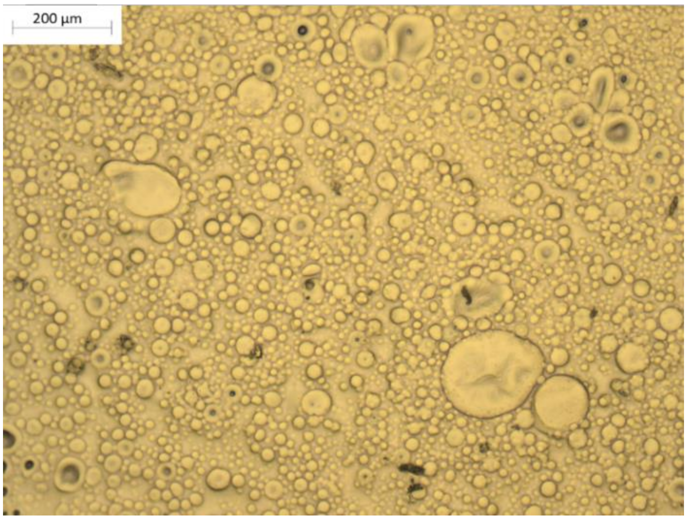

Figure 2. 13 Optical micrograph of Evo-Stick Control epoxy coating: unfiltered with resin dissolved in acetone and crosslinker dissolved in IMS.

Although the two parts dissolved individually, often precipitation would occur once they were mixed together after they had been filtered (Figure 2.14).

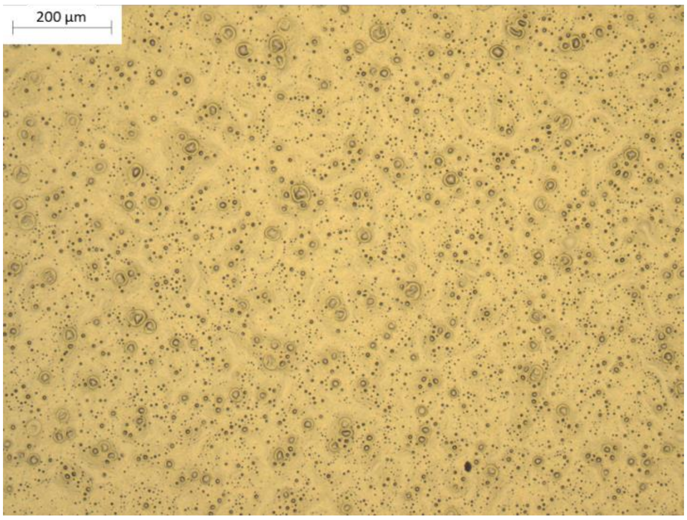

Figure 2. 14 Optical micrograph of Evo-Stick Control epoxy coating: filtered with crosslinker dissolved in IMS and resin dissolved in acetone.

In general, the resin components of the epoxies dissolved well in acetone and produced suspensions in other solvents; similarly, the crosslinking agents were better dissolved in toluene. Evo-Stick Control was found to have the best coverage and consistency in its texture (Figure 2.15).

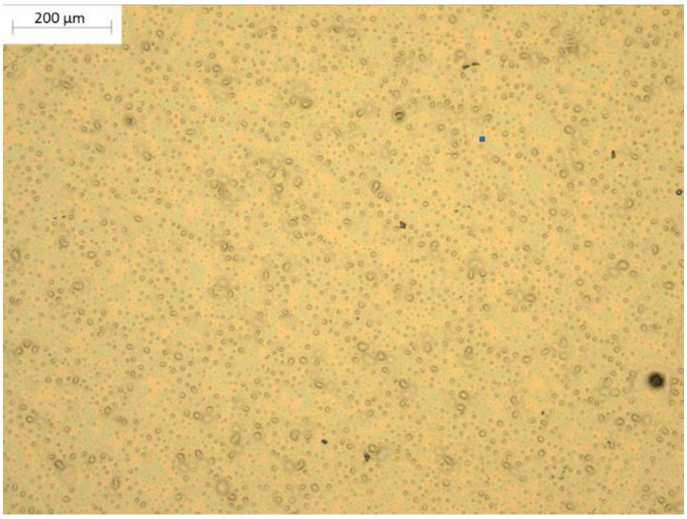

Figure 2. 15 Optical micrograph of Evo-stick Control epoxy coating: unfiltered, crosslinker dissolved in acetone and resin dissolved in acetone.

Evo-Stick Control with the resin component dissolved in acetone and the crosslinker dissolved in toluene and filtered using a 0.2 µm syringe filter after having been combined gave the best results (Figure 2.16).

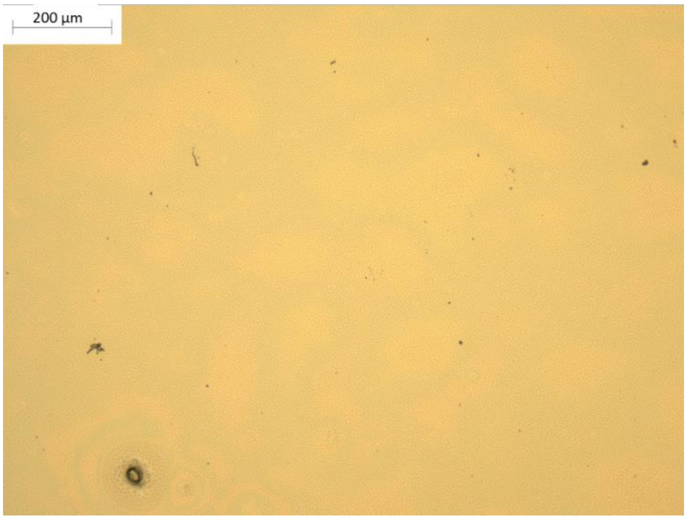

Figure 2. 16 Optical micrograph of Evo-Stick Control epoxy coating: filtered, resin dissolved in acetone and crosslinker dissolved in toluene.

In order to ensure that no epoxy was in contact with the spacers during the EHD patterning, the epoxy was spin coated into an area of the top ITO electrode that had been creating by masking the outer area with a thin polymer film. The volatile solvents, acetone and toluene, were evaporated during the spinning process leaving a thin liquid epoxy layer. Once the epoxy had been deposited, the thin polymer film was removed and any excess epoxy remaining was removed with low-lint swabs to ensure that none remained between the spacers.

The electrodes were then placed together, in contact at the spacers, and the voltage applied. The voltage was left on for between 4-6 hrs to ensure that the epoxy had fully cured before the removal of the voltage. As they grew, the contact of the pillars with the top electrode of the epoxy could be observed by a ‘frosting’ that appeared. This is shown in Figure 2.17. The square outline of frosting is the pillars in contact with both electrodes (since this was an early EHD test the spacer material, which can be seen around the frosting, was in a circular pattern).

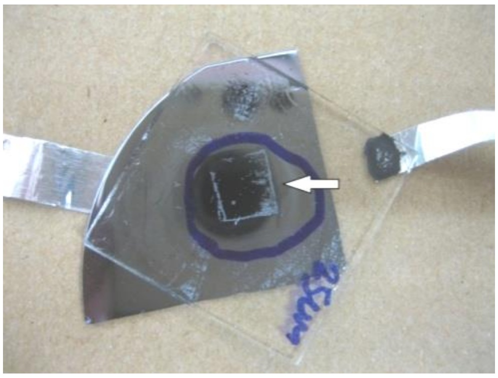

Figure 2. 17 Pillar evolution could be observed as 'frosting' (the rectangle indicated by the arrow) on the surface.

2.6 Moulding and surface replication

In order to utilise the fabricated EHD patterned surfaces they needed to be replicated, both over larger areas and on other surfaces and substrates. This was done by taking a PDMS (Sylgard 184 Silicone Elastomer Kit: Dow Corning) mould of the EHD patterned surface and using this in hot embossing and modified nano-imprint lithography techniques.

To fabricate a mould of the EHD patterned surface PDMS base was mixed with the curing agent in a 10:1 ratio and was degassed in a desiccator attached to a vacuum line. The mould of the EHD structured surface was taken by forming a well around the surface with reusable putty and filling the well with the PDMS, typically to a depth of 0.5cm. Once the PDMS had cured it was separated from the patterned surface and trimmed to size by removing the excess material around the edge. A cross-section schematic of this process is shown in Figure 2.18.

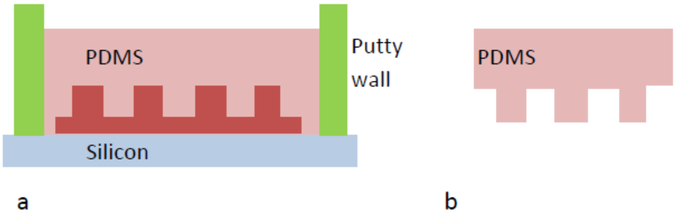

Figure 2. 18 a. PDMS moulding of an EHD patterned surface (red) b. Completed PDMS mould, separated and trimmed.

These moulds were then used to create further surfaces and enabled the patterns to be replicated over areas larger than that of the original patterned surface. To replicate the pattern in epoxy resin a modified nano-imprint lithography technique was utilized (Figure 2.19). The mould itself was placed pattern side up onto a spin coater. Epoxy solution, of the type used to fabricate the EHD surfaces themselves was then dispensed onto the PDMS and the mould subsequently coated with uncured epoxy resin (Figure 2.19).

As the liquid spread across the surface the epoxy filled the indentations in the mould (Figure 2.19 b). The mould was then placed epoxy side down onto a surface and a pressure applied to ensure good contact between the epoxy coated mould and the substrate material (Figure 2.19 c). The pressure was applied until the epoxy had cured. Once cured, the mould was removed leaving a replica of the patterned surface in epoxy on a variety of substrates such as NaCl disks for IR transmission tests and silica slides for UV-Visible transmission tests (Figure 2.19 d).

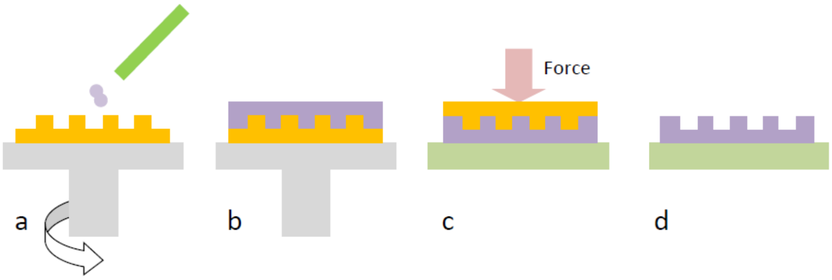

Figure 2. 19 a. Spin coating a mould of an EHD surface (orange) with epoxy (purple) b. Mould coated with uncured epoxy c. Applying force to the mould upturned on a substrate (green) d. Printed epoxy surface on substrate.

The technique produced good replication of the original surfaces shown in Figure 2.20.

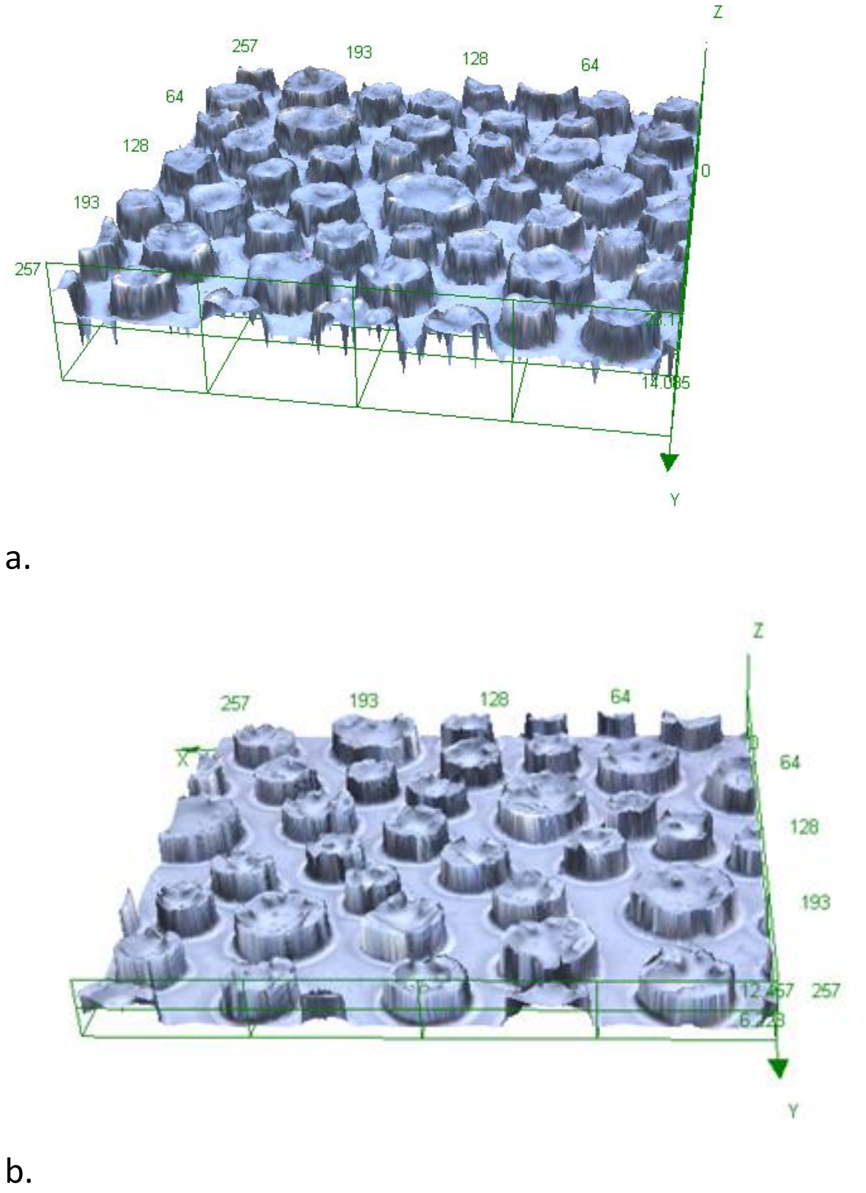

Figure 2. 20 LEXT 3D confocal scans of a. the original EHD surface and b. the replica surface printed using the epoxy spin coated mould (note: not corresponding regions), axis scales are in µm.

Hot embossing is frequently used to replicate patterns in thermoplastics at the nano and micro scales (Brown, et al., 2013) (Brown, et al., 2013) (Fiorini G, et al., 2003) (Fiorini G, et al., 2003). Hot embossed PMMA and PS surfaces were fabricated by coating a layer of the thermoplastic polymer up to 20 µm thick from solution in toluene, onto a microscope slide (Figure 2.21). The mould was placed in contact with the PMMA or PS with a pressure applied using a weight and the slide was then heated to 120°C. Once the polymer had softened the mould was impressed into the softened material using a force of approximately 11N (Figure 2.21 a & b). After 1 h the polymer coated slide and mould were left to cool. Once cooled the force and the mould were removed leaving the pattern stamped into the polymer surface (Figure 2.21 c).

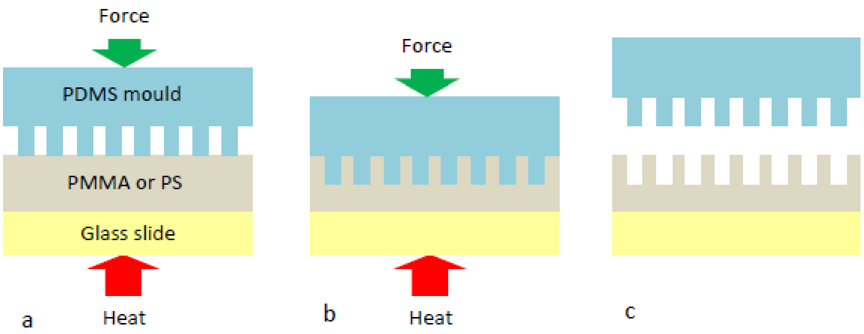

Figure 2. 21 Schematic of the hot embossing method a. A PDMS mould is placed in contact with a polymer coated slide b. The mould is impressed into the polymer c. The mould is removed from the cooled polymer.

This technique also produced good replicas of the EHD structured surfaces in thermoplastics. A hot embossed PS surface and the original are shown in Figure 2.22.

In addition to being used for NIR transmission and reflection tests, the moulds were also used for replicating the surfaces in materials to be used for tissue culture purposes. The prepared substrates were placed in wells of standard tissue culture plates and colonised with both lens and retinal cell lines in order to investigate the growth of these cell lines on micro-structured surfaces.

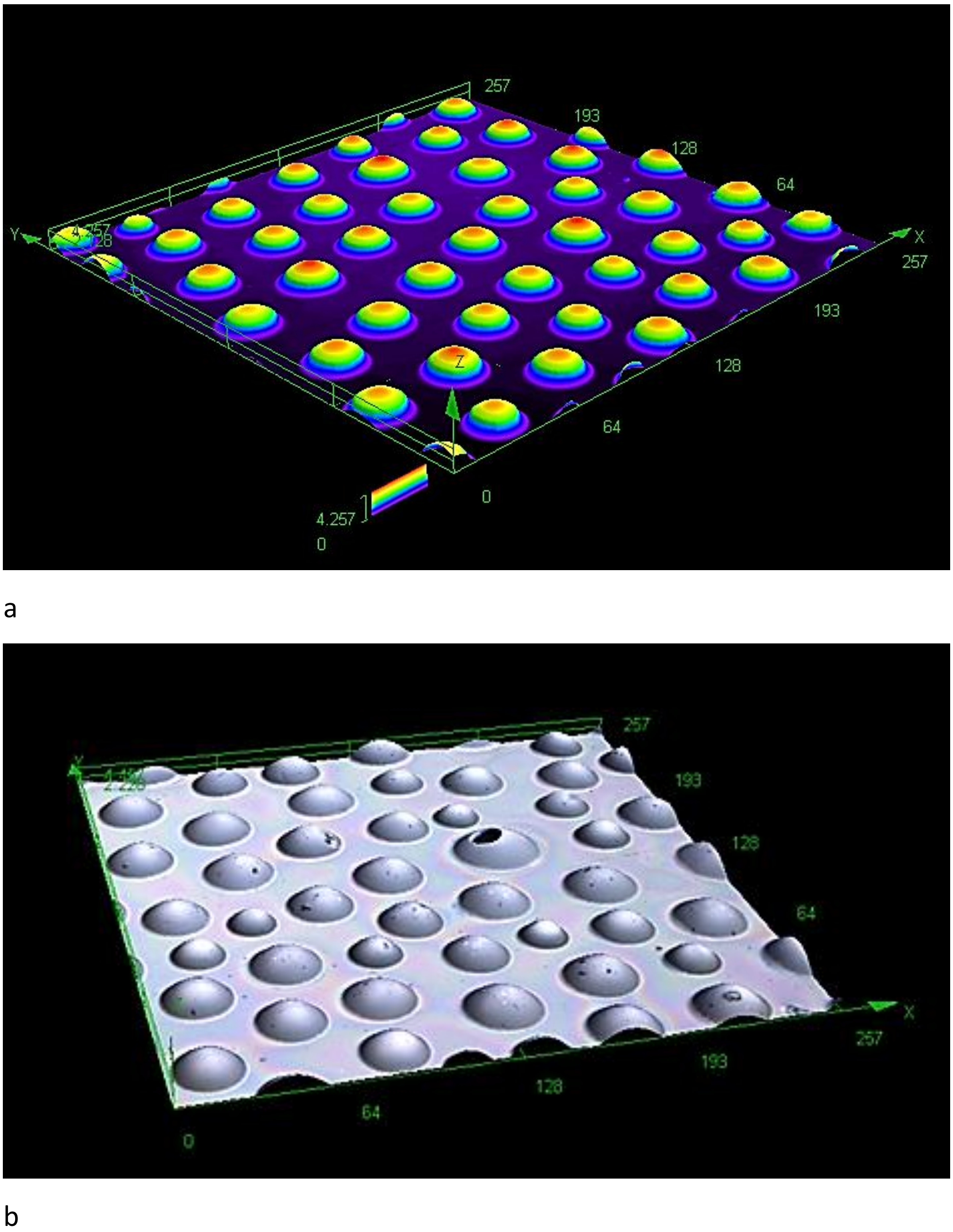

Figure 2. 22 LEXT 3D confocal scans of a. the original EHD fabricated surface and b. the hot embossed replica (not a corresponding region).

2.7 Thickness testing

Several methods were first employed to establish the thickness of coated layers. Initially cross-section views of a double layer of unpyrolized TiO_2 sol were taken using scanning electron microscopy (SEM) and an uncoated glass slide was also viewed for comparison. A thin layer of material can be seen on the surface of the glass shown by the arrow in Figure 2.23 a. From the image this layer was estimated to be less than 0.5µm thick. The inaccuracy of this method meant that a more conclusive procedure was needed.

Interferometry was also tried, to give a rough idea of the thickness of the deposited layers. A double layer of unpyrolized TiO_2 sol was coated onto an ITO glass substrate. Using a double layer of sol simplified the analysis, since the second layer partially covered an initial layer so both layers were visible. In Figure 2.23 b an interferometer screenshot image from a cross-section of a double layer of TiO_2 sol is shown. A plan view of the sample is shown on the left, together with a horizontal line showing the position of the cross-section (shown on the right). An interferometer screenshot showing the enlarged cross-section is shown in Figure 2.23 c. The top surface of the second layer of TiO_2 can be seen, beginning on the left of the image at 254nm, the top surface of the single layer can be seen as a short line on the right side of the profile at a height of around -254nm.

Although this method of interferometry is not ideal for analysing surfaces where the features have large differences in height (often due to phase mismatching in the light reflected from the different heights), the resulting data show a jump of roughly 300nm in Figure 2.23 b and c. This agrees well with the image taken from the SEM of the cross-section of a microscope slide.

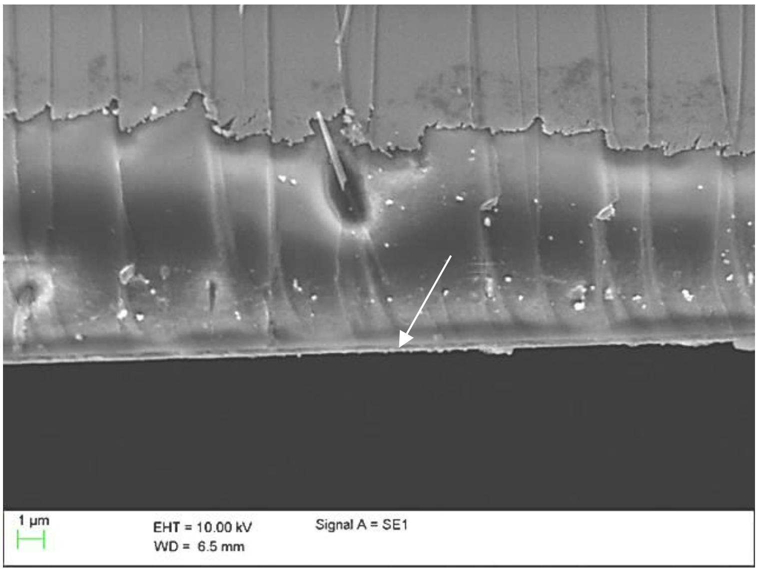

a. SEM image of a cross-section of a double layer of TiO_2 sol.

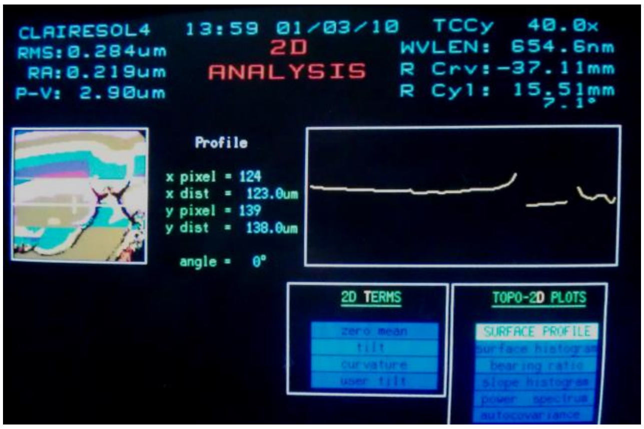

```
CLAIRESOL4     13:59 01/03/10    TCCy    40.0x
RMS:0.284um         2D        WVLEN: 654.6nm
 RA:0.219um      ANALYSIS     R Crv:-37.11mm
P-V: 2.90um                   R Cyl: 15.51mm
                                       7.1°

          Profile

       x pixel = 124
       x dist  =  123.0um
       y pixel = 139
       y dist  =  138.0um

         angle =   0°
```

b. Interferometer screenshot image from a cross-section of a double layer of TiO_2 sol.

```
CLAIRESOL4   13:59 01/03/10              40.0x
RMS:   139nm     PROFILE     WVLEN: 654.6nm
 RA:   110nm   (124,139)    No Terms Sub
P-V:   709nm       0°
```

c. Interferometer screenshot showing the enlarged cross-section.

Figure 2. 23 SEM and interferometer screenshot images used to estimate layer thicknesses.

2.7.1 Ellipsometry

Ellipsometry was used to obtain information on the thickness of a number of different samples. In addition to measuring film thickness it can also provide information on the optical constants of the film, i.e. the refractive index *n* and extinction coefficient *k* (J.A. Woollam Co, n.d.). The method is based on the measurement of the change in polarization of a polarised beam reflected from the sample surface at non-normal incidence (J.A. Woollam Co, n.d.) (Goncalves & Eugene, 2002).

The method quantifies the phase difference in the components of the reflected electric field both parallel (*Es*) and perpendicular (*Ep*) to the plane of incidence Δ and also the change in the ratio of their amplitudes $(\tan \Psi)$ incidence (J.A. Woollam Co, n.d.) (Goncalves & Eugene, 2002).

In basic ellipsometry, a monochromatic light source is collimated and then linearly polarised. The resulting reflected beam is elliptically polarised, and an analyser measures this degree of polarisation as shown in Figure 2.24 (Goncalves & Eugene, 2002).

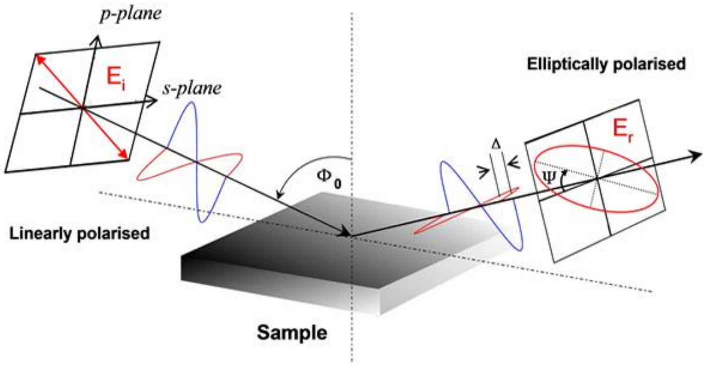

Figure 2. 24 Schematic of the principal aspects of ellipsometry.

A JA Woolam M-2000D1 ellipsometer was used to measure the thickness of a layer of thin solid film coated onto a solid substrate which here was a titanium dioxide sol on quartz glass. The beam was focussed onto a pin head sized area of the sample and the change in amplitude (Psi) and change in phase (delta) values of the reflected beam were measured between the wavelengths 193-1698nm. The analysis range was then set from 500nm to eliminate wavelengths over which there was a large amount of noise (possibly due to the absorption of the incident radiation). The radiation was measured in wavelength increments of 1.6nm.

Data were taken from the sample and then a model that represented the sample according to theory was produced. Fitting the gathered data to the model then gave information of the measured material. For material where the optical constants are known these values are taken from a library of materials data (for example the optical constants of silicon and quartz glass). For the material where the optical constants are not known (a PVA film and a TiO_2 sol for example) an additional layer is included in the model.

For a TiO_2 sol sample, spun for 30 s onto a quartz slide, four measurements were taken at an initial point and then at spots at displacements of 0.1cm, 0.2 cm and 0.5 cm along a single axis from the initial point. This gave information about the uniformity of the layer thickness. The thickness of the residual silicon oxide on the substrate was also measured as it was used in the model to fit the data. The thickness of the sol was measured to be 116.58 nm.

2.7.2 Spectroscopy: Ultraviolet-visible (UV-Vis) and near-infrared (NIR)

Spectroscopy was also used to estimate the film thicknesses by both absorption and reflectance. A Varian Cary 100 Bio UV-Vis Spectrophotometer was used to take transmission readings of thin films coated onto glass in the UV-Vis range. A Buchi NIR Flex spectrophotometer was used to take reflectance readings of thin films coated onto silicon in the NIR range.

UV-Visible absorption was used as thin film interference created fringes in the spectra shown in Figures 2.25 and 2.26. These peaks are a function of the thickness of the film so can be used to estimate this value. Figure 2.25 shows the UV-Vis interference peaks from a. ITO and b. TiO_2 layers both deposited by sputter coating.

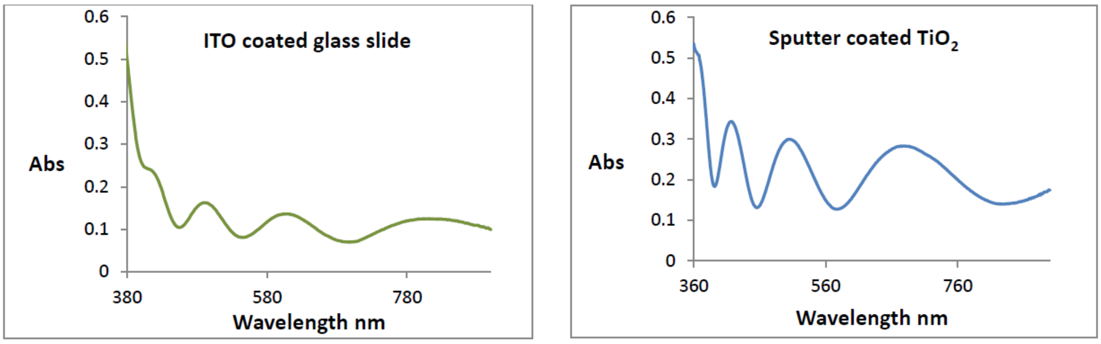

Figure 2. 25 UV-Visible absorption spectra of a. sputter coated ITO glass b. sputter coated TiO_2 on glass.

Figure 2.26 shows the absorption peaks for two spin-coated TiO_2 sol layers. Many types of glass absorb the shorter wavelengths which prevent the interference fringes from being observed shown in Figure 2.26 a. The interference peaks from the layer of sol can only be seen in Figure 2.26 b, where the material was coated onto quartz glass.

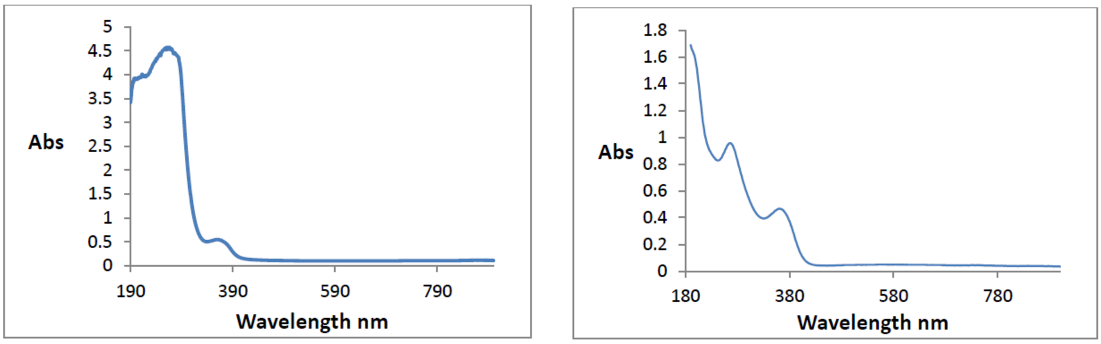

a b

Figure 2. 26 UV-Vis absorption spectra for TiO_2 sol spin coated onto a. glass b. quartz.

The method of determining coating thickness involves choosing two peaks from a UV-Vis absorption spectrum. By using the wavelength corresponding to the peaks and the number of cycles between them (Figure 2.27) the following simultaneous equations can be solved to determine the layer thickness. The refractive index of the material is also required:

$$2nt = (m + \frac{1}{2})\lambda_1 \tag{2.1}$$

And

$$2nt = \left(m + x + \frac{1}{2}\right)\lambda_2$$

(2.2)

where n=refractive index, t=film thickness (m), λ=wavelength (m), x=no. of cycles between the 2 wavelengths and m is a constant.

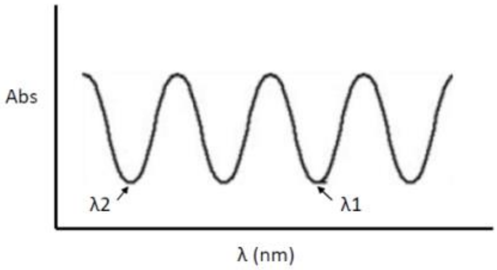

Figure 2. 27 Schematic of absorption spectrum showing 2 selected peaks.

Using the method described above the thickness of the sputtered ITO was calculated to be 557nm which is close to the 700nm quoted by the supplier Diamond Coatings. The sputter coated TiO_2 was calculated to be 489nm and the thickness of the spin coated sol on quartz gave a thickness of 164.2 nm which is in close agreement with the ellipsometry measured value of 116.58nm shown previously. Errors in estimation of the refractive index of the materials tested could account for the discrepancy although in general the agreement showed that this method was sufficient to give estimates of the layer thicknesses used.

2.7.3 NIR testing

The method of using UV-Visible absorption required the substrate material to be transmissive, which was not always possible for the materials required for the experiments, so NIR reflectance was also used in accordance with the method set out by Hind (Hind & Chomette, 2011). A BUCHI NIRFlex N-500 was used in reflectance mode using the solids module single sampling. NIR reflectance spectra were taken from thin films coated onto silicon wafers using the spectra of an area of the uncoated wafer spectra as the reference spectra from 4000-10000 cm^{-1}. Again, thin film interference created periodic peaks and troughs in the spectra which were a function of the thickness of a coating. Similarly to the previous method 2 peaks in the spectra are selected and their wavenumber values used in equation (2.3).

The equation set out by Hind states that the thickness of the film d is given by

$$d = \frac{m}{2D_n\sqrt{(n^2 - sin^2\theta)}} \tag{2.3}$$

where *m*=number of cycles between the 2 peaks selected, *n*=refractive index, ϑ=angle of incidence, and *Dn*=wavenumber count between the peaks used i.e. peak 2 minus peak 1 (cm^{-1}).

Examples of the spectra obtained from spin coated solutions of PMMA dissolved in toluene are shown below; each sample was tested on 3 separate occasions. Using equation (2.3) for PMMA in toluene spun at 3000rpm, the spectra produced a value of 1.02 µm. This value was calculated by inserting the value of 8504 cm^{-1} as peak 2, 5208 cm^{-1} as peak 1 and the number of cycles as 1 (Figure 2.28) into equation (2.3). The refractive index used for the PMMA was 1.5.

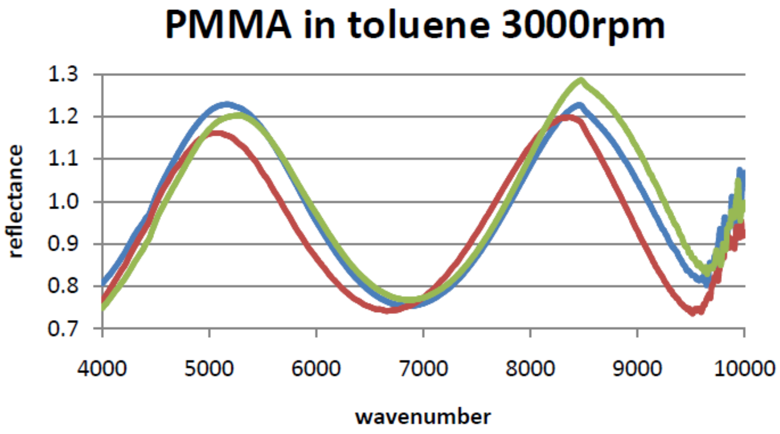

Figure 2. 28 NIR reflectance spectra PMMA spin coated at 3000rpm.

PMMA spun at 2000rpm gave a thickness value of 1.17 µm using 7316 cm^{-1} as peak 2 and 4440 cm^{-1} as peak 1 in equation (2.3) and the number of cycles as 1 (Figure 2.29). The layer was thicker than the sample spun at a higher speed as expected.

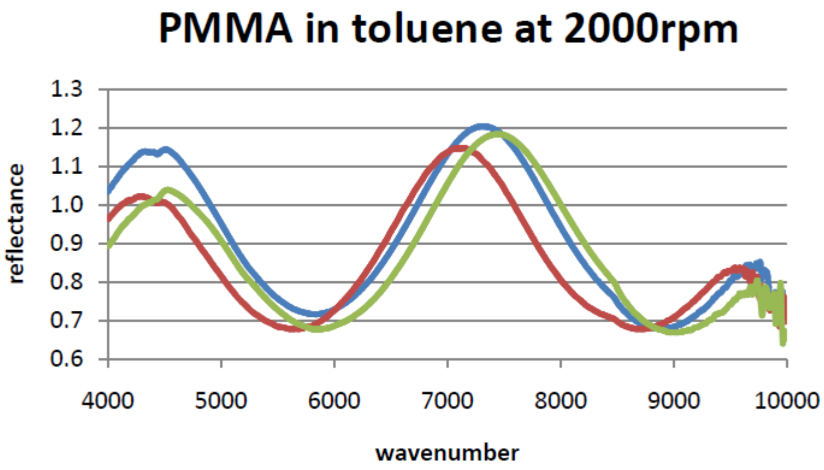

Figure 2. 29 NIR reflectance spectra of PMMA spin coated at 2000 rpm.

Again, using the value of 8610 cm^{-1} as peak 2, 6170 cm^{-1} as peak 1 and 1 cycle in equation (2.3) from the spectra in Figure 2.30, the thickness (1.37µm) of a thin film spun at 1500rpm found was larger still, due to the slower spin speed used.

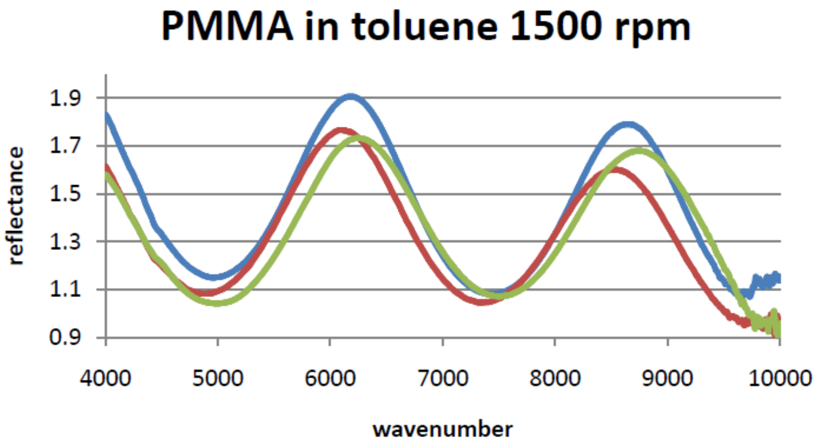

Figure 2. 30 NIR spectra of PMMA spin coated at 1500rpm.

Thinner films produce fewer peaks across a given range of wavelengths and hence there is a finite value to the minimum thickness of coating that can reasonably be calculated for a given band of wavelengths. This principle is demonstrated in the series of spectra in Figure 2.31 where a. shows a double layer, b. shows a single layer and c. shows a single layer that is very thin.

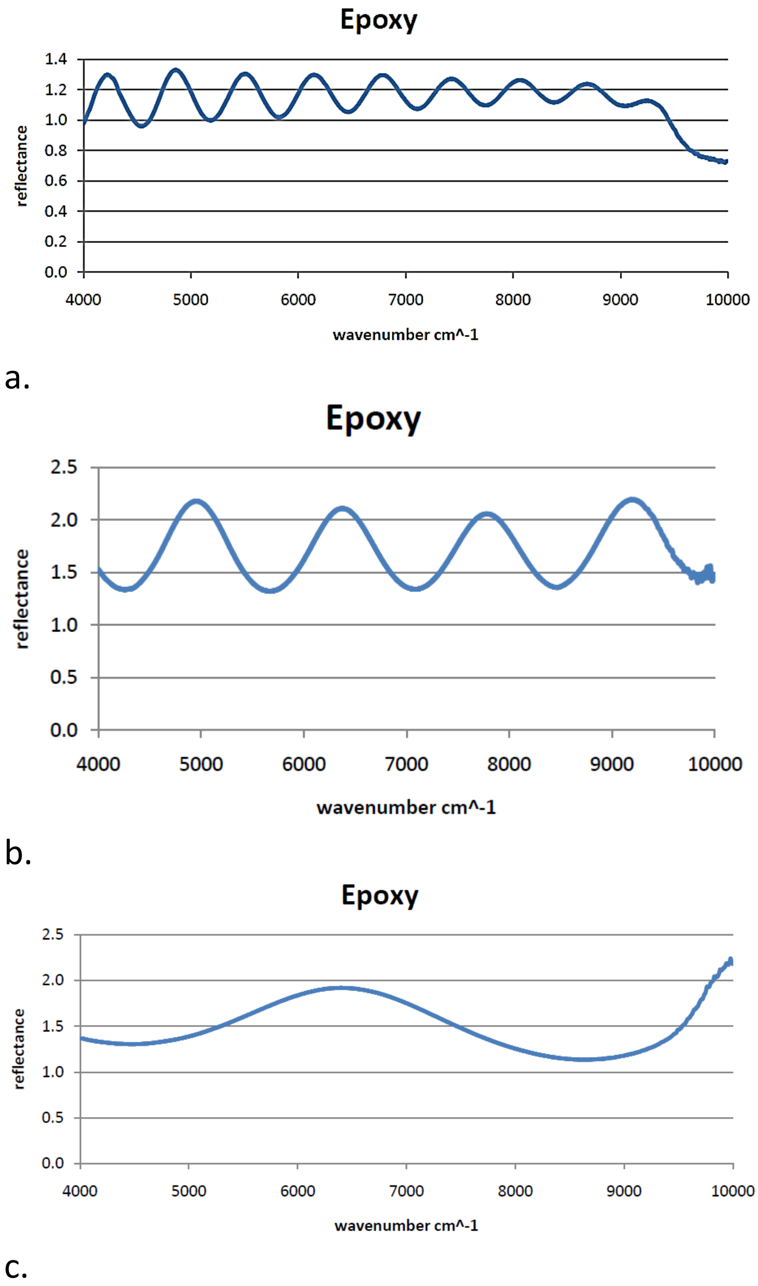

Figure 2. 31 NIR reflectance spectra of a. double layer of epoxy b. a single layer and c. a thinner single layer

Using the NIR reflectance spectra of the double layer of epoxy a thickness of 4.8 µm was calculated using 8688 and 4816 cm-1 as peaks 2 and 1 respectively, 6 cycles and the refractive index estimated at 1.6. The single layer was calculated as being 2.2 µm thick, using 7750 and 4950 cm-1 as peaks 2 and 1 respectively, and 2 cycles. The thinnest single layer was estimated as 0.7 µm thick using 8732 and 4496 cm-1 as peaks 2 and 1 respectively and 1 cycle.

As the width of the peaks becomes larger it is increasingly difficult to estimate accurately the wavelength at which the peaks and troughs occur (Figure 2.31 c), although for this study it was enough to obtain an estimate of the layer thicknesses used. Once the EHD patterned surfaces had been fabricated, the estimates of the thickness were then validated by using a laser confocal measuring microscope (LEXT-see below).

More details of these results are outlined in the Results Chapter 3 in section 3.2.

2.7.4 LEXT 3D laser measuring microscopy

A LEXT 3D laser measuring microscope OLS 4100 was used to obtain the most accurate information about the spacer materials, layer thicknesses, overall topography of surfaces produced and the experimental parameters used and so this method was the foremost used. Since the epoxy was transparent and so reflections were produced from both top surface of the epoxy structures and the silicon substrate the multilayer setting was selected. This setting meant that the microscope could determine the position of both surfaces since traditionally the microscope would only the position with the highest magnitude of reflection would be registered. Spike removal was also used which reduced noise from the sample. In measurement mode using a 405nm laser, surfaces were analysed using the 20x and 50x objectives.

The thickness of the cured deposited epoxy layer was measured by removing a thin line of the spin coated film, exposing the underlying silicon wafer substrate. This area was then scanned, giving the epoxy thickness shown in Figure 2.32. The colour image is a plan view, with the blue area being the exposed silicon wafer and the green areas the coated epoxy. A cross-section view is shown beneath the plan view, giving an epoxy thickness of 3.098 µm. The position of the cross-section is shown by the horizontal line on the plan view image.

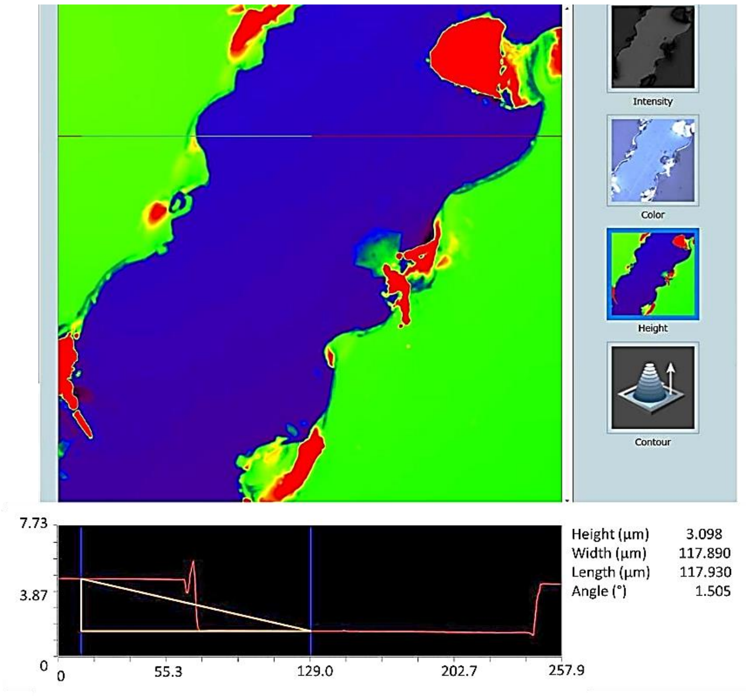

Height (µm) 3.098
Width (µm) 117.890
Length (µm) 117.930
Angle (°) 1.505

Figure 2. 32 LEXT confocal scan plan view of spin coated epoxy thickness value (µm).

The spacer thicknesses used in the manufacturing was taken indirectly by using the height of the flattened top surfaces of the pillars in an array, but by using a similar method to that for the epoxy thickness. In the plan view image in Figure 2.33 the pillars can be seen on the right of the picture with the exposed silicon substrate on the left. A height of 5.648 µm for the tops of the pillars is shown in the cross-section image below. The flat tops were created as the pillars made contact with the top electrode. The cross-sectional dimensions and overall shape of the disks and pillars produced were examined by this method.

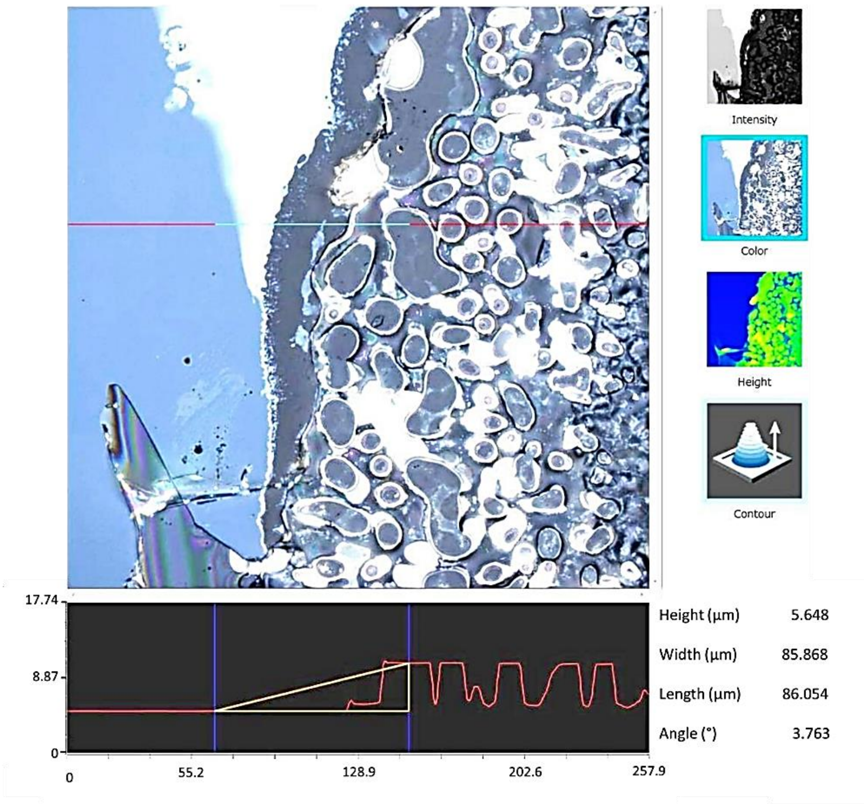

Height (µm) 5.648
Width (µm) 85.868
Length (µm) 86.054
Angle (°) 3.763

Figure 2. 33 LEXT confocal plan view to measure spacer height using the top surface of the pillars (scale in µm).

2.8 Relative permittivity and capacitance

The dielectric behaviour of the patternable polymer has a large influence on the morphology of the EHD patterns. Dielectrics are insulator materials which become polarised in an electric field. The extent of this phenomenon is expressed as permittivity, measured in farads per metre. There are several mechanisms by which this happens. Electronic (or optical) polarisation occurs when the electron cloud surrounding each atom becomes distorted. The molecules in a polar substance can rotate on their axes to be aligned with the field (orientational polarisation). Furthermore, the atoms themselves in the polar molecules can be displaced altering the distance between them (atomic polarisation) (Anderson, et al., 2003). In real materials, there will also be defects such as free electrons and unbound ions, which can migrate through the material under the application of an electric field. When they reach the electrode of opposite polarity, they can discharge and this results in a very small current through the material. If they are unable to discharge they will accumulate at the opposite electrode in a very thin layer, and this is called interfacial polarisation (Anderson, et al., 2003).

If a dielectric material is placed between the two plates of a parallel plate capacitor, the value of the capacitance changes in relation to the ability of the material to polarise. The greater the ability for the material to polarise the greater the capacitance since the polarisation of the material is essentially the storage of energy. In the EHD experiments the difference between the electric field in the polymer and that in the air gap is what creates the electromagnetic stress on the surface of the polymer and causes it to deform. As a result, the relative permittivity of the deformable liquid has a large influence on the wavelength of the instability.

Relative permittivity is the ratio of the absolute permittivity of the material to the permittivity of a vacuum and so is a dimensionless value and is also known as the dielectric constant. Capacitance (F) is given by:

$$C = \frac{\varepsilon_r \varepsilon_0 A}{d} \tag{2.4}$$

where ε_r is relative permittivity (dielectric constant) of the filler material, ε_0 is permittivity of free space (8.8542×10^{-12} Fm^{-1}), A is area of the capacitor (m^2) and d is the gap between the plates (m).

Hence capacitance can be used to indirectly measure the relative permittivity of a material using:

$$\frac{Cd}{\varepsilon_0 A} = \varepsilon_r \tag{2.5}$$

In most of the literature, the value for the relative permittivity of epoxy resin in its cured state is around 3 and there are many different types of epoxy which all contain different constituents and cure by different means (Akbas, et al., 2009) (Akbas, et al., 2009) (epotek, n.d.) (The Engineering Toolbox, n.d.). Given the impact that it has on the wavelength of the instability, it was important to establish the value for the actual epoxy used in these experiments over the entirety of its curing duration.

The fact that the epoxy material starts as a liquid consisting of reactive agents means that all the above mechanisms for polarisation are possible in theory. The molecules will be able to move freely, as will ions and unbound electrons. The relative permittivity of the epoxy was studied by way of capacitance measurements.

A benchtop Leader 745 G LCR (inductance (L), capacitance (C), and resistance (R)) Analyser was used for the measurements. The two parts of the epoxy resin were mixed and then constrained between two foil electrodes within 2 sizes of rubber washer 1.5cm square and 2 cm square, both being 3mm in depth to contain the epoxy. The capacitor cell was placed in a moulded metal box to isolate it from stray capacitance from other sources which would affect readings. The change in capacitance over the cure time of the epoxy was taken.

A DC bias of 1.5V was applied across the epoxy the results shown here being for a frequency of 1kHz. For a frequency of 120Hz however, the results were undetermined as the readings fluctuated widely.

The values of the capacitance whilst no sample was in the circuit and the value of the cell without the epoxy present were taken so that they could be eliminated from the calculations of the relative permittivity of the epoxy itself.

Values of capacitance of the epoxy in picofarads were recorded every two minutes for the first hour and then every thirty minutes thereafter. The values increased slightly during the initial few minutes and then dropped rapidly. Once the epoxy had cured the average value was around 3. Measurements were taken for at least a 4 h period, which was the average cure time of this epoxy. It was solid after this time so the value of relative permittivity would have no effect on the wavelength of the instability at this point. There was some variability in the results which is likely to be due to trapped air, slight variations in the manufacturing of testing cells and also the ambient temperature.

2.9 Viscosity

The viscosity of the patternable material does not affect the wavelength of the instability but influences the rate at which the pillars form and bridge the gap between the electrodes. It also affects the other morphologies that can then follow, such as the phase inversion of the pattern i.e. pillars of air in an epoxy matrix and other complex structures. The viscosity of the epoxy (Evo-Stick Control) was tested with a Brookfield DVII+ Pro viscometer.

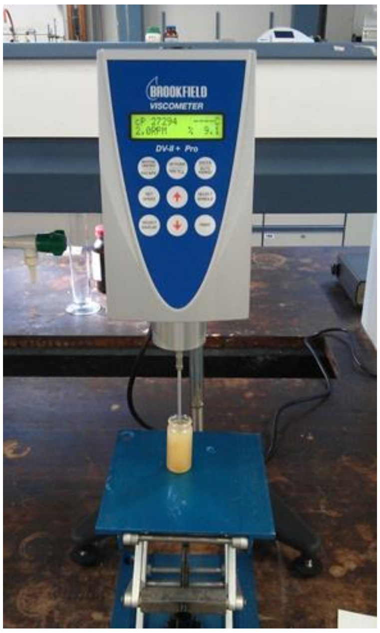

Figure 2. 34 Viscosity testing.

The two parts were combined and a small gauge spindle was used, due to the high viscosity of the epoxy. Epoxy resins show anomalous rheological behaviour and display different viscosities at different rates of shear, so the assumption of a Newtonian fluid does not apply (Clayton & Dekker, 1988). The viscosity of Evo-Stick Control was tested at 2 RPM (average viscosity 27069 cP) and 10RPM (average viscosity 21865 cP).

2.10 Tissue culture

The surfaces were investigated for use as tissue culture surfaces. Surfaces were replicated using the hot embossing method set out in section 2.6. The hot embossed surfaces were washed prior to use and sterilised by UV radiation. Cryopreserved stocks of the cells were rapidly thawed to 37° and then added to warmed growth media in culture flask. Once cells had reached the desired confluency they were dispersed by trypsinisation using 0.25% w/v trypsin 0.2% w/v EDTA in phosphate-buffered saline (PBS) (Trease, et al., 2016). The trypsin was inactivated by resuspension in growth media containing serum. Cells were then seeded out on the specialised plates placed in standard tissue cultureware (Nunclon™ Delta surface, Thermoscientific) with a flat tissue culture surface well left for comparison.

Cells were allowed to adhere and spread on the surfaces for 24 h and were then photographed using an optical light inverted transmission microscope (Trease, et al., 2016).

3. Results

During EHD patterning, a voltage is applied across a layer of air on top of a layer of liquid polymer creating an electric field in both layers. The polymer has a higher relative permittivity than air so a different electric field exists in the two materials. This creates an electrostatic pressure at the polymer/air interface. In response to the electrostatic pressure the polymer material flows and causes waves on the surface to grow in amplitude until they touch the top electrode. Once a single pillar has developed, this destabilises the material around it which then forms into further pillars that eventually cover the surface (Figure 3.1).

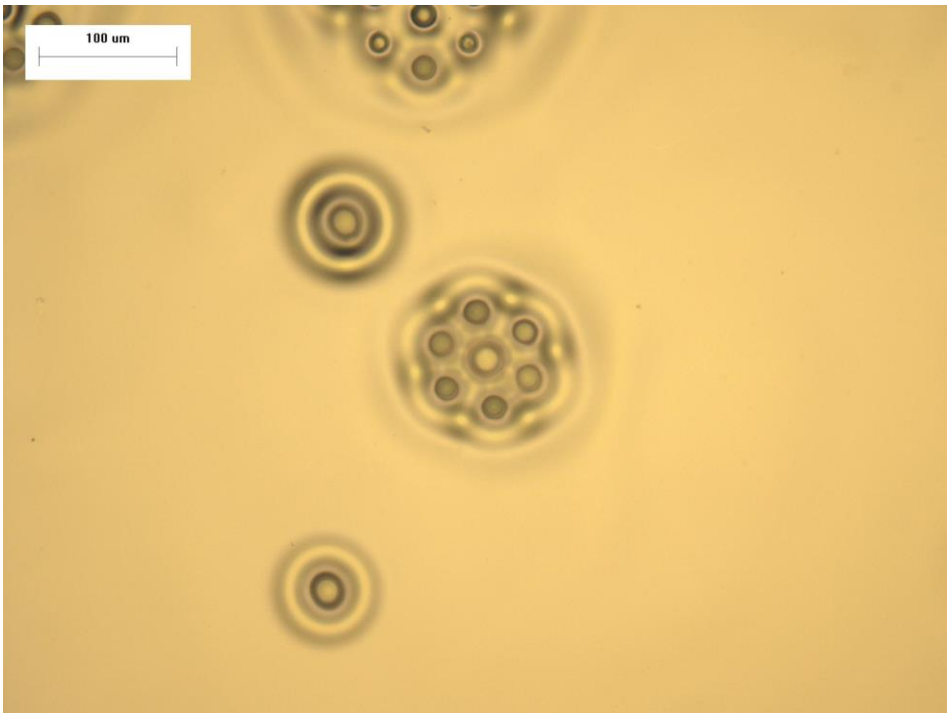

Figure 3. 1 Plan view optical micrograph of EHD pattern formation and initiation sites (scale bar 100 µm).

The EHD patterns generated are dependent on the fabrication geometry, voltage and several material characteristics. The parameters and characteristics were explored using procedures set out in the Experimental Chapter 2. The initial thickness of the spacer and polymer layers used, were estimated using the NIR spectra prior to the fabrication experiments. Accurate measurements were taken, using the LEXT laser confocal microscope, after the fabrication experiments had been completed, and it was these values used in the results and calculations given here.

3.1 Materials: characteristics and thin film fabrication parameters

3.1.1 Relative permittivity

The relative permittivity of the patternable material (here an epoxy resin) has an impact on the scale of the patterns produced. The relative permittivity of cured epoxy resin has been widely reported in the literature since it is often used as an electrical insulator however there are few studies on the value of uncured epoxy resin (Chauhan & Singh, 2000) . Furthermore, the chemical characteristics of epoxies are very varied and so the relative permittivity of the Evo-Stik Control epoxy used in this study was tested via the method set out in section 2.8.

Manipulation of the relative permittivity of the polymer layer was also considered as a way of changing the wavelength of the patterns being produced so its value needed to be known. Inorganic fillers with high relative permittivity's have been used to increase the relative permittivity of the patternable polymer which would reduce the scale of the pillars. Bae *et al*, used inorganic fillers with high relative permittivity's, such as titanium dioxide nanoparticles, in PS to reduce the scale of EHD fabricated patterns (Bae, et al., 2008).

Preliminary tests using titanium dioxide (TiO_2) nanoparticles dispersed into the epoxy had a negligible impact on the scale of patterns produced. The results of the consequent testing of the relative permittivity of the epoxy demonstrated that for this material, which already had a high relative permittivity, manipulation of the value would have little to no visible effect on the scale of patterns produced. The PS used by Bea *et al* had a much lower relative permittivity so the inclusion of a filler material would have had a greater impact on the permittivity of the composite material.

The relative permittivity of Evo-Stik Control epoxy resin was tested using the technique set out in the Experimental Chapter 2 Section 2.8. The results of 5 samples of are shown in Figure 3.2 (the samples are labelled by date).

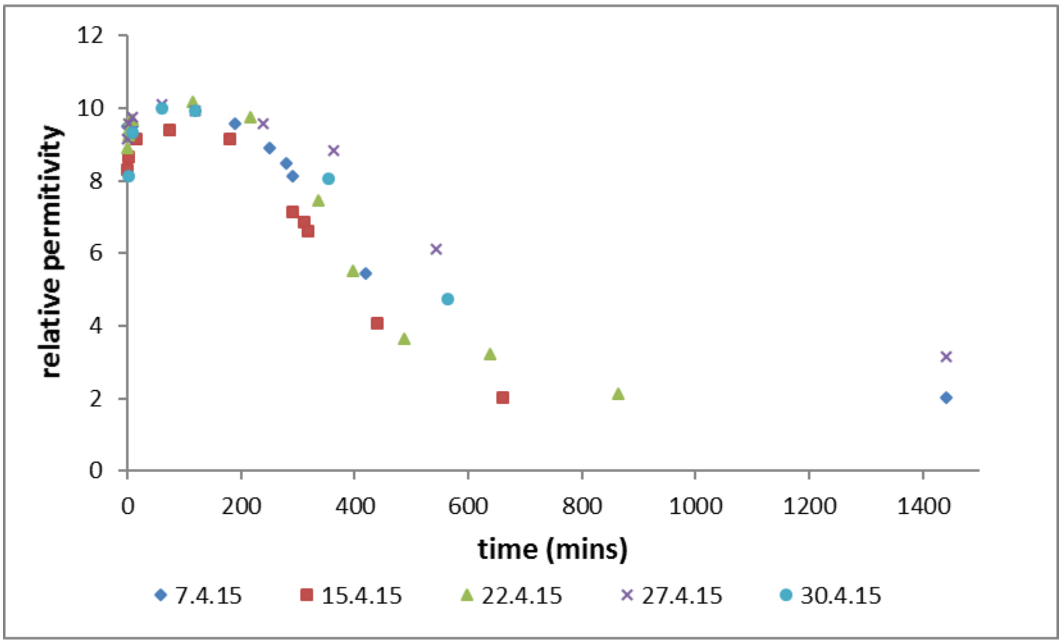

Figure 3. 2 Change in the relative permittivity over the curing time for 5 samples of Evo-Stik epoxy resin.

In the literature cured epoxy is stated as having a relative permittivity which ranges from 3-6. From Figure 3.2 it can be seen that, in its uncured state, the relative permittivity of this epoxy resin is initially higher, at a value between 8-10 when time=0 mins and it initially rises until at time =150 mins when it begins to drop. During curing the relative permittivity drops but remains high over the initial (240 mins) curing time of the resin. After 240 mins the resin is solid to the touch but is still pliable and has not fully cured. These results echo those of Haran *et al* who found the relative permittivity started high and lowered over the cure time of the epoxy (Haran, et al., 1965).

In the experiments the initial value averaged 8.9. It then rose initially approaching a value of 10 after approximately 2 h. After this time the value dropped steadily. After 4 h, when the material was solid to the touch the value was still high at between 8 and 9. The value continued to drop even though from the practical perspective the material was solid although it was still pliable and not hard and brittle. After roughly 11h it reached a value of between 2 to 4 and began to level out (the resin had changed in texture by this time to become more brittle). This value agreed the values in the literature for cured epoxy. The actual curing time for this epoxy, as stated by the manufacturer, was 16 h.

The reduction in the relative permittivity value presumably corresponds to the drop in mobility of dipole orientation due to the increased viscosity of the material as it cures and also the drop in the ability of polar molecules to align to the field also due to the increased viscosity of the resin. Experiments conducted by Nixdorf and Busse found that the conductivity of epoxy also reduced during the cure time of the epoxy (Nixdorf & Busse, 2001).

Overall a good similarity and general trend can be seen between the samples tested giving a good insight into the changes in the relative permittivity that occurred over the cure time of the material. The discrepancy in the values measured could be attributed to several things. Changes in ambient temperature could affect the rate of curing of the material. The 2 parts of the epoxy (the resin and the hardener) were mixed by hand; non-uniform mixing could also affect the cure rate. Air bubbles could have become trapped during mixing and the inclusion of these bubbles could again cause disagreement between the values recorded. The age of the material and batch that it was sourced from could affect it also.

3.1.2 Effect of the relative permittivity on wavelength

The effect that the value of the relative permittivity has on the wavelength of the instability is shown in Figure 3.3 for 2 methods of calculation; the perfect dielectric model according to Schäffer using equation (1.17) and the perfect dielectric model according to Pease and Russel using equation (1.21) (Schäffer, et al., 2001) (Pease & Russel, 2004). It shows that at values of 4 and over, the impact on the wavelength is negligible. From the above results, it seems that the epoxy only approaches this value after approximately 11 h, once it is hard and brittle to the touch. Therefore, the change in the relative permittivity that occurs in the EHD fabrication time of the surfaces produced here would not affect the wavelength of the patterns created.

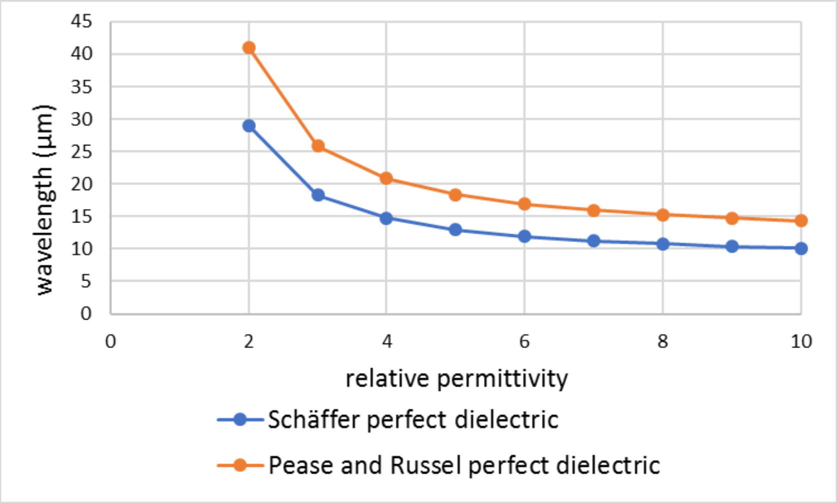

Figure 3. 3 Effect of relative permittivity on wavelength for an electrode spacing of 2 µm, a polymer thickness of 1 µm and a voltage of 50V.

During the EHD experiments the surface instability developed from seconds to a few minutes after applying the voltage. The time taken depended on several things such as the spacer thickness and the epoxy thickness. Over this time period, the value of the relative permittivity remained around 8. This is high in comparison to the value for thermoplastics PS (2.6) and PMMA(3.6) which have been routinely used for these kind of experiments in other studies (Wu, et al., 2006) (Wu, et al., 2006) (Peng, et al., 2003) (Peng, et al., 2003) (Wang, et al., 2014). For most of the experiments after about 200 minutes the value dropped suddenly due to gel formation. The time it took for the epoxy to become a solid was in the region of 240 minutes and in general the value had dropped to around that quoted in the literature of between 2 and 4.

3.2 Spacer layer and resin layer thickness

Spacer materials were chosen for their electrical properties (good insulators) and ability to be deposited as thin films. PDMS, PMMA and PS are easily dissolved in solvents and are frequently used to create thin films for various applications. The electrical resistivity of PMMA is between 10^{14} - 10^{15} Ωcm and that of PS is 10^{20}-10^{22} Ωcm.

The distance between the electrodes used in the EHD experiments has a significant impact on the patterns produced as does the initial patternable film thickness. The thin spacers were fabricated by removing material from a spin coated layer as set out in the Experimental Chapter 2 section 2.3.1, so the area of the electrode that the spacer material covered was a very small portion, on average 1.5 cm^2.

Estimations of the thickness of the spin coated films that were used as spacer materials were carried out by using UV-Vis and NIR spectra via the procedure set out in the Experimental Chapter 2 sections 2.7.2 and 2.7.3. Values of the epoxy resin layer thickness were also gathered this way. As described in the Experimental Chapter 2 section 2.7.2 ellipsometry was used to confirm the results and validate the methods of the initial UV-Vis spectra technique used to establish the thickness of ITO coated glass and spin coated PVA and TiO_2 layers. More accurate values of the electrode gap used in the EHD patterning experiments and the epoxy layers were taken after EHD fabrication using a LEXT laser confocal microscope also described in the Experimental Chapter 2 section 2.7.4.

Initial EHD experiments that were tested, as per the method set out by Voicu *et al,* used a TiO_2 sol-gel as the patternable polymer. These experiments had a poor success rate with only very small areas of patterning showing. The sol dried very quickly which could have been a reason for the poor success but testing the thickness of the sol layer deposited with ellipsometry showed that the layer was much thinner than desired with an average depth of 82nm. The area where the pillars developed was at the rim of the deposited material in what would have been the edge bead (Figure 3.4).

Figure 3. 4 Plan view optical micrograph of EHD patterned titanium dioxide sol-gel scale bar 100µm.

3.2.1 NIR

Several different spin coated polymer layers were used in experiments with epoxy resin as the patternable material and the thicknesses of the layers were calculated using the method set out in the Experimental Chapter 2 section 2.7.3. To calculate the thickness from NIR spectra, a value for the refractive index of the polymer was required. Although the refractive index of a material is wavelength dependent and varies, the impact that the value had on the calculations of thickness was marginal. So, refractive indices quoted in the literature were used in the calculations.

PMMA

PMMA of an average Mw 120,000 from Sigma Aldrich was used as a spacer layer. The method of producing thin films of PMMA from solution in toluene was adapted from Walsh and Franses (Walsh & Franses, 2003). A higher concentration of PMMA was used however since, for this study, thicker films than those produced by Walsh and Franses were required. Toluene was chosen for preference, since it is less volatile than the more commonly used chloroform, producing better quality films (Walsh & Franses, 2003). The refractive index of PMMA was quoted as 1.49 at a reference temperature of 20 degrees using the sodium line 589.3nm.

A solution of PMMA 15% in toluene solution was prepared by stirring PMMA powder in toluene using a magnetic stirrer for 4 h at room temperature. 200μl of the solution was spin coated at a variety of speeds onto a silicon wafer using dynamic dispense. The wafer was spun until the solvent had evaporated, a duration of approximately 20 s, which was observable by the film colour change ending. The NIR reflectance spectra of the thin films produced was taken using a plain silicon wafer as the reference sample. Examples of the spectra are shown in Figure 3.5.

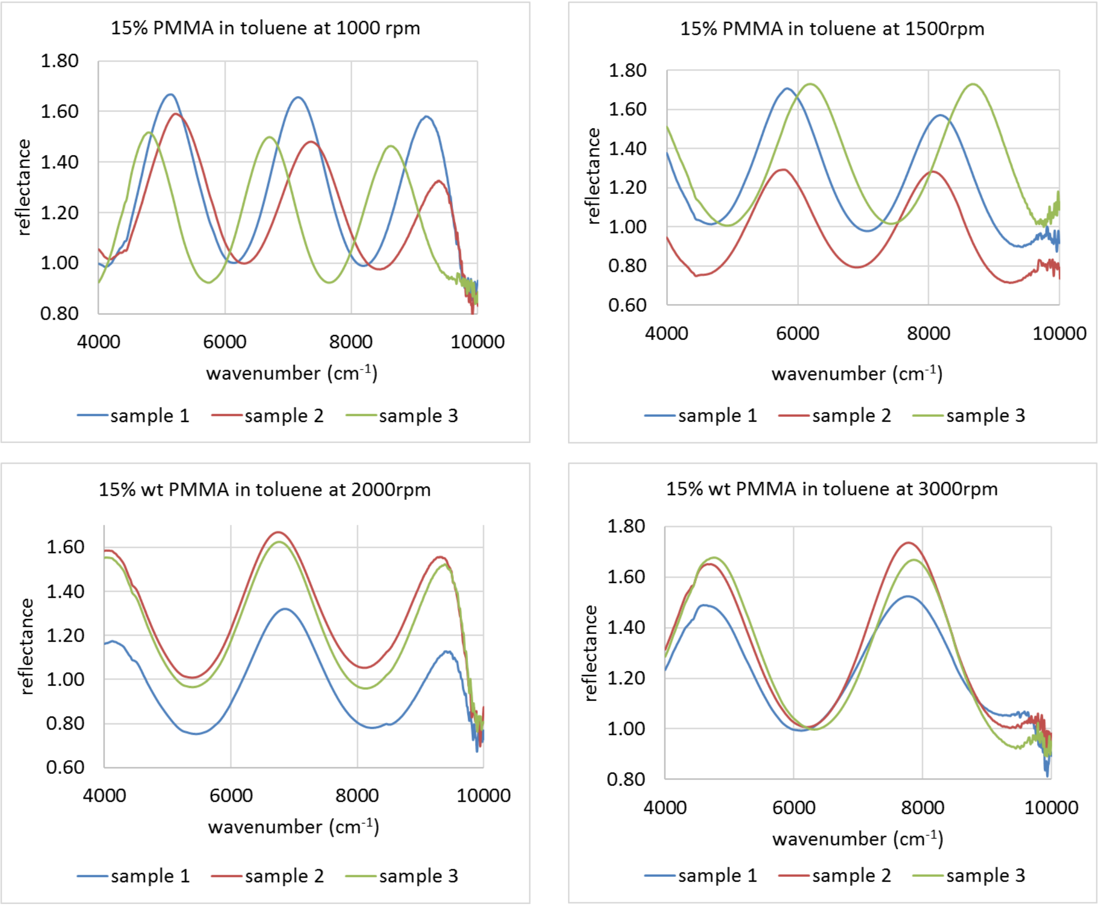

Figure 3. 5 NIR spectra for 15% PMMA in toluene solution for 4 different spin speeds.

As expected higher spin speeds produced thinner layers of PMMA from solution. The films produced at higher speeds showed greater uniformity than at the lower speeds. The graph of spin speed versus thickness for the PMMA solution is shown in Figure 3.6.

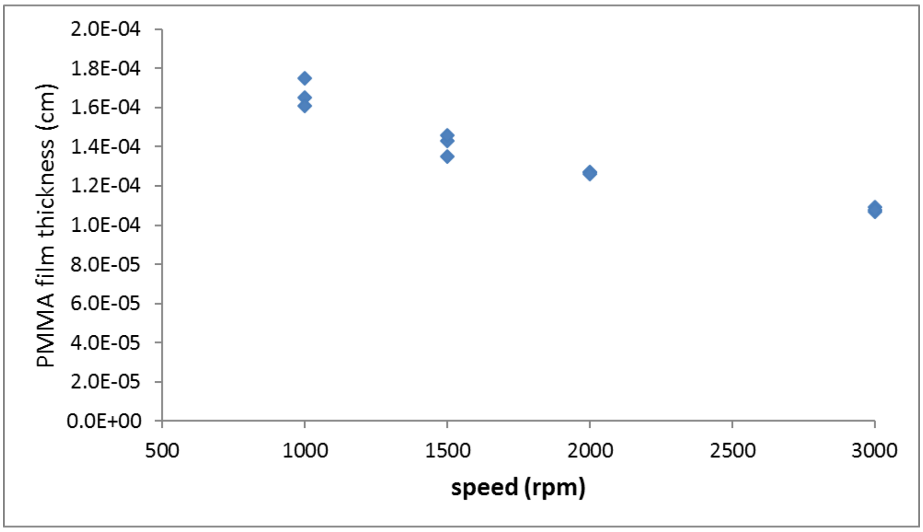

Figure 3. 6 PMMA 15% in toluene spin speed versus thickness.

PS

Polystyrene was also used to produce the spacer layers adapted from the method described by Chakraborty *et al* (Chakraborty, et al., 2003). Polystyrene pellets MW 290,000 from Sigma Aldrich were dissolved in toluene using a magnetic stirrer for 8 h at room temperature.0.1ml of a 0.13g/ml solution of polystyrene in toluene was deposited using dynamic dispense at speeds from 1000 to 3000rpm onto silicon wafers. The refractive index value used in the calculations was taken from the manufacturer at 1.5916. The NIR spectra were also taken using uncoated silicon wafers as reference and the spectra and the calculated thickness produced are shown in Figure 3.7. Again, as expected, higher spin speeds produced thinner films.

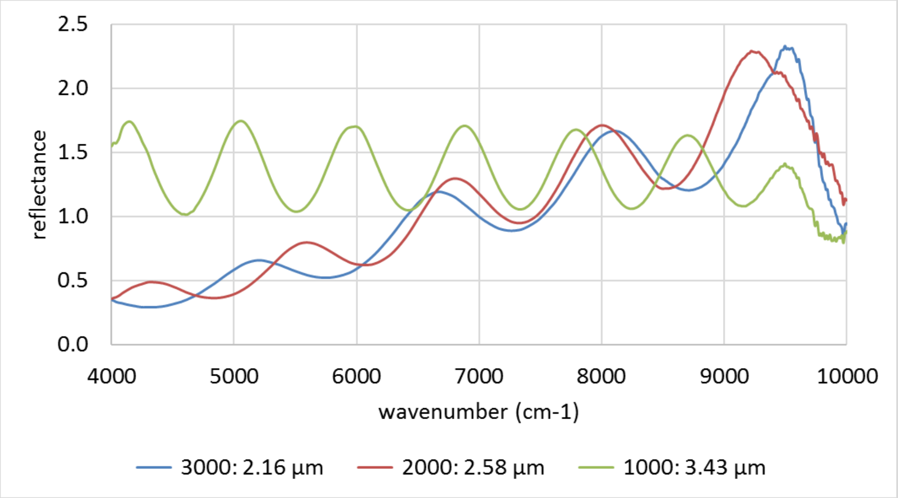

Figure 3. 7 PS in toluene 0.13g/ml at various spin speeds and the thickness produced.

PDMS

Difficulties in producing thicker films using PS and PMMA meant that PDMS elastomer was used to produce thicker spacer layers. The thickness of solution required to fabricate coatings of PS and PMMA of the equivalent thickness (around 10 µm) produced layers which were very uneven. PDMS elastomer is known for its good insulating qualities and is ubiquitously used in micro and nano fabrication.

PDMS (Sylgard 184) combined in a 10:1 base to curing agent was mixed and 0.1ml was deposited using dynamic dispense onto silicon wafers. As the PDMS was not diluted, and solidifies by curing over many hours at room temperature, the duration that the layer was spun for had a marked effect on the thickness of the coating produced and could be used to manipulate the thickness of the deposited layers. This contrasts with the

PMMA and PS deposited from solution where the drying of the solvent limited the time the solution could be spun for.

The spectra for 3 samples all spun at 3000rpm are shown in Figure 3.8. The duration of spinning was 1,3, and 5 mins with the layer of PDMS decreasing as the spin time increased as expected, although this decrease was not linear.

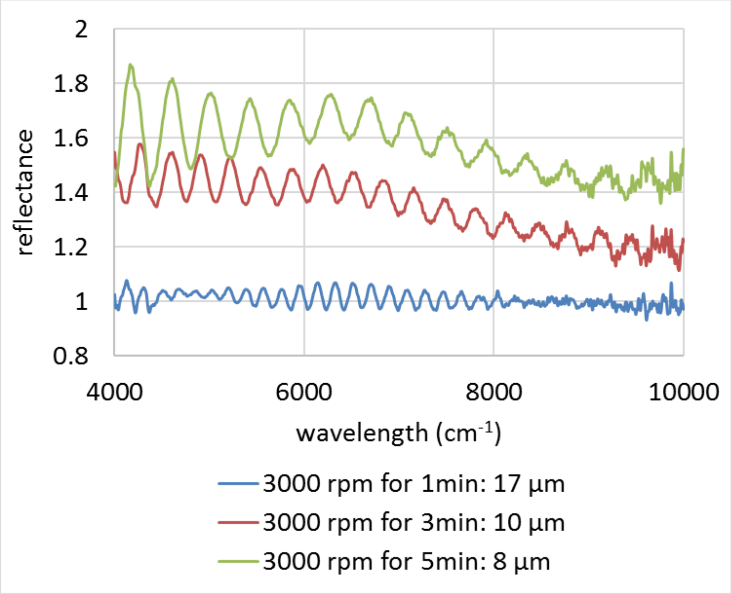

Figure 3. 8 NIR spectra and thickness of PDMS spun at 3000rpm for an increasing duration.

Replicating the results was also successful and 10 µm was consistently replicated using a speed of 3000 rpm with a duration of 3 mins. Increasing the spin speed whilst decreasing the spin time produced a similar result as a speed of 4000 rpm and a duration of 2 mins also produced a thickness of 10 µm. The spectra and thickness are shown in Figure 3.9.

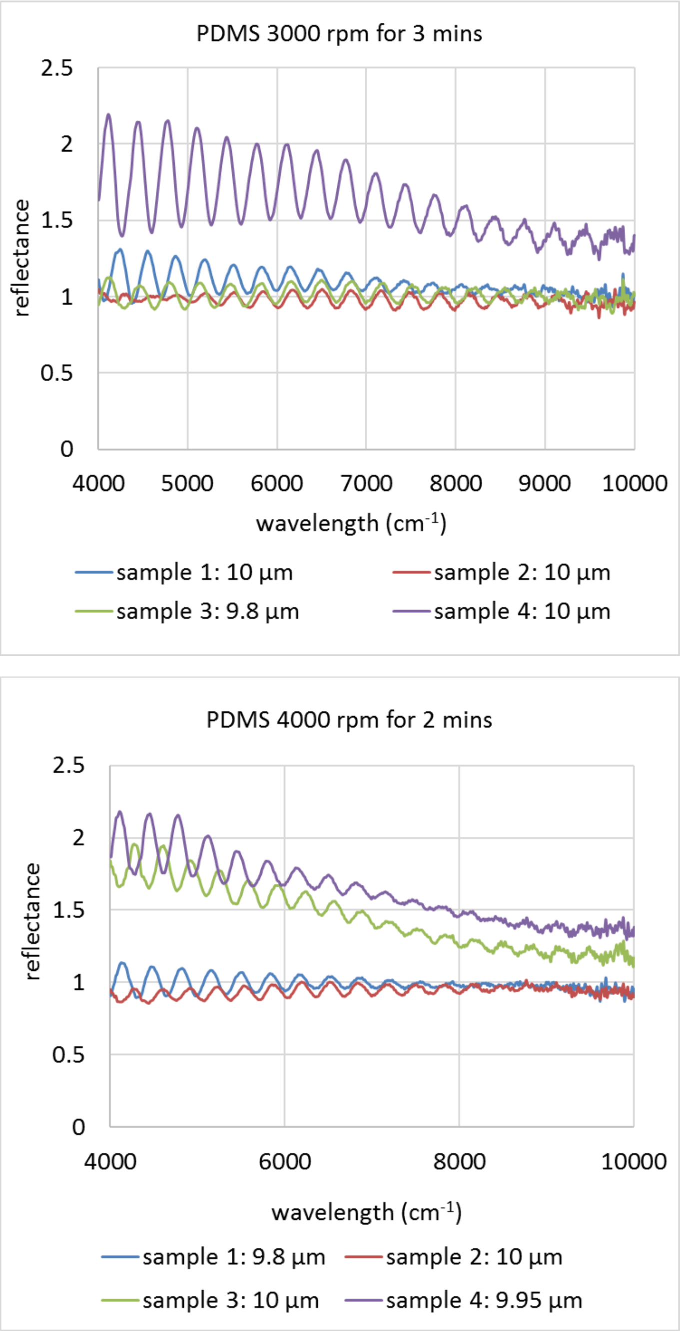

Figure 3. 9 NIR spectra for PDMS 10µm thick.

Epoxy resin

The above thin films were adapted from references in the literature. A technique of producing a thin film from Evo-Stik Control epoxy resin was specifically developed for this study as set out in the Experimental Chapter 2. Solutions of various concentrations of the epoxy resin in a toluene/acetone mixture solution were tested at a variety of spin speeds to obtain a range of thicknesses. The NIR technique can estimate the thickness of layers down to approximately 1 µm. Below this peaks in the spectra were so wide that it was difficult to obtain reliable data. Thicknesses of spin coated layers at different speeds and concentrations are shown in Figure 3.10.

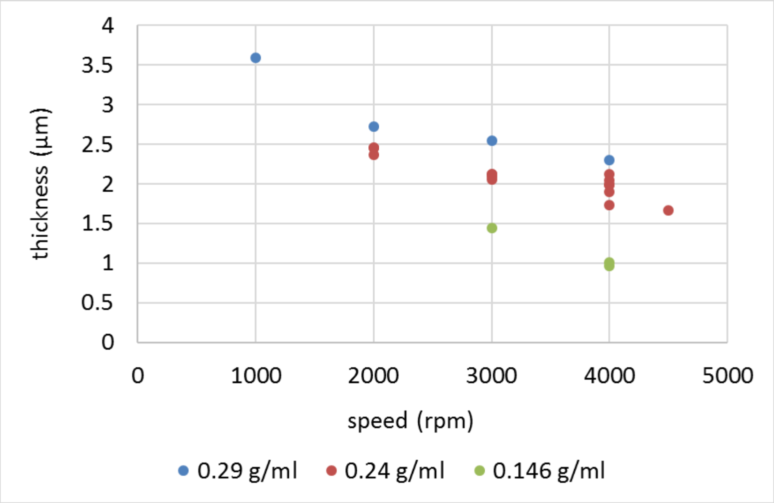

Figure 3. 10 Epoxy coating at various concentrations and spin speeds.

The NIR technique could also be used to evaluate the thickness of multiple layers of epoxy coated on top of one another. A layer of epoxy was spin coated at 2000 rpm onto a silicon wafer and allowed to cure. An area of the film was then masked using a thin removable plastic film and a second layer of epoxy spun at 3000 rpm was deposited on top. The thin plastic film mask was removed leaving a surface with both layers. The NIR spectrum are shown in Figure 3.11 and the thickness of the single layer was shown to be 3.9 µm and the double layer a total of 5 µm.

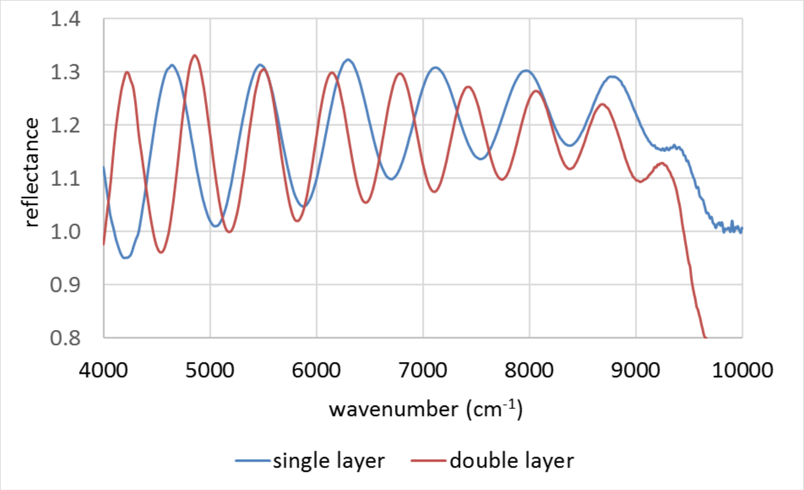

Figure 3. 11 Double and single layer epoxy spectrum.

3.3 EHD patterned surfaces using Evo-stik epoxy resin

The method used to deposit thin layers of cold-cure Evo-Stik Control epoxy was developed in tandem with a method of structuring the surface using EHD patterning.

The EHD patterning technique was developed with the aim of using simple bench-top techniques to produce microscale structures and eliminate the need for vacuum coating, photolithography and a clean-room. This technique resulted in a fabrication procedure which could be utilised in a very wide range of research environments. The equipment used is available in any laboratory with perhaps the exception of a spin-coater and a high voltage source.

Dip-coating, spray-coating and spin-coating were tested to produce a thin layer of epoxy; spin-coating was found to be most effective. The resin used for the following results was Evo-Stik Control. The initial solution used to spin coat the epoxy layer differed depending on the thickness that was desired, however the solvent fully evaporated during the spin coating process leaving only a thin layer of epoxy. As a result the epoxy composition for all of the EHD experiments was assumed to be identical and to be the epoxy alone. The inclusion of solvent in the patternable fluid was not allowed for in calculations. The parameters that differentiated each sample was the epoxy thickness, the spacer layer thickness and the applied voltage.

EHD patterns, using Evo-Stik Control as the resin, were produced using an applied voltage of 30, 61 or 162V with epoxy layers that varied from 0.4µm to 15µm and spacers that ranged from 3µm to 40µm. A wide range of wavelengths were produced, ranging from 3 µm to 200 µm. Once a method of producing the EHD patterned surfaces, using a cold-cure resin had been developed, the objective was to reduce the scale of the instability so that smaller patterns could be produced. The aim was for these structures to function as surfaces which would selectively absorb certain wavelengths of radiation. The results of the EHD experiments and the parameters used are summarised in table 3.1. The individual surfaces are discussed more fully in the following sections.

Table 3. 1 Table of fabrication parameters and resulting wavelengths.

Sample	Epoxy/ solvent (1:1 acetone to toluene)	Resin thickness (µm)	Electrode gap (µm)	Voltage (V)	Wavelength (µm)
Figure 3.12 A	0.3g/ml	1.2	9	61	33
Figure 3.12 B	0.3g/ml	3.5	8.9	61	52
Figure 3.12 C	0.3g/ml	2.7	6.6	61	55
Figure 3.12 D	0.3g/ml	4	7.5	30	44
Figure 3.13 A	0.6g/ml	9.6	25.7	162	109
Figure 3.13 B	0.3g/ml	6	17	162	231
Figure 3.18 A	0.6g/ml	13.3	25.3	162	46.7
Figure 3.18 B	0.6g/ml	6.7	26.5	162	42
Figure 3.18 C	0.6g/ml	5.4	14.1	162	65
Figure 3.18 D	0.3g/ml	4.6	26.7	162	28
Figure 3.19 A	0.146g/ml	1.8	3.7	162	7.1
Figure 3.19 B	0.3g/ml	4.5	9.6	162	19
Figure 3.20 A	0.3g/ml	1	4.9	80	42
Figure 3.23 A	0.29g/ml	1.9	3.1	111	7.2
Figure 3.23 B	0.29g/ml	1.8	3	145	6
Figure 3.24 A	0.24g/ml	1	1.8	61	9.6
Figure 3.24 B	0.24g/ml	0.3	0.9	162	3.8
Figure 3.25 A	0.29g/ml	1	1.8	110	7.3
Figure 3.25 B	0.24g/ml	0.4	1.4	110	3.4

There were several assumptions made about the epoxy. One was that its polarisability was uniform across all the experiments. It seems likely that in fact this would have varied as the freshness of the prepared solution changed. Typically, a prepared solution was used over a duration of 2 weeks. After leaving the solution in storage for a period of several weeks it formed a gel-like material whereby the epoxy had crosslinked in solution. Leaving the formed gel in the air allowed the solvents to evaporate and what was left was the solid epoxy. The effect of adding a solvent to the epoxy slowed its ability to crosslink; however, given enough time the epoxy would eventually polymerise so there would be changes in the material dependent on how long it had been stored. The flow behaviour of the deposited epoxy material was also assumed to be constant, although again this would change with batch freshness, especially given the fact that the epoxy did eventually crosslink in solution. The viscosity of the patternable polymer affects the rate of column formation during EHD patterning. The viscosity of the raw epoxy was tested and the material was found to have non-Newtonian viscosity by exhibiting shear thinning. The EHD patterning experiments were all performed at ambient temperature which changed across a range expected with changing seasons, and the temperature would have affected the cure time and viscosity of the epoxy.

The range of pattern wavelengths produced and the aspect ratio of the pillars varied considerably. The results were dependent on the initial conditions of fabrication such as the electrode spacing and epoxy thickness. Whilst every effort was made to reduce contamination, occasionally particulates contributed to stray current across the electrodes which reduced the initial applied voltage.

As expected, the pillars had roughly six nearest neighbours. There are several possible reasons why a strictly hexagonal pattern did not result: very high electric fields lead to a range of fastest growing wavelengths which causes a larger distribution of pillar spacings, and high fill factors lead to coalescence of the pillars, which causes disorder and larger-diameter columns.

Wavelengths were determined by taking the average centre-to-centre distance value, from a random selection of closest neighbours across the surface. The standard deviation gives some insight into the regularity of the pattern. In general, a more regular pattern will have a lower standard deviation.

3.3.1 Larger-scale EHD patterned surfaces

The surfaces in Figure 3.12 all show similar characteristics. There are clear gaps between the pillars and epoxy resin still exists on the substrate surface in these spaces. The pillars do not show good hexagonal close packing. Figures 3.12 A and B were both fabricated using a similar electrode gap of 9 µm and a voltage of 61V. Both patterns appear to lack order but the pillars in B are more evenly spaced and more uniform in diameter. The pillars on the surface in Figure 3.12 A have a greater variation in diameters and more uneven gaps between them. Assuming the epoxy is behaving as a perfect dielectric, the electric fields in the polymer were 0.85 and 1.16MV/m in A and B respectively; these were at the lower end of all the experiments tested in this study, mainly due the voltage applied which was 61V (many other experiments were conducted with an applied voltage of 162V).

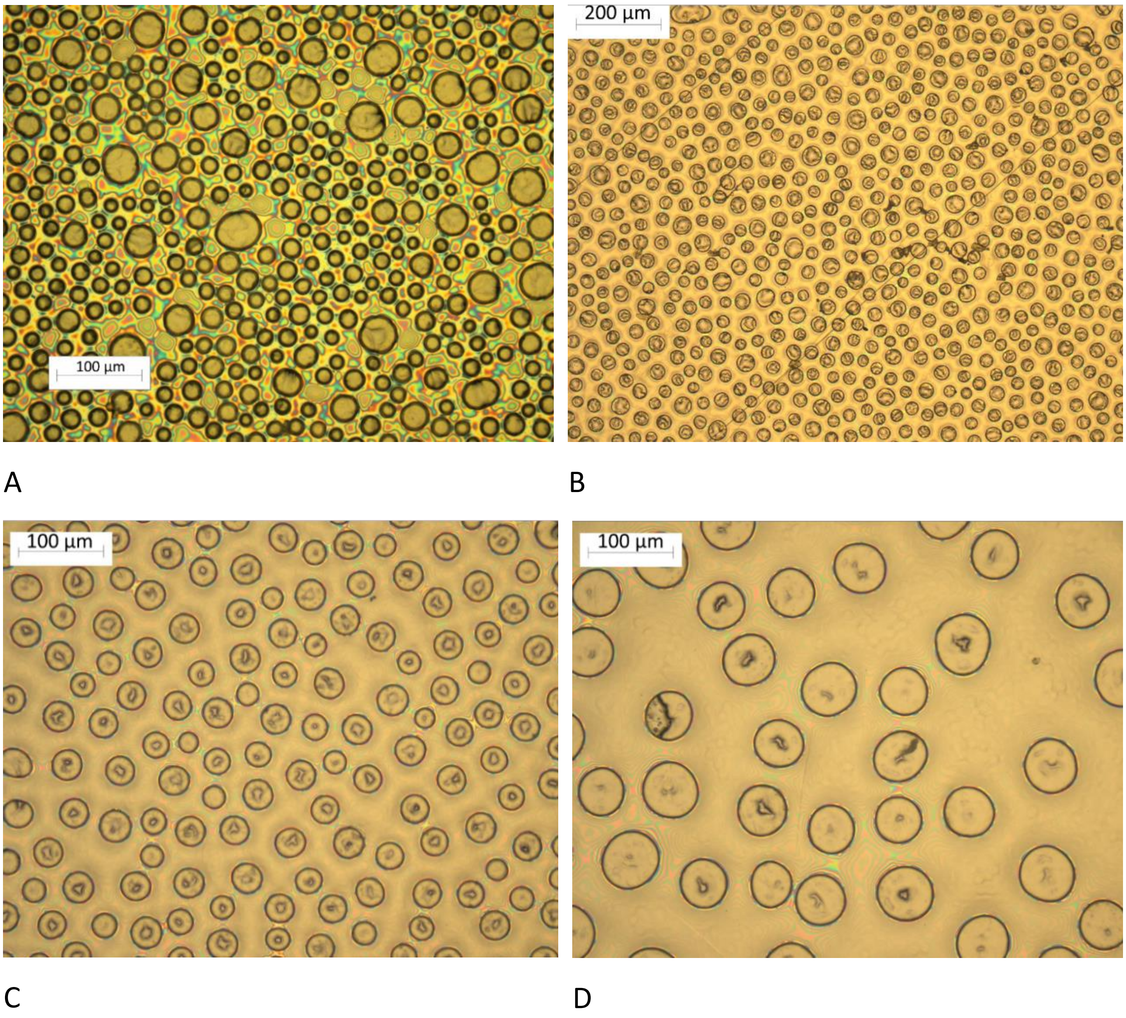

Figure 3. 12 Plan view optical micrographs of EHD instability patterned surfaces.

The epoxy thickness in A was smaller than that of B. The epoxy layer in B had been left to cure for 2 h before the voltage was applied which means that the viscosity would have altered. The higher viscosity of the more cured resin would have slowed the formation of the columns, and hence led to more uniformity in their distribution. The results in Figure 3.2 show that the dielectric constant would not have altered significantly over this time period.

Samples in Figure 3.12 C and D show a similar arrangement of pillars to A and B. The voltage used for C was 61V, whereas the voltage used for D was 30V. The pillars in C are smaller in both diameter and spacing which is consistent with the higher electric field in the polymer layer being 1.58 and 0.8MV/m respectively assuming the epoxy is behaving as a perfect dielectric. Both were left to cure for up to 2 h before the voltage was applied which again could account for the higher uniformity across the pattern and diameters of the pillars.

The arrangement of the pillars in sample Figure 3.13 A is similar to those in Figure 3.12, although it is on a scale up to 3 times larger, with a wavelength around 100 µm. The applied voltage used was 162V but over a much larger electrode gap so the electric field was similar to the surfaces in Figure 3.12. During the fabrication of the surface in Figure 3.13 a current was observed to flow as the pillars bridged the gap between the electrodes which rose to 19.4 µA (the short circuit current was 26 µA). This current was then observed to drop to 3 µA once the resin had cured (after around 4 h).

The diameter and spacing of the pillars in Figure 3.13 B were the largest fabricated in this study and are visible to the naked eye. They were approximately 6 times larger than the theoretical values for the fabrication parameters used, which suggested a possible short circuit that lowered the actual electric field between the electrodes. However, the pillars produced demonstrated the variety in the scale of surfaces that could be fabricated by this method. Paler circles can be seen where the columns have adhered to the top electrode and been removed from the surface when the electrodes were separated.

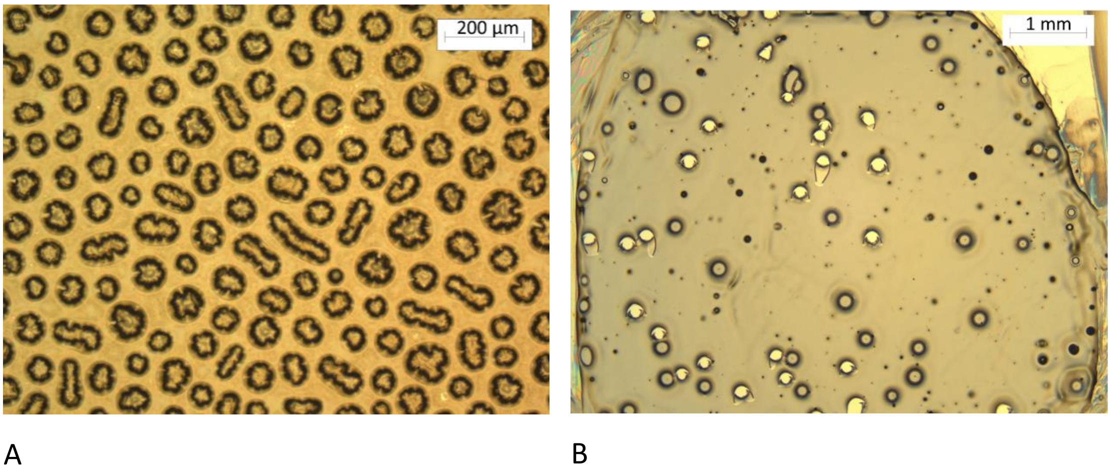

Figure 3. 13 Plan view optical micrographs of EHD instability patterned surfaces.

For the above samples in Figures 3.12 and 3.13 a variety of voltages were applied over a range of spacer distances but all producing similar fields of around 1MV/m in the polymer. In the lower voltage experiments no current was observed to flow and the low field seems to have resulted in surfaces that lack a regular hexagonal order. Most of the samples had a high fill factor (the ratio of resin thickness to electrode gap) which should have resulted in a large amount of coalescence which does not seem to have occurred. The low electric field meant that the spacing between the pillars was large so perhaps this affected the ability of the pillars to coalesce. Their wavelength did not correlate well with theoretically predicted values using the same fabrication parameters; however, this is in direct relation to the lack of hexagonal pattern uniformity.

The pattern formation was filmed with an optical microscope using a spacer of 9.3 µm, an epoxy layer of 3 µm and an applied voltage of 61V. Images from the film taken at various time intervals are shown in Figures 3.14 - 16. A micrograph of the final surface produced with the filmed area highlighted is shown in Figure 3.17. The pillars on the right, with the largest diameter, are those which were the first to form and therefore had a longer time over which to accumulate material and grow.

Filming was started simultaneously with the application of the voltage so the time stated is the duration of the fabrication process; the image shows 1mm width of surface (Figure 3.14). When the pillars contacted the top electrode, they appeared as a dark-edged shape which grew in area as the pillar accumulated more material.

The first image, at approximately 1 s, shows that the epoxy surface was not entirely smooth and homogeneous, and slight waves and phase separation can be seen; also, the initial formation of a pillar can already be seen in the bottom right quadrant. A defect in the coating is visible in the bottom centre of the picture. After 25 s, on the right side of the image it can be seen that some more of the first pillars had contacted the top electrode. The initial shape of their cross-section is not rounded or even, and in some places is quite angular.

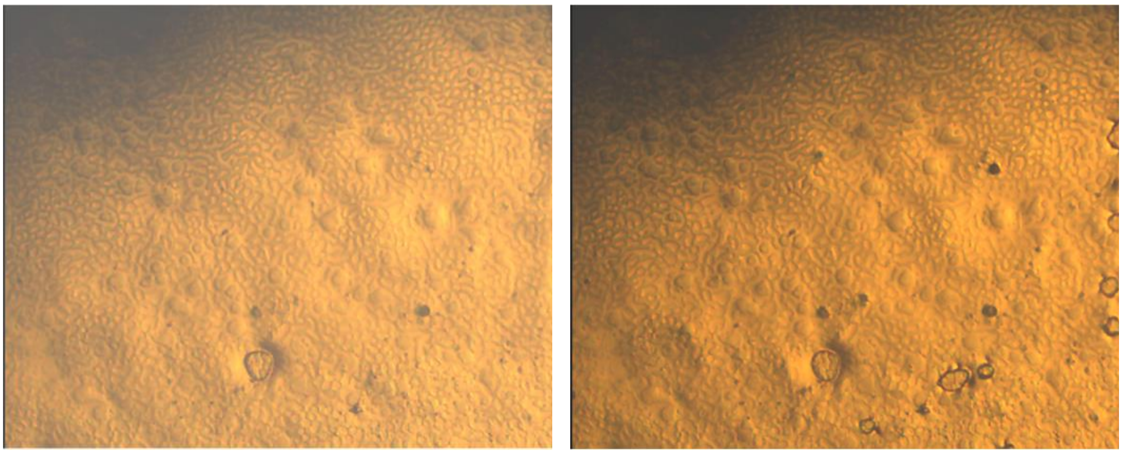

1 s 25 s

Figure 3. 14 Stills from EHD patterning fabrication film using optical microscopy, image width approximately 1mm.

After 1 min (Figure 3.15) pillars began to appear across the rest of the surface, especially in the areas of epoxy that seemed to be higher in the initial image, which is as expected. After 4 mins many of the first pillars had accumulated almost all the material they would eventually consist of based on the fact that their diameters had increased only very little in the image of the cured surface. At least 2 structures (centre left) had merged and two, which appear to be touching in the bottom right of the picture, had not merged. After 10 mins the cross-sections appeared to be more rounded and the two pillars touching in the bottom right of the corner seemed to have a larger gap between them. After 13 mins the whole surface was populated with structures and the gaps between them were continuing to be filled with more columns.

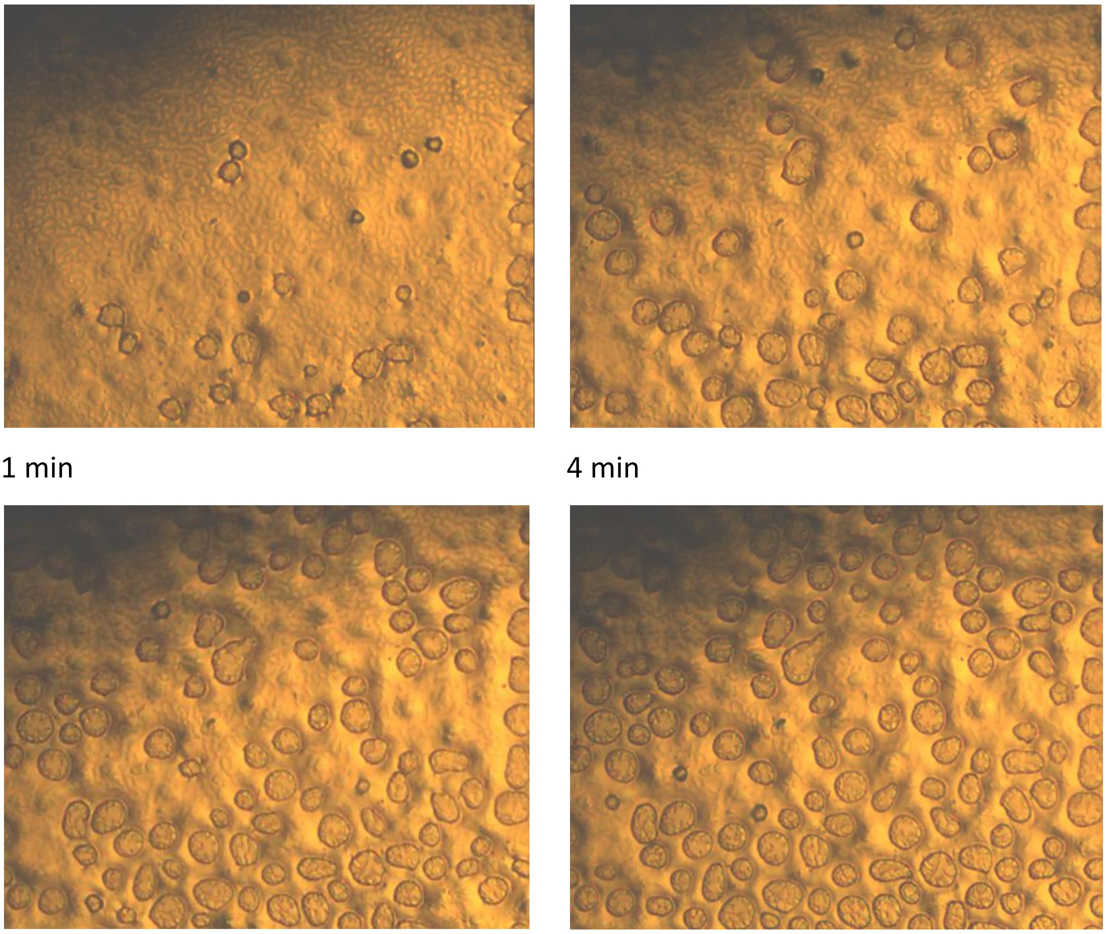

1 min

4 min

10 min

13 min

Figure 3. 15 Stills from EHD fabrication film image width approximately 1mm.

After 17 mins the surface appeared stable and the most recently formed pillars were growing in diameter very slowly. At 23 min, development of the structure had stopped; there is little difference to be seen from this image and the image of the fully-cured surface in Figure 3.17, even though at this point the epoxy would still have been around 3 h from curing and solidification. More accentuated waves in the epoxy remaining between the structures can be seen. No new pillars formed in the interval between the last image taken from the film (here at 23 min; Figure 3.16) and when the epoxy had cured around 2 h later. The most significant change is that the cross-section of the shapes had become more rounded and in many cases more circular.

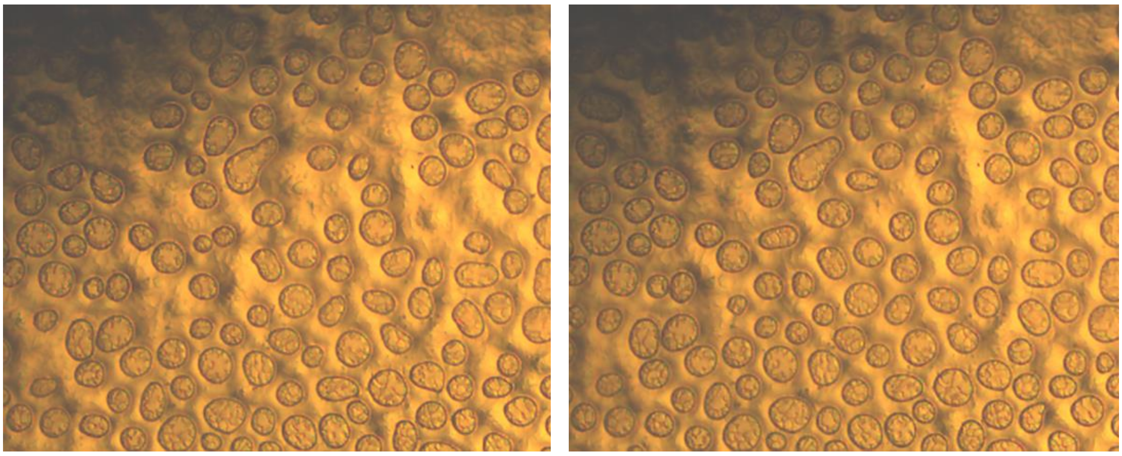

17 min 23 min

Figure 3. 16 Stills from EHD fabrication film image width approximately 1mm.

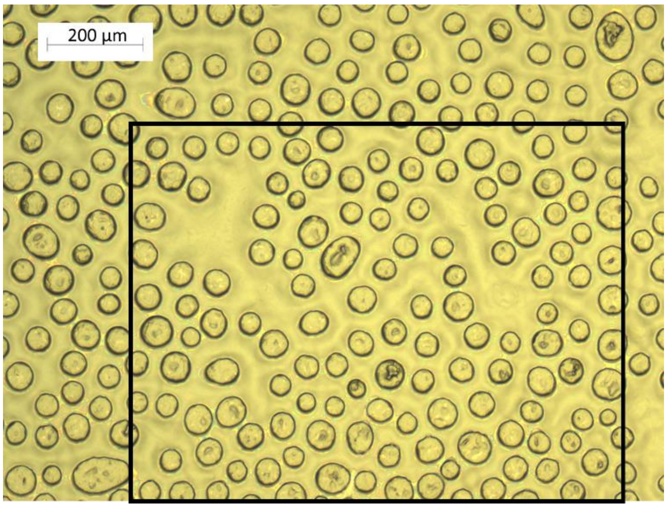

Figure 3. 17 Optical micrograph of the filmed EHD instability patterned surface once fully cured (the filmed area is outlined).

The pillars in the surface filmed formed very quickly (within half an hour) once the voltage had been applied, and this was true of many of the fabrication experiments described, although in some cases the pillars took longer to appear. The rate at which the pillars grew is related to the viscosity of the material with pillars growing faster in less viscous material as would be expected.

Use of a higher voltage (above 100V) created surfaces with a greater variety of morphologies than those described previously in the literature, depending on the epoxy thickness and electrode spacing used. The structures tended to have a higher aspect ratio than those produced using a lower voltage although the centre to centre distance or wavelength was not dissimilar in many cases.

Both surfaces in Figure 3.18 A and B have wavelengths in the region of 40 µm. Epoxy material remains between the pillars on both samples. Figure 3.18 A was fabricated from epoxy that had been stored, combined in solution, for 10 days. Storage of the epoxy led to unevenness during spin coating, which can be seen in the non-uniformity of the pillar spacing across the surface. It also meant that the resin cured more quickly once it had been deposited, presumably because it had begun to crosslink whilst being stored.

A current of 17 µA was observed to develop during the fabrication of Figure 3.18 C as the pillars crossed the gap. The pattern of the pillars is reasonably even, and the diameters of the pillars have good uniformity with the exception of a few which have merged and coalesced. 3D images of surfaces in Figure 3.18 C and D are shown below in Figure 3.18 E and F. The structures have flattened tops and a well-arranged order. The flattened tops are of an even height, indicating that they had reached the top electrode. The pillars remained intact when the two electrodes were separated which is true of most of the samples produced. This was surprising given the adhesive nature of the resin material. It meant that creating a non-stick surface on the top electrode, to aid separation as has been done in other studies, for example by using an alkane monolayer, was not necessary (Schäffer, et al., 2001).

The surfaces shown in Figure 3.18 C and D show little or no epoxy left in the spaces in between the pillars. The arrangement of the pillars shows more order and this is possibly why more of the material has been used up in comparison to those shown in Figures 3.12 and 3.13. A more regular order to the pillars means that there would be fewer large gaps between the pillars so that epoxy could not be absorbed into a forming column. The wavelength of D however is less than half that of C.

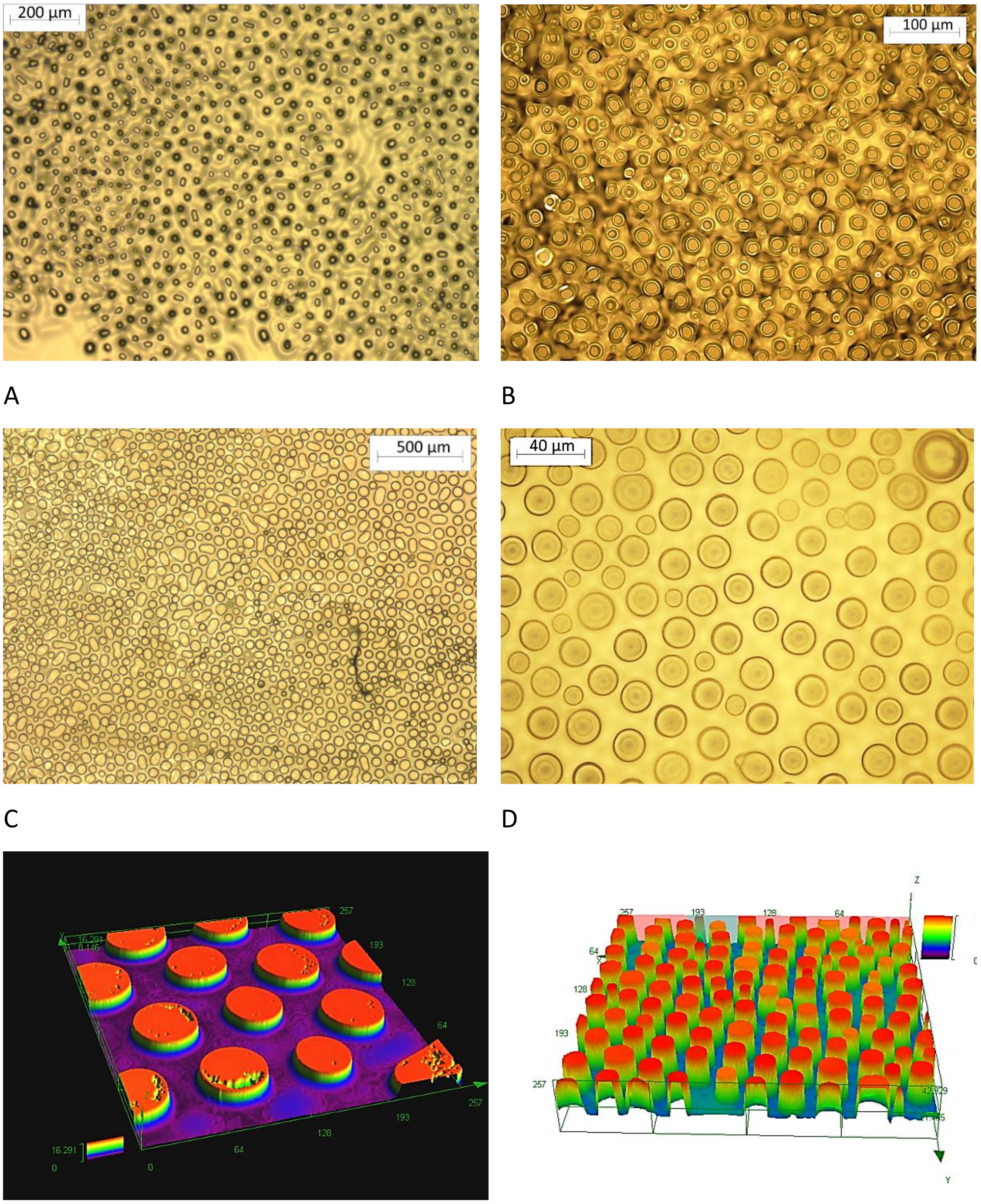

A B C D E F

Figure 3. 18 EHD fabricated surfaces. A-D are optical micrograph plan views. E and F are a LEXT confocal 3D scans of the surfaces in C and D respectively.

The surfaces in Figure 3.19 A and B displayed the most regularity in the pattern, across the entire structured surface. Again, a current (17µA) was observed to flow when the pillars had reached the top electrode, during the fabrication of Figure 3.19 A. The electrode spacing used was 3.7 µm and the epoxy thickness was 1.8 µm so the smallest presented so far. Unsurprisingly the wavelength was also the smallest of the samples represented so far, averaging 7.1 µm centre-to-centre distance.

The surfaces shown in Figures 3.19 A and B are shown with a cross-sectional view also. In order to measure the pillar height from the silicon surface, for the surface in Figure 3.19 B, an area of the patterned epoxy has been removed which can be seen as the purple area in the 3D image. Both A and B show the pillars are all the same height, which indicates that they have all reached the top electrode which has arrested their height growth. In Figure 3.19B cross-section, epoxy material still exists between the bases of the pillars around 2 µm in thickness. In the cross-section a sharp indentation can be seen in the epoxy that closely surrounds each pillar, which shows a region that has been depleted of epoxy material. The pillars are also wider at the base than at the tip which would account for the apparent close packing seen in the top down image Figure 3.19 B but apparently lacking in the 3D image. The existence of epoxy at the base of the pillars in both samples shown in Figure 3.19 A and B implies that the epoxy had cured before the surface had fully evolved.

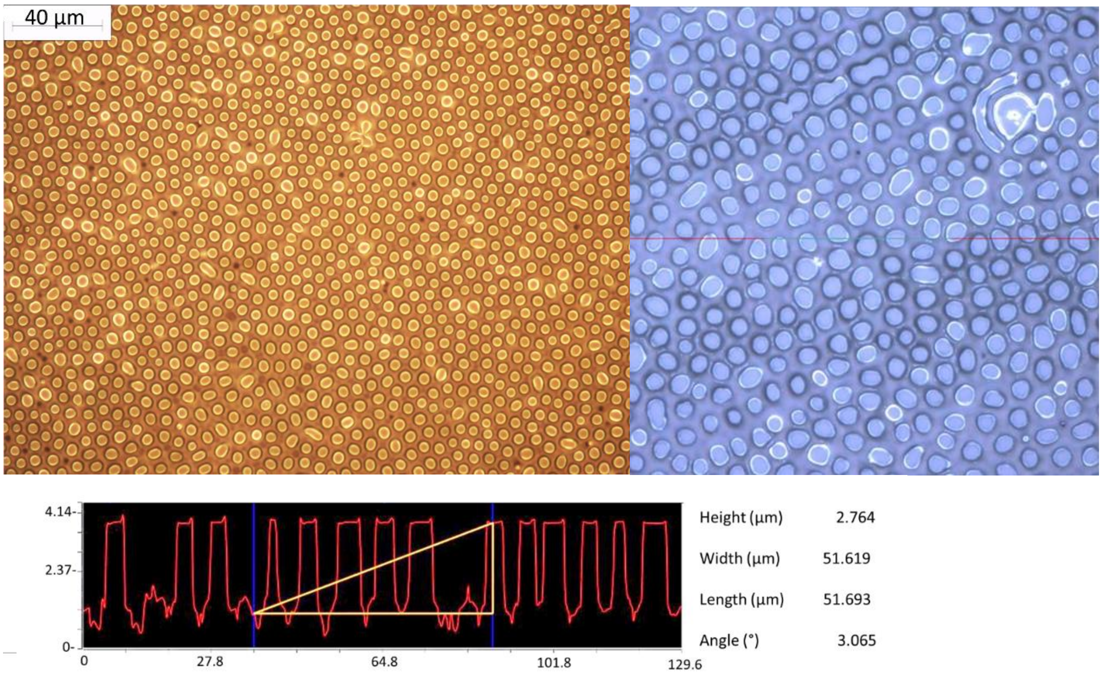

3.19 A. Optical micrograph plan views (top left and right), LEXT confocal 3D cross-section of EHD surface (bottom). The image width (top right) is 130µm, cross-section scale is in µm.

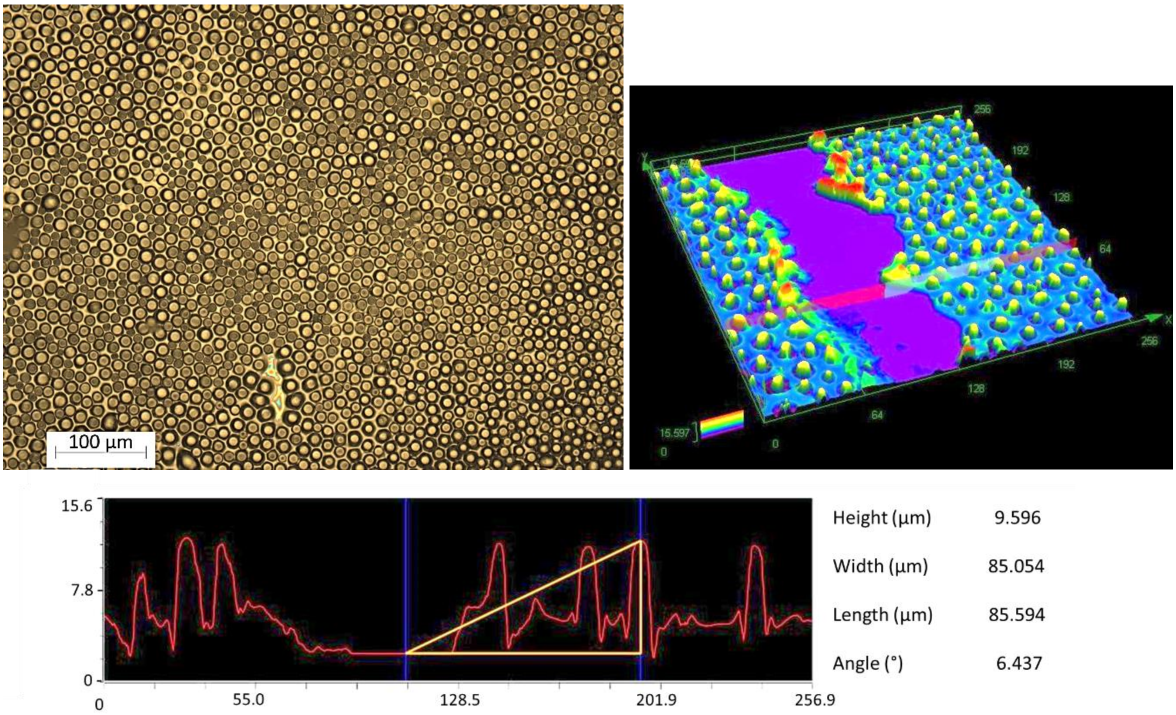

3.19 B. Optical micrograph plan view (top left), LEXT confocal 3D scan (top right) of EHD fabricated surface with associated LEXT confocal 3D scan cross-section.

Figure 3. 19 Plan view and 3D cross-section images of EHD fabricated surfaces.

The surface shown in Figure 3.20 shows a reasonably organised hexagonal arrangement to the pattern with good uniformity in the diameter of the structures. The epoxy resin used here was 1 µm thick and the electrode spacing in the region of 4.9 µm. Again, in this surface most of the epoxy has been used in the formation of the structures and little remains between them, apart from where there are large gaps. The electrodes were separated before the resin had cured and so the liquid epoxy was evenly dispersed as drops on the ITO glass and silicon wafer electrode surfaces. Surface tension caused the drops to form regular rounded topped shapes (seen in the cross-section in Figure 3.20 B), similar to the process used by Lee *et al* to fabricate a micro lens array (Lee, et al., 2011). The surface shown here was formed on the bottom electrode; examination of the top electrode showed the same structures but with no resin residue between the shapes.

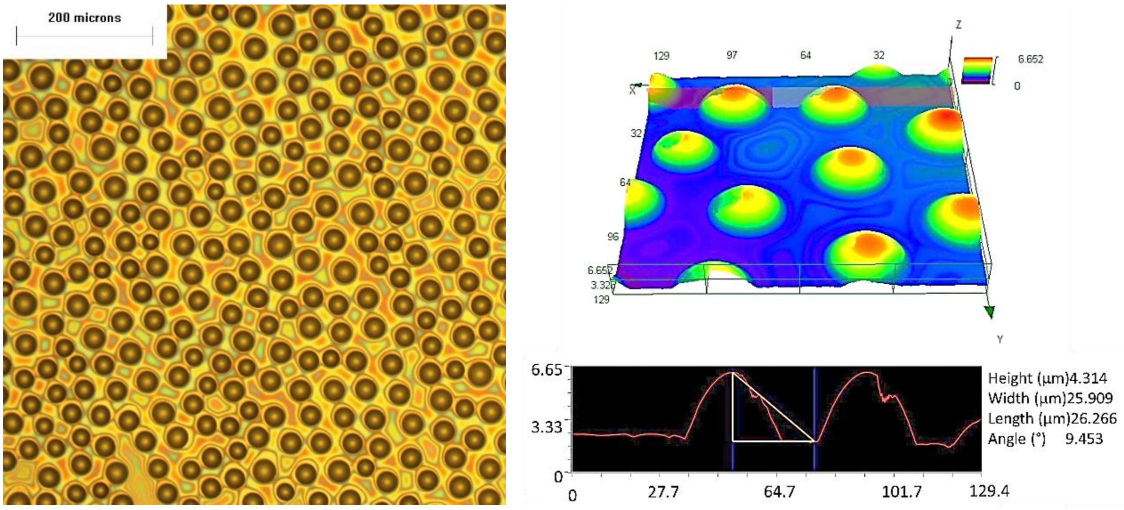

A Scale bar 200µm

B

Figure 3. 20 Optical micrograph plan view and B. LEXT confocal 3D image of an EHD fabricated surface.

3.3.2 Coalescence

Once the patterns have reached the top electrode the pattern continues to evolve if the material is still liquid. The material has deformed in response to electrostatic charge at the interface and thus the overall surface energy changes. Through the deformation, the electrostatic charge has been reduced and now surface energy takes over the process. To reduce the surface tension the pillars start to coalesce and merge together. Coalescence is characterised by a surface where the structures no longer have a circular shape and the hexagonal packing pattern is lost. Evidence of this can be seen in the surface in Figure 3.21 A and B. Elliptical pillars are the result of two or more merging together, trails form where many have merged in a line.

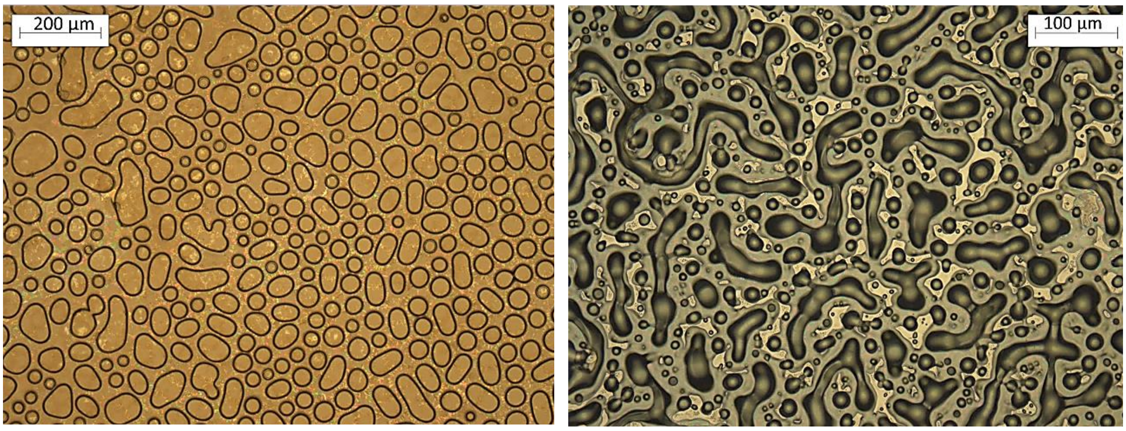

A Fill factor 0.42

B Fill factor 0.6

Figure 3. 21 Optical micrographs of coalesced surfaces.

The resultant pattern is a result of the need to minimise the total (surface and electrostatic) energy, and it changes continually until the material is solidified. The amount of coarsening and coalescence is greatly influenced by the fill factor or ratio of the electrode gap filled by the liquid polymer, as demonstrated by Verma *et al* (Verma, et al., 2005). In general, a fill factor of over 0.3 will result in a surface of coalesced structures. The fill factor of the surface in Figure 3.21 A was 0.42 and that of Figure 3.21 B was 0.6, so both surfaces were likely to coalesce to some degree and the pattern in B has been lost almost entirely. The calculations used in the above study were for a constant value of viscosity and dielectric constant. However, for epoxy resin these values change over the cure time of the material, so calculations using these assumptions may not be valid, and certainly not all the surfaces whose fabrication parameters indicated they were likely to coalesce, did so. The fill factor of the surface shown in Figure 3.22 A was 0.35 and yet it was the surface which showed the most coalescence.

In general, a larger fill factor means that a smaller wavelength develops, but also that the surfaces features coalesce more quickly. Over time, more and more pillars join merge until the phases invert to form a surface composed of circular air holes in an epoxy matrix as can be seen in the surfaces in Figure 3.22 A (the cross-section is shown in Figure 3.22 C). In the surface in Figure 3.22 B (cross-section D) aspects of the original surface structure of pillars are still visible.

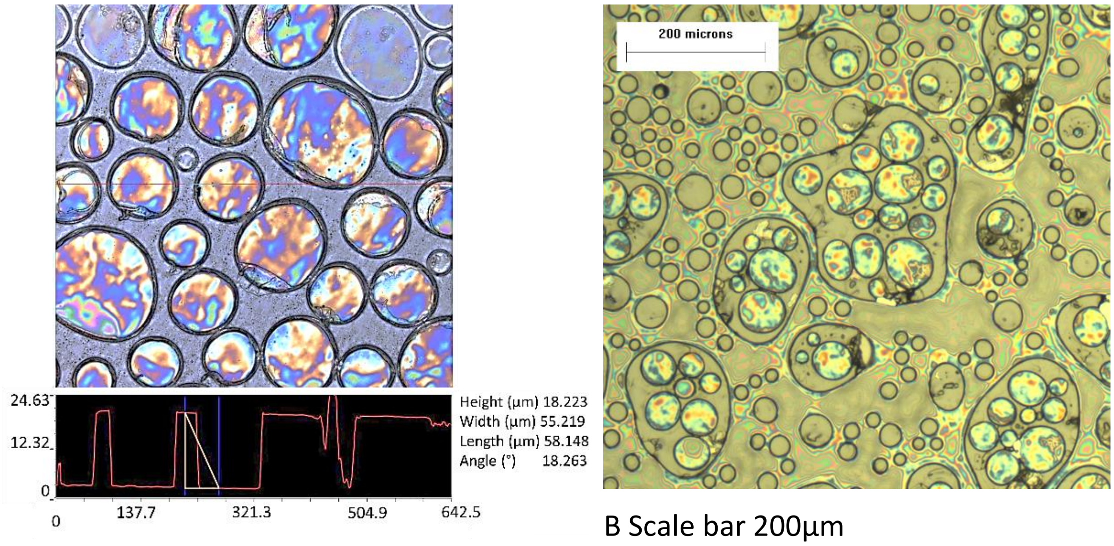

B Scale bar 200µm

A Scale in µm fill factor 0.35

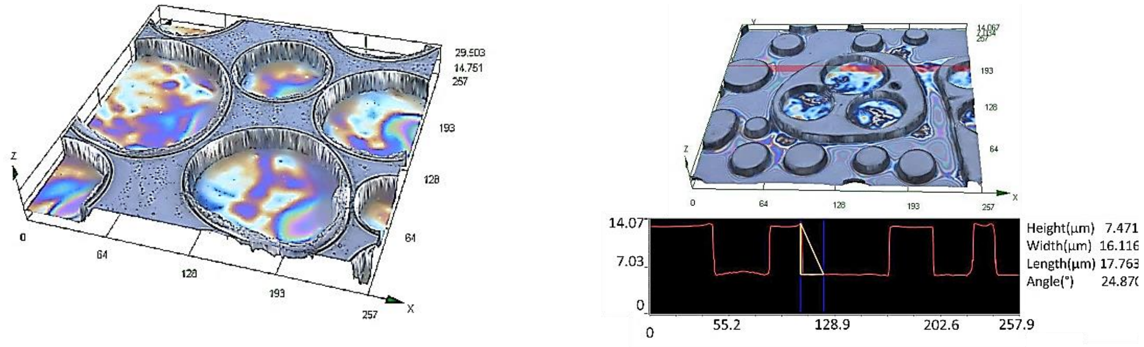

C Scale µm

D Scale µm

Figure 3. 22 Examples of 2 coalesced surfaces. A. LEXT confocal plan view of surface 1 and C, the 3D view of the same surface. B. Optical micrograph of surface 2 and D, LEXT confocal 3D scan of the same surface.

Many of the experiments conducted resulted in surfaces where the features had coalesced. Pre-curing the epoxy before applying the voltage lessened this to some extent. It was a particular issue with the epoxy material, which was much less viscous than the thermoplastics used in most other studies, so the rate at which patterns formed was fast. The aim of producing smaller pillars meant that a delicate balance needed to be found between increasing the fill factor so that smaller pillars would be produced, and avoiding coalescence of the pattern produced.

3.3.3 Reduction of the instability wavelength

The scale of the wavelengths in the surfaces shown in Figures 3.12 to 3.22 are between 7 and 200 µm. The objective of producing surfaces to interact with solar radiation meant that the scale needed to be reduced. The dielectric constant of the epoxy was already high, so the electrode and epoxy thickness were reduced in order to produce patterns at a smaller scale. In theory, increasing the voltage drop across the electrodes would also have produced smaller structures, however when higher voltages were tried (up to 400V) there was a great deal of destructive electrical discharge between the electrodes. Given the combination of electrode spacing and voltage which was being used, it was likely that the breakdown voltage of air was being exceeded, so the lower voltage of 162V was re-adopted.

The surfaces produced in Figure 3.23 had epoxy thicknesses of 1.9 µm for A and 1.8 µm for B and both had spacers of 3 µm (the cross-section of each surface is shown below each image). The patterns produced had wavelengths of 7.2 and 6 µm respectively although the pillars did not cover the entire surface and the pattern was very disordered in places. Because of the lack of order, a great deal of epoxy remained between the pillars; furthermore, the pillars did not seem well formed and cross-sections showed they were very tapered and pointed in shape (Figure 3.23 C and D). Bright patches show where a column has adhered to the top electrode and the overall morphology of the surfaces is very different to that of the well-defined structures shown above.

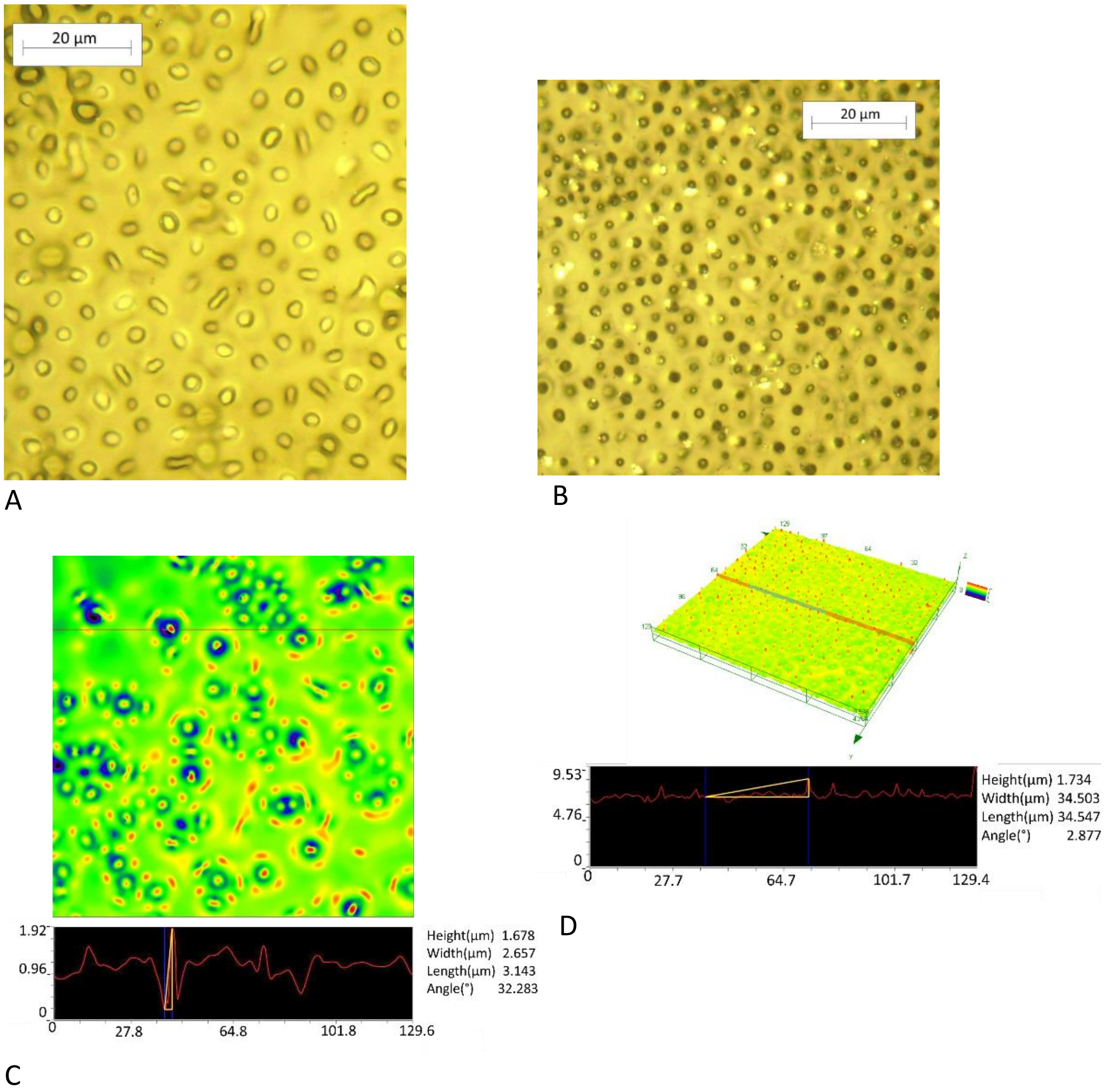

Figure 3. 23 A. The optical micrograph of an EHD fabricated surface and C. the LEXT confocal scan of the same surface (scale in µm). B. Optical micrograph of an EHD fabricated surface and D. the LEXT 3D confocal scan of the same surface (scale µm).

The surface in Figure 3.24 A was manufactured using a similar electrode spacing and epoxy thickness to the one above (1 µm), but a lower voltage of 61V was applied. A current was observed (0.01mA) but it was not sufficient to reduce the voltage drop across the electrodes to any great extent and so the voltage across the electrodes was measured at 61V. The structures on the resulting surface in Figure 3.24 A (the cross-section is shown in C) were more defined and covered a larger area of the electrode with more regularity than the surfaces shown in Figure 3.23, although their wavelength was somewhat larger due to the lower voltage used. The patterns from the experiment shown in Figure 3.24 B contained one of the smallest wavelengths produced in this study, about 3 µm, and was produced using the higher applied voltage of 162V. The pattern produced seemed to have greater order than those shown in Figure 3.23 above, but on inspection with a 3D laser microscope (Figure 3.24 D) it was found that the structures had coalesced and coarsened to the extent that the shape of the original pillar structures had been obliterated. The ordered circles that can be seen are the sites of pillars that have conducted current which has coloured the conductive ITO coating during the experiment. The epoxy pillars that produced these shapes have aggregated into random forms.

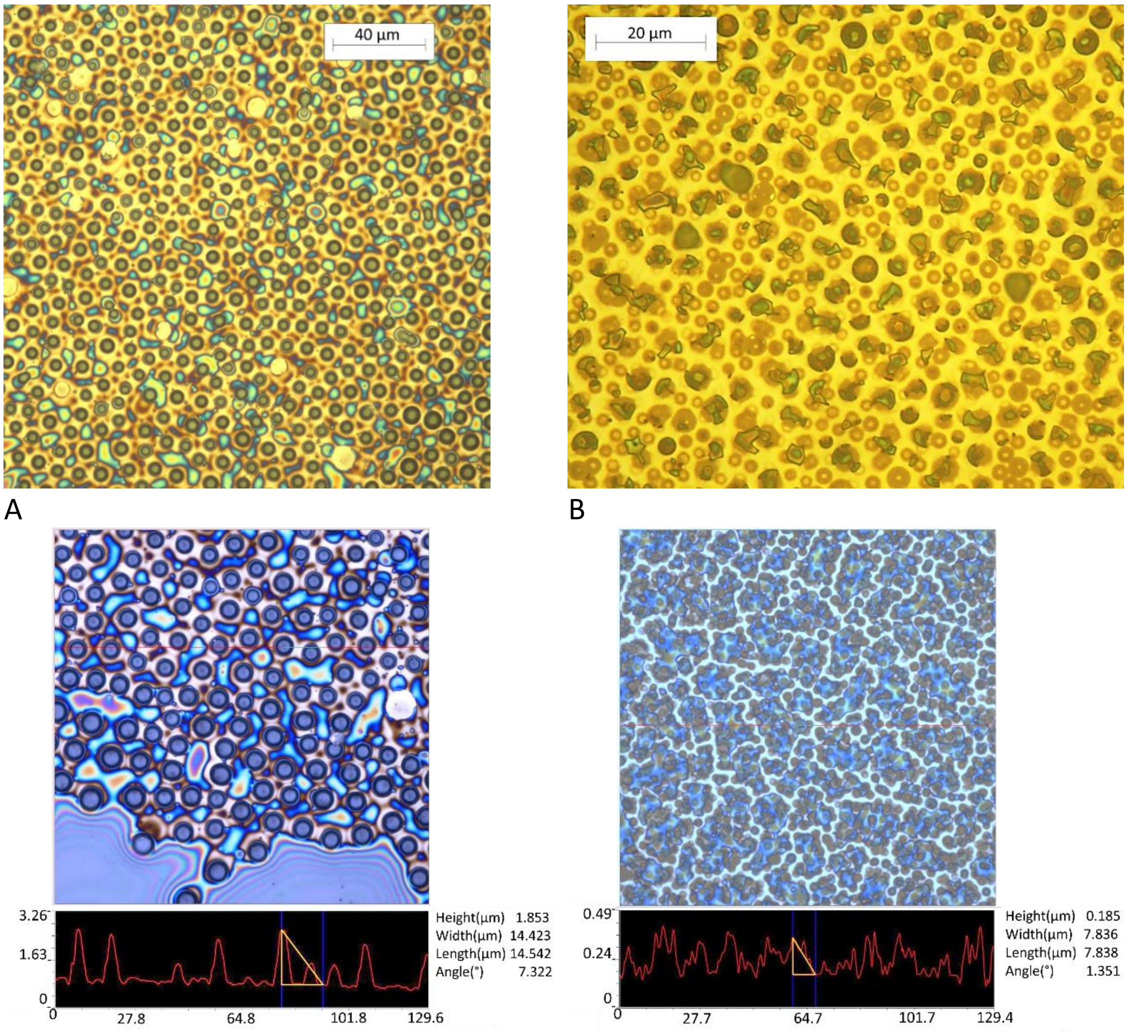

C Scale µm D Scale µm

Figure 3. 24 A. The optical micrograph of an EHD fabricated surface with the LEXT plan view of the same surface shown in C and B. the optical micrograph of an EHD fabricated surface and the LEXT confocal image of the same surface in D.

The surfaces shown in Figure 3.25 displayed surface features at a scale of a few µm. Cross-section views (Figure 3.25 C and D) showed that the structures were not defined pillars. The surface in Figure 3.25 A also contained concentric circle features which are shown in the cross-section image, Figure 3.25 C.

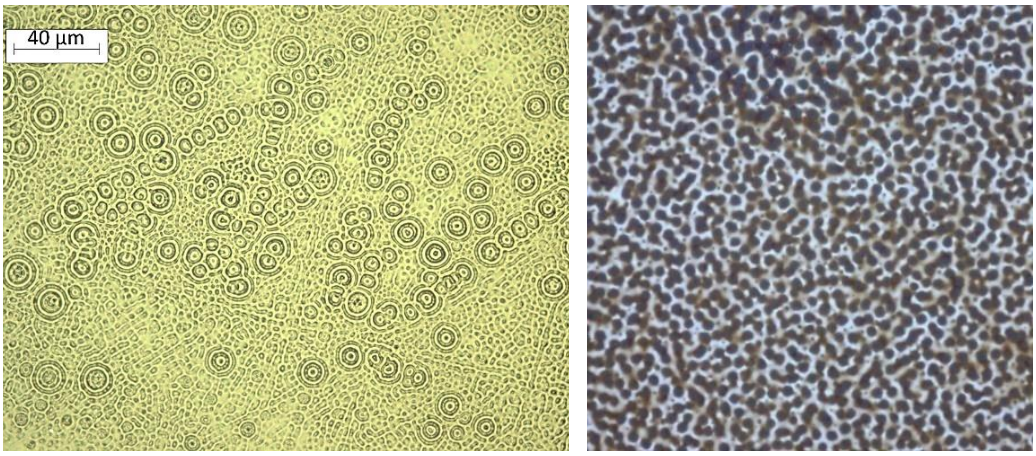

A

B Image width130 µm

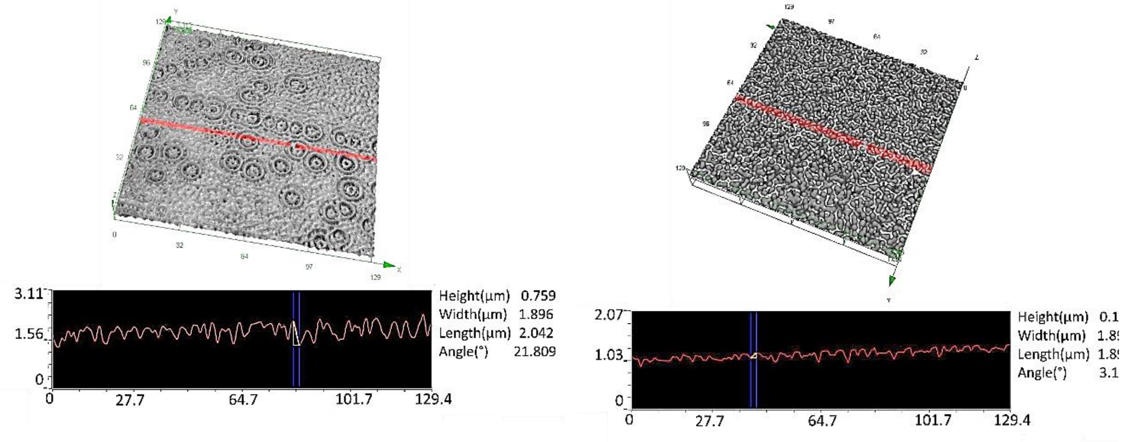

C

D

Figure 3. 25 A. The optical micrograph of an EHD fabricated surface with the LEXT 3D scan shown in C. below and B. a LEXT plan view of EHD fabricated surface with the LEXT 3D scan in D. below.

In many of the experiments, where the spacer gaps were above 5-7 µm, a current was observed to flow once the pillars had contacted the top electrode. In many experiments where the spacer gap was below 5 µm, current flowed across the capacitor before patterning took place. In experiments using a larger electrode gap, the pillars formed when the voltage drop across the electrodes was still at its maximum value. Where current was observed to flow before patterning took place, the voltage across the electrodes was not at its maximum value, which would have lowered the electric field and limited the achievable resolution of the patterns.

The smaller electrode gaps required thinner epoxy layers also and to achieve this, very dilute solutions were used. The low concentration meant that sometimes the epoxy did not distribute evenly during spin–coating, creating surfaces that were not homogeneous and interfered with the fabrication of regularly ordered structures. On some samples there were localised areas where the pattern was well-formed but, over the entire surface, patterns lacked order and there was a great deal of variation in pillar diameter and spacing. High voltages meant that sometimes there was localised discharge across the surface and this limited the reduction in electrode spacing (around 1 µm) that could be used. Furthermore, as the electrode spacings became smaller more problems with defects and dust naturally occurred. The fabrication parameters and resulting wavelengths for all the surfaces shown above are given in Table 3.1 (a full table of the gathered data is given in Appendix C.

3.3.4 Star burst shapes and travelling pillars

In a small selection of experiments, with smaller electrode gaps, starburst patterns (Figure 3.26 A, B, C and D) and pillars with trails (Figure 3.26 E and F) appeared. These experiments generally had an electrode gap of approximately 3.5 µm or less. Examination of the two electrodes showed that the pillars travelled laterally whilst in contact with both electrodes. The star burst shapes seemed to have evolved where several pillars in a roughly circular shape had bridged the electrode gap, and had then spread out into a circle of a larger diameter. From their appearance, it seems that the pillars repelled one another, but also some of the pillars have trails showing that their direction of movement appears to be more random.

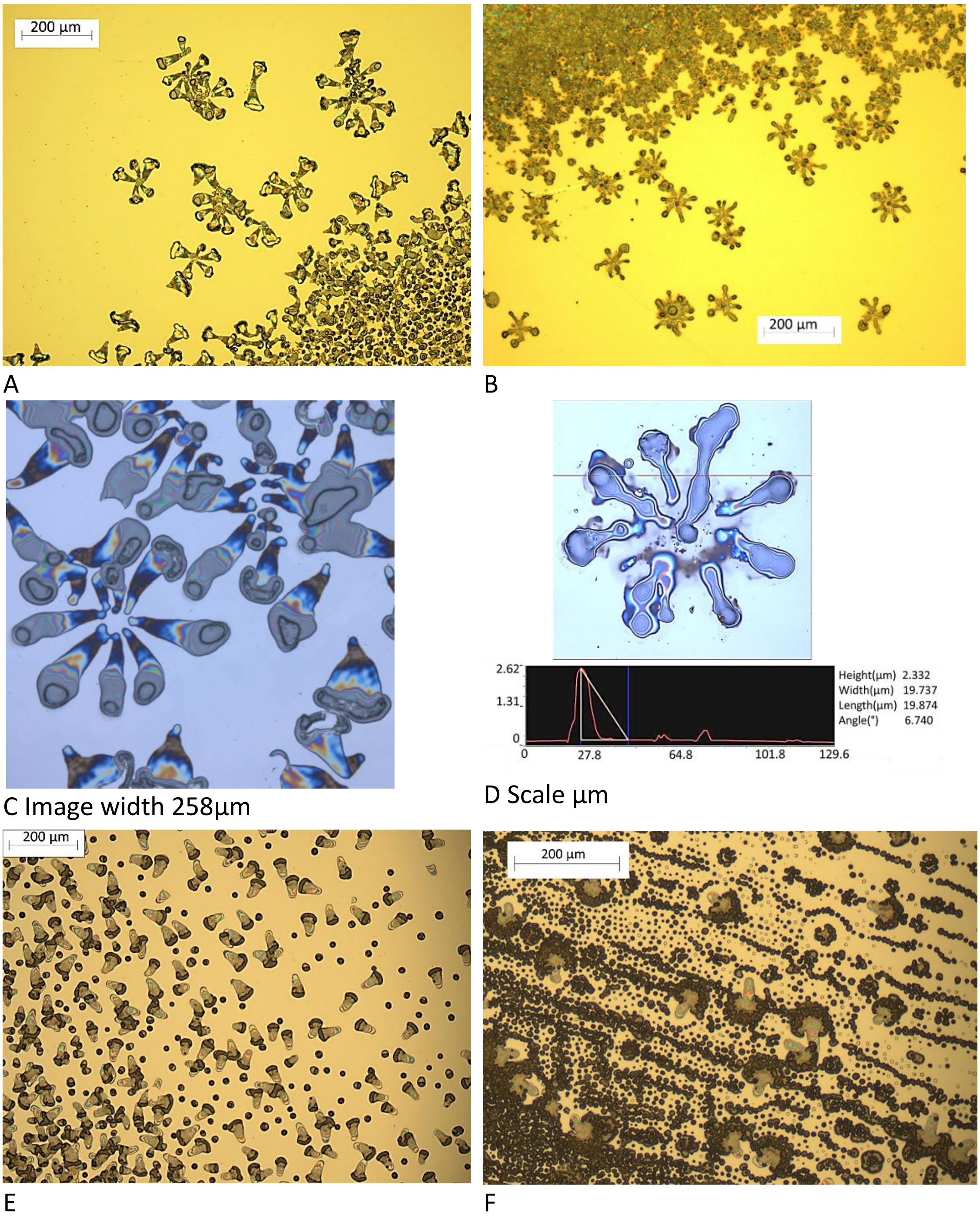

A

B

C Image width 258µm

D Scale µm

E

F

Figure 3. 26 Star bursts and travelling pillars. A. The optical micrograph of a surface containing star bursts with the associated LEXT plan view of the same surface in C below. B. An optical micrograph of a second surface of star bursts with the associated LEXT 3D scan in D below. E and F optical micrographs of 2 surfaces with travelling pillars.

At the base of each trail, what appears to be the imprint of the initial site can be seen as a small paler circle at the start point. The trails then increase in width along their length. This pattern could have been because they started to move as soon as the tip of the pillar touched the top electrode and then widened as they moved due to collecting epoxy material as they travelled laterally along the electrode surface.

The source of the force to move them could have been due to a build-up of charge on their surface which eventually created enough repulsive force to propel them away from one another. The increase in current that was observed when the pillars bridged the electrode gap could indicate that there were mobile charges present in the material. This concurs with results found by (Nixdorf & Busse, 2001) who found that the conductivity of epoxy resin dropped during polymerisation.

The movement of the pillars during fabrication is not a phenomenon that to the author's knowledge has yet been predicted by theory or reported in other studies. If a wider range of materials were to be patterned by EHD it seems likely that amongst them would be others that would show this kind of behaviour and so it would be needed to be included in modelling especially when small electrodes gaps were being used.

3.4 Air conduction experiments

The source of the current flow when the electrode spacing was very small, was investigated by recording the current flow between electrodes in an environment that was under a vacuum and one which contained air. If conduction through the air was occurring, then the current should drop when the electrodes were placed in a vacuum. Two electrodes of the same style used in the EHD experiments minus the epoxy layer, were connected to a 162V source and placed in a vessel which could be evacuated and then re-pressurised. The vessel was evacuated and then re-pressurised at varying intervals and the current recorded.

Figure 3.27 A shows the current observed when the vessel was first evacuated and then air let in slowly over the first 18 s, at which point the valve was fully opened. At 28 s, the vessel was again evacuated and the re-pressurising valve was opened slowly and then fully at 45 s. The current ranged from 6.5 to 10.1 µA.

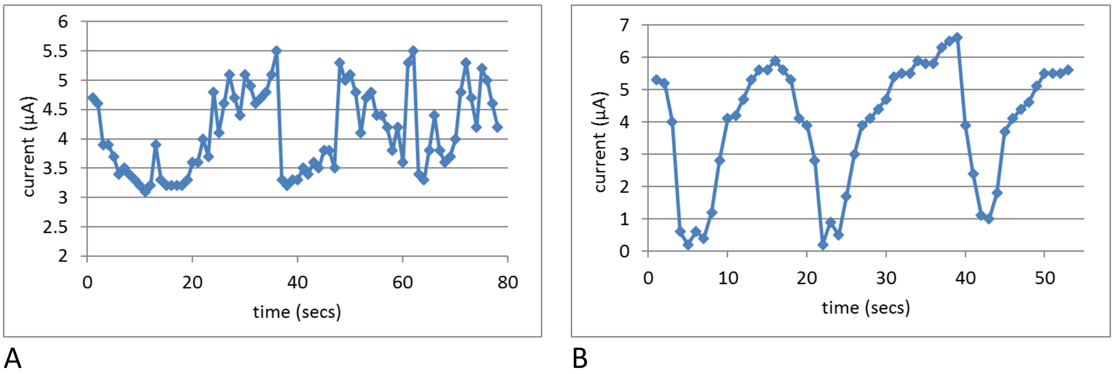

Figure 3. 27 Air conduction experiments showing electrical conduction (A) over time.

Figure 3.27 B also shows current flow recorded during a similar experiment. The first part of this recording was taken at the start of evacuating the vessel. When a change in the current was observed, at the point that the vessel was fully connected to the vacuum, the chamber was isolated, and an air admission valve was opened. Once the current had increased (at 16 s) the vessel was re-evacuated and then re-pressurised at 24 s. This cycle was then repeated once more. The current varied from 0.2 to 6.6 µA.

Whilst not being conclusive, a change in the current was observed with a change in the environment although the conduction route could come from dust or other particles rather than through the air itself. However, this does provide evidence to support the view that there is a small discharge through the air under normal fabricating conditions.

3.5 Transmittance Spectra

The objective of using the EHD patterns as absorbing surfaces was investigated using the IR spectrum, since in most cases the scale of the pillar surfaces produced was large in comparison to the wavelength of optical or UV radiation. A number of the most regular surfaces shown above were moulded in PDMS. The moulds were used to replicate the surface in various materials (such as epoxy, PS and PMMA), using modified printing techniques and embossing, on several substrates.

The surfaces were replicated in epoxy on NaCl disks using the printing method set out in the Experimental Chapter 2 section 2.6 and transmittance spectra in the IR spectrum were taken. A plain epoxy layer was fabricated in the same way as the patterned surface but instead of a patterned mould, a flat PDMS disk was used. IR transmission spectra from 600 to 4000 wavenumbers cm^{-1} were taken. The chemical absorbtion due to molecular bonds and functional groups can be seen in the spectrum, such as the peak at around 3200 cm^{-1} which is characteristic of OH bonds. However, the overall structure of a patterned surface would cause a change in the general curve of the baseline and it can be seen that the overall baseline is different for the patterned epoxy compared to the unpatterned one. General scattering from the patterned surface would produce a spectrum with the same baseline as the plain surface but lower transmission. However, the spectra shown by some of the surfaces displayed a change in the baseline to particular shape which implied that there was an interaction between the structured surface and the IR radiation which was wavelength dependent.

The IR transmittance spectrum, of a printed surface together with a plate epoxy layer for comparison is shown in Figure 3.28 A. A 3D image of the printed surface used, is shown in Figure 3.28 B and a top down image of the same surface is shown in Figure 3.28 C. The spectrum from the patterned surface shows a lower transmission than the plain epoxy. The overall shape of the spectrum is a curve centred around 1700 cm^{-1} (5.8 µm).

The overall concept was to create surfaces that had a pillar spacing that would be comparable to the wavelength of radiation of interest. The wavelength of the surface which produced the above spectrum was much larger wavelength than 5 µm so other features which can be seen on the surface could have been responsible for the interaction.

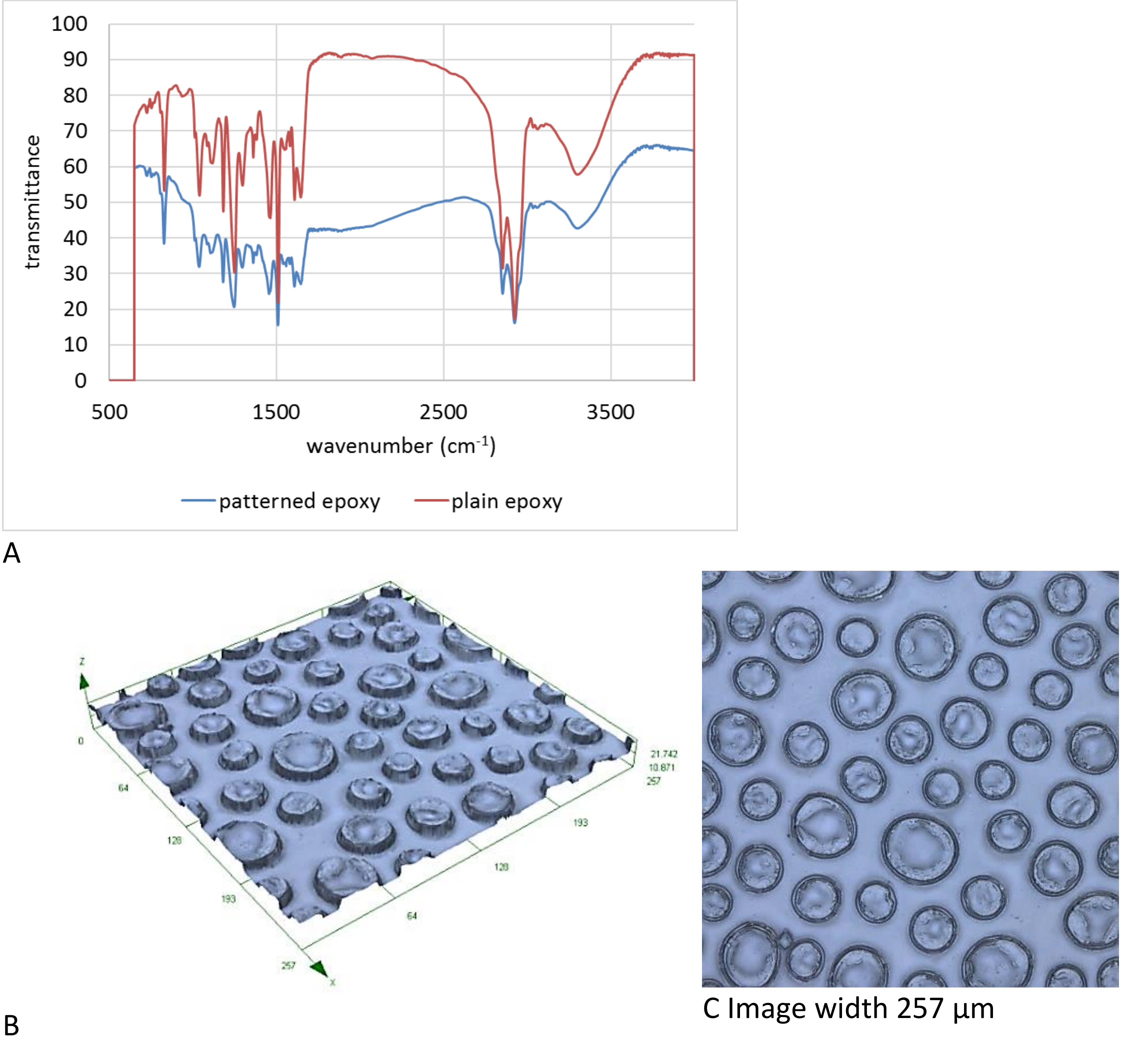

C Image width 257 µm

Figure 3. 28 A shows an FT-IR transmission spectrum of a print of the surface shown in Figure 3.12 B. The LEXT confocal 3D scan of the printed surface is shown in B and a LEXT optical micrograph plan view of the same printed surface is shown in C.

Figure 3.29 A. shows the spectrum in for the patterned surface shown in Figure 3.29 B (also shown below in also Figure 3.20) which also shows a baseline that is different to the plain epoxy. From the spectrum it seems that the wavenumber range that interacts most with the surface features is between 2500 and 4000cm^{-1} (a wavelength of 4 to 2.5 µm). The diameters of pillars on this surface have a large range, from around 20µm to around 31µm with an average of 27µm. The average centre to centre pillar spacing is 42µm. These values are smaller than the average spacing of the surface in Figure 3.28 above which is 54µm, whilst the average diameter of the pillars on this surface is similar at 29µm. The smaller centre to centre spacing is consistent with the shift in interaction towards the higher wavenumbers that is seen in the IR spectra for the surface.

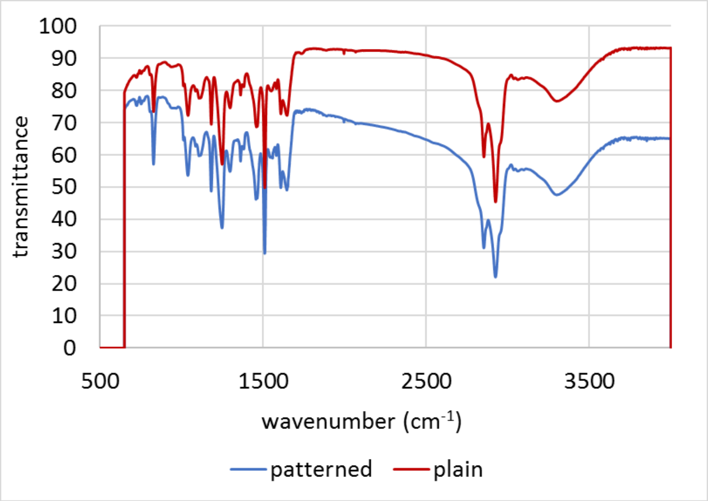

A

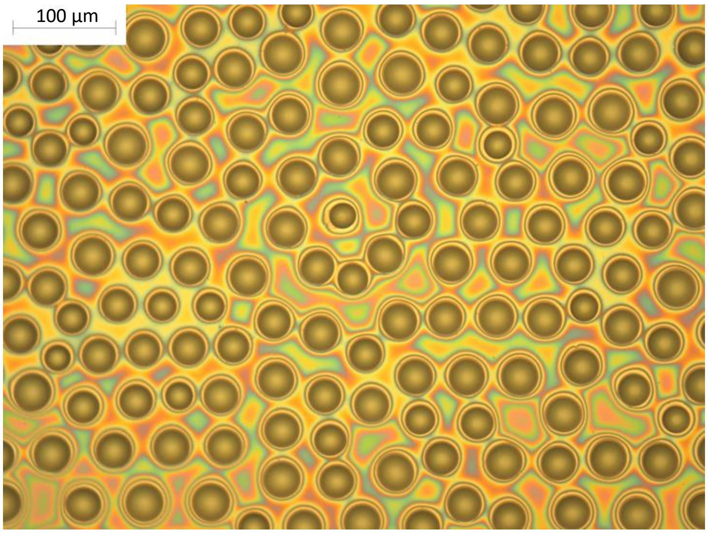

B

Figure 3. 29 A. FT-IR surface from Figure 3.20 and B. an optical micrograph of the same surface

The transmission spectrum curve from the patterned surface shown in Figure 3.30 A shows a trend downward as the wavenumber increases and potentially means that the wavelength of greatest interaction is above 4000 wavenumbers cm^{-1} (2.5 µm). This again is consistent with scale of the patterned surface that was used to create the spectrum. The pattern of the surface is shown in Figure 3.30 B and it can be seen that the features are smaller again than those shown above and that the gaps between some of the structures are as small as 2µm.

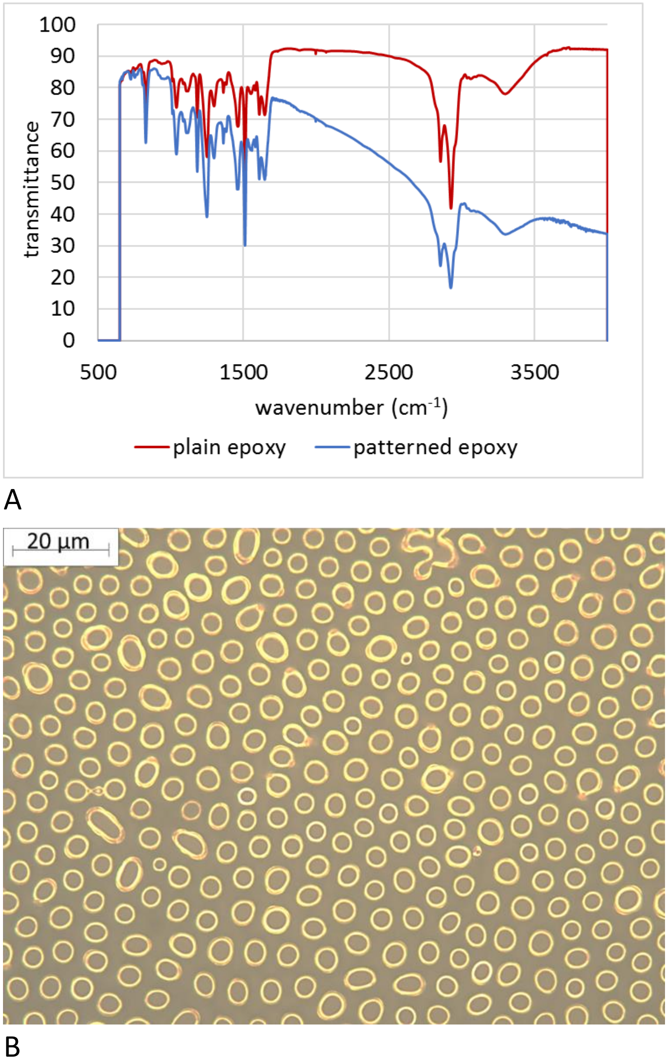

Figure 3. 30 FT-IR spectra for the surface in B (scale bar 20µm).

Since the objective was for the structured surfaces to interact with shorter wavelength radiation several of the surfaces with smaller structured patterns were also printed in epoxy onto NaCl disks. Their IR spectra were taken in the same way as those above, but these showed ambiguous results. Between wavenumbers of 600 cm^{-1} to 4000 cm^{-1} (16.7 to 2.5 µm wavelength) these surfaces produced spectra that were characteristic of general scattering in that the baseline had lowered, but the overall shape of the baseline was the same as for the unpatterned surface.

The surface shown in Figure 3.25 A (replicated here in Figure 3.31 A) did display some interaction with wavenumbers between 6000 cm^{-1} and 11000 cm^{-1} (1.7 to 0.9 µm so shorter wavelengths) shown in Figures 3.31 B and C. The transmittance spectrum in Figure 3.31 B, is for the surface printed in epoxy onto a quartz glass microscope slide, compared to an unpatterned epoxy film and plain quartz glass; Figure 3.31 C shows the same surface imprinted into PS on a plain glass slide in comparison to an unpatterned PS thin film on the same substrate and also the plain substrate. The spectrum in epoxy on quartz lowers steadily from 0.8 to 0.6 whereas the spectrum in PS on plain glass lowers from 0.7 to 0.65 in a steady curve to around 10500 cm^{-1} when it appears to begin to rise again.

The surface shown in Figure 3.31 A did appear to contain features in the range of 1 to 2 µm which could account for the interaction with the higher wavenumbers (shorter wavelengths), but the overall pattern is very random and chaotic. The profile of the surface features is also very shallow (i.e. they are below around 2 µm in height). The fact that overall shape of both spectra is somewhat different could be because the pattern is not regular.

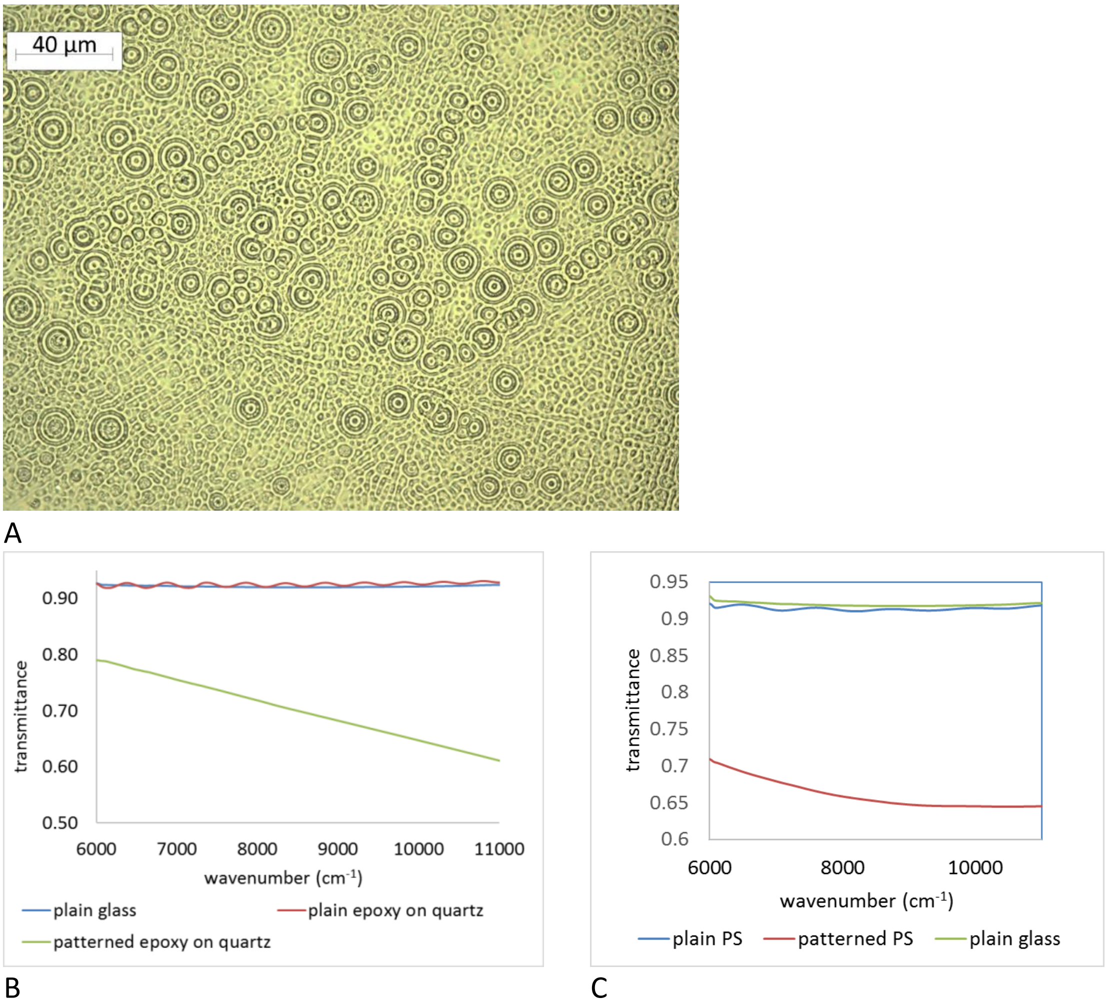

Figure 3. 31 A. EHD surface pattern for the spectra shown in B and C. IR transmission spectra of B. the epoxy patterned surface on quartz glass with plain glass and plain epoxy for comparison and C. and the PS patterned surface with plain glass and plain PS for comparison.

In general, the smaller structured surfaces lacked form and regularity and this is perhaps why they did not display an interaction which was wavenumber specific. It was initially supposed that the wavelength of the instability needed to be comparable to the wavelength of radiation for interaction to occur but the results support the expectation that the scale of the other features on the surface such as the gaps between the features and their diameter would also have an effect.

3.6 Diffraction patterns

The above spectra are a good indicator that there is interaction between the scale of the printed surfaces and specific wavelengths of radiation however the tests are not conclusive and other exploration is needed before definite assertions should be made. It could be possible that the surfaces are acting as diffraction gratings and diffracting a proportion of the investigation beam away from the detector sensor which would show as a reduction in transmission.

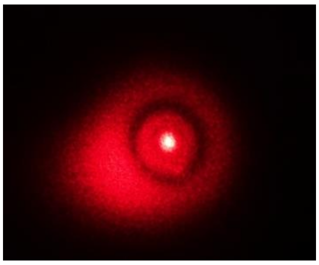

Figure 3. 32 Photograph of a diffraction pattern created by the beam of a red laser.

Diffraction again is wavelength dependent and initial exploration with a red laser did produce patterns which are indicative of diffraction although the wavelength is shorter. The beam of a red laser (of wavelength 633nm) was transmitted through the mould of the surfaces shown above and some of the surfaces displayed the pattern of concentric circles which is characteristic of diffraction. The diffraction pattern for the surface shown in Figure 3.29 B is shown in Figure 3.32 where 2 dark rings and 2 red rings surround the central spot of the main beam. The diffraction rings that are produced are also indicative of the regularity of the pattern.

3.7 Tissue culture surfaces

Micro structured surfaces are employed in a large variety of applications and the versatility of the pillared surfaces produced by EHD patterning would be a great advantage of the technique. The ability of the EHD technique developed here to be utilised for other purposes was explored by using the prepared samples as tissue culture surfaces. They are more frequently being used as tissue culture substrates since they benefit the in-vitro growth of cells in several ways. Traditionally, cells are grown in monolayers on flat tissue culture plates, which is very unlike the conditions in the living animal. The morphology of cells grown in this manner can be very different to that of living tissue. This has wider implications for the validity of using these methods as models for living tissue, since the morphology of cells has been shown to have an effect on their gene expression and cell to cell interaction (Kim, et al., 2010) (Rashidi, et al., 2014).

Structured surfaces can guide the morphology of the cell to become more like that found in living tissue. Structured surfaces, that are used for tissue culture, have features in the micro and nano range which is comparable to the size of the cells grown. Pillared surfaces are used in tissue culture for a variety of reasons including the study of the contractile forces within the cell, cell motility and they have been found to both aid and prevent the adhesion of cells (Rodrguez, et al., 2014) (Sohol, et al., 2011). Since the structures of the EHD fabricated surfaces were on a comparable scale to that of many cells they were replicated onto glass slides and were investigated for use as tissue culture substrates.

The results summarised here were published and the full document can be found in Appendix D. The smallest scale surface used was that of the pattern shown in Figure 3.31 A. The surface structures were below 2 µm in height and the pillars and other features were as small as around 1 µm in diameter. This is very much smaller than the cells themselves that are roughly elliptical and have a length of around 50 µm. This surface appeared to have no effect on the growth of the cells and their morphology was no different to that exhibited when they were grown on a flat tissue culture surface (Trease, et al., 2016).

The surface shown in Figure 3.30 was also used to fabricate a tissue culture surface in PMMA. The scale of the structures was larger, with the columns having a diameter of approximately 7 µm and a height of approximately 4 µm. In Figure 3.33 A and B it can be seen that the cells adhered well to the flat unpatterned polymer but did not adhere to the pillared areas (Trease, et al., 2016).

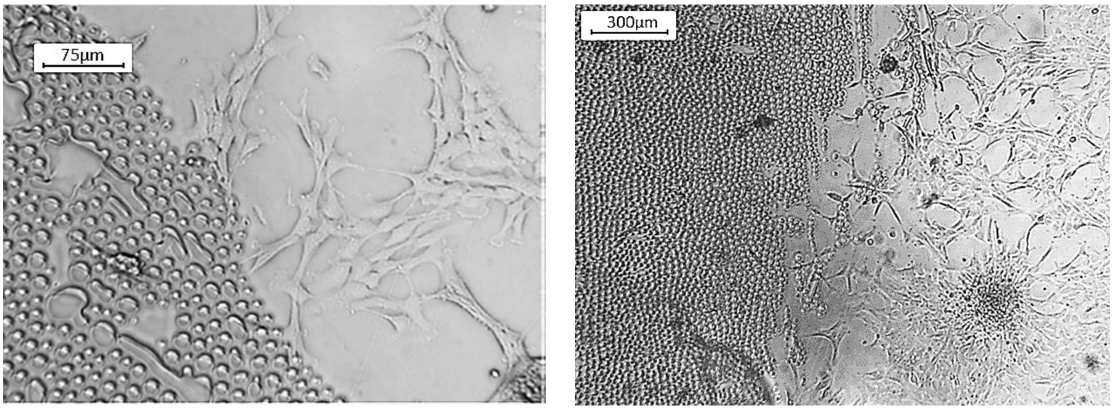

A B

Figure 3. 33 A and B Optical micrographs of lens epithelial cells cultured on EHD patterned hot embossed PMMA scale bar 75μm, scale bar 300μm (Trease, et al., 2016).

The surface shown in Figure 3.29 (also Figure 3.20) was fabricated in PS on glass for tissue culture. The profile of the structures on this surface are rounded as can be seen in Figure 3.20 B and so do not have a flat top. The cells appeared to be guided by the mounds on the surface (Figure 3.34 A and B) and many became elongated (Figure 3.34 A) in comparison to the normal morphology of lens epithelial cells growing on flat tissue culture plates (Figure 3.34 C and D).

Ordinarily the cells are non-adherent to a flat untreated PS surface however in these experiments the cells seemed to proliferate to full confluency (i.e. when the cells have completely covered the growth surface) and, whilst the area in between the mounds was the glass slide substrate, the cells did not seem to preferentially adhere to these areas as would be expected.

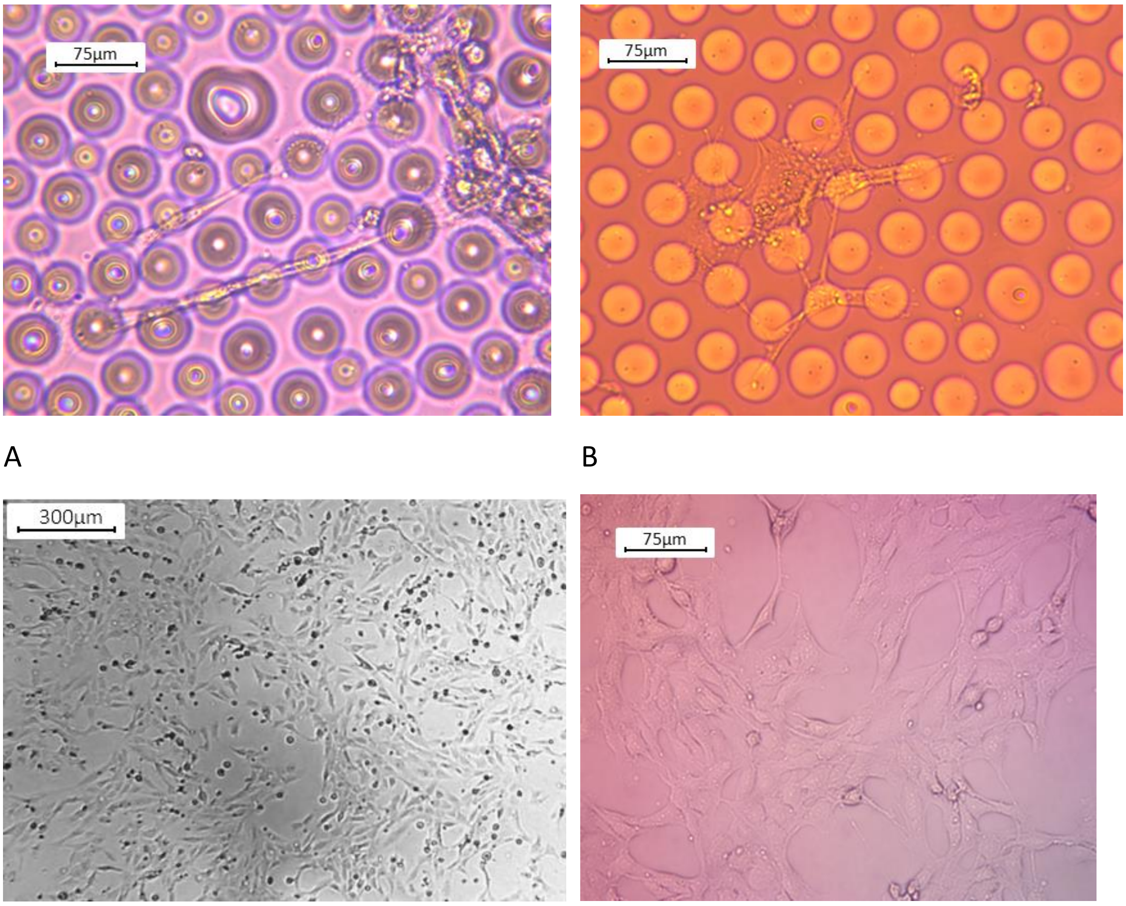

A B

C D

Figure 3. 34 Optical micrographs of A. and B. Lens epithelial cells growth on structured PS surface. C. Lens epithelial cells grown on a flat tissue culture plate. D. close-up of lens epithelial cells grown on a flat tissue culture substrate (Trease, et al., 2016).

A second cell line with a different morphology was also assessed. Typically, on flat tissue culture surfaces (plasma treated PS), Hep G2 cells (liver carcinoma cell line) grow in agglomerations (Figure 3.35 A). On epoxy resin they grew as separated cells and appeared to adhere more to the epoxy surface than the tissue culture surface. This meant that they interacted well with the structured surfaces when grown on EHD patterned substrates (Figure 3.35 B) (Trease, et al., 2016).

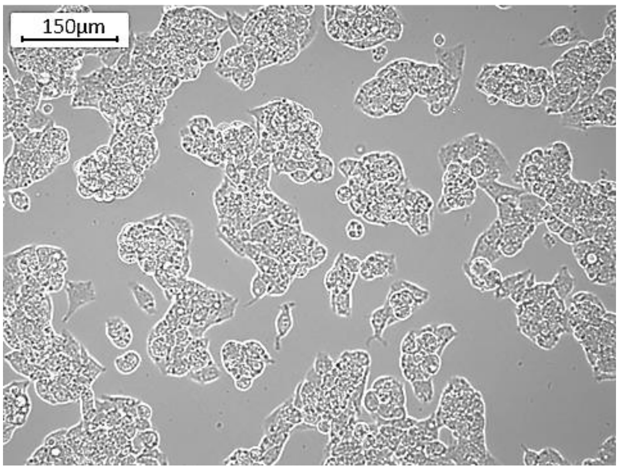

A. Optical micrograph of Hep G2 cells grown on tissue culture plate

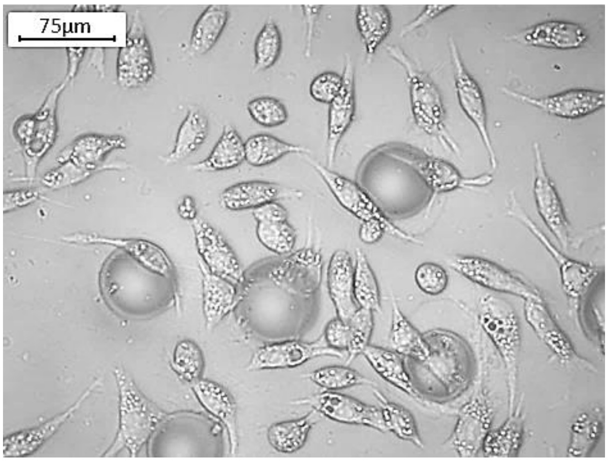

B. Optical micrograph of Hep G2 cells grown on EHD patterned epoxy scale bar 75µm

Figure 3. 35 Hep G2 cells showing the change in morphology and surface interaction.

4. Discussion and conclusion

4.1 Experimental results compared with theory

Since the development of EHD instabilities as a process for micro- and nano-patterning, several methods for modelling the systems have been proposed and we discuss some of them here. The centre-to-centre pillar spacings of the epoxy surfaces fabricated in this study were analysed in order to compare them to the wavelengths predicted using several theories for the associated experimental parameters. The lengths of 30 random centre-to-centre spacings of next-neighbour pillars on the fabricated surfaces were recorded. The average value of these spacings was used as the characteristic wavelength of that surface.

The characteristic wavelengths were compared with the wavelengths predicted by the perfect dielectric model proposed by Schäffer and the perfect and leaky dielectric models proposed by Pease and Russel under several conditions. In the perfect dielectric models, the polymeric material is modelled as a dielectric insulator with no flow of charge. In the leaky dielectric model developed by Pease and Russel the polymer is modelled as leaky by allowing small amounts of charge to flow through the material and accumulate at interfaces. These models have been used by several different groups, since they provide straightforward equations to use that have been stated explicitly to predict the wavelength of a surface using a given set of parameters (Goldberg-Oppenheimer, 2011) (Voicu, et al., 2007) (Bae, 2012) (Wu, et al., 2006) (Goldberg-Oppenheimer, et al., 2011) (Wang, et al., 2014).

Comparing the experimental results from this study with those given by the models has provided insight into the formation mechanism and gives a better understanding of the dielectric behaviour of the epoxy polymer. Understanding the formation mechanism helps to design experiments which would result in the fabrication of surfaces with the geometries that are required for use as solar selective or antireflection coatings. Figure 4.1 shows the comparison between the predicted values from all the three theories outlined above using the lubrication approximation and our data. The wavelength predicted by Schäffers perfect dielectric model was obtained by using equation (1.17). The predicted wavelengths for the perfect and leaky dielectric models proposed by Pease and Russel were obtained from using equations (1.21) and (1.25) respectively.

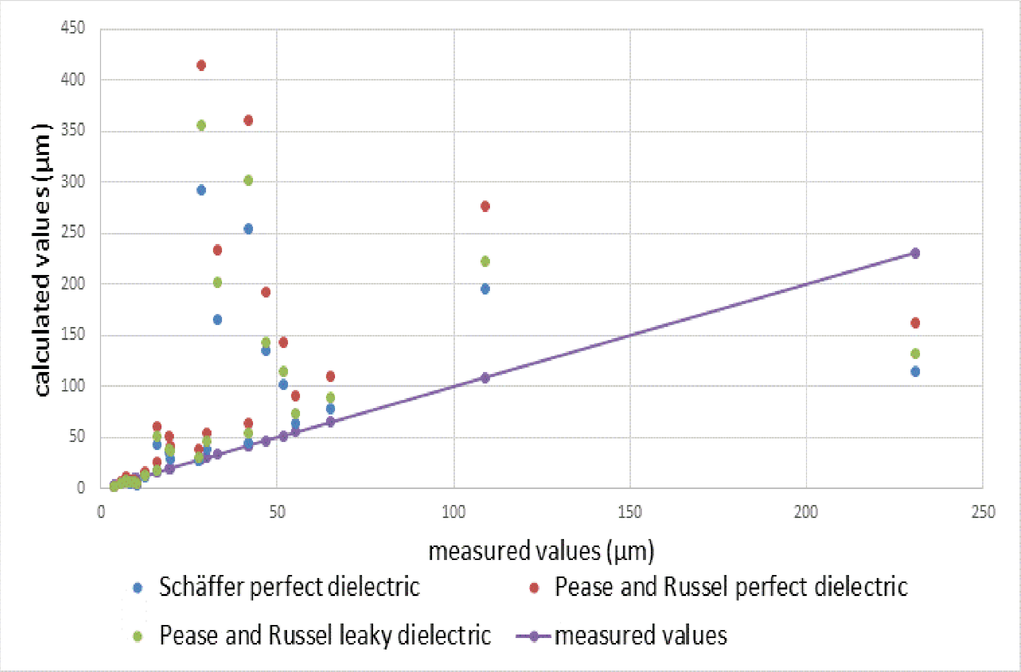

Figure 4. 1 Graph of measured wavelengths from the fabricated epoxy surfaces compared with those predicted by theory for the associated experimental parameters.

For over a half of the surfaces produced experimentally, all these models agree reasonably well with the measured wavelengths. For the surfaces where the wavelengths are over 15 μm the measured wavelengths overall tend to be smaller than those predicted by these theories shown by the straight line and in several cases the ratio of the measured and predicted values is very large (up to 14). Below 15 μm, the difference is less but with experimentally derived data being both larger and smaller than the theoretical predictions (see Figure 4.2).

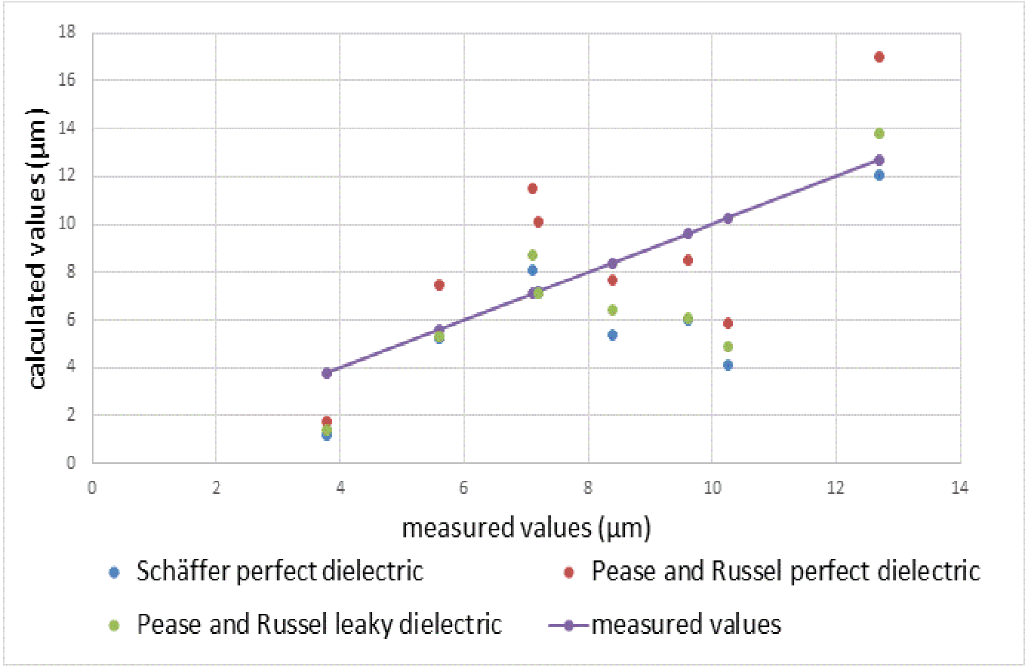

Figure 4. 2 Graph of measured wavelengths below 15µm from the fabricated epoxy surfaces compared with those predicted by theory for the associated experimental parameters.

Several papers have identified that the arbitrary application of these models to experimental analysis may not justifiable. Many assumptions were made in the formation and simplification of the theories which may invalidate the models for certain experimental conditions. Although the experimental results shown here are mostly within a factor of 2 times the predicted values, the lack of absolute corroboration with the theory means that particular care had to be taken to validate the application of these models. The parameters that have been examined are detailed here.

4.2 Perfect dielectric models with the lubrication approximation

Our results have been compared to two models assuming a perfect dielectric, and for clarity the results of just the perfect dielectric models shown in Figures 4.1 and 4.2 can be seen in Figures 4.3 and 4.4. Figure 4.3 shows results for all the fabricated surfaces and Figure 4.4 shows just the surfaces with wavelengths below 15 µm.

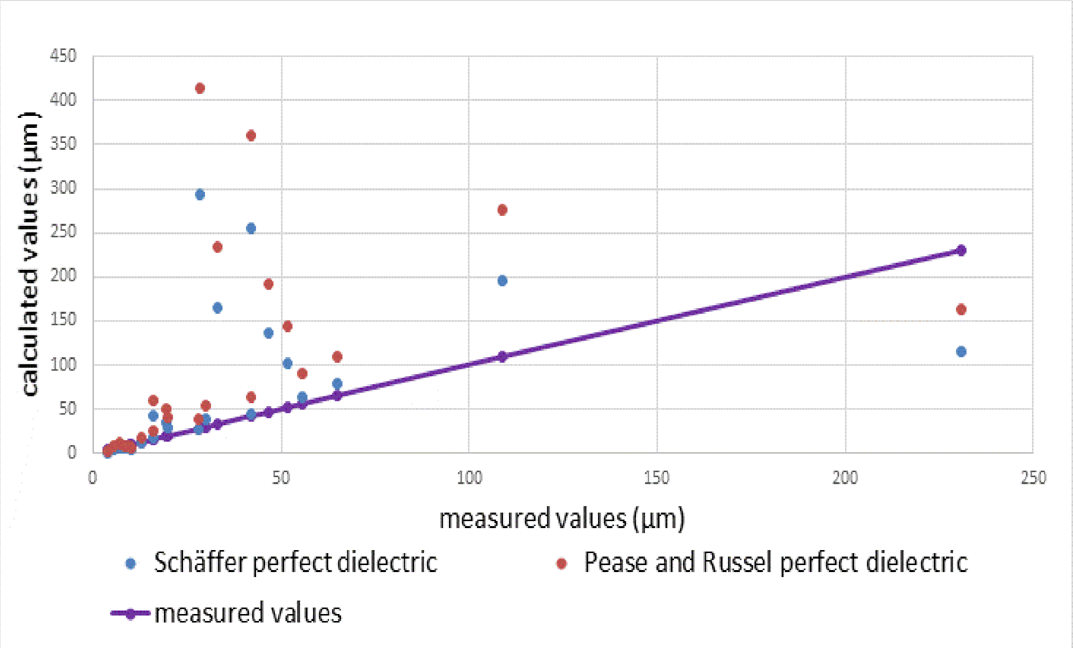

Figure 4. 3 Average measured wavelengths for all epoxy surfaces compared with those predicted by perfect dielectric models.

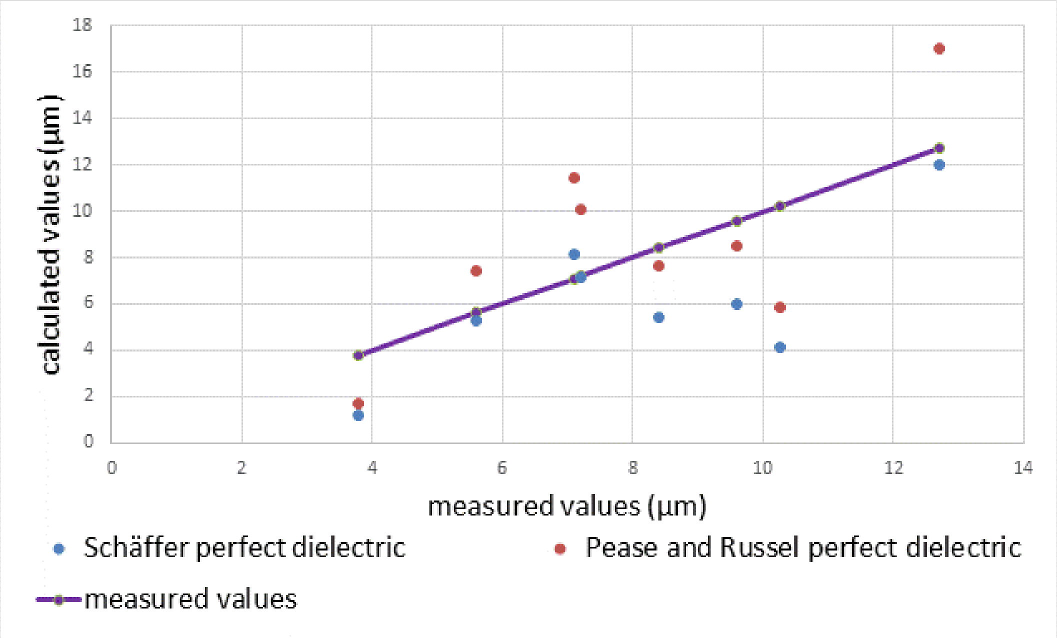

Figure 4. 4 Average measured wavelengths for epoxy surfaces below 15µm compared with those predicted by perfect dielectric models.

The relative permittivity of the epoxy started at a comparatively high value of approximately 9 and reduced over time as the material cured. When a material behaves as a perfect dielectric, i.e. when there is no flow of charge or charge accumulation at the polymer/air interface, the wavelength of the surface which is fabricated is determined by the difference in the permittivity of the polymer and the gap material (for the experiments in this study this was air). Pease and Russel demonstrated that this ratio must be large for the smallest wavelengths and pillars to be fabricated. However, the reduction in the wavelength size that can be achieved by increasing the relative permittivity of the polymer, decays exponentially as the relative permittivity increases (Figure 3.3). The graph in Figure 3.3 shows that above a value of around 4-5, an increase in the relative permittivity of the polymer has very little effect on the reduction of the wavelength.

Initially it was assumed that the epoxy polymer used in this study would behave as a perfect dielectric, since epoxy resin is generally considered to be an insulator, and the high value of the relative permittivity would have been an advantage to using this material. However, analysis of the experiments showed that it was likely this was not the case: from the observations of the current flow, it would seem that this material was behaving as a leaky dielectric. This would have partially cancelled the potential benefit of the high relative permittivity of the material (although theoretical studies have shown that leaky dielectrics have the potential to produce even smaller scaled wavelengths).

4.2.1 Schäffer’s perfect dielectric under a lubrication approximation

Schäffer's perfect dielectric model (outlined in Chapter 1 Section 1.3.2) is based on the principle that the patternable polymer does not conduct charge and that only polarization charges are responsible for the instability. The model also assumes that the waves which form have long wavelengths in comparison with the electrode gap and polymer film thickness, an assumption which has been termed the lubrication approximation.

Schäffer’s practical experiments differed from epoxy experiments performed in this study in several ways; very small electrode gaps and very thin polymer layers, often below 1 μm were used, resulting in comparatively large wavelengths. In Schäffer’s experiments for example, an electrode gap of 1.28μm resulted in a wavelength of 16.3μm, and an electrode gap of 0.39μm resulted in a wavelength of 3μm using 50V and 40V respectively (Schäffer, et al. 2001). Both wavelengths are much larger than the electrode gap (12 and 7 times larger) and the structures would be more accurately described as disks rather than pillars. In these cases, the assumption that the wavelength is much larger than the electrode gap is valid.

The scales of many of the epoxy experiments carried out in this study were very different, since the epoxy and electrode gaps covered a much greater range of thicknesses from just below 1 μm up to approximately 40 μm. These values are large in comparison to Schäffer's thicknesses and also those of many other experimental groups working in this area. Furthermore, in several of the epoxy experiments carried out in this study, the scale of the instability (or wavelength) was comparable to, or within a factor of 2 of the electrode gap. For example, an electrode spacing of 26μm produced a wavelength of 28μm using an applied potential of 162V. Thus, we should examine whether the lubrication approximation is valid. Although the spacer and polymer thickness were larger than those of many other groups, they are still not yet within the gravity regime where gravitational effects have a large enough influence to be considered in the equations, for this to be the case the electrode gap and polymer thickness would need to be in the order of mm so this has not been considered to contribute to the difference.

In Figures 4.3 and 4.4, which show just the perfect dielectric models it can be seen that, in general, Schäffer's perfect dielectric model fits our data better than that of the perfect dielectric model of Pease and Russel. Data from Pease and Russel's leaky dielectric model is also shown in Figures 4.1 and 4.2. Both Pease and Russel's models and Schäffer's model assume the lubrication approximation, but of the theories that make this assumption, Schäffer's perfect dielectric model is closest to the results from experiments in this study. When comparing their model to that of Schäffer, it was noted by Pease and Russel that Schäffer's model appeared to agree better with experimental results from other groups. Schäffer's model predicted results which also agreed very well with his own experimental results (Pease & Russel, 2004).

Despite the better fit with Schäffer's perfect dielectric model, the observation of current flow through the capacitor, when pillars were in contact with both electrodes and its subsequent disappearance when the epoxy had cured, implies that the epoxy was not in fact behaving as a perfect dielectric. It is likely that this contributes at least partly to the difference between the measured data and these models, especially considering the fact that the lubrication approximation is unlikely to be valid (discussed later in this section).

4.2.2 Pease and Russel perfect dielectric model with the lubrication approximation

Pease and Russel's model, outlined in Chapter 1 section 1.3.3, gave explicit equations (1.21) and (1.25) for both a perfect dielectric and a leaky dielectric case, and again these were easy to use to obtain theoretical results to compare with our fabricated surfaces using the corresponding experimental parameters. Their model included the leaky regime since it had become apparent that when thermoplastics (PS and PMMA for example) were used at high temperatures they were more capable of conducting current, although they were traditionally thought of as insulators. Furthermore, the use of other liquid materials which could have other electrical properties meant that a more comprehensive model would be required.

The Pease and Russel model has similarities to Schäffer's although most significantly the model allowed the conductivity of the polymer to be altered. It could range from a material acting as a perfect insulator to a perfect conductor which enables a greater range of materials to be modelled.

Models of EHD patterning needed to include the dielectric having a very small flow of charge, along with the associated accumulation and distribution of mobile charges which gather at the interfaces, especially at the polymer and air gap interface. Again, a lubrication approximation was assumed. The presence of electrical charges at the interface alters the surface tension of the polymer, which is termed 'electrocapillarity' (Chakraborty, 2014). To encompass this effect, the models assumed that the electrocapillary length, and hence the scale of the instability, was large in comparison to the vertical dimensions of the experiments (i.e. the polymer thickness and electrode gap).

However, similarly to Schäffer's perfect dielectric model, Pease and Russel's perfect dielectric model assumed that charges were not permitted to move through the polymer and it was polarisation displacement charging at the polymer/air surface that was deemed to cause an effective charge density. Unlike Schäffer's model Pease and Russel's used a Maxwell electrical stress tensor to define normal and tangential stresses at the polymer/gap material surface by using the electrostatic charge at the interface which was then combined with the fluid dynamics to predict the patterning behaviour.

From Figure 4.3 and 4.4 it can be seen that at larger wavelengths Pease and Russel's perfect dielectric model seems to be in the poorest agreement with our data, and their leaky dielectric model was closer to it, but not as close as Schäffer’s perfect dielectric model.

4.3 Leaky dielectric with the lubrication approximation

It had been shown that the inclusion of a small amount of mobile charge decreases the wavelength of the instability by a considerable amount. This was the motivation for Pease and Russel to develop a model which allowed for the movement of mobile charges in the polymer. In the perfect dielectric model the electric field in the polymer is different to that in the air. It is the difference in these two values, due to the difference in the relative permittivity of the materials and the height of the polymer/air interface and electrode heights, that creates a pressure at the interface and drives the formation of the structures.

In the leaky dielectric model proposed by Pease and Russel, the field in the polymer is neglected as it is assumed that none in the polymer exists due to the conduction of charges. The entire potential is modelled as being dropped across the air gap and the pressure at the interface is due to the interface spacing and the electric field in the air. The dielectric constant of the polymeric material has no impact on the wavelength of the structures when the material is modelled as a leaky dielectric and the parameter is not included for the equation of wavelength for a leaky dielectric.

A cured epoxy resin is considered to be a good insulator with a resistance of >10^{10} Ωcm (Masterbond, n.d.). In the experiments performed here the material is used in its uncured state and its dielectric properties are therefore different to that of the cured material.

From the observations of current flow during the experiments, two conduction regimes seemed to occur which seem to reflect data in the graph. When the spacer gap was large (above approximately 5µm) when the pillars had made contact with the top electrode, a current was observed to flow through the capacitor as discussed in the Results Chapter

3. This current reduced over the curing time of the epoxy. It is likely that ions remained in the epoxy resin as a residue from the manufacturing process, primarily Na^+ and Cl^-. In the uncured material, these would have been able to move quite easily in response to the applied potential causing the observed current flow. Once the material had hardened the ions would have been locked in place and the reduction in current flow at that stage reflects this. The earlier signs of charge transport imply the material should be considered as a leaky dielectric, and hence may have created smaller wavelengths than were predicted by theory.

Interestingly, a second regime was also observed during the experiments where a smaller spacer (approximately 5µm) was used. Current was observed to flow even before the pillars had contacted the top electrode. Further experiments indicated that this current could have been conduction through the air layer since the field in the layer was often higher that the breakdown voltage of air (using the simple calculation of the applied voltage divided by the electrode gap the general value was over $10MVm^{-1}$). This has also been considered as a reason that, at smaller intended wavelengths, the measured values are larger than the predicted ones.

The graph of the leaky dielectric model compared with the measured values is shown in Figure 4.5 and again for many of the fabricated surfaces there is good agreement between the predicted results and measured results. Where discrepancy exists, the measured results tend to be lower than those predicted by the theory even though Pease and Russel's model for a leaky dielectric predicts smaller wavelengths than their model for a perfect dielectric. The conduction of current implies the material is leaky although the Schäffer's perfect dielectric model still appears to fit our results better.

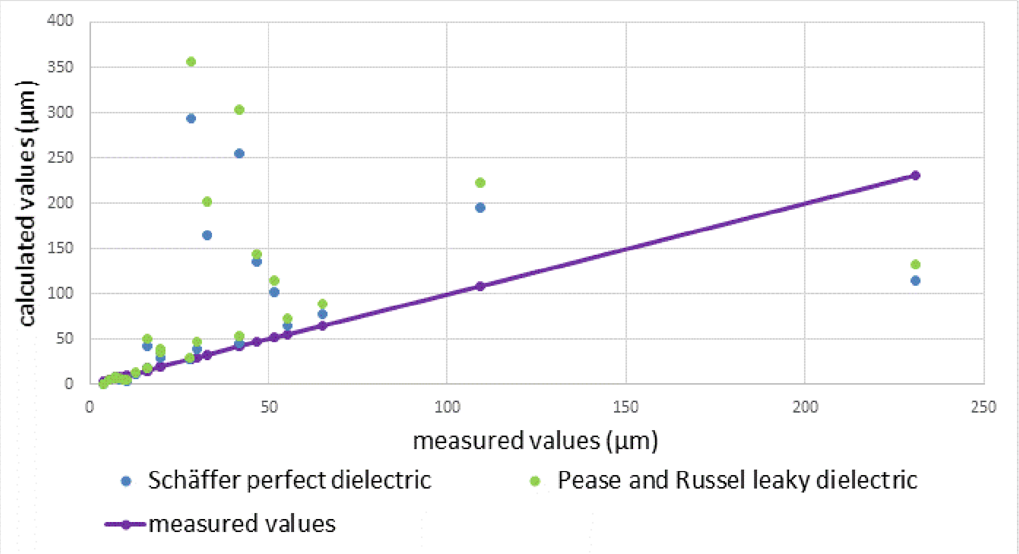

Figure 4. 5 Pease and Russel's leaky dielectric model compared with Schäffer's perfect dielectric model.

Due to the material behaving as a leaky dielectric the charge accumulation at the polymer/air gap interface has been found to decrease the wavelength of the instability in comparison to a perfect dielectric, models predict it will also increase the growth rate (Gambhire & Thaokar, 2012).

Pease and Russel assumed an electrostatic steady state in the leaky dielectric model. Further theoretical studies have shown that, when using a leaky dielectric model, a delicate balance exists between the charge accumulation time and the evolution time of the instability which in the model is related to the conductivity of the polymer (Gambhire & Thaokar, 2012). The rate of pillar formation depends largely on the strength of the field but it also depends on the viscosity of the fluid, so the interplay between process time (pillar formation) and conduction time can mean that a steady state is not actually achieved and this could cause discrepancy between the measured results and those predicted by theory as it could invalidate the electrostatic assumption (Gambhire & Thaokar, 2012).

High fields and low viscosity lead to short pattern formation times. If conductivity is sufficiently low, patterning can occur before charge has accumulated at the interface (Gambhire & Thaokar, 2012). In effect this means that the polymer is leaky but it has the potential to behave similarly to a perfect dielectric. Modelling has shown that the use of an AC potential with a frequency that is higher than the charge migration time of the polymer enables that a polymer of any conductivity can be made to behave like a perfect dielectric. Gambhire and Thaokar noted that the only way to truly realise a perfect dielectric system was to use an AC field with high frequencies, and so in practice all DC experiments should be modelled as a leaky dielectric system (Gambhire & Thaokar, 2012). In reality, it shows that the system is highly complex, involving many mechanisms that could contribute to understanding differences between theory and experimental results.

Schäffer's practical experiments used melted thermoplastic polymers (PS and PMMA) which resulted in long process times (the time it took for the patterns to form). Applying the potential for a duration of 24h was reported and so it was likely that a steady state could be achieved. The viscosity of the epoxy material used in this study was low in comparison to that of a thermoplastic melt and the fields used here were high. Thus, pillar growth generally took place immediately the potential was applied, and in many cases the entire area of the epoxy film was patterned within seconds. This effect can be seen in the time-lapse images shown in the Results Chapter 3 section 3.3.1

The field used in the filmed experiment was one of the lowest (6.5 MV m^{-1}) used and, despite this, pillars evolved immediately and the entire surface was covered within approximately 20 min of the application of the potential. Additionally, from values given in the literature, the conductivity of an uncured epoxy resin ($\approx 10^{-3}$ $(\Omega m)^{-1}$) (Nixdorf & Busse, 2001) is high in comparison to that of a polymer melt ($\approx 10^{-12}$ $(\Omega m)^{-1}$) (Schäffer, 2001), so although patterning took place very quickly it could be assumed that charge still had time to accumulate at the interface, and hence a leaky dielectric model would be more valid than a perfect dielectric.

Pease and Russel's perfect and leaky dielectric models considered many more aspects of the experiments which could influence the results such as the existence of an insulating oxide layer on the silicon substrate and the conductivity of the polymer. The complexity of the Pease and Russel models in comparison with Schäffer's indicates that many more materials and experimental characteristics need to be known to accurately model and predict the systems well, especially the conductivity of the polymer. Again, the fact that the lubrication approximation may not be valid could contribute to the difference between the predicted and measured values.

4.4 Difference between the models and measured data.

The modulus of the difference between the predicted results and the measured results was calculated as a percentage of the measured results. The percentage differences for the Schäffer perfect dielectric and Pease and Russel's perfect and leaky dielectric theories under the lubrication approximation (outlined in Chapter 1) vs the approximate electric field between the electrodes are shown in Figure 4.6. The electric field between the two electrodes was approximated by dividing the applied potential by the electrode gap. The value of the electric field between the electrodes is an approximation, since the actual value depends on how much of the gap is filled with the epoxy and whether the material is behaving either as a leaky dielectric or a perfect dielectric. The leaky dielectric model assumes the potential is dropped across the air gap alone, whereas the perfect model involves some of the potential being dropped across the polymer layer. The approximate value used here allows a comparison to be made between both leaky and perfect dielectric theories.

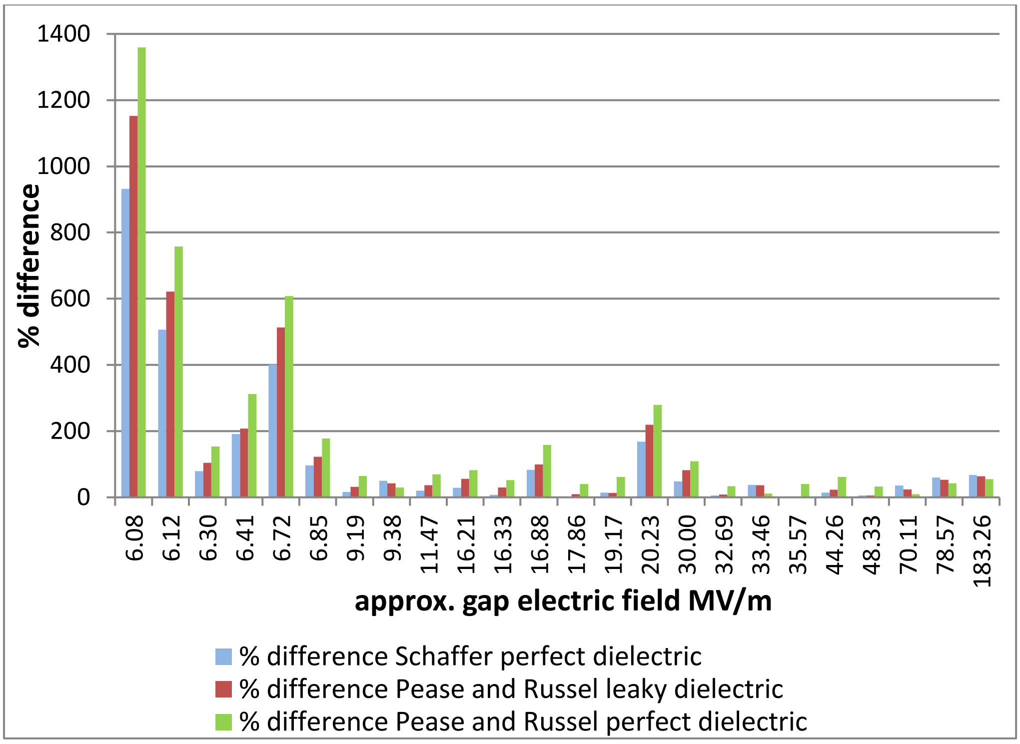

Figure 4. 6 The percentage difference between the measured values and the calculated values for all three theories shown vs approximate electrode gap field used in the fabrication of the surfaces.

When compared with our values, the Pease and Russel model for the perfect dielectric theory was the least accurate of the models, mainly because Schäffer's model predicted shorter wavelengths. However, at the shortest wavelengths our values were larger than those predicted and so their model was more accurate than Schäffer's for the same reason.

The equations used by Pease and Russel require many more parameters in the experiments to be known, such as the contact potentials. These values are not normally known with accuracy and, in the calculations made here, the contact potentials have been omitted. The applied voltage is very large and it was assumed that the effects of the applied voltage were far greater than those of the contact potentials although this may not necessarily be the case.

From Figure 4.6, it seems that the biggest differences between predicted and measured values were at the lowest electric fields. This is in contradiction to some of the predictions given in the literature, where it is proposed that higher fields would result the greatest differences between theory and experimentation (Lau & Russel, 2011) (Pease & Russel, 2004). At higher fields a wider spectrum of wavenumbers is capable of being amplified. This should result in a greater number of wavelengths being amplified on the surface; hence the difference between prediction and fabrication (Pease & Russel, 2004). However, the widening of the spectrum of amplified wavenumbers is also true of the leaky dielectric system which appeared to be the regime under which the polymer was operating, so this could account for the differences at the lower fields.

4.5 Relaxation of the lubrication approximation

The lubrication approximation is the most obvious caveat which means the models described previously are not appropriate for the experiments carried out here. Several groups have developed more generalised models which relax the assumption that the scale of the instability is much larger than the polymer film or electrode gap thicknesses. This resulted in some more complex models, for which explicit equations providing the wavelength of the fabricated surfaces, were not able to be developed. When certain assumptions were made however, these equations could be simplified to more explicit definitions.

Pease and Russel's model was generalised to enable the lubrication theory conditions to be relaxed, and this was done by altering the scaling used in the simplification of their model. In order to determine whether fabrication conditions fall under the lubrication approximation, Pease and Russel derived experimental conditions which must be met for both the leaky and perfect models. In general, if $(H/L)^2 << 1$ then the lubrication approximation holds, where $(H/L)^2 = (\varepsilon^g \varepsilon_0 X^2/\gamma H)$ where ε^g is the permittivity of the gap fluid, ε_0 is the permittivity of free space, X is the total potential, γ is surface tension and H is the electrode gap (Pease & Russel, 2004). This condition is defined by the electrode gap *H* and a representation of the electrocapillary length (*L*). The electrocapillary length is set by the voltage and the electrode gap, which means it scales with the field, a higher field resulting in a smaller electrocapillary length.

The inclusion of applied voltage, in the assumption of the characteristic electrocapillary length, makes the definition applicable to real-world experiments since these mostly include a voltage, in excess of 50V, across very small gaps. This is demonstrated by Schäffer's experiments where around 50V was applied across a gap in the region of nanometres. Although the electrode gaps used in several the epoxy experiments performed here are much larger than those of Schäffer, the applied potential is much higher, so the electrocapillary length is still small.

None of the experiments carried out in this study satisfied the condition above, which suggests a more generalized model should predict the results more accurately. It is difficult to satisfy this condition when an applied voltage much greater than a few volts is used, and Pease and Russel concluded that many of the previous experiments, including even those performed by Schäffer, may not be applicable for the lubrication approximation (Pease & Russel, 2004).

When the charge conduction is fast, the leaky dielectric growth exponent in the relaxed lubrication approximation model, can be simplified to a definition which can be used to compare the values in the experiments with the theory. This modified growth exponent *m* is given by (1.24).

The fast charge conduction condition is determined by the conductivity parameter (1.19) ($S = \sigma\mu\gamma H^3/ \varepsilon^{g3}\varepsilon_0^3 X^4$), which represents the ratio of the process time to the charge conduction time. When $S >> 1$, the condition is met and (1.24) can be used to model the data.

The growth curve m (1.24) was modelled using Mathcad software for the parameters associated with all the surfaces fabricated (an example worksheet is shown in Appendix E). The fastest growth rate wavenumber was then converted to its associated wavelength using the definitions set out by Pease and Russel (Pease and Russel 2004). Two methods for converting the fastest growth rate wavenumber were defined, for both a hexagonal packing pillar arrangement and a square packing pillar arrangement. The conversion for square packing is given by equation (4.1). When hexagonal packing is being modelled 2π is replaced by 4π/ ($3^{1/2}$).

$$\lambda = \frac{2\pi L}{k_{max}} \tag{4.1}$$

Where

$$L = \sqrt{\frac{\gamma H^3}{\varepsilon^g \varepsilon_0 \chi^2}}$$

and γ=surface tension (N/m), H = electrode gap (m), ε^g= polymer relative permittivity, ε_0= vacuum permittivity and χ= potential (V) (Pease & Russel, 2004).

The results are shown in Figure 4.7, compared with Schäffer's perfect dielectric model. Preliminary tests of the conductivity of the uncured epoxy gave the value as much lower than the literature at around $3*10^{-10}$ $(\Omega m)^{-1}$ (Nixdorf & Busse, 2001). The applicability of the fast charge growth exponent to the data gathered in the epoxy experiments was assessed by calculating the S parameter for the conditions of each experiment. If S>>1 then the model applies. The values connected by blue lines in Figure 4.7 are the experiments for which this model should be the most applicable however they appear to have the most discrepancy with our results. The S parameter is largely dependent on the electrode gap H, ($S=\sigma\mu\gamma H^3/ \varepsilon^{g3}\varepsilon_0^3 X^4$) and on the value of the potential χ. The highest values of S for our experimental parameters occurred when H was large and χ was small. This can be thought of as the conditions when charge conduction was fast in comparison to the process times and for these experiments the large electrode gap would have meant the longest process times. The discrepancy between our data and the model indicates that there are still variables within our experimental regime not accounted for in the models used.

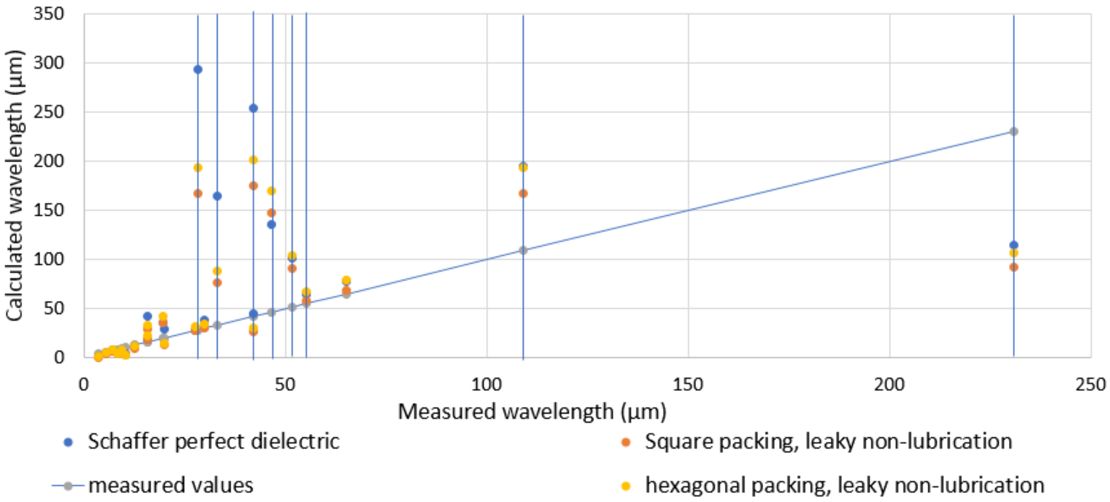

Figure 4. 7 Pease and Russel's relaxed lubrication approximation with fast charge conduction compared to Schäffer's perfect dielectric model.

Similarly to the models described previously, Figure 4.7 does show that the shorter wavelength surfaces were more accurately predicted by the non-lubrication theories than those that had longer wavelengths. At longer wavelengths, all the theories investigated here predicted larger values than those fabricated, and the theories that predicted the shortest wavelengths (the non-lubrication theories) showed better agreement. For surfaces with wavelengths below 15 µm the calculated values for the two non-lubrication models predict smaller spacings than those measured, and thus it appears that the perfect dielectric lubrication model fits better.

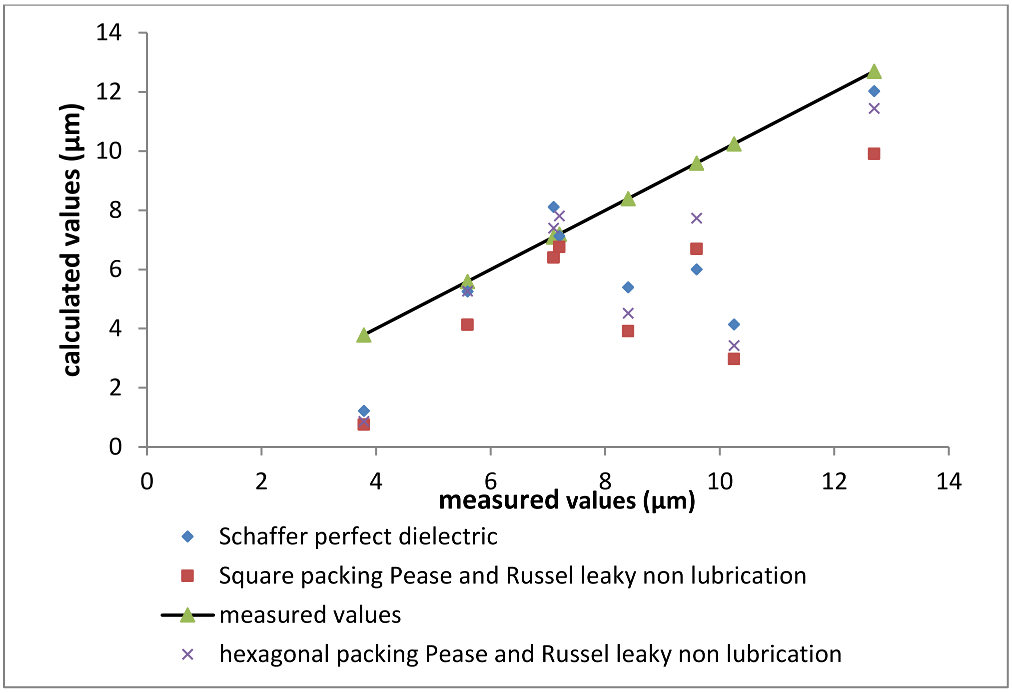

Figure 4. 8 Calculated vs measured values for surfaces with wavelengths below 15µm.

The percentage differences for the hexagonal and square packing conditions along with Schäffer's perfect dielectric are shown in Figure 4.8. The % difference between predicted and measured values for the models was within a factor of 2 (i.e. below 100% difference) for most of the samples. The square packing model appears to fit the better of the 2 non-lubrication models. On the surfaces where a good order can be seen the pillars are in a hexagonal arrangement. For many surfaces however, the packing appears to be neither hexagonal nor square and so the fit of either theory could be assumed.

For lower electric fields the non-lubrication models are in better agreement with the measured values than Schäffer's perfect lubrication model. As the value of the field increases, the perfect lubrication model fits better. This could be because at these higher values electrical breakdown in the layers is preventing the scale of the wavelengths decreasing, and so the perfect lubrication model, which predicts longer wavelengths, begins to agree better. Lau and Russel asserted that breakdown in the layers would most likely be a limiting factor in the reduction of the wavelengths that would be achieved using EHD, and stated that even though models predicted very small wavelengths, the experimental values rarely dropped below 1 or 2 µm (Lau and Russel 2011). The data here does appear to confirm this.

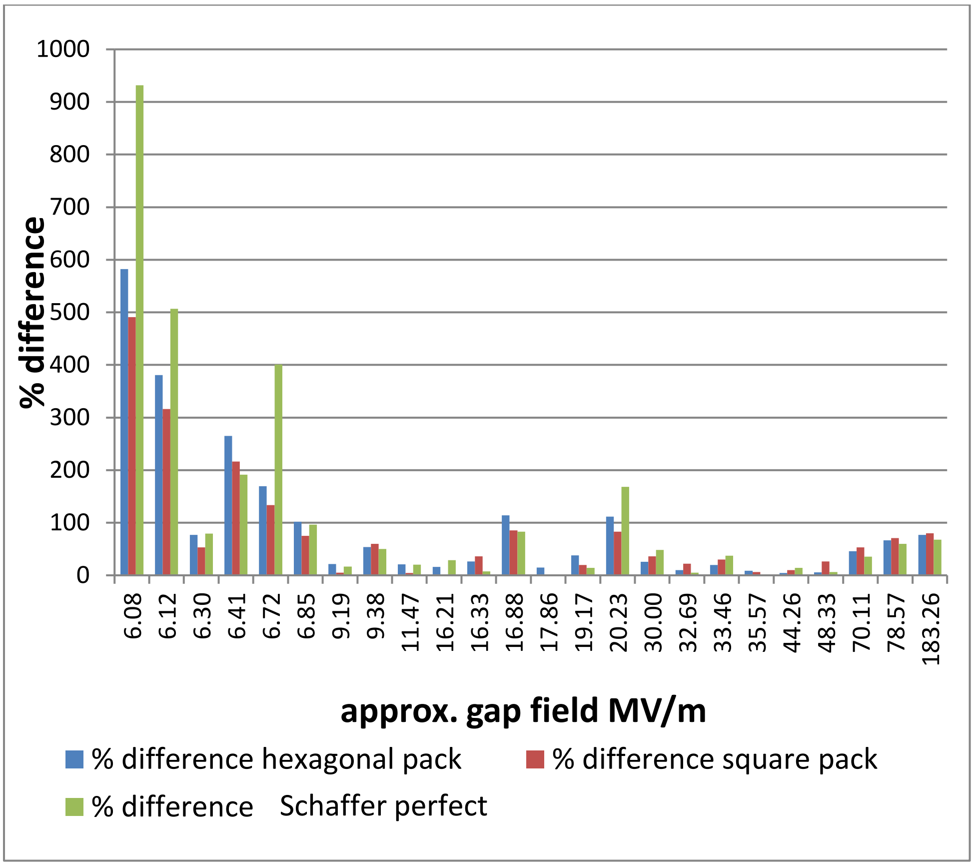

Figure 4. 9 Hexagonal and square packing predictions % differences.

4.6 Long range order

Many of the surfaces did not display either short- or long-range ordering. Disruption to the formation of an ordered arrangement during EHD patterning can be due to several factors (Figure 4.10 A). A single pillar acts as an initiator site. Further pillar formation occurs around the initial pillar and the ordered domain extends until the pillars meet others formed around a different initiator site. These domains can be clearly seen in Figure 4.10 B. For long-range order to occur, the domain of an initiator pillar must be large and the other pillars that form must have a similar if not identical wavelength. If pillars form simultaneously with a wide range of wavelengths, domains are small and uneven.

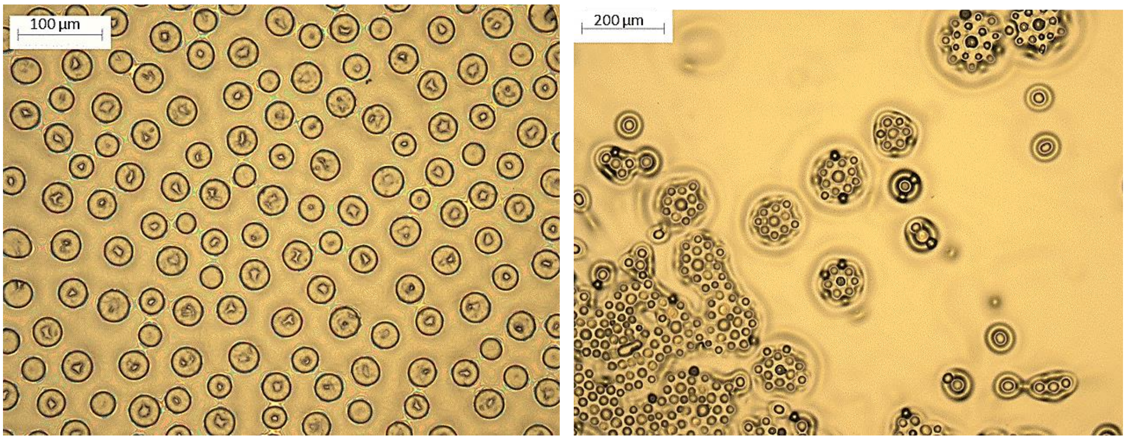

A B

Figure 4. 10 Optical micrographs showing A. a lack of order in an EHD patterned surface. and B. domains of pattern formation.

A graph of the growth exponent *m*, vs the wavenumber *k* results in a curve showing the spectrum of wavenumbers that will be amplified for a given set of experimental parameters. Using higher fields results in a wider range of wavelengths being amplified leading to disorder, as demonstrated in Figure 4.11 A and B. The growth exponents *m* (1.24) for 2 fields are shown. An electrode gap of 3.5µm and an epoxy thickness of 2.2µm were used in this model, which is representative of some of the geometries used in this study. Figure 4.11 A shows the range of wavenumbers (*k*) amplified using an applied potential of 160V. Figure 4.11 B shows the associated curve using an applied potential of 60V. The larger field has the potential to amplify a wider range of wavenumbers; the range of wavenumbers amplified is smaller for the lower field and the growth exponent is also lower (Pease and Russel 2004). Similar widening of the curve can also be seen when perfect and leaky dielectrics are compared, so leaky dielectrics are likely to produce less-organised surfaces.

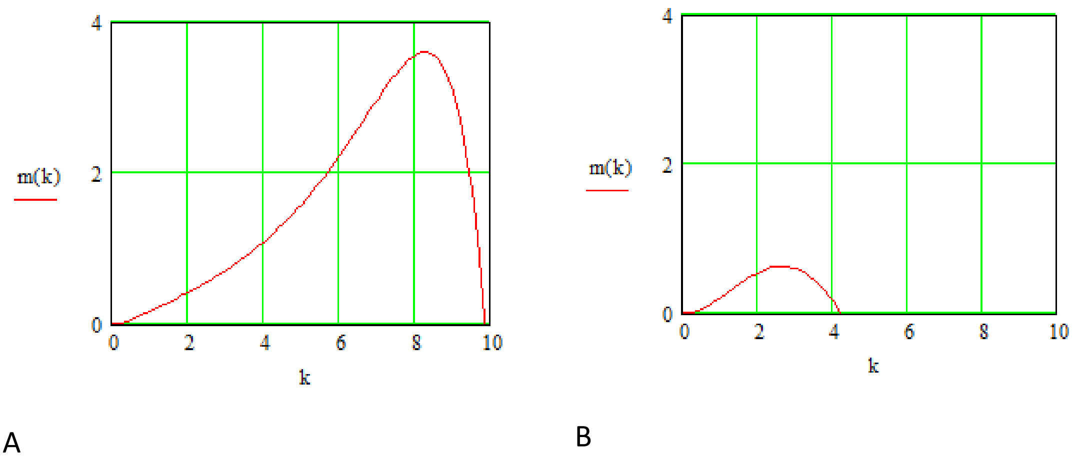

Figure 4. 11 Growth exponent m (1.24) vs wavenumber k for A. 160V and B.60V

Electrical breakdown in the layers can result in disorder and this could be why the shorter wavelength patterns (those below 12 µm) seemed to lack order (Pease and Russel 2004). Pease and Russel identified that at the high voltages required to produce smaller sale patterns, breakdown was likely to occur and in response to this developed an inequality which could be applied to estimate the highest voltage that could be used for a given electrode configuration. The breakdown voltage of air is around 3x10^{6} Vm^{-1} and the breakdown voltage from the literature of epoxy resin is around 20kVmm^{-1} (Tipler, 1987) (Berger, 2000). Given the high fields used here, up to 180 MV m^{-1}, it is likely that there was conduction through both the air and the epoxy.

In Pease and Russel's model for the leaky dielectric case, the field in the polymer is neglected and the entire voltage is dropped across the air gap. If this is the case then the field in the air is even higher than the electrode gap fields approximated above, since these have not included the thickness of the polymer and have simply used the electrode gap spacing. Pease and Russel also stated that a leaky dielectric is more likely to break down than a perfect dielectric.

Coalescence of the surfaces has also led to disorder and on some surfaces the original arrangement of the pillars has been lost due to the continuing evolution of the surface after the initial patterning took place. This is partly due to the high fill factor of the epoxy between the electrodes, the lag time between pattern formation and the curing of the epoxy, and of the high fields used which accelerates the coalescence of the pillars for specific fill factors. The low viscosity of the epoxy compared to thermoplastics increases the rate of pillar formation, and so is a great benefit, but at high enough fill factors it also contributes to the acceleration of the coalescence. Combined with the fact that no other mechanism was used to solidify the resin, the lack of control over the solidification has exacerbated the problems of coalescence.

Coalesced patterns are shown in Figure 4.12 A and B. In Figure 4.12 A the original pillar diameters and wavelength can still be discerned but the merged pillars have formed ellipses and have disrupted what would have been a reasonably well-ordered surface. In Figure 4.12 B the shadows of the initial structures formed can be seen in grey (thought to be the breakdown of the ITO layer due to the current that flows through the polymer) and these were well ordered arrays. However, the merging of the material on the surface, seen in blue, has completely obscured the original pattern.

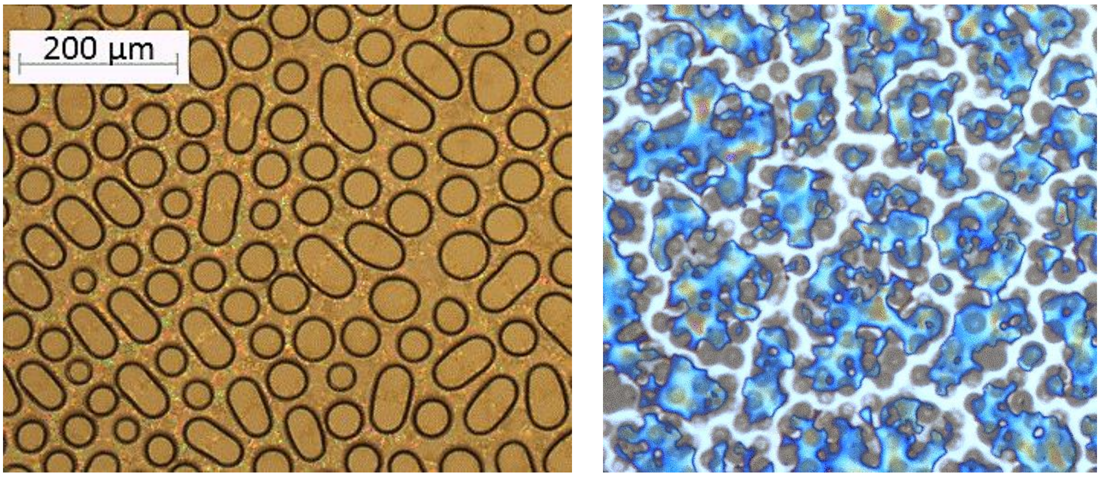

A B Image width 65µm

Figure 4. 12 Optical micrographs of EHD pattern disruptions due to coalescence.

The coarsening of the pattern is due largely to the fill factor of the original epoxy thickness to electrode gap. When a low fill factor is used formation of the pillars depletes the volume of fluid on the electrode isolating the pillars. When a high fill factor is used there is a great deal of material left on the electrode between the pillars, even when the pillars have contacted the top electrode, which allows a path for the pillars to merge. This difference can be seen in Figures 4.14 and 4.15, where one surface seems depleted of epoxy, whereas on the other a great deal still exists.

Where it was observed that the pillars had traversed across the surfaces, whilst in contact with both electrodes, the regularity of the pattern was extremely disrupted.

Long-range order has been identified as a goal for a number of groups for EHD patterning, but the only way that true long-range order is seen on an EHD-formed surface is if patterned electrodes are used. However, the objective of this study was to avoid using more complicated techniques, and in any case surfaces that lack precise long-range ordering can still be of great use in many applications.

4.7 Viscosity

It should be noted that both Schäffer's and Pease and Russel's models assumed that the material behaves as a Newtonian fluid i.e. stress is related linearly to the rate of applied strain. Elasticity in the polymer film is not accounted for in their models, and inertia is assumed to be zero. A non-Newtonian fluid displays both elastic and viscous effects. The relaxation time of a substance is the time it takes for stress in the material, created by an external force, to relax; in effect it is the time taken by molecules to reorder themselves into a new shape in response to the applied stress. When the time scale for the material to flow is long compared to relaxation time of the material viscous effects dominate behaviour; when the time scale is short the material behaves more elastically. Schäffer states that the large viscosities of the polymer melts he was using, leading to the long process times involved in the formation for his structures (sometimes more than 24 h), validates the assumption that the behaviour of the material is Newtonian. This assumption is also made by Pease and Russel. Several other experimental studies have also stated that the time it took for their structures to form was up to several days (Harkema, 2005). For these experimental conditions this assumption would also have been valid.

In this study the fabrication times of the epoxy surfaces were very often short. Patterning often took place within seconds especially when higher fields were used and was generally complete within 30mins of applying the potential. Even when shorter-chain thermoplastic melts were used in previous studies to reduce the pattern formation time, the process time for the epoxy was still far shorter.

Further models have been developed which have included elasticity in their numerical calculations. From these models, it has become more apparent that the viscoelastic behaviour of the polymer has an impact on the pattern formation although again these models are also based on the polymer being a thermoplastic melt.

The Deborah number (De) of a process is the ratio of the time scale of the flow of the material to the relaxation time of the material. The retardation time is the time it takes for the applied stress to be transferred from its point of source through the material. Wu and Chou investigated the effects of elasticity in their model of the EHD process and included non-Newtonian behaviour in their modelling by including both the relaxation time and retardation time of the fluid. Wu and Chou also assumed the creeping flow model, excluding the effects of inertia, and found that below a critical De number, the wavelength of the instability was not affected by the De value. Above a critical De number a window of stable growth rates can be seen, but without the inclusion of inertia in the equations a dominant wavelength cannot be defined.

More recently Tomar *et al* echoed this result. Tomar *et al* found that numerically inertia had a 'profound' influence on the regularity of the dispersion relation and that their numerical results agreed with those of Wu and Chou (Tomar, et al., 2007) (Wu & Chou, 2005). Their results demonstrated that when elasticity contributes to the stress in the polymer inertia should not be omitted from the equations which in effect is when the relaxation time is longer than the timescale of the flow. They demonstrated that very large growth rates occur for a narrow band of wavelengths, caused by increased response times due to elasticity in the material. So, the range of wavelengths amplified is very small which explained the highly organised patterns that can be produced using EHD instabilities.

The relaxation and retardation of the epoxy material used here are not known accurately and so more work would have to be performed in order to validate the assumption that the material is behaving as Newtonian or non-Newtonian. Since the studies described above have demonstrated that elasticity can affect the wavelength of the instability; this is another parameter which could be responsible for the differences between the results from the models used here and the experimental results.

The viscosity of the epoxy was low in comparison to that of a thermoplastic PS melt being approximately 25 Pa s and $1.5*10^4$ Pa s respectively. Under test conditions (using a Brookfield viscometer) the epoxy also demonstrated non-Newtonian characteristics in that its viscosity lowered with increasing shear rate: 2RPM (average viscosity 27069 cP) and 10RPM (average viscosity 21865cP). The rate at which the structures appeared was due to the high electric fields used combined with the low viscosity of the epoxy. The demonstrations in the work by Wu and Chou and Tomar *et al* imply that accurate predictions of the wavelengths produced by experiments may not be possible for situations where elasticity is involved in the process but inertia is being omitted from the calculations.

4.8 Summary of the comparisons with the models

As has been stated the models used here have been applied to experiments that have been performed using EHD instability patterning by several groups, since the equations are explicit and concise. Several of these have been under similar experimental conditions to those assumed in the models but not all. The assumptions made in the models developed by Schäffer and Pease and Russel may not adequately cover the experimental regimes under which the epoxy resin experiments here were operating. Firstly, a long-wavelength instability compared to the electrode spacing is assumed which is not generally the case in these experiments. High viscosities and long process times are assumed in the models; polymer properties are assumed to be constant, such as viscosity and electric effects and inertia is excluded which may not be the case when epoxy is used. Given these assumptions it could be asserted that these models may not accurately describe the pattern formation, and could account for the discrepancy between predictions and results. Lastly the models were based on using a polymer melt and it is likely that the epoxy resin is behaving differently to a heated thermoplastic. Given these facts the results and predictions are in reasonably good agreement.

4.9 Aspect ratio

Typically, aspect ratios (height /width) for EHD fabricated surfaces are low and range from 0.29-0.83 (Figure 4.13) which makes them wider than tall and their shape is more disk-like than a pillar (Grilli, et al., 2011).

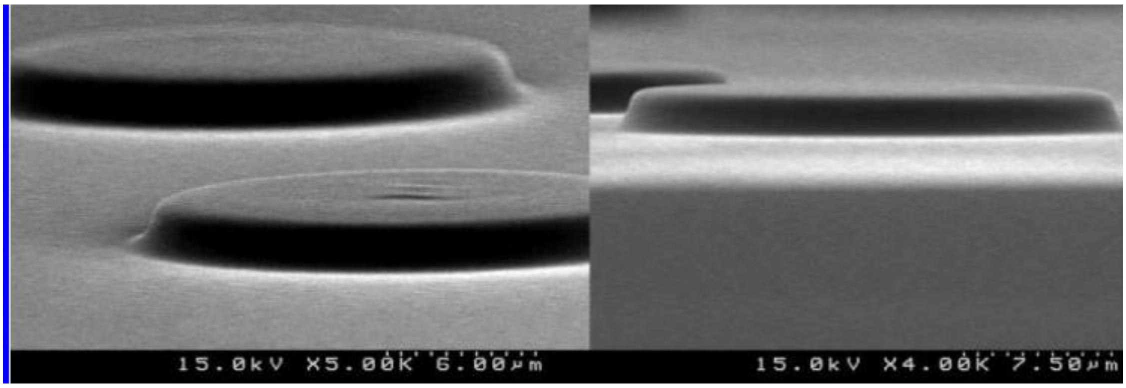

Figure 4. 13 SEM tilt view of photocurable thiol vinyl ether array (pillars measure approx. 2.5 µm tall and 17 µm in diameter) (Dickey, et al. 2006).

Some of the epoxy surfaces fabricated here demonstrated aspect ratios of more than double this value with the highest being 1.92 meaning that the height is greater than the width and the structure is more like a pillar. This is demonstrated in the surfaces shown in Figures 4.14 and 4.15 which have aspect ratios of 1.56 and 1.92 respectively. The difference between these surfaces and that of the lower aspect ratio of 0.15 in Figure 4.13 can be seen clearly. The surface in Figure 4.15 shows a large amount of epoxy residue between each structure however, which could be a disadvantage.

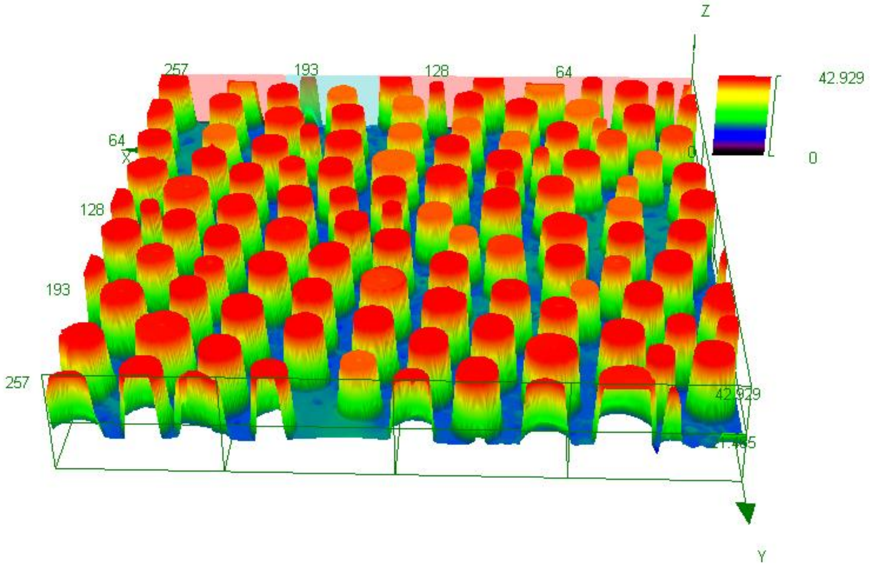

Figure 4. 14 LEXT 3D scan epoxy EHD surface with an aspect ratio of 1.56.

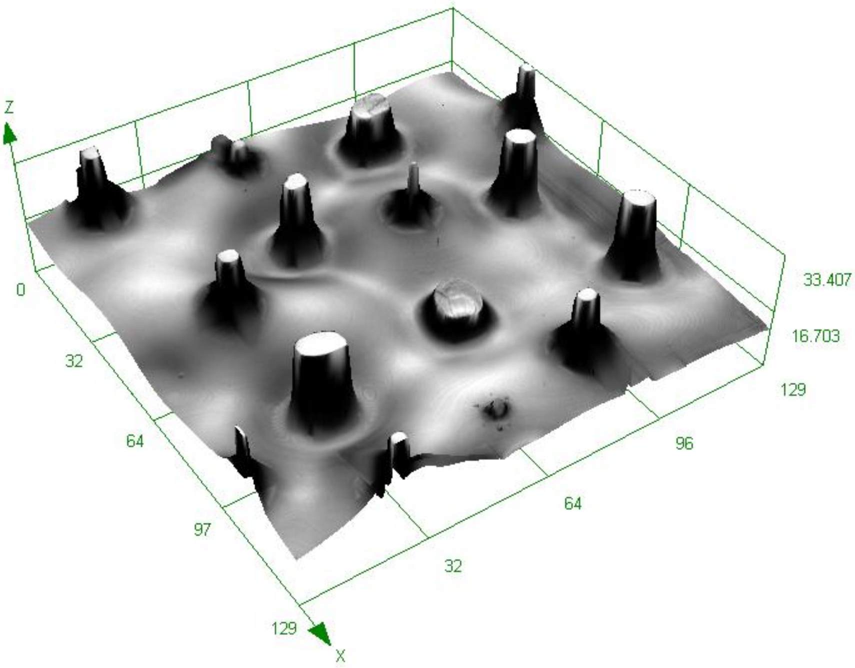

Figure 4. 15 LEXT 3D scan epoxy EHD surface with an aspect ratio of 1.92 (scale in µm) Several broken pillars are visible also.

The aspect ratios obtained in the epoxy resin are likely to have been because comparatively high voltages were applied to the experiment. This allowed larger electrode gaps to be used whilst still forming pillars. Li *et al* demonstrated that there was a critical value of the electric field that is required for pillars to form (Li, et al., 2013). Many applications for pillar array surfaces require higher aspect ratios than many of the surfaces produced previously with EHD patterning with low aspect ratios. Pease and Russel identified that with the high viscosity thermoplastics the process times required to form structures with high aspect ratios could be as long as months. The ability to produce surfaces with the higher aspect ratios shown in epoxy could be a great advantage. The use of a higher field does overcome several challenges such as increasing aspect ratios and decreasing the scale of the instability but also introduces new ones such as the lack of long range order and dielectric breakdown.

4.10 Reduction of the instability wavelength

The smallest wavelength epoxy surfaces that were produced were approximately 3.4 µm. This was a micron larger than the objective of producing surfaces with wavelengths of 2.5 µm. Several of the surfaces were however tested for their interaction with IR radiation and a reduction in transmission was observed. Where other groups have produced surfaces with comparable wavelengths the pillars on these surfaces had aspect ratios that were extremely small and the pillars were wider rather than higher which is not the desired geometry for a solar selective surface.

As was discussed in the results section, increasing the electric field produces smaller pillars. This method was used in this study and was achieved by reducing both the thickness of the polymer and the electrode gap. It was found that there was a limit to the reduction in the thickness of the epoxy layers which could be fabricated, which in turn meant that the reduction in scale of the surfaces was also limited. Furthermore, using such thin polymer layers also introduced other issues such as stray current flowing between the electrodes which appears to be due to conduction through the air which then reduced the electric field. When a surface was fabricated using the highest fields the resulting pattern could be very disordered. Also, when smaller wavelengths were produced using a flat electrode the aspect ratio was very low and optical trapping surfaces require higher aspect ratios than those produced.

The reduction of the wavelength of the pillars has been identified in other studies as an objective for EHD experiments and it has been found to introduce many challenges. Increasing the voltage, reducing the electrode gap or epoxy thickness and lowering the surface tension of the polymer have all been identified as ways of reducing the wavelength however reducing the electrode gap also limits the maximum voltage that can be applied. Lau and Russel used an electrode gap of 171nm and a PMMA layer of 48nm which resulted in a wavelength of approximately 2µm with a disordered pattern. A potential of only 10V was applied which led to the disorder due to the breakdown of thin PMMA film and this limited the size of the pillars produced (Lau & Russel, 2011). Here much higher fields were used and air conduction experiments appeared to show there was some breakdown of the air layer here also.

Pease and Russel predicted that even with large voltages and small values of surface tension, it would be difficult to drop the spacing much below the electrode spacing and even more challenging to lower the wavelengths produced by an order of magnitude (Pease & Russel, 2004).

The limitations on the reduction of the length scales was also discussed by Lau and Russel who identified the problem that the very fields that produced the wavelengths that were desired were also those which a. caused dielectric breakdown in the materials in the electrode gap and b. caused disorder on the surfaces both of which effects were seen here and this study seems to concur with the results found by Lau and Russel (Lau & Russel, 2011).

Dust may have caused some of the conduction through the smaller electrode gaps in this study. The reduction in scale of the electrode gap would mean that eventually a clean room would be required to eliminate dust particles. This could be a limitation of the use of this benchtop technique however despite these issues many good surfaces were fabricated.

4.11 Tissue culture surfaces

Pillared surfaces are often used in tissue culture and have been employed to study a multitude of mechanisms and processes within the cell from being used as a mechanism to distribute cells evenly within a micro-chamber, to investigating how cells assess the rigidity of the substrate material (Kaminaga, et al., 2015) (Ghassemi, et al., 2012).

Recently Kamande *et al* demonstrated that an epoxy master, used for producing PDMS moulds for cell culture, had several benefits over the more traditional method of using SU8 photoresist to pattern a silicon wafer. The use of epoxy benefited from less contamination from toxic silanes to improved durability of the master (Kamande, et al., 2015). Frey *et al* used an EHD patterned PMMA master to produce hot embossed PS surfaces, treated with reactive ion etching, on which to study cell migration (Frey, et al., 2006). Here we combined both of these ideas using the epoxy EHD surfaces as both moulds for cell culture substrates and cell culture substrates. The tissue culture studies demonstrated that a simply manufactured epoxy resin surface can support tissue growth and the surfaces can also be replicated in several different materials using moulding and hot embossing.

The results from initial investigative experiments implied that the cells studied here had a preference the scale of surface pattern on which they would grow. More commonly photolithography has been used but as shown by Kamande *et al* our process would be cheaper and more accessible and the fact that the surfaces can be replicated exactly, in several materials means that comparative studies so important in biological investigations can be performed.

4.12 IR spectra interaction

Despite the issues surrounding the reduction in scale of the patterns, some surfaces were tested for interaction with IR radiation. The surfaces used were chosen for their uniformity of pattern ordering, and pillar height. These surfaces did show an interaction with radiation although the use of the surfaces as radiation trapping layers still requires further investigation. Moulds taken from the surface were used to reproduce the structures in epoxy resin on salt disks in order to investigate their interacting with IR radiation. Transmission spectra of three of the fabricated surfaces indicated that the surface was interacting with infrared radiation in some way. The interaction is unlikely to be enhanced or modified absorption due to chemical bonding and seems likely to be interference.

In theory, the structured surfaces would behave as optical trapping surfaces as described in the introduction and the structures on the surface would interact with wavelengths of a similar scale or below. Of the three spectra shown in Section 3.5.1 Figures 3.28, 3.29 and 3.30, the wavenumber with the greatest transmission loss increased with a decrease in the size of the structures on the surface as expected, however the wavenumber with the greatest transmission loss was shorter than expected given the size of the structures. The largest structured surface has an average centre to centre spacing of the pillars of 54μm however the trough of the transmission spectra is at approximately 1700cm^{-1} wavenumbers (5.9μm wavelength) so much shorter than the wavelength of the pattern. The same is true of the transmission loss with the other surfaces tested. The scale of other features on the surface were examined to identify if these were responsible for the interaction. The pillar spacing and the diameter of the pillars was still larger than would be expected although some surface details were smaller than this.

4.13 Analysis and Future Projects

Initially a method of producing layers of the epoxy resin of the desired thickness was obtained. Once a consistent method had been discovered the use of EHD instabilities to produce surface structures in the cold curing epoxy resin produced good reliable results.

In comparison to using a thermoplastic, which was heated to obtain fluidity, the use of the wet epoxy meant that the spin coated layer could not easily be investigated for defects before it was patterned. Pin-holes and dust for example, were found only after patterning had taken place which meant that a number of experiments failed. However, the use of the epoxy instead of thermoplastics also had a great many benefits such as the lowered viscosity of the material.

The cure time for the epoxy means that there was a time limit on the length of pattern formation that can take place i.e. for certain experimental conditions like using a low electric field it could take longer for the pattern to evolve than the cure time of the material. However, the low viscosity and use of high electric fields meant that the patterning took place very quickly although the lack of control over the solidification of the material did confer other issues.

The improved understanding of the way the epoxy material behaves electrically when used for EHD instability patterning means there are a number of modifications that could be made to the experiments and several potential areas for further investigation. The knowledge that the material is behaving as a leaky dielectric, allowing a flow of current, is key. The use of a variable frequency AC potential could be used to compare the behaviour of the material as a perfect or leaky dielectric. An understanding of whether its high permittivity or its conductivity is more beneficial when trying to lower the scale of the patterns could be useful. Further modelling and experimentation would also be required to determine which of these methods would produce the best results. Many of the parameters which are required for producing surfaces of the desired geometries such as high aspect ratios and small wavelengths introduce a range of challenges into the fabrication process. Using models for the careful selection of the experimental parameters could reduce some of the challenges found here.

Whilst the self-solidifying mechanism of this material is beneficial, a way of controlling the curing could be investigated. This could include applying a short duration of heating to speed up the process, since the lag time between forming the surfaces and the gel point of the polymer often led to losing the consistency of the structures. This would certainly be beneficial in the case where small electrode gaps were being used to form small pillars.

Many materials properties of the epoxy offer scope for further study. A better understanding of the change in viscosity of the polymer over time would be beneficial.

In previous studies carried out using thermoplastics, material properties such as the viscosity and dielectric constant remain constant over time whereas in epoxy they change. The viscosity has a substantial impact on the growth rate and if the material were behaving like a perfect dielectric (when used with high frequency AC for example) then the dielectric constant has a significant impact on the wavelength. A further investigation of whether the material is behaving as a Newtonian or a non-Newtonian fluid in these experiments could be useful when investigating which theoretical model to use.

A particular advantage that could be investigated further is the potential for producing surfaces with good aspect ratios. The fast growth rate meant that it was realistic to form pillars which were taller rather than wider.

4.14 Conclusions

We have demonstrated a robust way of fabricating thin films, in cold cure epoxy using a spin coating technique, which results in reproducible and predictable coatings for given initial solution concentrations of the epoxy and the spin speed. These coatings were then used to fabricate micro-structured surfaces.

Ambient cured epoxy resin is a novel material with which to produce EHD patterned surfaces. This study has demonstrated that this material can be used as the patternable polymer and has both benefits and drawbacks with regards to EHD patterning. A very wide range of wavelengths were produced from approximately 3-200 µm using a large variety of electric fields ranging from approximately 6-180 MVm^{-1}. This study also demonstrated that it was possible to combine this technique with moulding and hot-embossing to produce accurate replications of the surfaces on a wide range of substrates and in a variety of materials.

The comparison of the measured results to modelled predictions provided further insight into which the regime the epoxy was operating under when the patterning took place. Furthermore, the study analysed the applicability for the models to the experiments by assessing the assumptions that were made in the modelling process and identifying differences between these assumptions and the experiments performed.

Overall this study has demonstrated that simple bench-top techniques can be utilised to produce pillared surfaces in epoxy resin, patterned on a scale which interact with both IR radiation and cells in vitro. This could be of great benefit since the methods which involve the use of clean rooms, silicon photolithography and vacuum etching techniques are not available universally and costs are incurred in gaining access to them for exploratory studies. The technique of using EHD patterned surfaces in epoxy resin as mould masters for initial investigative experiments could reduce costs and allow the use of micro-patterned materials to be available to a greater range of researchers.

Appendix A. Solar Selective Coatings: Industrial State-of-the-Art

Paper removed for copyright reasons:

Can be found at Trease, Claire H., Hadavinia, Homayoun, Barrington, Peter E. (2013) Solar selective caotings : industrial state-of-the-art, Recent patents on materials science 2013, 6, 1-19

Appendix B. Mathcad worksheet for equation 1.20 Figure 1.26

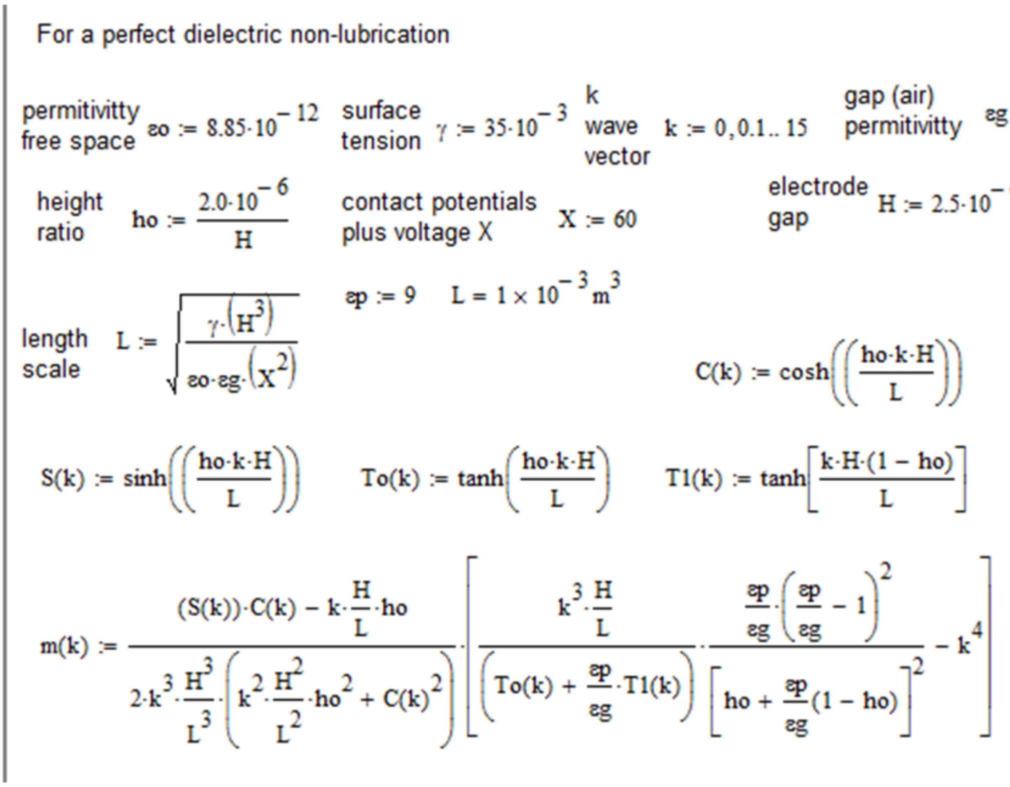

For a perfect dielectric non-lubrication

permitivitty free space $\varepsilon o := 8.85 \cdot 10^{-12}$

surface tension $\gamma := 35 \cdot 10^{-3}$

k wave vector $k := 0, 0.1 .. 15$

gap (air) permitivitty $\varepsilon g := 1$

height ratio $ho := \dfrac{2.0 \cdot 10^{-6}}{H}$

contact potentials plus voltage X $X := 60$

electrode gap $H := 2.5 \cdot 10^{-6}$

length scale $L := \sqrt{\dfrac{\gamma \cdot \left(H^3\right)}{\varepsilon o \cdot \varepsilon g \cdot \left(X^2\right)}}$

$\varepsilon p := 9$ $\quad L = 1 \times 10^{-3} \, m^3$

$C(k) := \cosh\left(\left(\dfrac{ho \cdot k \cdot H}{L}\right)\right)$

$S(k) := \sinh\left(\left(\dfrac{ho \cdot k \cdot H}{L}\right)\right)$ $\quad To(k) := \tanh\left(\dfrac{ho \cdot k \cdot H}{L}\right)$ $\quad T1(k) := \tanh\left[\dfrac{k \cdot H \cdot (1 - ho)}{L}\right]$

$$m(k) := \frac{(S(k)) \cdot C(k) - k \cdot \dfrac{H}{L} \cdot ho}{2 \cdot k^3 \cdot \dfrac{H^3}{L^3} \cdot \left(k^2 \cdot \dfrac{H^2}{L^2} \cdot ho^2 + C(k)^2\right)} \cdot \left[\frac{k^3 \cdot \dfrac{H}{L}}{\left(To(k) + \dfrac{\varepsilon p}{\varepsilon g} \cdot T1(k)\right)} \cdot \frac{\dfrac{\varepsilon p}{\varepsilon g} \cdot \left(\dfrac{\varepsilon p}{\varepsilon g} - 1\right)^2}{\left[ho + \dfrac{\varepsilon p}{\varepsilon g}(1 - ho)\right]^2} - k^4\right]$$

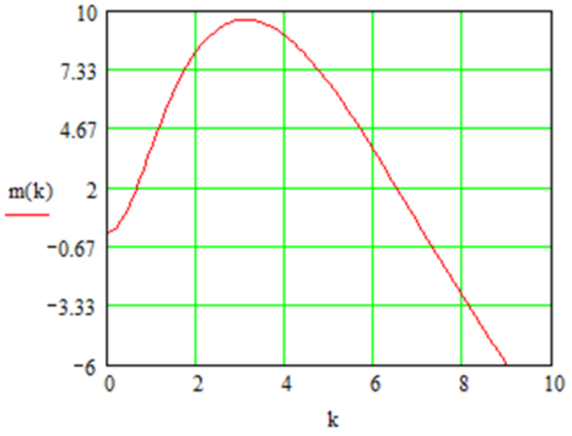

wavenumber to wavelength conversion

$$\frac{2 \cdot \pi \cdot L}{3.1} = 8.397 \times 10^{-6}$$

$$\frac{\left(\dfrac{4 \cdot \pi}{\dfrac{1}{3^{\frac{1}{2}}}} \cdot L\right)}{3.1} = 9.696 \times 10^{-6}$$

Appendix C. Data gathered from EHD fabricated surfaces and wavelengths predicted by theory for the experimental parameters.

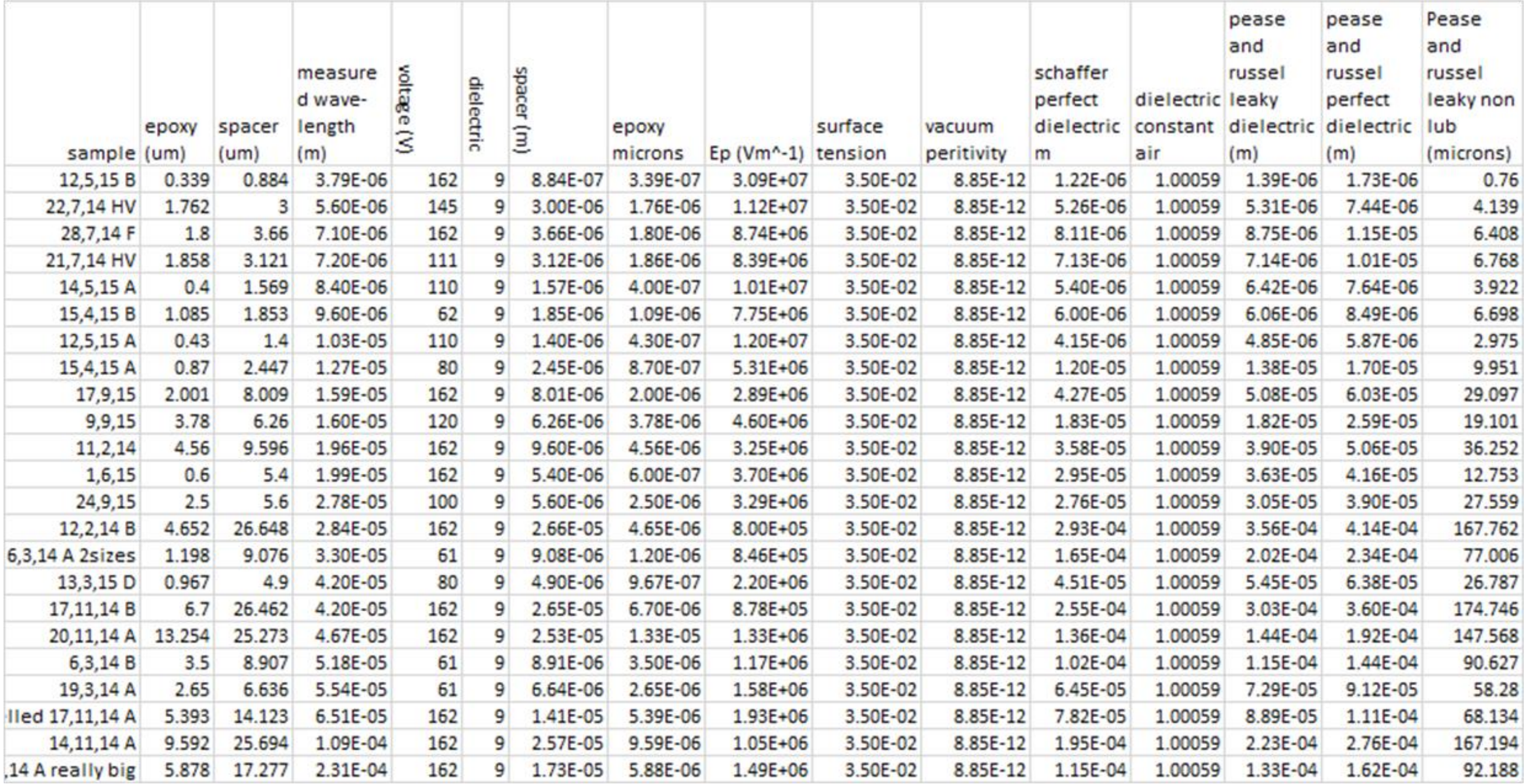

sample	epoxy (um)	spacer (um)	measured wave-length (m)	voltage (V)	dielectric	spacer (m)	epoxy microns	Ep (Vm^-1)	surface tension	vacuum peritivity	schaffer perfect dielectric m	dielectric constant air	pease and russel leaky dielectric (m)	pease and russel perfect dielectric (m)	Pease and russel leaky non lub (microns)
12,5,15 B	0.339	0.884	3.79E-06	162	9	8.84E-07	3.39E-07	3.09E+07	3.50E-02	8.85E-12	1.22E-06	1.00059	1.39E-06	1.73E-06	0.76
22,7,14 HV	1.762	3	5.60E-06	145	9	3.00E-06	1.76E-06	1.12E+07	3.50E-02	8.85E-12	5.26E-06	1.00059	5.31E-06	7.44E-06	4.139
28,7,14 F	1.8	3.66	7.10E-06	162	9	3.66E-06	1.80E-06	8.74E+06	3.50E-02	8.85E-12	8.11E-06	1.00059	8.75E-06	1.15E-05	6.408
21,7,14 HV	1.858	3.121	7.20E-06	111	9	3.12E-06	1.86E-06	8.39E+06	3.50E-02	8.85E-12	7.13E-06	1.00059	7.14E-06	1.01E-05	6.768
14,5,15 A	0.4	1.569	8.40E-06	110	9	1.57E-06	4.00E-07	1.01E+07	3.50E-02	8.85E-12	5.40E-06	1.00059	6.42E-06	7.64E-06	3.922
15,4,15 B	1.085	1.853	9.60E-06	62	9	1.85E-06	1.09E-06	7.75E+06	3.50E-02	8.85E-12	6.00E-06	1.00059	6.06E-06	8.49E-06	6.698
12,5,15 A	0.43	1.4	1.03E-05	110	9	1.40E-06	4.30E-07	1.20E+07	3.50E-02	8.85E-12	4.15E-06	1.00059	4.85E-06	5.87E-06	2.975
15,4,15 A	0.87	2.447	1.27E-05	80	9	2.45E-06	8.70E-07	5.31E+06	3.50E-02	8.85E-12	1.20E-05	1.00059	1.38E-05	1.70E-05	9.951
17,9,15	2.001	8.009	1.59E-05	162	9	8.01E-06	2.00E-06	2.89E+06	3.50E-02	8.85E-12	4.27E-05	1.00059	5.08E-05	6.03E-05	29.097
9,9,15	3.78	6.26	1.60E-05	120	9	6.26E-06	3.78E-06	4.60E+06	3.50E-02	8.85E-12	1.83E-05	1.00059	1.82E-05	2.59E-05	19.101
11,2,14	4.56	9.596	1.96E-05	162	9	9.60E-06	4.56E-06	3.25E+06	3.50E-02	8.85E-12	3.58E-05	1.00059	3.90E-05	5.06E-05	36.252
1,6,15	0.6	5.4	1.99E-05	162	9	5.40E-06	6.00E-07	3.70E+06	3.50E-02	8.85E-12	2.95E-05	1.00059	3.63E-05	4.16E-05	12.753
24,9,15	2.5	5.6	2.78E-05	100	9	5.60E-06	2.50E-06	3.29E+06	3.50E-02	8.85E-12	2.76E-05	1.00059	3.05E-05	3.90E-05	27.559
12,2,14 B	4.652	26.648	2.84E-05	162	9	2.66E-05	4.65E-06	8.00E+05	3.50E-02	8.85E-12	2.93E-04	1.00059	3.56E-04	4.14E-04	167.762
6,3,14 A 2sizes	1.198	9.076	3.30E-05	61	9	9.08E-06	1.20E-06	8.46E+05	3.50E-02	8.85E-12	1.65E-04	1.00059	2.02E-04	2.34E-04	77.006
13,3,15 D	0.967	4.9	4.20E-05	80	9	4.90E-06	9.67E-07	2.20E+06	3.50E-02	8.85E-12	4.51E-05	1.00059	5.45E-05	6.38E-05	26.787
17,11,14 B	6.7	26.462	4.20E-05	162	9	2.65E-05	6.70E-06	8.78E+05	3.50E-02	8.85E-12	2.55E-04	1.00059	3.03E-04	3.60E-04	174.746
20,11,14 A	13.254	25.273	4.67E-05	162	9	2.53E-05	1.33E-05	1.33E+06	3.50E-02	8.85E-12	1.36E-04	1.00059	1.44E-04	1.92E-04	147.568
6,3,14 B	3.5	8.907	5.18E-05	61	9	8.91E-06	3.50E-06	1.17E+06	3.50E-02	8.85E-12	1.02E-04	1.00059	1.15E-04	1.44E-04	90.627
19,3,14 A	2.65	6.636	5.54E-05	61	9	6.64E-06	2.65E-06	1.58E+06	3.50E-02	8.85E-12	6.45E-05	1.00059	7.29E-05	9.12E-05	58.28
lled 17,11,14 A	5.393	14.123	6.51E-05	162	9	1.41E-05	5.39E-06	1.93E+06	3.50E-02	8.85E-12	7.82E-05	1.00059	8.89E-05	1.11E-04	68.134
14,11,14 A	9.592	25.694	1.09E-04	162	9	2.57E-05	9.59E-06	1.05E+06	3.50E-02	8.85E-12	1.95E-04	1.00059	2.23E-04	2.76E-04	167.194
,14 A really big	5.878	17.277	2.31E-04	162	9	1.73E-05	5.88E-06	1.49E+06	3.50E-02	8.85E-12	1.15E-04	1.00059	1.33E-04	1.62E-04	92.188

Appendix D. Cell morphology and growth observation studies on novel, chemically unmodified and patterned polymer surfaces for advanced tissue culture applications

Paper removed for copyright reasons. It can be found at:

Trease, C.H., Longman, M.R., Augousti, A.T., Foot, P.J.S. and Pierscionek, B. (2017) Cell morphology and growth observation studies on novel, chemically unmodified and patterned polymer surfaces for advanced tissue culture applications. Polymer, 109, pp. 13-24.

http://dx.doi.org/10.1016/j.polymer.2016.12.032

Appendix E. Mathscad worksheet for equation (1.24)

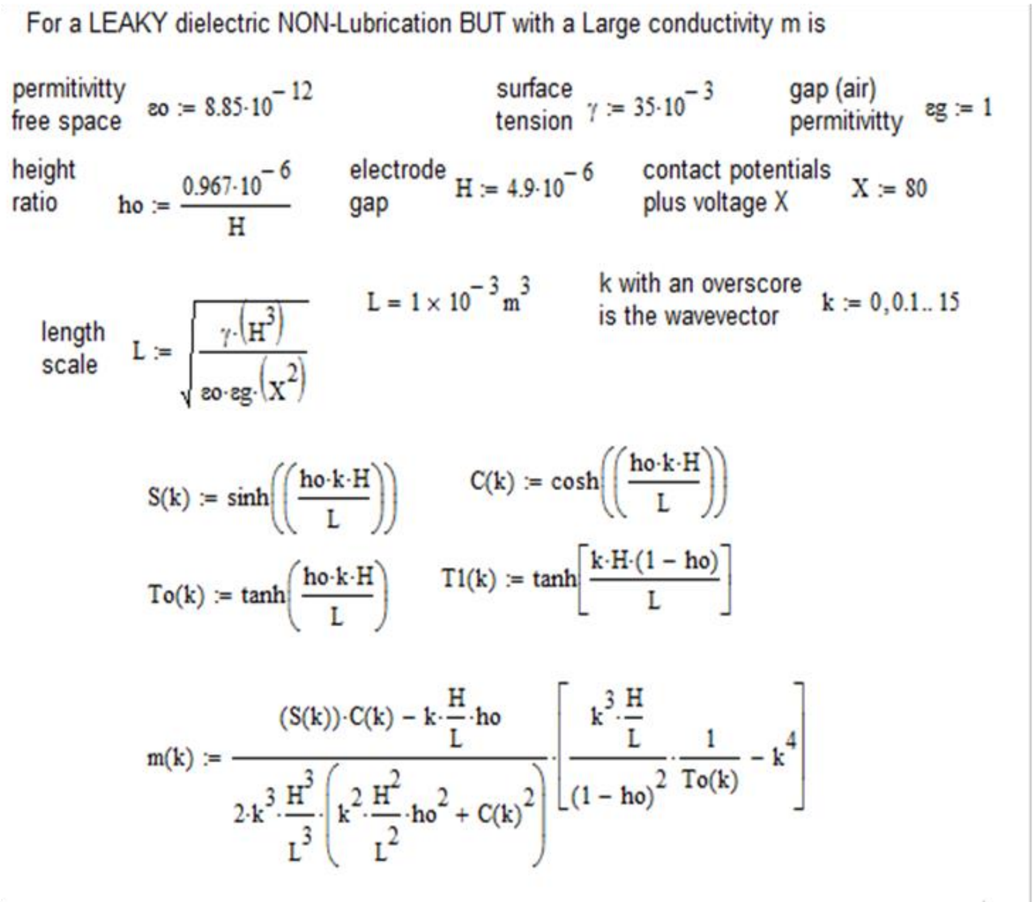

For a LEAKY dielectric NON-Lubrication BUT with a Large conductivity m is

permitivitty free space $\varepsilon o := 8.85\cdot10^{-12}$

surface tension $\gamma := 35\cdot10^{-3}$

gap (air) permitivitty $\varepsilon g := 1$

height ratio $ho := \frac{0.967\cdot10^{-6}}{H}$

electrode gap $H := 4.9\cdot10^{-6}$

contact potentials plus voltage X $X := 80$

length scale $L := \sqrt{\frac{\gamma\cdot\left(H^3\right)}{\varepsilon o\cdot\varepsilon g\cdot\left(X^2\right)}}$

$L = 1\times10^{-3}\,m^3$

k with an overscore is the wavevector $k := 0, 0.1 .. 15$

$S(k) := \sinh\left(\left(\frac{ho\cdot k\cdot H}{L}\right)\right)$

$C(k) := \cosh\left(\left(\frac{ho\cdot k\cdot H}{L}\right)\right)$

$To(k) := \tanh\left(\frac{ho\cdot k\cdot H}{L}\right)$

$T1(k) := \tanh\left[\frac{k\cdot H\cdot(1-ho)}{L}\right]$

$$m(k) := \frac{(S(k))\cdot C(k) - k\cdot\frac{H}{L}\cdot ho}{2\cdot k^3\cdot\frac{H^3}{L^3}\cdot\left(k^2\cdot\frac{H^2}{L^2}\cdot ho^2 + C(k)^2\right)}\cdot\left[\frac{k^3\cdot\frac{H}{L}}{(1-ho)^2}\cdot\frac{1}{To(k)} - k^4\right]$$

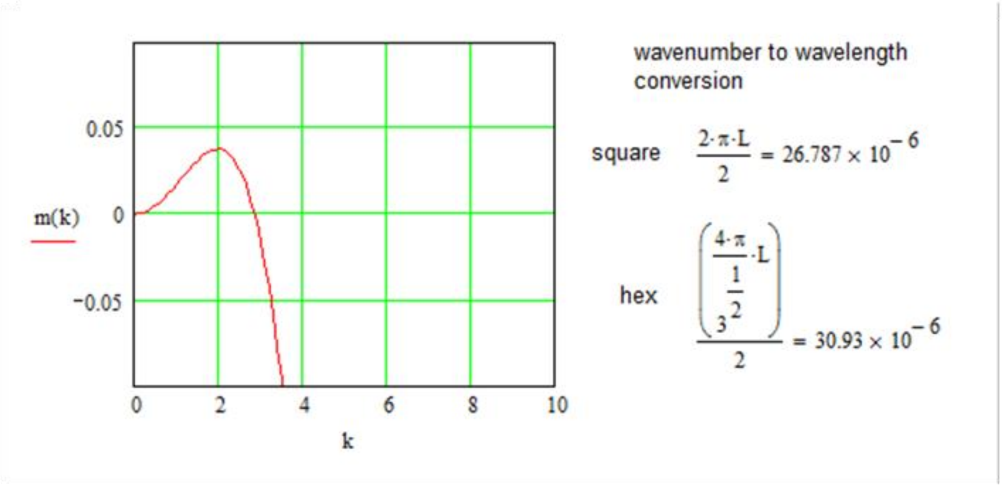

wavenumber to wavelength conversion

square $\frac{2\cdot\pi\cdot L}{2} = 26.787\times10^{-6}$

hex $\frac{\left(\frac{4\cdot\pi}{3^{\frac{1}{2}}}\cdot L\right)}{2} = 30.93\times10^{-6}$

References

Agnihotri, O. & Gupta, B., 1981. *Solar Selective Surfaces.* New York: John Wiley and Sons.

Aiken, D., 2000. Antireflection coating design for series interconnected multi-junction solar cells. *Progress in Photovoltaics: Research and Applications 8(6),* pp. 563-570.

Akande, A. & Adedoyin, J., 2001. Correlation of charge transfer in metal/polymer contact with contact potential. *Journal of Electrostatics 51-52,* pp. 105-110.

Akbas, H. Z., Durmus, H. & Ahmetli, G., 2009. Dielectric properties of cured epoxy with teta. *Ozean Journal of Applied Science 2(4),* pp. 443-449.

Allerd, D., Reyes, J. & Piontkowski, J., 1986. *Selective absorber amorphous alloys and devices.* US, Patent No. US4582764.

Anderson, J. C., Leaver, K. D., Leevers, P. & Rawlings, R. D., 2003. *Materials Science for Engineers.* Cheltenham: Nelson Thornes Ltd.

Antonaia, A. & Esposito, S., 2009. *Method for producing a cermet-based spectrally selective coating for the receiver tube of a solar concentrator, and material thus obtained.* WO, Patent No. WO2009107157.

Bae, J., 2012. Electrohydrodynamic instabilities of polymer thin films: filler effect. *Journal of Industrial and Engineering Chemistry 18 (1),* pp. 378-383.

Bae, J. et al., 2008. Effect of nanoparticles on the electrohydrodynamic instabilities of polymer/nanoparticle thin films. *Macromolecules 41(7),* pp. 2722-2726.

Bandyopadhyay, D. & Sharma, A., 2007. Electric field induced instabilites in thin confined bilayers. *Journal of Colloid and Interface Science 311,* pp. 595-608.

Barshilia, H., Grips, V. & Rajam, K., 2009. *Solar selective coating having higher thermal stability useful for harnessing solar energy and a process for the preparation thereof.* US, Patent No. US7585568.

Bayati, M. et al., 2010. Characterization of Al2O3–TiO2 nano porous solar absorbers derived via MAO/sol-gel hybrid process. *Surface and Coatings Technology 205 (7),* p. 2483–2489.

Berger, L., 2000. *CRC Press Handbook of Chemistry and Physics 85th ed.* Boca Raton: CRC Press LLC.

Bogaerts, W. & Lampert, C., 1983. Review materials for photothermal solar energy conversion.. *Journal of Materials Science 18(10),* pp. 2847-75.

Bostrom, T., 2008. *Nickel-alumina coated solar absorbers.* US, Patent No. US20080210219.

Boström, T. et al., 2008. ERDA of Ni-Al2O3/SiO2 Solar thermal selective absorbers. *Solar Energy Materials and Solar Cells 92,* pp. 1177-82.

Boyle, G., 2004. *Renewable Energy: Power For A Sustainable Future 2nd ed.* Oxford: Oxford University Press in Association with the Open University.

BP p.l.c, 2016. *Renewable energy 2015 - in review: Solar Energy.* [Online] Available at: http://www.bp.com/en/global/corporate/energy-economics/statistical-review-of-world-energy/renewable-energy/solar-energy.html
[Accessed 7 December 2016].

Brewer Science, n.d. *www.brewerscience.com/spin-coating-theory.* [Online] Available at: http//www.brewerscience.com/spin-coating-theory
[Accessed 22 February 2016].

Brown, A., Burke, G. A. & Meenan, B. J., 2013. Patterned cell culture substrates created by hot embossing of tissue culture treated polystyrene. *Journal Material Science: Materials in Medicine 24(12),* pp. 2797-807.

Cargill, S., Desmulliez, M. & Yu, W., 2011. Electro-hydrodynamic instability patterning of polymers. *Journal of Physics: Conference Series 301.*

Chakraborty, M., Chowdhury, D. & Chattopadhyay, A., 2003. Spin-coating of polystyrene thin films as an advanced undergraduate experiment. *Journal of Chemical Education 80(7),* pp. 806-809.

Chakraborty, S., 2014. Electrocapillary. In: *Encyclopedia of Microfluidics and Nanofluidics.* New York: Springer Science and Business Media.

Chattopadhyay, S. et al., 2010. Anti-reflecting and photonic nanostructures.. *Materials Science and Engineering Reports 69(1-3),* pp. 1-35.

Chauhan, R. & Singh, B., 2000. Rotating machine insulation materials and techniques - an overview. *Indian Journal of Engineering and Materials Sciences 7,* pp. 370-374.

Chen, G., Hu, L., Chen, X. & Chiesa, M., 2010. *Sub-Wavelength metallic cone structures as selective solar absorber..* World, Patent No. WO2010065635.

Chen, J. & Lux-Steiner, M. C., 2012. *Solar thermal assembly has substrate, where nano-material has structures of similar sub-wavelength range, and is arranged immediately on light absorbing layer.* Germany, Patent No. DE102010034901.

Chou, S. & Zhang, L., 1999. Lithographically induced self-assembly of periodic polymer micropillar arrays. *Journal of Vacuum Science Technology B 17(6),* pp. 3197-3202.

Chu, Y. & Meisen, P., 2011. *Review and Comparison of Different Solar Energy Technologies,* San Diego: Global Energy Network Institute (GENI).

Clasen, R. & Nejati, M., 2010. *Method for the production of thin layers of metal-ceramic composite materials.* US, Patent No. US20100035081.

Clayton, M. & Dekker, M., 1988. *Epoxy Resins - Chemistry and Technology.* New York: John Wiley and Sons.

Craighead, H. & Howard, R., 1981. *Light-absorbing materials.* US, Patent No. US4284689.

De Jong, J., 1978. *Method for the application of a spectral-selective coating on a plate.* US, Patent No. US4105822.

De Jong, J., 1980. *Production of spectrally selective coatings on enamelled metal surfaces.* Great Britan, Patent No. GB2039865.

Debe, M., 1997. *Composite article comprising oriented microstructures..* US, Patent No. US5645929.

Deshpande, P. et al., 2004. Cylindrically symmetric electrohydrodynamic patterning. *Physical Review E 70 (4),* p. 041601.

Dickey, M. et al., 2006. Photocurable pillar arrays formed via electrohydrodynamic instabilities. *Chemistry of Materials 18(8),* Volume 18, pp. 2043-2049.

Diedenhofen, S. L. et al., 2009. Broad-band and omnidirectional antireflection coatings based on semiconductor nanorods. *Advanced Materials 21(9),* pp. 973-978.

Dimitriev, Y., Ivanova, Y. & Iordanova, R., 2008. History of sol-gel science and technology (review). *Journal of the University of Chemical Technology and Metallurgy 43 (2),* pp. 181-92.

Dow Plastics, 1999. *Dow Liquid Eposy Resins.* s.l.:The Dow Chemical Company.

Duffie, J. A. & Beckman, W. A., 2006. *Solar Engineering of Thermal Processes. 3rd ed.* New Jersey: John Wiley and Sons, Inc..

Eder, D., Steiner, U. & Goldberg-Oppenheimer, P., 2011. Carbon nanotube alignment via electrohydrodynamic patterning of nanocomposites. *Advanced Functional Materials 21(10)*, p. 1895–1901.

Energy Initiative Massachusetts Institute of Technology, 2015. *The Future of Solar Energy an Interdisciplinary MIT Study,* Cambridge, Massachusetts: Massachusetts Institute of Technology.

epotek, n.d. *Tech Tip 25 Dielectric properties of epoxies.* [Online] Available at: http://www.epotek.com/site/files/Techtips/pdfs/Tech_Tip_25_-_Dielectric_Properties_of_Epoxies.pdf
[Accessed 3rd March 2016].

Espin, L., Corbett, A. & Kumar, S., 2013. Electrohydrodynamic instabilities in thin viscoelastic films - AC and DC fields. *Journal of Non-Newtonian Fluid Mechanics 196,* pp. 102-111.

Es-Souni, M., 2009. *Process for producing a sol-gel-based absorber coating for solar heating.* US, Patent No. US20090269487.

Fiorini G, S. et al., 2003. Fabrication of thermoset polyester microfluidic devices and embossing masters using rapid prototyped polydimethylsiloxane molds. *Lab On Chip 3(3),* pp. 158-63.

Flory, F., Escoubas, L. & Berginic, G., 2011. Optical properties of nanostructured materials: a review. *Journal of Nanophotonics 5,* pp. 052502 1-20.

Franssila, S., 2010. *Introduction to Microfabrication. 2nd ed..* West Susssex: John Wiley & Sons Ltd.

Fraunhofer Institute for Solar energy Systems, ISE, 2016. *Photovoltaics Report,* Freiburg: Fraunhofer ISE.

Frey, M. et al., 2006. Cellular responses to substrate topography: Role of myosin II and focal adhesion kinase. *Biophysical Journal 90,* pp. 3774-3782.

Gambhire, P. & Thaokar, R., 2011. Linear stability analysis of electrode instabilites at fluid interfaces in the "small feature" limit. *European Physics Journal E 34 (8) :84.pp 11084-9*

Gambhire, P. & Thaokar, R., 2012. Role of conductivity in the electrohydrodynamic patterning of air-liquid interfaces. *Physical Review E 86,* Volume 86, p. 036301.

Ghassemi, S. et al., 2012. Cells test substrate rigidity by local contractions on submicrometer pillars. *Proceedings of the National Academy of Science of USA 109(14),* pp. 5328-5333.

Gilbert, L., Messier, R. & Roy, R., 1981. *Highly solar-energy absorbing device and method of making the same.* US, Patent No. US4252865.

Golay, M., 1961. *Semi-conductor heat absorption means.* US, Patent No. US3000375.

Goldberg-Oppenheimer, P., 2011. *Electrohydrodynamic Patterning of Functional Materials.* s.l.:University of Cambridge, Cavendish Laboratories, Department of Physics, Churchill College.

Goldberg-Oppenheimer, P., Eder, D. & Steiner, U., 2011. Carbon nanotube alignment via electrohydrodynamic patterning of nanocomposites. *Advanced Functional Materials 21(10)*, p. 1895–1901.

Goldberg-Oppenheimer, P., Mahajan, S. & Steiner, U., 2012. Hierarchical electrohydrodynamic structures for surface-enhanced raman scattering. *Advanced Materials 24 (23)*, p. OP175–OP180.

Goncalves, D. & Eugene, I., 2002. Fundamentals and applications of spectroscopic ellipsometry. *Quimica Nova 25(5),* pp. 794-800.

Googin, J. M., Schmitt, C. R., Schreyer, J. M. & Whitehead, H. D., 1977. *Solar radiation absorbing material..* US, Patent No. US4048980.

Googin, J., Schmitt, C., Schreyer, J. & Whitehead, H., 1977. *Solar radiation absorbing material..* US, Patent No. US4048980.

Greenberg, C., 1977. *Selective solar energy receiver and method for its production.* US, Patent No. US4061830.

Grilli, S. et al., 2011. 3D lithography by rapid curing of the liquid instabilites at nanoscale. *Proceeding of the National Academy of Sciences 108(37),* pp. 15106-15111.

Grips, V., Rajagopal, I. & Rajagopalan, S., 1991. *Black chromium plating bath useful for solar reflecting coatings.* US, Patent No. US5019223 A.

Guarnieri, C., 1985. *Radiant energy collector having plasma-textured polyimide exposed surface.* US, Patent No. US4521442.

Guarnieri, C. R., 1985. *Radiant energy collector having plasma-textured polyimide exposed surface..* US, Patent No. US4521442.

Hall, D. B., Underhill, P. & Torkelson, J. M., 1998. Spin coating of thin and ultrathin polymer films. *Polymer Engineering and Science 38(12),* pp. 2039-2045.

Hall, R. & Gunning, W., 1993. *Broad band light absorbing film.* US, Patent No. US 5179469 A.

Haran, E., Gringras, H. & Katz, D., 1965. Dielectric properties of an epoxy resin during polymerization. *Journal of Applied Polymer Science 9,* pp. 3505-3518.

Harding, G., McKenzie, D. & Window, B., 1978. *Method and apparatus for reactive sputtering.* US, Patent No. US 4128466 A.

Harkema, S., 2005. *Capillary Instabilities in Thin Polymer films Mechanism of Structure Formation and Pattern Replication.* s.l.:Department of Polymer Physics,University of Groningen, The Netherlands.

Hind, A. R. & Chomette, L., 2011. *The determination of thin film thickness using reflectance spectroscopy.* s.l.:Agilent Technologies.

Hoeflaak, M. & Jonkers, G., 1985. *Paint for applying spectral-selective coatings and process for the preparation thereof, solar heat absorbing device and solar collector containing such a device.* Canada, Patent No. CA 1187638 A.

Hultmark, G., 2001. *Method for manufacturing an absorbent layer for solar collectors, a device for performing the method and an absorbent layer for solar collectors.* US, Patent No. US 6171458 .

J.A. Woollam Co, n.d. *Spectroscopic Ellipsometry: Tutorial 1.* [Online] Available at: http://www.jawoollam.com/tutorial_1 [Accessed 25 February 2016].

Juang, R.-C.et al., 2010. Preparation of solar selective absorbing coatings by magnetron sputtering from a single stainless steel target. *Thin Solid Films 518(19),* pp. 5501-5504.

Kalogirou, S., 2009. *Solar Energy Engineering: Processes and Systems..* Oxford: Academic Press.

Kamande, J., Wang, Y. & Taylor, A., 2015. Cloning SU8 silicon masters using epoxy resins to increase feature replicability and production for cell culture devices. *Biomicrofluidics 9(3),* pp. 036502 1-11.

Kaminaga, M. et al., 2015. Uniform cell distribution achieved by using cell deformation in a micropillar array. *Micromachines 6,* pp. 409-422.

Katumba, G. et al., 2008. Solar selective absorber functionality of carbon nanoparticles embedded in SiO2, ZnO and NiO matrices.. *Physica Status Solidi C 5(2),* pp. 549-51.

Kennedy, C., 2008. *Progress to develop an advanced solar-selective coating.* Las Vegas, United States Government.

Kennedy, C.E, 2010. *High temperature solar selective coatings.* US, Patent No. US20100313875.

Kennedy, C. E., 2002. *Review of mid-to-high temperature solar selective absorber materials.,* Colorado: National Renewable Energy Laboratory.

Kennedy, C. E. & Price, H., 2005. *Progress in Development of High-Temperature Solar Selective Coating.* Orlando, s.n., pp. 6-12.

Kim, D. & Lu, W., 2006. Interface instability and nanostructure patterning. *Computational Materials Science 38,* pp. 418-425.

Kim, M., Kino-Oka, M. & Taya, M., 2010. Designing culture surfaces based on cell anchoring mechanisms to regulate cell morphologies and functions. *Biotechnology Advances 28,* pp. 7-16.

Kozelj, M. et al., 2010. *Coil-coated spectrally selective coatings on copper or aluminum with pigments modified by aminosilane.* World, Patent No. WO 2010133693 A1.

Kuckelkorn, T. & Graf, W., 2010. *Radiation-selective absorber coating with an adherent oxide layer and method of making same.* US, Patent No. US7793653.

Kuehn, R., Mikelsons, V. & Dorer, G., 1986. *Radiation absorbing surfaces.* US, Patent No. US4582111 [.

Kuehn, R., Mikelsons, V. & Dorer, G. L., 1986. *Radiation absorbing surfaces..* US, Patent No. US4582111.

Kunic, R. et al., 2011. Life expectancy prediction and application properties of novel polyurethane based thickness sensitive and thickness insensitive spectrally selective paint coatings for solar absorbers. *Solar Energy Materials and Solar Cells 95 (11),* p. 2965–2975.

Lampert, C., 1987. Advanced optical materials for energy efficiency and solar conversion. *Solar and Wind Technology Journal 4(3),* pp. 347-79.

Lau, C. & Russel, W., 2011. Fundamental limitations on ordered electrohydrodynamic patterning. *Macromolecules 44 (19),* p. 7746–7751.

Lazarov, M. & Mayer, I., 1997. *Material consisting of chemical compounds, comprising a metal from group IV A of the periodic system, nitrogen and oxygen, and process for its preparation.* US, Patent No. US5670248.

Lazarov, M. & Mayer, I., 1998. *Method for depositing thin layers of a material consisting of chemical compounds comprising a metal from group IV of the periodic system, nitrogen and oxygen onto heatable substrates.* US, Patent No. US 5776556 A.

Lee, Y., Kim, Y, Kim, Y., Yu, J.et al., 2011. Microlens array fabricated using electrohydrodynamic instability and surface properties. *Optics Express 19(11),* p. 10673.

Li, B., Ding, Y. & Yang, Q., 2013. A numerical study of nanoscale electrohydrodynamic patterning in a liquid film. *Soft Matter 9,* pp. 3412-3423.

Li, H. et al., 2013. Simulation and modelling of sub-30 nm polymeric channels fabricated by electrostatic induced lithography. *Royal Society of Chemistry Advances 3,* pp. 11839-11845.

Lin, Z. et al., 2002. Structure formation at the interface of liquid/liquid bilayer in electric field. *Macromolecules 35,* pp. 3971-3976.

Li, X. et al., 2014. Formation of arbitrary patterns in ultraviolet cured polymer film via electrohydrodynamic patterning. *The Scientific World Journal, Volume 2014, Article ID 840497*

Lundh, M., Blom, T. & Wäckelgård, E., 2010. Antireflection treatment of Thickness Sensitive Spectrally Selective (TSSS) paints for thermal solar absorbers. *Solar Energy 84(1),* pp. 124-129.

Mahajan, S., Steiner, U. & Goldberg-Oppenheimer, P., 2012. Hierarchical electrohydrodynamic structures for surface-enhanced raman scattering. *Advanced Materials 24 (23),* p. OP175–OP180.

Mahoney, A., Reed, S., Ashley, C. & Martinez, F., 2003. *Solar selective absorption coatings.* US, Patent No. US6632542.

Manigandana, S. et al., 2010. Electric field induced dewetting and pattern formation in thin conducting polymer film. *Sensors and Actuators B:Chemical 144(1),* pp. 170-175.

Masterbond, n.d. *Optimizing Electrical & Electronic Insulation Properties for Epoxies.* [Online] Available at: http://www.masterbond.com/techtips/optimizing-electrical-electronic-insulation-properties-epoxies
[Accessed 11 January 2016].

Mattox, D., 2010. *Handbook of Physical Vapor Deposition (PVD) Processing. 2nd Edition.* Kiddlington: William Andrew of Elsevier.

McMahon, T. & Green, A., 1997. *PbS-Al selective solar absorber.* US, Patent No. US4029853.

McMahon, T. & Jasperson, S., 1974. PbS–Al Selective Solar Absorbers. *Applied Optics 13 (12),* pp. 2750-51.

Melcher, J., 1963. *Field-Coupled Surface waves.* Cambridge, MA: The M.I.T. Press.

Meyer-Arendt, J., 1989. *Introduction to Classical and Modern Optics.* London: Prentice Hall International Editions.

Mills, D., 1986. *Solar selective surface coating.* US, Patent No. US4628905.

Morariu, M. et al., 2003. Hierarchical structure formation and pattern replication induced by an electric field. *Nature Materials 2*, pp. 48-52.

Muenker, A. & Young, A., 1981. *High temperature solar absorber coating and method of applying same.* US, Patent No. US4268319.

Needham, D., 1981. *Solar energy absorption material or coating comprising an arylene sulfide polymer.* US, Patent No. US4262661.

Nils Malmgren AB, n.d. *Epoxy plastics' general chemical and physical properties.* [Online] Available at: http://www.nilsmalmgren.com/epoxy-chemistry/epoxy-plastics-general-chemical-and-physical-properties/
[Accessed 25 February 2016].

Nixdorf, K. & Busse, G., 2001. The dielectric properties of glass-fibre-reinforced epoxy resin during polymerisation. *Composites Science and Technology 61,* pp. 889-894.

Norsk Hydro ASA, 2010. *New rolled products for solar technology.* [Online] Available at: http://www.hydro.com/en/press-room/Archive/2010/New-rolled-products-for-solar-technology/
[Accessed 8 January 2017].

Oelhafen, P. & Schüler, A., 2005. Nanostructured materials for solar energy conversion. *Solar Energy 79,* pp. 110-121.

Oetting, W. et al., 2010. *Method for the production of an absorber plate for solar collectors.* US, Patent No. US 20100236543 A1.

Orel, B. & Orel, C., 1990. Coil-coating paints for solar collector panels—I. Characterization and performance tests. *Solar & Wind Technology 7(6),* pp. 699-705.

Orel, Z., Leskovsek, N., Orel, B. & Hutchins, M., 1996. Spectrally selective silicon paint coatings: Influence of pigment volume concentration ratio on their optical properties. *Solar Energy Materials and Solar cells 40 (3),* pp. 197-204.

Ossila, n.d. *Spin Coating: A Guide to Theory and Techniques.* [Online] Available at: http://www.ossila.com/pages/spin-coating [Accessed 22nd February 2016].

Ostermann, D., 2011. *Layer system for solar absorber.* US, Patent No. US20110232723.

Ostermann, D., 2012. *Method and device for producing a highly selectively absorbing coating on a solar absorber component, and solar absorber having such a coating.* World, Patent No. WO2011117256.

Pattader, P., Banerjee, S. A. & Bandyopadyay, D., 2011. Multiscale pattern generation in viscoelastic polymer films by spatiotemporal modulation of electric field and control of rheology. *Advanced Functional Materials 21,* pp. 324-335.

Pease, L. & Russel, W., 2002. Linear stability analysis of thin leaky dielectric films subjected to electric fields. *Journal of Non-Newtonian Fluid Mechanics 102,* pp. 233-250.

Pease, L. & Russel, W., 2003. Electrostaically induced submicron patterning of thin perfect and leaky dielectric film: A generalized linear stability analysis. *Journal of Chemical Physics 118 (8),* pp. 3790-3803.

Pease, L. & Russel, W., 2004. Limitations on length scales for electrostatically induced submicrometer pillars and holes. *Langmuir 20,* pp. 795-804.

Peng, J., Han, Y., Yang, Y. & Li, B., 2003. Pattern formation in polymer films under the mask. *Polymer 44(8),* p. 2379–2384.

Rajagopal, I., 1999. *International Workshop on Surface Engineering and Coatings: June 25-30 1998 Bangalore.* Mumbai: Allied Publishers Ltd..

Ramezani Sani, S., Morteza Ali, A. & Jafari, R., 2011. A comparison between optical properties of TiO2 nanowires obtained by EMA method and experiment. *Physica B: Condensed Matter 406(18),* p. 3383–3388.

Rashidi, H., Yang, J. & Shakesheff, K., 2014. Surface engineering of synthetic polymer materials for tissue engineering and regenerative medicine applications. *Biomaterials Science(10) p 1318-1331.*

Raynaud, G., Morin, F. & Brossard, L., 1986. *Preparing selective surfaces for solar collectors by dry oxidation and selective surfaces so obtained.* US, Patent No. US4574778.

Reddy, P., Bandyopadhyay, D. & Sharma, A., 2010. Self-organized ordered arrays of core-shell columns in viscous bilayers formed by spatially varying electric fields. *Journal pf Physical Chemistry C 114,* pp. 21020-21028.

Reichert, W. & Ganz, K., 2002. *Solar collector element.* US, Patent No. US20020073988.

Reichert, W. & Ganz, K., 2004. *Composite material.* US, Patent No. US6692836.

Reuter, F. & Menzel, T., 1979. *Solar energy absorbent coatings.* Great Britan, Patent No. GB2004770.

Richards, B., 2004. Comparison of TiO2 and other dielectric coatings for buried contact solar cells: a review. *Progress in Photovoltaics: Research and Applications 12(4),* pp. 253-281.

Richards, B. S., 2004. Comparison of TiO2 and Other Dielectric Coatings for Buried contact Solar Cells: a Review. *Progress in Photovoltaics: Research and Applications,* pp. 253-281.

Rincón, M. et al., 2007. Optical characterisation of tandem absorber/reflector systems based on titanium oxide-carbon coatings. *Solar Energy Materials and Solar Cells 91,* pp. 1421-25.

Roberts, S. & Kumar, S., 2009. AC electrohydrodynamic instabilities in thin liquid films. *Journal of Fluid Mechanics 631*, pp. 255-279.

Rodrguez, M. et al., 2014. Measuring the contractile forces of human induced pluripotent stem cell-derived cardiomyocytes with arrays of microposts. *Journal of Biomechanical Engineering 136(5) pp 0510051.*

Russel, C. & Russel, W., 2011. Fundamental limitations on ordered electrohydrodynamic patterning. *Macromolecules 44(19)*, p. 7746–7751.

Sahu, N., Parji, B. & Panigrahi, S., 2009. Fundamental understanding and modelling of spin coating process: A review. *Indian Journal of Physics 83(4),* pp. 493-502.

Saito, R. et al., 2004. Optical absorption of graphite and single-wall carbon nanotubes. *Applied Physics A 78 (8),* pp. 1099-1105.

Sansom, E., Gharib, M. & Rinderknecht, D., 2011. *Fabrication of anchored carbon nanotube array devices for integrated light collection and energy conversion.* US, Patent No. US20110236619.

Saville, D., 1997. Electrohydrodynamics: The Taylor-Melcher leaky dielectric model. *Annual Review of Fluid Mechanics 29,* pp. 27-64.

Schardein, D. & Lloyd, R., 1978. *Process for applying thin molybdenum containing coatings on aluminum for solar energy absorption.* US, Patent No. US 4104136 A.

Scherber, W. & Dietrich, G., 1979. *Solar collector panel and method of making.* US, Patent No. US4148294.

Schmidt, R., 1966. *Solar heat absorbers comprising alternate layers of metal and dielectric material.* US, Patent No. US 3272986 A.

Schneiders, A. et al., 1979. *Preparation of selective surfaces for high temperature solar energy collectors.* Great Britan, Patent No. GB2016527.

Schäffer, E., 2001. *Instabilities in Thin Polymer Films: Structure Formation and Pattern Transfer.* s.l.:University of Konstanz, Department of Physics.

Schäffer, E., Thurn-Albrecht, T., Russell, T. & Steiner, U., 2001. Electrohydrodynamic instabilities in polymer films. *Europhysics Letters 53 (4),* 53(4), p. 518–524.

Selvakumar, N. & Barshilia, H., 2012. Review of physical vapor deposited (PVD) spectrally selective coatings for mid- and high-temperature solar thermal applications. *Solar energy Materials and Solar Cells 98,* pp. 1-23.

Selvakumar, N., Manikandanath, N., Biswas, A. & Barshilia, H., 2012. Design and fabrication of highly thermally stable HfMoN/HfON/Al2O3 tandem absorber for solar thermal power generation applications. *Solar Energy Materials and Solar Cells 102,* pp. 86-92.

Shah, T., Malecki, H., Adcock, D. & Heick, K., 2010. *Solar receiver utilizing carbon nanotube infused coatings.* US, Patent No. US20100258111.

Shankar, V. & Sharma, A., 2004. Instability of the interface between thin films subjected to electric fields. *Journal of Colloid and Interface Science 274,* pp. 294-308.

Sharma, V., 1981. *Fabrication of spectrally selective solar surfaces by the thermal treatment of austenitic stainless steel AISI 321.* US, Patent No. US 4268324 A.

Smith, C., 2012. *Trinity College Dublin: Surface and Interface Physics, Ellipsometry.* [Online] Available at: https://www.tcd.ie/Physics/Surfaces/ellipsometry2.php [Accessed 25 February 2016].

Sohol, R. et al., 2011. Effects of micropost spacing and stiffness on cell motility. *IET Micro and Nano Letters 6(5),* pp. 323-326.

Spanoudis, L., 1982. *Solar energy collector having solar selective coating of low reflectance.* US, Patent No. US4334523.

Straub, J., 1977. *Selective solar energy absorption.* US, Patent No. US 4036206 A.

Tabor, H., 1959. *Receiver for solar energy collectors..* US, Patent No. US2917817.

Taylor, J. F., 2001. Spin coating: An Overview. *Finishing For Electronics*, January 2001, pp. 16-21.

Telkes, M., 1977. *Selective black for absorption of solar energy.* US, Patent No. US4011190.

The Engineering Toolbox, n.d. *relative permitivity.* [Online] Available at: http://www.engineeringtoolbox.com/relative-permittivity-d_1660.html [Accessed 6th February 2016].

Tian, E., Svobodny, T. & Philips, J., 2011. Thin liquid film morphology driven by electro-static field. *Applied Mathematics and Mechanics 32(8),* pp. 1039-1046.

Tian, H. et al., 2013. Numerical characterization of electrohydrodynamic micro- or nanopatterning processes based on a phase-field formulation of liquid dielectrophoresis. *Langmuir 29(15)*, pp. 4703-14.

Tipler, P., 1987. *College Physics.* US: Worth Publishers Inc..

Tomar, G., Shankar, V., Sharma, A. & Biswas, G., 2007. Electrohydrodynamic instability of a confined viscoelastic liquid film. *Journal of Non-Newtonian Fluid Mechanics 143,* pp. 120-130.

Trease, C., Hadavinia, H. & Barrington, P., 2013. Solar selective coatings: the industrial state-of-the-art. *Recent Patents on Materials Science 6(1),* pp. 1-19.

Trease, C. et al., 2016. Cell morphology and growth observation studies on novel, chemically unmodified and patterned polymer surfaces for advanced tissue culture applications. *Polymer 109,* pp. 13-24.

University of Louisville: Micro/Nanotechnology Centre, 2013. *Spin coating theory.* s.l.:s.n.

Van Buskirk, O., 1982. *Solar selective surfaces.* US, Patent No. US4310596.

Verma, R., Sharma, A., Kargupta, K. & Baumik, J., 2005. Electric field induced instability pattern formation in thin liquid films. *Langmuir 21,* pp. 3710-3721.

Voicu, N., 2009. *Pattern Morphologies in Thin Liquid Films.* s.l.:University of Groningen.

Voicu, N. et al., 2007. TiO2 patterning using electro-hydrodynamic lithography. *Soft Matter (5),* 3(554-557), pp. 554-557.

Walsh, C. & Franses, E., 2003. Ultrathin PMMA films spin coated from toluene solutions. *Thin Solid films 429,* pp. 71-76.

Wang, F. et al., 2014. Optically induced electrohydrodynamic instability -based micro-patterning of fluidic thin films. *Microfluidics and Nanofluidics, 16* pp. 1097-1106.

Watase, M., Kudo, T. & Kanesaki, A., 1983. *Selective solar energy absorber.* Great Britan, Patent No. GB2102025.

Westin, G., Pohl, A. & Ekstrand, A., 2006. *Composite materials and method of its manufacture.* WO, Patent No. WO2006073357.

Wijewardane, S., 2009. Potential applicability of CNT and CNT/composites to implement ASEC concept: A review article. *Solar Energy 83 (8),* p. 1379–1389.

Woodman, T., 1981. *Paint composition for the spectrally selective coating of metal surfaces, method of producing coatings therewith and an article produced thereby.* US, Patent No. US 4277537.

Woodman, T. & Fischer, A., 1979. *Spectrally selective surfaces and method of fabricating the same.* US, Patent No. US4153753.

Wu, L. & Chou, S., 2005. Electrohydrodynamic instability of a thin film of viscoelastic polymer underneath a lithographically manufactured mask. *Journal of Non-Newtonian Fluid Mechanics 125,* pp. 91-99.

Wu, N., Pease, L. & Russel, W., 2006. Toward large-scale alignment of electrohydrodynamic patterning of thin polymer films. *Advanced Functional Materials 16(15),* pp. 1992-1999.

Wu, N. & Russel, W., 2009. Micro- and nano-patterns created via electrohydrodynamic instabilities. *Nano Today 4,* pp. 180-192.

Yanagida, K., Hirokane, T., Tsukiyasu, T. & Sato, T., 1984. *Material for selective absorption of solar energy and production thereof.* US, Patent No. US4442829.

Yang, Q., Li, B. & Ding, Y., 2013. A numerical study of nanoscale electrohydrodynamic patterning in a liquid film. *Soft Matter 9,* Volume 9, pp. 3412-3423.

Yan, X., Liu, G., Dickey, M. & Willson, C., 2004. Preparation of porous polymer membranes using nano- or micro-pillar arrays as templates. *Polymer 45(25),* pp. 8469-8474.

Yin, Y., Hang, L. & Mills, D., 2009. *Solar Absorptive Material For a Solar Selective Surface Coating.* US, Patent No. US20090151777 A1.

Yin, Z., Light selective absorbing coating and its process 2010. s.l. Patent No. US20100035034.

Yuste, F. et al., 2011. *Selective solar absorbent coating and manufacturing method.* US, Patent No. US20110249326.

Yu, W., Cargill, S., Leonard, M. & Desmulliez, P., 2008. Micro-fabrication on 3-D surface by electrostatic induced lithography. *Electronics System-Integration Technology Conference,* pp. 111-116.

Zeman, M. et al., 2012. Advancedl light management approaches for thin-film silicon solar cells. *Energy Procedia 15,* pp. 189-199.

Zhang, Q.-C., 2000. Recent progress in high-temperature solar selective coatings. *Solar Energy Materials Solar Cells 62,* pp. 63-74.

Zhang, Q.-C. & Mills, D., 1997. *Solar selective surface coating.* WO, Patent No. WO9700335.

Zhang, Q.-C., Mills, D. & Monger, A., 1996. *Thin film solar selective surface coating.* US, Patent No. US5523132.

Zhang, Q.-C.et al., 1998. New cermet solar coatings for solar thermal electricity applications. *Solar Energy 64 (1-3),* pp. 109-114.